DEVELOPMENT OF AN OFF-ROAD CAPABLE TIRE MODEL FOR VEHICLE DYNAMICS SIMULATIONS

by

Brendan Juin-Yih Chan

Dissertation submitted to the faculty of the Virginia Polytechnic Institute and State University in partial fulfillment of the requirements for the degree of

Doctor of Philosophy
In
Mechanical Engineering

Dr. Corina Sandu
Dr. Mehdi Ahmadian
Dr. Saied Taheri
Dr. Dennis Hong
Dr. Marte Gutierrez
Dr. Harry Dankowicz
Mr. David Glemming

14th January 2008
Blacksburg, Virginia

Keywords: Terramechanics, tire model, vehicle dynamics, off-road

DEVELOPMENT OF AN OFF-ROAD CAPABLE TIRE MODEL FOR VEHICLE DYNAMICS SIMULATIONS

Brendan Juin-Yih Chan

(ABSTRACT)

The tire is one of the most complex subsystems of the vehicle. It is, however, the least understood of all the components of a car. Without a good tire model, the vehicle simulation handling response will not be realistic, especially for maneuvers that require a combination of braking/traction and cornering. Most of the simplified theoretical developments in tire modeling, however, have been limited to on-road tire models. With the availability of powerful computers, it can be noted that majority of the work done in the development of off-road tire models have mostly been focused on creating better Finite Element, Discrete Element, or Boundary Element models.

The research conducted in this study deals with the development of a simplified tire brush-based tire model for on-road simulation, together with a simplified off-road wheel/tire model that has the capability to revert back to on-road trend of behavior on firmer soils. The on-road tire model is developed based on observations and insight of empirical data collected by NHSTA throughout the years, while the off-road tire model is developed based on observations of experimental data and photographic evidence collected by various terramechanics researchers within the last few decades.

The tire model was developed to be used in vehicle dynamics simulations for engineering mobility analysis. Vehicle-terrain interaction is a complex phenomena governed by soil mechanical behavior and tire deformation. The theoretical analysis involved in the development of the wheel/ tire model relies on application of existing soil mechanics theories based on strip loads to determine the tangential and radial stresses on the soil-wheel interface. Using theoretical analysis and empirical data, the tire deformation geometry is determined to establish the tractive forces in off-road operation.

To illustrate the capabilities of the models developed, a rigid wheel and a flexible tire on deformable terrain is implemented and output of the model was computed for different types of soils; a very loose and deformable sandy terrain and a very firm and cohesive Yolo loam terrain. The behavior of the wheel/tire model on the two types of soil is discussed. The outcome of this work shows results that correlate well with the insight from experimental data collected by various terramechanics researchers throughout the years, which is an indication that the model presented can be used as a subsystem in the modeling of vehicle-terrain interaction to acquire more insight into the coupling between the tire and the terrain.

ACKNOWLEDGEMENT

I wish to thank my advisor Dr. Corina Sandu, who, over the course of my time as a graduate student, has been a great source of inspiration. Throughout my time here, Dr. Sandu has served as both a mentor and friend, and I greatly appreciate her support. I wish to also thank the members of my Ph.D. committee for their guidance and support throughout the entire research effort, and for their counsel in my work during my time at Virginia Tech. My gratitude goes forth to Dr. Mehdi Ahmadian, Dr. Saied Taheri, Dr. Dennis Hong, Dr. Marte Gutierrez, Dr. Harry Dankowicz and Mr. David Glemming from Goodyear Tire and Rubber Company. Their input to my work has often provided me with guidance that steered me in the right direction. In addition to the faculty, I would also like to thank the department and the various sources of funding that has graciously funded my studies.

I would also like to thank Dr. Steve Southward and Dan Reader in PERL for allowing the use of the equipment in the quarter car rig in Danville. Their assistance during the time we were assembling the tire mechanics rig are greatly appreciated. My gratitude also goes to Scott Israel for his hospitality during my time in Danville. Special thanks also go to Dr. Kamel Salaani from NHTSA for on-road tire testing data used in this dissertation.

I would like to thank all my colleagues at AVDL for their contributions and input to my work. Amongst the group of friends and colleagues that have helped me throughout the years, many of you have helped me in your own little ways. The list of colleagues that have helped me includes but is not limited to Dr. Jeong-Hoi Koo, Dr. Fernando Goncalves, Emmanuel Blanchard, Dr. Mohammad Elahinia, Lin Li, Brian Southern and Brent Ballew.

I would like to express my deepest gratitude to my family, and in particular to my mother, Mdm. Sim Kui Hua, for her tireless devotion and love can never be repayed.

Finally, I would like to express my sincerest gratitude to my dearest Ing-Ling for putting up with everything. Her support and encouragement has been a constant source of inspiration to me, through the late nights and the long days. I am forever indebted to her.

"Every body continues in its state of rest, or of uniform motion in a right line, unless it is compelled to change that state by forces impressed upon it."

- Sir Isaac Newton
  Newton's First Law of Motion
  Philosophiae Naturalis Principia Mathematica (1687)

CONTENTS

LIST OF TABLES

LIST OF FIGURES

1. Introduction

This chapter provides a brief introduction into the research conducted towards the completion of this dissertation, and the motivation behind this study. The objectives of the research are also presented, as well as a short outline of the following chapters.

1.1 Preliminary Overview: The big picture

The invention of the wheel nearly 5000 years ago continues to spur intensive studies aimed at improving its performance as a locomotion tool. Compared to the wheel, the tire is a relative recent invention, but its development was not an instantaneous event. There were a lot of iterations and variants of the tire that were created before the current design came into being. In 1844, Charles Goodyear discovered the process of vulcanization for rubber, which made it feasible to be used for tires. The next step was the invention of the air-filled (pneumatic) tires for bicycles by John Dunlop. In the year 1895, André Michelin became the first person to try to use pneumatic tires on an automobile; but it was Philip Strauss that invented the first successful tire, which combined the tire structure and an air-filled inner tube. In 1903, P.W. Litchfield of the Goodyear Tire Company patented the first tubeless tire, but this did not end at that time into a commercially available product. Frank Seiberling then created grooved tires which significantly improved road traction. Later, with the addition of carbon to the rubber used in the tire structure, the B.F. Goodrich Company developed tires similar to today's products and with longer service life than previous attempts.

The tire is a critical element of the vehicle, as it serves many purposes. Amongst the *raison d'etre* for tires are:

1. Supporting the vehicle load. The tire has to support the weight of the vehicle and of all the passengers for extended periods of time.
2. Providing traction to the vehicle. The tire is the compliant "gearing mechanism" that allows the power of the engine to be transformed into motion via the interface with the running support.
3. Acting as the secondary suspension in tandem with the vehicle primary suspension. The tire is responsible for filtering out most of the road irregularities,

particularly the ones that excite the suspension with frequencies higher than the "wheel hop" frequencies.

4. Helping the vehicle to steer. By changing the toe angle of the tire, one should be able to steer the vehicle in the direction of intended motion.

Currently, all the tires used for on-the-road driving have adopted the radial-ply construction [1]. This design was originally conceptualized by Michelin but quickly became standard as it holds many advantages over the other designs. The structure of the tire does not consist of just the vulcanized rubber, since, among other faults, it will be too weak to support the vehicle weight. Tires are made of several layers of rubber and cords of polyester, steel, and/or other textile materials. This intricate network of various materials gives the tire strength and shape and is usually referred to as the carcass. The main types of construction for tires can be seen in Figure 1-1.

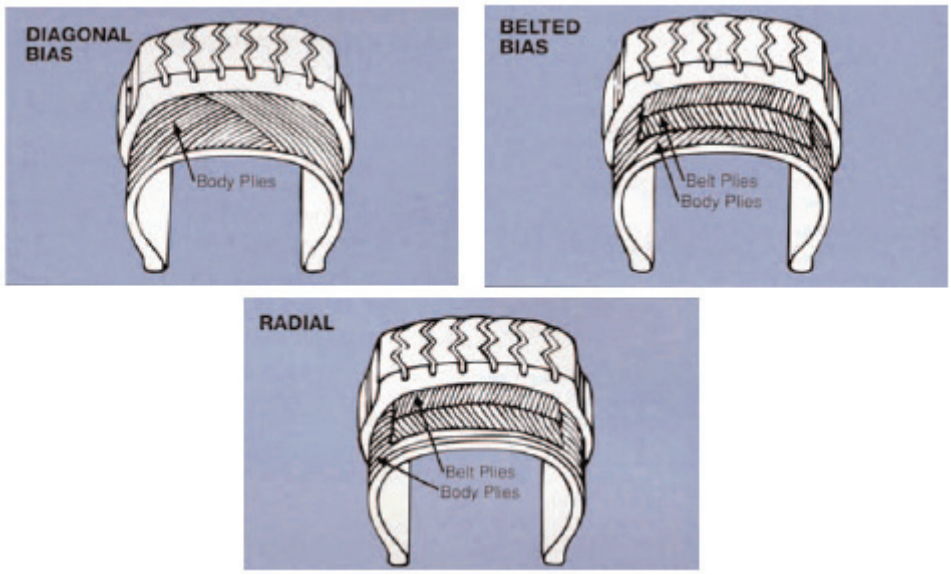

Figure 1-1. Different configurations of the belt plies on various tire types (Reprinted from [1], obtained from NHTSA report DOT-HS-810-561 under the FOIA)

The diagonal bias design, also known as the bias-ply or cross design, was used almost exclusively until the 1950s. Today, it is still used by some large trucks, trailers, and farming tractors, but have largely been displaced by radial-ply tires for passenger car vehicles. The bias-ply tire has the advantage that is easy to manufacture. However, it

suffers from a conceptual design flaw since as the tire deflection increases, the internal shearing of the tire cords generates heat and causes chafing of the different layers of material within the structure, which significantly reduces the service life of the tire. The addition of a belt in the tread region creates the bias-belted design, which adds stiffness to the tire, prolonging the service life of the tire. Even so, this design suffers from the same *Achilles heel* as the bias-ply tire, in which the heat generation resulting from the friction of the internal structure has not decreased much from the bias-ply design. This design was then replaced with the radial-ply design, which has the cords running from bead-to-bead of the tire. This design provides maximum ride comfort without sacrificing the longetivity of the tire. A well-designed radial-ply tire is estimated to provide an increase of service life by 80% over the bias-ply design [2]. Thus, most tire manufacturers shifted towards the production of the radial-ply tire, despite the higher manufacturing costs and the more complex manufacturing process. An overview picture of the materials forming the internal structure of a typical modern day passenger car radial-ply tire is shown in Figure 1-2.

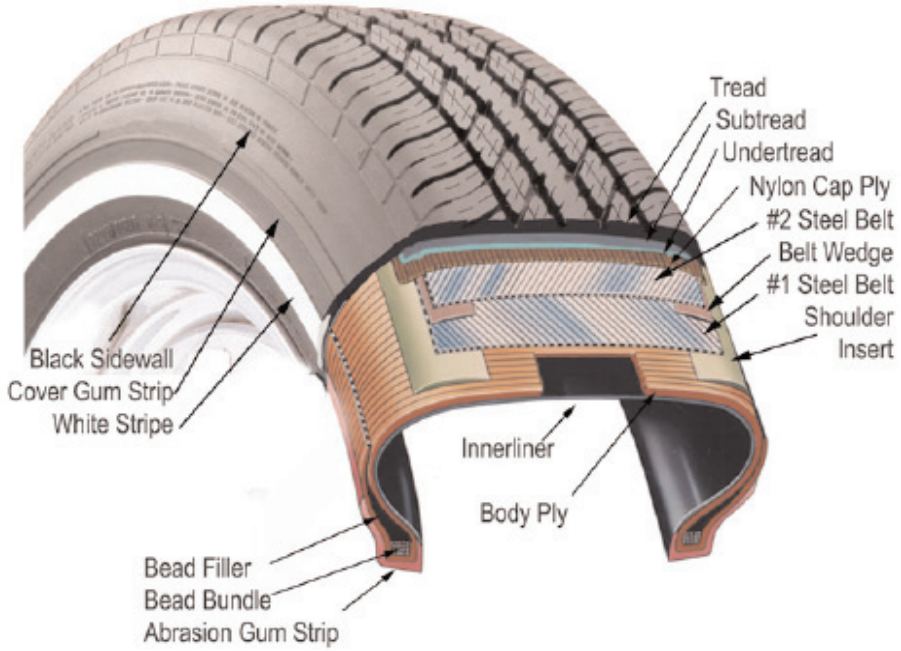

Figure 1-2. The construction of a modern day radial-ply tire (Reprinted from [1] , obtained from NHTSA report DOT-HS-810-561 under the FOIA).

From the tire modeling perspective, this transition towards radial-ply tire causes an increased complexity in tire models. The addition of a stiff belt in the circumferential direction of the tire, as well as the more compliant sidewall yield the need to utilize beam models to account for the lateral deflection of the tire. Primarily, the modeling efforts have focused in modeling of on-road tire behavior, with the development of various analytical/empirical models. The modeling efforts of off-road tires have been primarily confined to the terramechanics community, with the emphasis on determining the mobility of certain vehicles [3] rather than for vehicle dynamics simulations. Hence, it is hoped that the work presented in this document will provide a unifying analytical insight into tire modeling from the vehicle dynamics, terramechanics, and the multibody dynamics perspectives.

1.2 Research Objectives

The primary objectives of this research are to:

1. Explore the current state of the art in on-road tire modeling, which includes experimental and analytical modeling in order to understand the limitations and strengths of the most advanced approaches in tire modeling.
2. Explore the current state of the art in vehicle-terrain interaction in order to develop a new off-road tire model and to apply it within the terramechanics /vehicle dynamics framework.
3. Develop novel three-dimensional tire models, consisting of an on-road model that can be parameterized using conventional tire tests and an off-road tire model which can be parameterized using experimental data from terramechanics tests.
4. Employ soil dynamics and terramechanics knowledge to develop tire-soil interaction models.
5. Provide the implementation of the models within the MATLAB environment for applications in vehicle dynamics simulations.

1.3 Research Approach

To achieve the objectives of this study, we will develop three-dimensional tire models, and utilizing deformable soil models, we also will develop models of the dynamic

interaction between the tire and its running support, which can either be asphalt/tarmac or deformable soils. The tire model will be based on the forces and moments calculated at the contact patch of the tire, which will then be propagated onto the center of the wheel via the loaded radius and the tire forward and lateral scrub.

The following assumptions have been made for the development of the models mentioned above:

1. When the ground becomes very hard/rigid, the tire model switches to the behavior of a deformable tire operating on road.
2. The soil is mechanically modeled as a plastic material using the equilibrium equations based on strip load analysis.
3. The tire model is based on analytical mechanics and augmented with empirically obtained information to account for effects otherwise not possible to be captured.
4. The tire remains in contact with the ground at all times.
5. The tire model should revert to a pure longitudinal model or to a pure lateral slip model when the lateral, respectively the longitudinal slip is zero.
6. The tire inflation pressure and the temperature remain constant or change at a very slow rate during the entire simulation.

1.4 Research Contribution

The contributions of this dissertation to tire modeling and vehicle dynamics community are described next. The main focus of this research was to develop a unified framework for on-road/off-road vehicle dynamics modeling by seamlessly incorporating:

1. Component-based modular formulation for the dynamics of vehicle sub-systems.
2. Semi-empirical studies and theoretical principles for dynamic tire modeling.
3. Established experimental methods for tire testing, based on industry standards.
4. Theory of plasticity-based soil mechanics approach for the terramechanics models.

Among the most important contributions of the dissertation is the original development of a comprehensive formulation for an on-road tire model and for an off-road tire model with the inclusion of:

1. Lateral tire dynamics due to the shear phenomena at the contact patch and bulldozing on the sidewall of the tire.
2. A mechanics based approach for the computation of combined slip forces.
3. New formulations of tire slip which allows for a new formulation of the shear deformation of soil in both longitudinal and lateral directions in the contact patch.

Moreover, the development of a hybrid analytical-empirical method of characterizing the tire deformation (for both carcass and tread) on soft soil and the incorporation of tire mechanical properties in the force calculation add much needed insight into a field that has been traditionally dominated by empirical methods. Through the usage of a rigorous analytical-empirical method for characterizing soil behavior and tire-soil interaction via the application of plasticity theory, we hope to bridge the gap between these areas. Developing consistent, but stand-alone formulations for the on-road and for the off-road tire models, we will recover the on-road formulation from the off-road formulation if the soil is extremely rigid. During the research performed for this dissertation we have also designed and constructed a low-cost modular attachment for a tire mechanics test rig, which relies on the development of streamlined testing methodologies for tire mechanical properties.

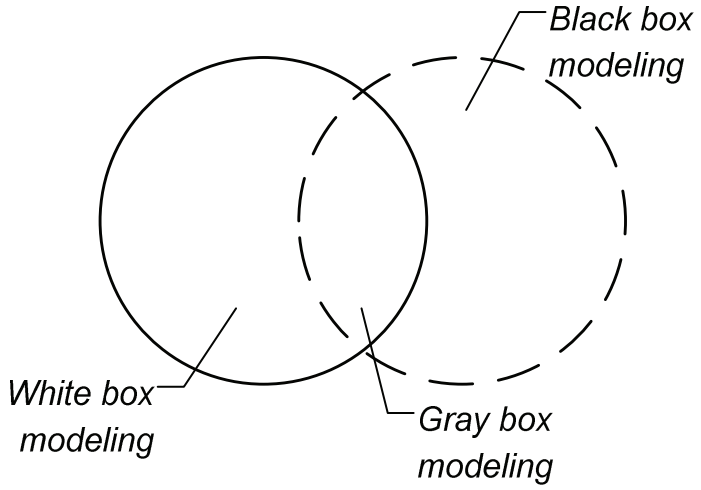

Figure 1-3. Gray box modeling as a blend between white box and black box modeling.

The results presented in this dissertation are expected to provide more insight into the tire-terrain interaction, and to open a new avenue for research in this area by shifting

from a “black box” (empirical) modeling approach to one based on the dynamics of the soil-tire interaction. With the development of this research, we hope to create a blend of “white box” (physical) modeling and “black box” modeling (shown graphically in Figure 1-3) to create an empirical/analytical model that does not only provide physical insight into the wheel/tire-ground interaction problem but also generate and accurate representation of their behavior during vehicle simulations.

1.5 Dissertation Outline

Background information for this study, which is introduced in Chapter 2, includes an explanation of the tire structure, a discussion of the methods for terramechanics characterization of traction, and a literature review on related research.

Chapter 3 focuses on the development of the on-road tire model, which will serve as the basis of for the off-road tire model. This on-road tire model employs some of the most advanced techniques and observations in tire modeling for vehicle dynamics simulations. The process of development for this tire model has been guided by analysis and studies of experimental data collected by NHTSA during the last few decades.

Chapter 4 discusses in detail the development of a rigid wheel model operating on soft soil, and also the development of a flexible tire model operating on soft soil. Both models are able to capture the tire dynamics under combined slip conditions in off-road vehicle dynamics simulations.

Chapter 5 presents the testing methodology developed to collect data needed for the tire models. This chapter also discusses the approach proposed for using the tire testing data to identify the parameters needed to characterize the tire models for on-road and off-road vehicle dynamics simulation.

Chapter 6 presents results for both on-road and off-road tire models in pure slip and in combined slip operations. These results are discussed from the qualitative perspective to provide an insight into the fundamental capabilities of off-road tire models on different soil types. The chapter also illustrates a good agreement between the response of the on-road tire model and experimental test data.

Chapter 7 discusses an investigation of an alternative lumped parameter-based approach to tire modeling, where the tire-terrain interaction is modeled using unilateral springs and dashpots.

Finally, Chapter 8 summarizes the results of the study and provides recommendations for future research.

2. Background and Review of Literature

The tire is one of the most complex subsystems of a vehicle. It is, however, the least understood of all the components of a car, compared with the driveline, engine and suspension. Tire modeling is an essential part of Computer Aided Engineering (CAE). Without a good tire model, the vehicle simulation handling response will not be realistic, especially for maneuvers that require a combination of braking/traction and cornering. In this chapter, some vehicle dynamics background will be presented, together with the basic terminology for tire parameters and modeling. In the next section, we will describe some of the most recent off-road tire models.

2.1 Background: Basic Tire and Vehicle Dynamics Terminology

In this section, some of the basic terminology used by the vehicle dynamics community [4] will be introduced. First, we will explain some of the basic terminology used throughout the dissertation, especially regarding the systems of coordinates, orientations, velocities, forces, moments, etc. Throughout this dissertation, we will primarily use nomenclature and definitions based on the SAE standard, which is employed by the industry for vehicle dynamics simulations. However, the development of the off-road model in chapter 4 will be based on the ISTVS axis system, and throughout the entire chapter 4, be transformed into the SAE system. Figure 2-1 shows the tire axis system recommended by SAE. The origin (or point of reference) of the tire axis system is the center of the tire contact patch. The most important definitions are presented, as they are defined in the SAE standards for tire modeling [5].

1. Slip angle (α)

   The angle between the travel direction of wheel and the direction in which the wheel is oriented where $|\alpha| < 90^{\circ}$. A positive slip angle corresponds to the tire moving to the right as it advances forward.

2. Angular velocity of the wheel (ω)

   ω, is the rotational velocity of the wheel measured at the center of the wheel-tire assembly.

3. Loaded Radius (R_l)

The loaded radius is defined as the distance from the center of the center of the tire contact to the wheel center, in the wheel plane.

4. Longitudinal Slip Ratio (s)

   Let us consider a tire rolling on a straight line, with the slip angle α. The effective angular speed of the tire is ω, and the effective linear speed (the linear speed of the center of the wheel in the longitudinal direction) is denoted by V. Due to the slip which occurs at the tire-road interface, there will be a difference between the theoretical tire velocity and its actual velocity, a phenomena captured mathematically by the longitudinal slip ratio, s.

$$s = s_d = 1 - \frac{V}{R_l \omega} \tag{2.1}$$

   Where the $|s| < 1$

5. Camber angle (γ)

   The camber angle is the inclination angle between the vertical (z-axis) and the wheel plane. A positive camber angle corresponds to the top of the tire being inclined outward from the vehicle.

6. Tire Forces (F_x, F_y, F_z)

   F_x - Longitudinal force of the tire, acting in the direction of the forward motion of the wheel, in the plane of the road.

   F_y - Lateral force of the tire, acting in the direction perpendicular to the longitudinal force, in the plane of the road.

   F_z - Vertical force of the tire, acting in the direction of the vector normal to the road plane.

7. Peak coefficients of friction (μ_{px}, μ_{py})

   μ_{px} = Maximum ratio of the longitudinal tire force to the vertical tire force.

   μ_{py} = Maximum ratio of the lateral tire force to the vertical tire force.

8. Sliding coefficients of friction (μ_{sx}, μ_{sy})

   μ_{sx} = Ratio of the longitudinal tire force to the vertical tire force at $|s| = 1$.

μ_{sy} = Ratio of the lateral tire force to the vertical tire force at $|\alpha| = 90^{\circ}$

9. Tire moments (M_x, M_y, M_z)

   M_x = Overturning moment of the tire, acting about the axis parallel to the longitudinal force vector.

   M_y = Rolling resistance moment of the tire, acting about the axis parallel to the lateral force vector.

   M_z = Aligning moment of the tire, acting about the axis parallel to the vertical force vector.

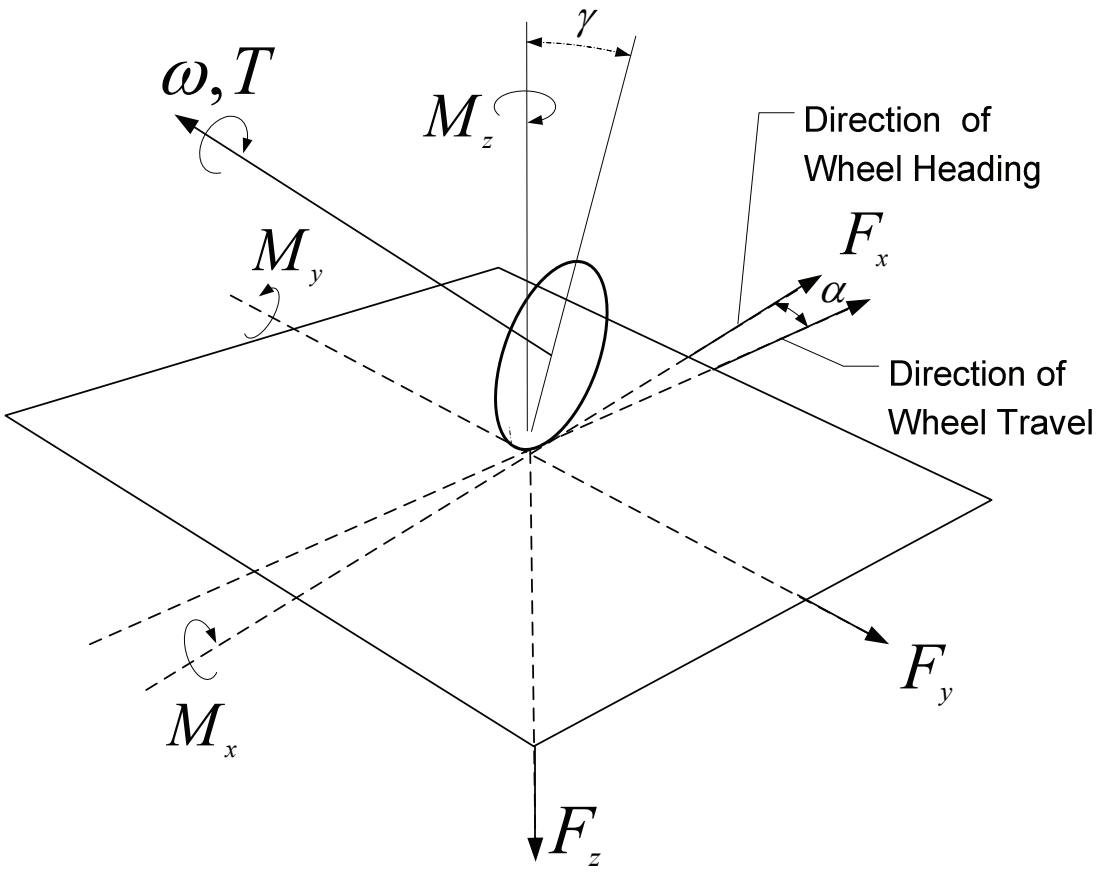

Figure 2-1. Definition of some of the tire terminology according to SAE J670[5].

2.2 Review of Literature: Terramechanics

In addition to an introduction to vehicle dynamics, it is also important to provide an introduction to terramechanics, as a lot of the theories used to develop the off-road tire

model comes from the work done by the terramechanics community. Terramechanics is the engineering field that studies the physical interaction of a vehicle, machinery, or implement with off-road terrain. One of the main research directions in terramechanics is the characterization of vehicle-terrain interaction. This topic has long been a subject of high interest for the Army, for planetary exploration agencies, as well as for agricultural, construction, and mining industries. However, capturing the dynamic contact between vehicle tires and deformable terrain is not an easy task, and has been challenging terramechanics researchers for over half a century [3, 6]. After the Second World War, the roads that were developed as the backbone infrastructure of logistics remained the primary locomotion path for the automobiles. Therefore on-road locomotion increased tremendously, and most of the vehicle dynamics research efforts have been dedicated to on-road driving. As a consequence, substantial developments related to the vehicle sub-systems and tires occurred, all oriented at improving on-road locomotion, while very little attention was given to off-road locomotion. In this study we paid special attention to those off-road locomotion research efforts that have taken place throughout the years. These approaches can be divided into three primary categories:

1. Empirical Methods
2. Analytical Methods
3. Finite Element (FE)/Boundary Element (BE)/ Discrete Element (DE)/(Lumped Parameter Approach) Methods

The review of literature for this section was done using the COMPENDEX, which is the most comprehensive and up-to-date bibliographic database of engineering research available via the Virginia Polytechnic Institute and State University library, containing over nine million references and abstracts taken from over 5,000 engineering journals, conferences and technical reports. A flowchart of the literature search conducted in the process of looking at the state-of-the-art work is shown in Figure 2-2.

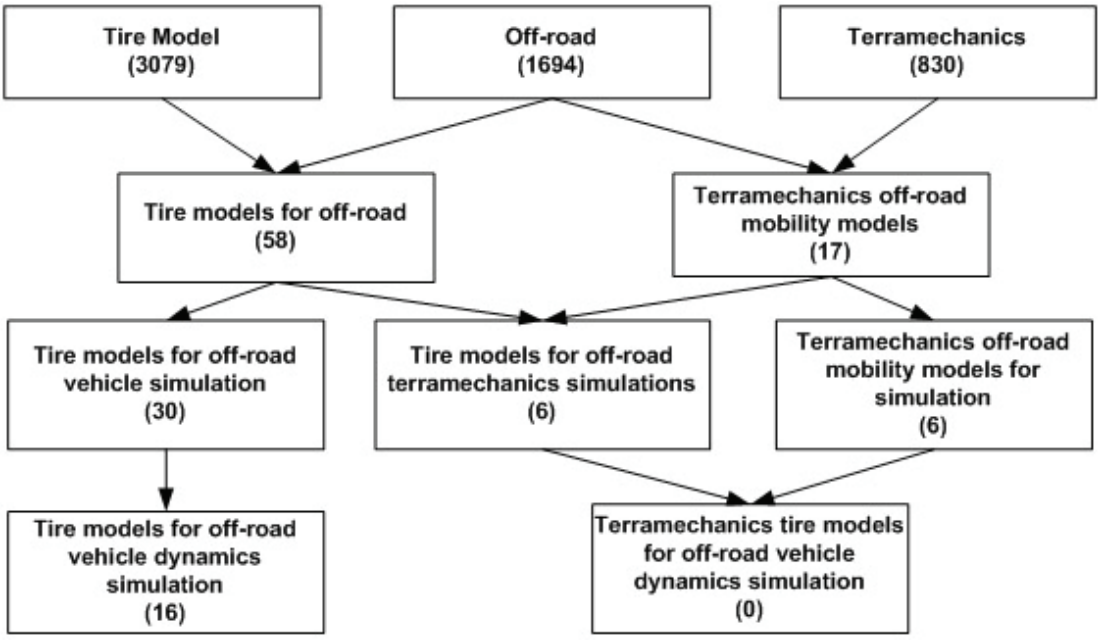

Figure 2-2. Flowchart of the literature search

The literature search started by using the key words "tire model", "off-road" and "terramechanics" and expanded from there. The number of results obtained is included in parentheses for each search, as shown in the flowchart.

2.2.1 Empirical Methods for Traction Modeling

The next few subsections will focus on the most up-to-date methodologies used to compute the tractive performance of the tires and tracks on deformable ground. One of the methods commonly used to predict the ability of a vehicle to negotiate over unprepared terrain is based on Bekker's bevameter technique [7]. Following World War II, the study of off-road vehicle-terrain interaction has been primarily driven by the work done by Dr. M. G. Bekker from the Land Locomotion Laboratory in the U.S. Army Detroit Arsenal. The formulation relies on semi-empirical equations that relate the vehicle sinkage and the vertical distribution of the pressure in the contact patch at the locomotion interface. The parameterization of equation (2.2) is done using the apparatus called bevameter, with a sinkage plate of specified dimensions.

$$\sigma_n = \left(\frac{k_c}{b} + k_\phi \right) z^n \tag{2.2}$$

Where:

σ_n = Pressure normal to the sinkage plate
k_c = Cohesion-dependent parameter
k_ϕ = Friction angle dependent parameter
n = Sinkage index
b = Plate width
z= Sinkage

To account for the soil shearing phenomenon at the tire-terrain contact, expressions that compute the shear stress (based on the shear displacement) have been developed for several soil types and validated against experimental data. However, in the relation provided by Bekker's Method, there is no coupling between the shear deformation of the soil and the normal stresses generated by the soil surface. According to Bekker, the shear stress at the interface of the sinkage plate, in the direction of applied tangential loading can be calculated with equation (2.3) :

$$\tau = \frac{K_3}{2K_1\sqrt{K_2^{\,2}-1}}\left(e^{\left(-K_2+\sqrt{K_2^{\,2}-1}\right)K_1 i} - e^{\left(-K_2-\sqrt{K_2^{\,2}-1}\right)K_1 i}\right) \tag{2.3}$$

Where:

K_1, K_2, K_3 = Empirical Constants determined by experiments

As evident from equation (2.3), the relationship between the soil shear and the soil compaction is purely empirical according to Bekker's Method, and thus it does not imply a strong causative physical connection with physically-based modeling. Nevertheless, in addition to Bekker's method, there are other empirical relationships that have been used by the terramechanics community for calculating the shear stress at the interface of locomotion. Among the most widely used shear stress formulations are those based on Janosi and Hanamoto approach [8], in which once the stresses normal to the loading surface have been calculated, the shear stresses tangential to the surface of the sinkage plate can be approximated using a combination of the Mohr-Coulomb Failure Criterion and the Janosi-Hanamoto relation (equation (2.4)) from [8].

$$\tau = \underbrace{(c + \sigma_n \tan(\phi))}_{Mohr-Coulomb\ Limit}(1 - e^{-\frac{j}{K}}) \tag{2.4}$$

Where

c = Soil cohesion
j = Soil-plate interface shear displacement
K = Shear deformation modulus in direction of motion
ϕ = Internal friction angle, representing the slope of the Mohr-Coulomb Failure Envelope

Equation (2.4) has been used successfully by various terramechanics researchers throughout the years to characterize the shear force generation mechanism at the vehicle-terrain interface. It is assumed that the direction that this shear stress acts on is parallel to the direction of the principle stress in the soil mass under the vehicle. The angle ϕ represents the slope of the Mohr-Coulomb Failure Criteria for soils and hence is limited to measurable values of 0° ~ 45°. Inspired by the work done by Bekker but unconvinced by the results for the pressure-sinkage relationship, Reece [9] proposed a new pressure-sinkage relationship based on the work done by Meyerhof [10] for the settlement problem. When the Meyerhof equation (2.5) , which is the solution to the plasticity equation under certain assumptions, is examined closely, it can be noticed that it has two parts. The first part of the equation contains terms pertaining to the cohesion of the soil and the second part consists of terms related to the surcharge and the soil weight. The calculations involved in the mathematical derivation of this equation are very complex and the details are presented in [10], for further reading. It can thus be stated that maybe one of the most important contributions of Meyerhof's work was that it encouraged Reece to develop a new pressure-sinkage relationship based on the solutions for the plasticity equation.

$$\sigma_n = ck_c' \left(\frac{z}{b}\right)^n + \frac{\gamma b k_\phi'}{2}\left(\frac{z}{b}\right)^n \tag{2.5}$$

Where:

σ_n = Pressure normal to the sinkage plate
k_c ' = Cohesion-dependent parameter
k_ϕ ' = Friction angle dependent parameter
n = Sinkage index
b = Plate width
γ = unit weight of the soil
c = cohesion variable of the soil

In [8], it was discovered that the friction angles measured from bevameter tests are significantly lower than the ones acquired using a triaxial test apparatus. It was surmised that the lateral failure experienced by the soil from the bevameter limits the magnitude of the lateral shear stresses, hence, although it can be used to characterize the strength of the wheel-soil interface, its usage to characterize the internal strength of the soil (below the surface of contact) may not be appropriate.

The applicability of Bekker's method for various classes of vehicle-terrain interactions has been extensively investigated by many researchers which identified the limitations of the methods. The literature also illustrates that Janosi's formula for modeling the shearing action at the soil-wheel interface has been successfully applied to various studies. It must be noted that the formula, although originally developed for tracked vehicles, has been applied successfully by researchers during the past few decades on various locomotion problems for wheeled vehicles, to a certain extent.

El-Gawwad et. al. [11] developed a multi-spoke tire model using Bekker's method and included the effect of straight lugs on vehicle-terrain interaction. The primary tire type on which this study focuses is that of an agricultural tire. The tire model developed attempted to take into account many important parameters which affect vehicle maneuvering such as slip angle, soil deformation modulus, lug dimensions, and lug spacing. A comparison was done between a smooth tire model and a tire model with lugs. The conclusions that drawn from the implementation of this tire model are:

1. The tire forces and moments decrease with increase in both lug height and ratio of (total area of lug)/(total area of tread).

2. The effect of including lugs on the tire model is that the side and tractive forces generated from the model are higher than on a smooth tire because of the dominant effect of the lugs on generating tractive forces in agricultural tires.
3. The overturning moment, aligning moment, and rolling resistance moment tend to decrease towards zero as the value of the Bekker parameters are increased. This is physically viable as it means that as the soil becomes stiffer, the effects of the lugs become less dominant as the deflection happens mainly at the tread.

However, most of the results in this study are steady-state results based on a tire model developed with the pressure/sinkage relationship developed by Bekker. The model is then extended [12] to include the effects of camber on the lateral and longitudinal slip on an off-road tire. A comparison was done again on a smooth tire and a tire with lugs to study the effect of slip angle, camber angle, and terrain characteristics on off-road tire performance. The results from this study conclude that for a cambered tire with lugs, larger longitudinal and lateral forces are generated as compared to a smooth tire. As expected, as soil stiffness increases, the effects of the lugs become less noticeable. The effect that angled lugs would have on generating normal and tangential forces for the multi-spoke tire model is also discussed in [11] and [12]. In this regard, it was determined that:

1. The angled lugs provide higher values of lateral force and reduce the magnitude of the tractive force for the tire model as compared to the straight lugs case.
2. The pull forces acting on the lugs increase with longitudinal slip, but as soil hardness and soil deformation modulus increases, the forces developed from the angled lugs becomes less significant.
3. Increasing lug height reduces the forces generated by the angled lugs but beyond a certain value, the lug height does not affect the tire performance.
4. Increasing the lug angle decreases the pull force on the tire but increases the lateral force at the tire. This suggests that an increase in the lug angle will increase the lateral stability of the tire.

Another popular empirical method for determining the mobility of wheeled/tracked vehicles on different terrain conditions was developed by the Waterways Experimentation Station (WES) [13] and it is called the cone penetrometer (or cone

index) method. The WES-method is based on the use of the apparatus named penetrometer to assess the "go/no-go" scenario for military vehicles and is originally developed by the U.S. Army Corps of Engineer at the WES in Vicksburg, Mississippi. The soil parameter of interest acquired using this method is the penetration resistance of the soil measured using a standard cone penetrometer. Primarily, this method has been used in the NATO Reference Mobility Model (NRMM) to determine the trafficability of military vehicles over different terrain types.

There are other empirical-analytical methods developed for agricultural applications such as the one proposed by Brixius [14], which also relies on data obtained by the cone penetrometer. Brixius expressed Gross Traction Ratio (GTR) and Motion Resistance Ratio (MRR) as a function of mobility number (N_B) and wheel slip (s). The relations developed by Brixius are shown in equations (2.6) - (2.9).

$$N_B = \left(\frac{CI \cdot b \cdot d}{W}\right) \cdot \left(\frac{1 + K_1\left(\delta / h\right)}{1 + K_2\left(b / d\right)}\right) \tag{2.6}$$

$$GTR = \frac{T}{r \cdot W} = C_1\left(1 - e^{-C_2 \cdot N_B}\right)\left(1 - e^{-C_3 \cdot s}\right) + C_4 \tag{2.7}$$

$$MRR = \frac{M}{W} = \frac{C_5}{N_B} + C_4 + \frac{C_6 \cdot s}{\sqrt{N_B}} \tag{2.8}$$

$$NTR = \frac{NT}{W} = GTR - MRR \tag{2.9}$$

Where:

N_B = the mobility number
b = the unloaded tire section width
r = the tire rolling radius
h = the tire section height
s = wheel longtudinal slip
NT = net traction or pull
T = axle torque
CI = cone index
d = unloaded tire diameter
δ= the tire deflection;
W = Dynamic vertical load on the tire
M = Motion resistance

NTR = Net traction ratio

Equations (2.6) - (2.9) include six coefficients (C_1–C_6) and two tire constants (K_1 and K_2), which are also to be determined empirically, in addition to the cone penetrometer index.

2.2.2 Analytical Methods for Traction Modeling

Upadhyaya and Wulfsohn [15] discussed various analytical, semi-empirical, and empirical traction prediction equations for tires and tracks that are used today. The analytical methods were developed based on using the physics of the interaction between the tire and soil to produce the relationships for the tractive forces. However, it has been shown that the purely analytical models never adequately described the interaction between the tire and the soil interface, since both the soil and the tire had inconsistent physical properties in nearly every instance. The semi-empirical models (based on empirical relationships developed for other ground engaging devices, such as grousers and farming implements) had similar physical methods for predicting tractive performance. Although the semi-empirical methods worked better than the purely analytical methods, the results were still marginal as the empirical methods of predicting traction were developed using operating vehicles' recorded data. As an input to characterize the soil conditions, the cone index was typically used as the sole characteristic of the soil property needed for the model. Tire inflation pressure was not used as a direct input for the equations, but it was accounted for by including the deflection of the tire and the weight of the vehicle. An increase in deflection (or decrease in tire pressure) would cause an increase in off-road traction.

In this respect, the most widely used model, the Wismur-Luth model [16, 17], was developed using bias-ply tires. When radial tires are used, the Wismur-Luth model tended to underpredict the traction of the vehicle. Most models that originated from Wismur-Luth model used variations of the Wismur-Luth equations to account for changes in experimental conditions, including the use of radial-ply tires. Brixius [14] then developed a traction prediction model for bias-ply tires based on similar methods, and suggested modifications of the relations for radial tires. However, Upadhyaya and Wulfsohn stressed in [18] that the empirical traction models seldom provided any insight

into the underlying mechanics and should be used with caution when evaluating new tire situations.

Muro and O'Brien [6], discussed a few formulations that are based on Bekker's methodology [7] where the traction properties of the tires are limited by the shear strength of the terrain. Schwanghart [19] expanded the applications of Bekker's equations by measuring the contact area of an off-road tire under various axle loads to derive a relationship between the average contact pressure and the tire air pressure, as well as developed an analytical expression for the lateral tire force generation.

Although the relations developed for mobility studies are based on assumptions that the vehicle is moving in quasi-steady state conditions, these formulations are integral as starting points for model development. Some of the relations may not be suitable for application in high-speed and transient maneuvers such as braking and cornering, thus limiting their use.

Karafiath and Nowatzki [20] applied plasticity theory and the slip line method in [21] to the vehicle mobility problem by computing the forward and backward slip line field of wheels. Based on plasticity theory, they have derived the basic differential equations of plasticity, as given by equation (2.10) for a mass of soil in 2-D under plane strain conditions together with the Mohr-Coulomb failure criteria. Since none of the exit angles, entry angles, and angle of maximum stress are known before the computation, two relationships define the connection between the three angles:

1. The force balance at each time step requires that the stresses supporting the load of the tire at the interface be equal to the stresses acting on the soil.
2. For rigid wheels, continuity requires the stresses at θ_m to be equivalent for the forward slip line and the rear slip line.

$$\begin{aligned}&\left(1+\sin\left(\phi\right)\cos\left(2\theta\right)\right)\frac{\partial\sigma}{\partial x}+\sin(\phi)\sin(2\theta)\frac{\partial\sigma}{\partial z}-2\sigma\sin\left(\phi\right)\\&\qquad\left(\sin\left(2\theta\right)\frac{\partial\theta}{\partial x}-\cos\left(2\theta\right)\frac{\partial\theta}{\partial z}\right)=\gamma\sin\left(\varepsilon\right)\end{aligned}\tag{2.10}$$

$$\begin{aligned}&\left(1-\sin\left(\phi\right)\cos\left(2\theta\right)\right)\frac{\partial\sigma}{\partial z}+\sin(\phi)\sin(2\theta)\frac{\partial\sigma}{\partial x}+2\sigma\sin\left(\phi\right)\\&\qquad\left(\cos\left(2\theta\right)\frac{\partial\theta}{\partial x}+\sin\left(2\theta\right)\frac{\partial\theta}{\partial z}\right)=\gamma\cos\left(\varepsilon\right)\end{aligned}$$

Karafiath used a method proposed by Sokolovskii [22] to modify equation (2.10) to calculate the characteristic curves and their associated stress conditions. By mapping the equations into a dummy plane, he was able to obtain the solutions for equation (2.10) and then transform the solutions back into the "real" plane. The general equilibrium equations arising from the resultant grid composed of the slip line fields are:

$$\begin{aligned} dz &= dx\tan\left(\theta \pm \mu\right) \\ d\sigma \pm 2\sigma\tan(\phi)d\theta &= \frac{\gamma}{\cos(\phi)}\left[\sin\left(\varepsilon \pm \phi\right)dx + \cos\left(\varepsilon \pm \phi\right)dz\right] \end{aligned} \tag{2.11}$$

For the case in which ε = 0 (free horizontal surface), the last two equations become:

$$\begin{aligned} dz &= dx\tan\left(\theta \pm \mu\right) \\ d\sigma \pm 2\sigma\tan(\phi)d\theta &= \frac{\gamma}{\cos(\phi)}\left[\sin\left(\phi\right)dx + \cos\left(\phi\right)dz\right] \end{aligned} \tag{2.12}$$

Where

σ_1 = Major principle stress
σ_3 = Minor principle stress
$\mu = \pi/4 - \phi/2$
γ = unit weight of the terrain soil
$\sigma = \left(\sigma_1 + \sigma_2\right)/2 + \psi$
$\psi = c \cdot \cot(\phi)$
ε = inclination of terrain

The equations are then solved via finite differences using the methods proposed by Sokolovskii [22], solving for the variables x, z, σ, and θ at each nodal point on the slip line intersections, as shown in Figure 2-3.

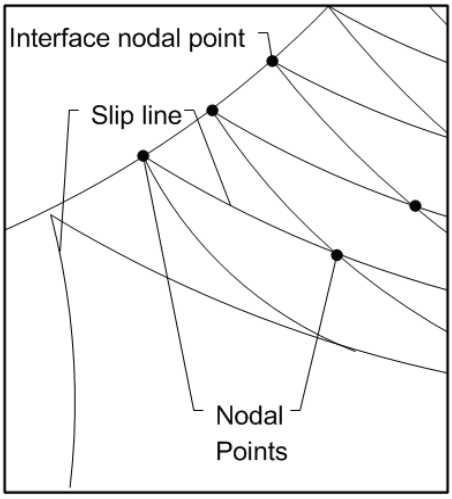

Figure 2-3. The relationship between the nodal points and the slip lines.

Further details of the implementation of the solution method are explained in [22], [23], and [20]. The slip lines shown in Figure 2-3 are calculated using the difference equations in [20]. After σ is calculated at discrete nodal points where the slip lines meet the contact surface of the tire, the value of the effective normal stress and the shear stress along the nodal points on the interface surface is computed as:

$$\begin{aligned} \sigma_n &= \left(\cos(\delta) + \sqrt{\cos^2(\delta) - \cos^2(\phi)}\right)\cos(\delta)\cdot\sigma - \psi \\ \tau &= \left(\sigma_n + \psi\right)\tan\delta \end{aligned} \tag{2.13}$$

Where

$$\delta = \tan^{-1}\left(\tau / \sigma_n\right)$$

σ_n = Normal/radial stress to the soil-wheel interface

τ = Tangential stress to the soil-wheel interface

Equation (2.12) can only be solved in closed form for the Prantl case where the weight of the soil is negligible, which is not a realistic assumption for practical purposes, and so equation (2.12) will be solved iteratively using the recurrence method proposed by Sokolovskii to yield the slip lines for the wheel/tire model proposed by Karafiath [20]. The radial and tangential stresses can be calculated at each interface nodal point on the surface of the wheel with equation (2.13). This method clearly has a strong foundation in plasticity and yields reasonable results but is derived based on planar

conditions and cannot be applied blindly to mobility problems without insight into the slip lines as the characteristics of the solutions for the plasticity equations. There are also various numerical issues in the usage of this method that require extensive knowledge of soil mechanics to recognize.

Lee et. al.[24] studied the effect of snow embedment on tires operating in combined slip. The effect of snow density on tire-snow interaction in the presence of uncertainty was assessed in [25]. The snow-depth dependent finite element analysis (FEA) and semi-analytical models that have developed recently at UAF can predict tire-snow interfacial forces at a given density under combined slip operating conditions. However, one major disadvantage of the models is that they are only applicable for fresh, low-density snow due to the unavailability of a density-dependent snow model. In [25], a study is then conducted to develop a preliminary density-dependent engineering snow model for a wide range of densities and to apply the model to tire-snow interaction by taking into consideration the uncertainty of snow characteristics. The snow is simulated as a pressure-sensitive Drucker-Prager material in order to establish the relationship between strengths in compression/tension.

2.2.3 Finite Element/Discrete Element/Lumped Parameter Models for Traction Modeling

The problem of dynamic rolling contact has been the subject of intensive research, which includes wheel-rail contact and tire-terrain contact. Recently, with the sudden increase of computing power, the focus was shifted towards developing three-dimensional models that include the effect of temperature and different loading scenarios. There are two main approaches to tire-terrain interaction modeling: finite/discrete element and analytical semi-empirical models.

Currently many researchers are working on complex three-dimensional tire models based on finite element models (FEM) which can take into account many peculiarities of the structure in the operational state (rolling tires). However, these FEM models need extremely powerful computers and high input data accuracy in vehicle dynamics simulations. In the late 1960s researchers in the tire mechanics field started to apply the FEM models for the calculation of the stress-strain state of pneumatic tires under different loading conditions. More complex classes of models were used for the tire as a

whole and for its parts. As a result of the development of FEM, it became possible to treat the tire as a three-dimensional deformable body. In the beginning, commercial universal program packages such as NASTRAN, ABAQUS, and UG were used. With the aid of these programs, tires were subjected to internal pressure and contact load on the basis of shell models and three-dimensional models were analyzed. However, Ridha [26] and Shoemaker [27] demonstrates the applicability of the Finite Element Method to the mobility problem and found a rather close correlation between computational results and experimentally collected data. In their study, it was deduced that the discrepancies between calculation and experiment may be caused by the necessity in tire modeling to account for the integrated complex behavior of the rubber-cord tire structure. These results demonstrate the limitation of the use of universal FEM packages for tire modeling. For further reading about FEM applications in tire modeling, an excellent discussion can be found in the survey paper written by Ridha [26] and Rothert et al.[28].

However, only recently has significant progress has been done in the field of terramechanics with the aid of commercial finite element software packages. FEM calculations of rolling contact between elastic tire and soft soil were implemented and studied by Shoop [29], Fervers [30] and others. In order to use the FEM in a two-dimensional approach, an adequate discretization of the tire structure and the soil needs to be done. The tire is modeled by a structure of three concentric rings (representing the rim, the carcass and the tread) and the Drucker-Prager material law (defining the failure limit dependent on the cohesion and the soil's angle of friction) had been implemented for soil by Abaqus/Explicit to describe the soil deformation.

Meaningful prediction of the tire dynamic characteristics, such as tire transient responses (i.e., braking and acceleration), had not been feasible for vehicle dynamics simulations due to the limitations of computational power demanded by commercial FE programs.

Shoop [29] explored modeling of tire on deformable terrain by using finite element analysis and the application of the Drucker-Prager cap plasticity model. The purpose of the study was to evaluate tire on snow models. The tire model was implemented and run in ABAQUS and the results were validated visually and numerically. The conclusions drawn from the results of this study are that in snow, tires can be approximated as rigid

wheels as their vertical deflections in snow are negligible. The model has been proven to be fairly accurate when used in steady-state operating conditions.

Schlotter [31] investigated the response time of an agricultural tire with respect to a fluctuating tire load. This study was meant to quantify the effect of tire load fluctuations on the generated tire lateral force.

Nakashima [32] discussed a method to combine Finite Element Analysis (FEA) and Discrete Element Analysis (DEA) to model tire-soil behavior. The soil is modeled as DE while the tire is modeled as FE. The main purpose of this study is to better describe the microscopic deformation of the soil.

Pan [33] presents an effort to produce a computationally inexpensive tire-soil interaction model by employing the use of empirical and semi-empirical models. In this study, all the deformable non-linear parts are modeled using Finite Element, and requires the adjusting of the parameters to match lab test results. Using this method, when the model is applied to a full multibody vehicle simulation over different soil types, it is required to provide data of rather high detail, which may not be necessarily available.

Fervers [30] investigated the interaction of a two-dimensional tire model with soft soil using Finite Element Analysis. The results from this study are encouraging in the sense that it demonstrates that a detailed of the model which includes the different layers of material forming the tire structure adds to the resolution of the model, proving that a detailed model can capture a reasonable amount of resolution in the tire dynamics of off-road simulations. This 3-D FEA tire model is composed of the various components of the tire stacked together in a multi-layered ring. It was presumed, however, that the 3-D elements can be transformed into 2-D half-space to save on computational time. For dynamic simulations, physical parameters, such as the constant of elasticity for the soil, must be determined accurately. It is also noted that more research must be done to link the dynamic properties of the soil with that of the model.

An effort was also initiated by the author of this dissertation [34] and Dr. Dankowicz to develop a lumped parameter model that has a more mechanically inclined approach towards tire modeling within the multibody dynamics framework. The work discussed in [34] will be presented in chapter 7 of this dissertation.

Nonetheless, even with all the recent improvements in computational technology, all the rolling contact calculations based on explicit FE program packages are computationally expensive, making a simulation of a real driven car with four tires currently not realistically possible for long distances or transient maneuvers. The FE/DE methods can certainly provide a detailed perspective of the tire-terrain interaction, but it is not realistic to use these models for real-time vehicle dynamics simulations.

2.3 Review of Literature: Tire modeling

As previously discussed in the introduction, for a long time, the tire modeling effort has been primarily focused on on-road tire models. Some of the more recent efforts in on-road tire modeling are available for reading in [35], [36], [37], and [38]. A good introductory text which can be a source of information for tires in general is the classic text by Clark [39] and Pacejka [40]. Since the focus of this document is on the development of an off-road capable tire model, the tire modeling discussion in the review of literature will be focused on state-of-the-art off-road tire models and off-road capable tire models.

From the terramechanics discussion in the previous section, we can surmise that much of the tire modeling efforts have been focused on mobility and traction. However, relatively little work has been done to model the combined traction and cornering behavior of deformable tires on deformable soils. The literature shows that the main focus was on modeling just the deformation of the tread without considering the deformation of the carcass when taking into account the overall tire deformation. Although the literature has been rather sparse, we will attempt to highlight the existing efforts that come the closest to what we want to accomplish in this study.

2.3.1 Off-road Tire Model: Grecenko Slip and Drift Model

The Grecenko Slip and Drift Model (SDM) was introduced in 1969 to model the behavior of a tire on off-road terrain with low sinkage. The core of the SDM tire model is the deformation gradient, which is defined by the binomic equation (2.14):

$$u = j / x = f\left(F_u / F_z\right) \tag{2.14}$$

Where

u = deformation gradient

j = shear deformation

x = coordinate along the contact patch

F_u = total shear force

F_z = total normal force

Grecenko also stipulated that the constraint equation (2.15) has to be fulfilled in the usage of the model.

$$(1-s)F_x \tan(\alpha) - F_y s = 0 \tag{2.15}$$

In this model, the coefficient of friction is also defined as a function of the gradient of deformation in the form of equation (2.16).

$$\mu = f(u) = \frac{u_m}{4}\left(\frac{2u}{u_k} + 3 - \left[\left(\frac{2u}{u_k} - 1\right)^2 + 8\right]^{1/2}\right) \tag{2.16}$$

Where

$$u_k = j / l\big|_{\tau=\tau_m}$$

$$\mu = \mu_x, \mu_y$$

The maximum shear stress is also defined as shown in equation (2.17).

$$\tau_m = f(j) = \tau_m \frac{j + j\big|_{\tau=\tau_m} - \left|j - j\big|_{\tau=\tau_m}\right|}{2j} \tag{2.17}$$

The effective shear stress in the direction of effective slippage in the contact patch can then be defined as:

$$\tau = \tau_m f(j) = \tau_m f(ux) \tag{2.18}$$

This will give us the total resultant shear force as:

$$F_u = \left(F_x^2 + F_y^2\right)^{1/2} = \tau_m b \int_0^l f(ux)dx \tag{2.19}$$

Other models which have an approach similar to the one presented by the SDM include the Jurkat and Brady model (JBM) [41] and the model by Del Rosario [42].

Most of the tire models for off-road vehicle simulations are developed consider only cases where the rut formation is shallow, and do not consider the effect of sinkage using as a serious factor in the calculation of tractive forces. By not taking into account sinkage as an important part of the model, the lateral bulldozing and compaction

resistance are indirectly neglected in the simulation, reducing the effectiveness and the realistic behavior of the models as multi-purpose off-road vehicle models.

2.3.2 Off-road Tire Model: Modified STI Tire Model

The Systems Technologies Inc.Tire Model (STI) tire model was originally developed for on-road simulation purposes. It was developed in 1997 ([43], [44]) as a theoretical model with empirical saturation functions, and has since been enhanced to make it more applicable to off-road tire simulations [45]. The on-road component has been an industry standard in vehicle simulations, being the main model used in vehicle dynamics simulations by the National Highway Traffic Safety Administration (NHSTA) and the National Advanced Driving Simulator (NADS). The initial attempt of the off-road version of the STI model was based on the work done by Metz [46], where an empirical method was suggested to model the tractive behavior of the tire.

The more recent off-road version of the STI tire model presented in [45] is based on the methodologies described in [3]. The vertical stress acting in the radial direction of the tire was calculated using Bekker's [7] pressure-sinkage relationship. An analytical model of the lateral plowing behavior of the tire during cornering was also included in the model development. For further details of this model the reader is refered to [3], [45], and [43]. The model implemented in [45] seems to consider the tire as a rigid wheel, and there are many drawbacks to this approach. When the tire is rigid all the time, there can be no relaxation of the tire structure, which leads to an overestimation or underestimation of the forces reacting from the soils. In addition, the combined slip behavior seems to be implemented as an empirical saturation function and provided little insight into the mechanical tractive force generation mechanism.

2.4 Review of Literature: Summary

An overview of the models for off-road locomotion has been given, together with the state-of-the-art on some of the more recent tire models. It is only by exploring what has been done in the past, that we can draw a conclusion on what needs to be done to improve the current tire-terrain models for off-road vehicle simulations. Some of the equations that were introduced in this section will be revisited in the chapters discussing

the development of the tire models. It is evident that much work still has to be done in order to develop an off-road tire model for vehicle dynamics simulations. Although much work has been done in this area, the models available seem to have several characteristics that limit their applicability to vehicle dynamics simulations. These characteristics are:

1. Models which are developed for mobility studies primarily focus on tractive capabilities and wheel load prediction, but have little or no lateral handling capabilities.
2. Models developed for off-road vehicle dynamics simulations with lateral handling capabilities either do not take into account the flexibility of the tire/wheel or the effect of compaction resistance of the wheel/tire on soil.
3. Models based on empirical equations usually require specialized apparatus or high input data for modeling applications.

3. Tire Model Mechanics: On-Road

3.1 Tire Forces and the Contact Patch

The tire forces arise as a result of the contributions of the pressure and stresses acting on each element of the contact patch of the wheel. For analytical models, the insight involved in estimating normal and the shear stress distributions are often derived from the experience acquired from analyzing tire testing data. Figure 3-1 shows the forces and moments acting on the center of the wheel. It has to be pointed out, however, that these forces and moments are caused by the interaction of the tire with the pavement, within the contact patch area.

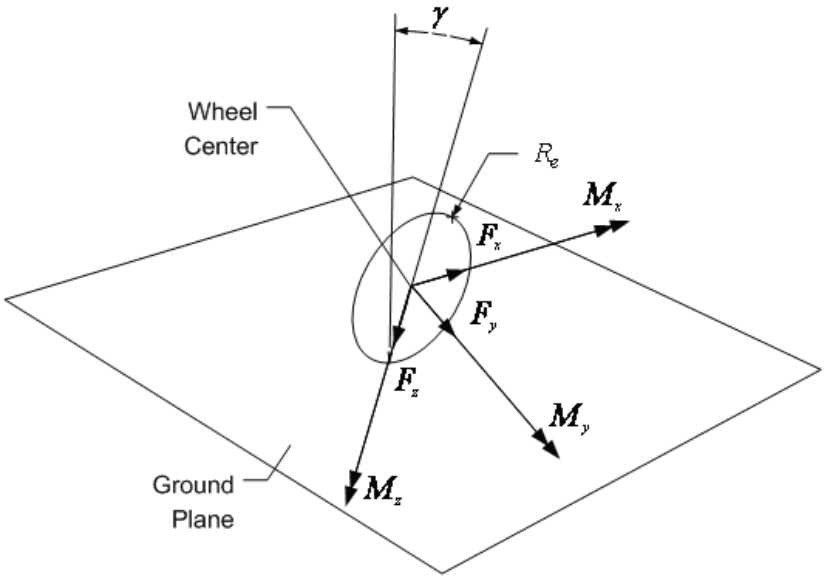

Figure 3-1. Forces and moments acting on the center of the wheel (Adapted from [39]).

The vertical force F_{zp}, lateral force F_{yp}, and longitudinal force F_{xp}, as well as the overturning moment M_{xp}, the rolling resistance moment M_{yp}, and the aligning moment M_{zp} at any arbitrary point P of coordinates (x,y) in the contact patch of area A, can be expressed as shown in equations (3.1)-(3.6) without any loss of generality:

$$F_{zp} = -\int_A p_z dA \tag{3.1}$$

$$F_{yp} = -\int_A p_y dA \tag{3.2}$$

$$F_{xp} = -\int_A p_x dA \tag{3.3}$$

$$M_{xp} = -\int_A p_z \cdot y \, dA \tag{3.4}$$

$$M_{yp} = \int_A p_z \cdot x \, dA \tag{3.5}$$

$$M_{zp} = \int_A \left(p_x \cdot y - p_y \cdot x \right) dA \tag{3.6}$$

Where

p_x = Longitudinal tire contact stress

p_y = Lateral tire contact stress

p_z = Vertical tire contact pressure

Considering the definitions of the forces in the contact patch thus stated, we can now apply a transformation to determine the forces acting at the center of the wheel in the wheel reference frame. By applying a rotation about the longitudinal axis of the tire, we can write a set of force/moment balance equations that relate the forces acting in the global reference frame to the local frame attached to the rolling wheel. Thus, the force equations can be written as:

$$\begin{bmatrix} 1 & 0 & 0 \\ 0 & \cos(\gamma) & -\sin(\gamma) \\ 0 & \sin(\gamma) & \cos(\gamma) \end{bmatrix} \begin{pmatrix} F_x \\ F_y \\ F_z \end{pmatrix} = \begin{pmatrix} F_{xp} \\ F_{yp} \\ F_{zp} \end{pmatrix} \tag{3.7}$$

By introducing R_l as the effective loaded radius of the tire, the moment equations can be written as:

$$\begin{bmatrix} 1 & 0 & 0 \\ 0 & \cos(\gamma) & -\sin(\gamma) \\ 0 & \sin(\gamma) & \cos(\gamma) \end{bmatrix} \begin{pmatrix} M_x \\ M_y \\ M_z \end{pmatrix} = \begin{pmatrix} M_{xp} - F_{yp} R_l \cos(\gamma) - F_{zp} R_l \sin(\gamma) \\ M_{yp} + F_{xp} R_l \cos(\gamma) \\ M_{zp} + F_{xp} R_l \sin(\gamma) \end{pmatrix} \tag{3.8}$$

Solving for the forces and the moments at the center of the wheel, as shown in Figure 3-1, we get:

$$\begin{pmatrix} F_x \\ F_y \\ F_z \end{pmatrix} = \begin{pmatrix} F_{xp} \\ F_{yp}\cos(\gamma) + F_{zp}\sin(\gamma) \\ F_{zp}\cos(\gamma) - F_{yp}\sin(\gamma) \end{pmatrix} \tag{3.9}$$

$$\begin{pmatrix} M_x \\ M_y \\ M_z \end{pmatrix} = \begin{pmatrix} M_{xp} - F_{yp}R_l\cos(\gamma) - F_{zp}R_l\sin(\gamma) \\ F_{xp}R_l + M_{yp}\cos(\gamma) + M_{zp}\sin(\gamma) \\ M_{zp}\cos(\gamma) - M_{yp}\sin(\gamma) \end{pmatrix} \tag{3.10}$$

Based on equations (3.9) and (3.10), and incorporating the results from equations (3.1)-(3.6), an analytical tire model can be developed, which accounts for a combination of the mechanics of the tire contact and some empirical correction factors, as it will be discussed in the sections ahead. Some of the figure generated in the sections ahead are generated from the parameters acquired in Chapter 5. The figures are mean to be taken from a qualitative perspective, in order to visualize graphically some of the phenomenon that are observed throughout this dissertation.

3.2 Tire Model Development: Brief Overview

For multibody vehicle dynamics simulations, it is generally easier to model the tire-road interaction as external forces and moments acting on the spindle to reduce the computational cost of a vehicle simulation because the tire is a complex toroidal structure supported by steel belts and rubber treads, as explained in the introduction. Purely analytical models are currently unable to completely account for many of the complex phenomena in vehicle simulations, especially in the combined slip regime of operation while purely empirical models are essentially “black boxes” which offer no insight into the physical characteristics of the tire. Whilst purely empirical models are adequate for vehicle dynamics simulations, the amount of data needed to characterize the model is usually extensive and its collection requires the use of specialized equipment.

The simplified analytical-empirical mathematical model developed in this dissertation is based on the observations of empirical data from testing as well as the

successful applications of classical analytical mechanics analysis on tire modeling from Fiala [47]. The present work is developed based on the following premises:

1. The contact patch is approximated with a rectangular shape for the contact area, from the observation of collected footprint data by researchers [1].
2. The contact pressure distribution is uniform in the lateral direction and represented with a warped ellipse in the longitudinal direction.
3. The friction coupling between the tire and the road varies with the normal force and the slip velocity.
4. The dynamic steering behavior is approximated with a second order lag between the slip angle at the center of the wheel and the slip angle at the contact patch.

Figure 3-2 illustrates schematically the fact that in this study we used analytical methods and empirically collected data to characterize the tire model. The model takes as inputs the longitudinal slip ratio, the slip angle, the vertical tire force, and the camber angle. It produces, as outputs, the longitudinal and the lateral tire forces, as well as the aligning moment and the overturning moment.

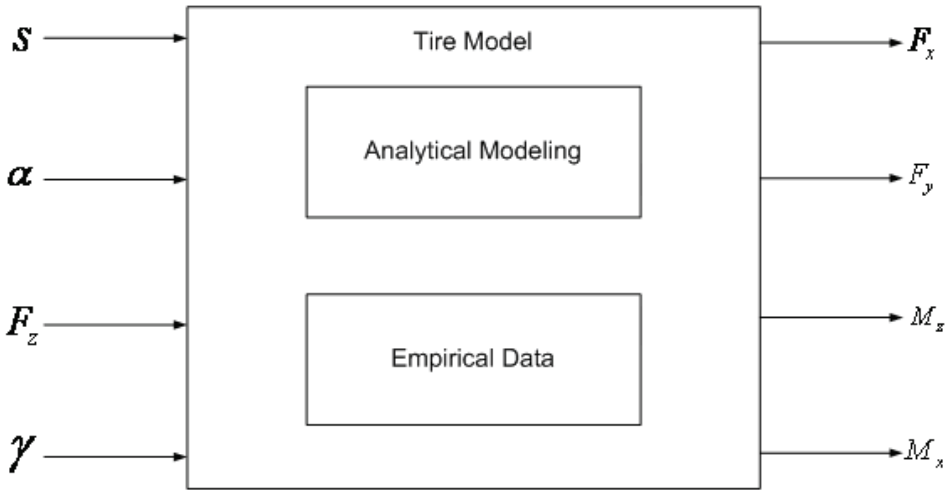

Figure 3-2. Proposed input-output relationship for the tire model developed

3.3 Vertical Pressure Distribution and Normal Force

During vehicle dynamics simulations, the lateral and the longitudinal forces generated are dependent on the tire vertical force or axle load. Hence, the discussion of the tire model developed in this work will begin with a discussion of the vertical contact patch pressure and the associated vertical tire force.

The tire vertical force is defined as a function of the vertical contact pressure distribution acting from the ground on the contact patch of the tire. In the development of analytical tire models, the contact pressure distribution is essential to characterize the tractive forces. There are various types of distributions proposed for modeling the vertical contact pressure, the most popular being the parabolic (Pacejka [40], Gim [48], Fromm [49]) and the elliptical distribution (Lee [36], Salaani [35]). Even though the more common approach for modeling the forward/backward shift of the pressure distribution involves the use of inclined parabolas [39], more recent works have explored the use of higher order polynomials to model the shifting of the normal pressure [50]. Figure 3-3 depicts the shift in the vertical pressure distribution under different regimes of operation. As shown in Figure 3-3 (a), when the tire is braking, the contact patch experiences a larger deformation in the leading edge than in the trailing edge, causing the center of pressure to shift forward. When the tire is loaded in a stationary non-rotating situation or in a condition where it is just purely rolling, as shown in Figure 3-3 (b), the center of pressure for the contact patch is about where the axle is, causing the pressure profile to have a more symmetric shape from the leading edge to the trailing edge. However, when the tire accelerates, the center of pressure in the contact patch shifts towards the back, causing a larger deformation in the trailing edge of the contact patch than in the leading edge.

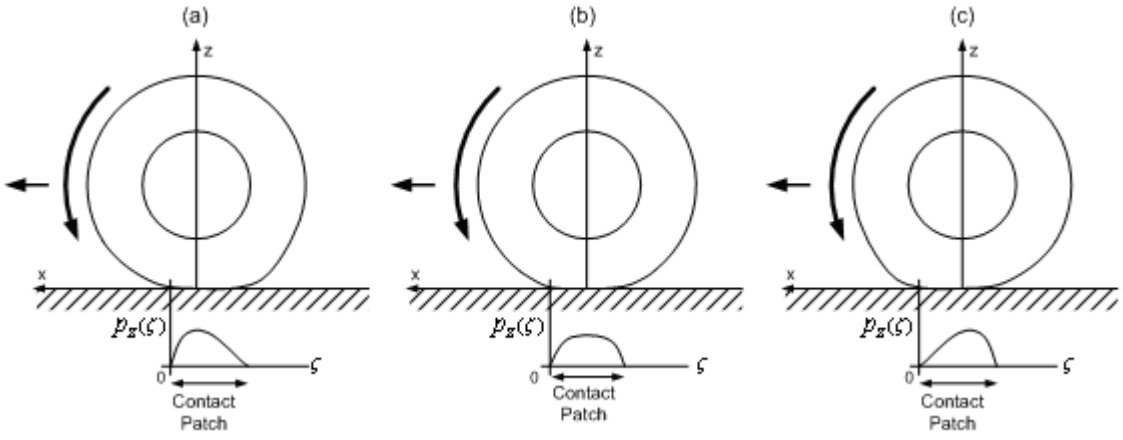

Figure 3-3. Progression of the vertical contact stresses of the tire in different regimes of handling: (a) braking, (b) stationary/steady-state rolling and (c) accelerating .

It is then plausible to assume that the vertical contact pressure acting across the contact patch can be approximated as a warped ellipse, primarily because the elliptical distribution fits experimental data more consistently [1]. This modification of the ellipsoid shape provides us with the capability to model the shift in the vertical contact pressure distributions shown in Figure 3-3. A graphical depiction of the unwarped elliptical pressure distribution is shown in Figure 3-4.

For within the plane of the tire model, we then assume that the pressure distribution can be approximated using equation (3.11), where ζ represents the coordinate where the pressure is computed, and varies between 0 and the length of the contact patch, l_p, s is the longitudinal slip ratio, P_{max} is the maximum pressure, and A_1 is a shape change factor, which attempt to capture the shift in the patch under varying slip conditions.

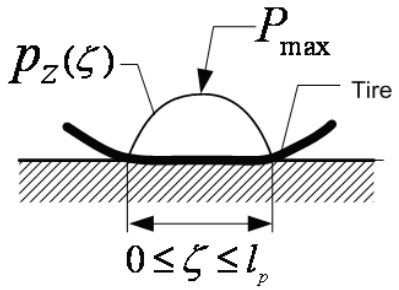

Figure 3-4. The elliptical pressure distribution of a tire vertical contact patch pressure, given the contact patch longitudinal length and the maximum pressure.

$$p_z(\varsigma) = P_{\max}\left(1 + A_1 s\left(\zeta - \frac{l_p}{2}\right)\right)\sqrt{1 - \frac{\left(\zeta - \frac{l_p}{2}\right)^2}{\left(\frac{l_p}{2}\right)^2}} \tag{3.11}$$

The vertical force can then be calculated using equation (3.1), where equation (3.11) will be integrated to yield the vertical tire force, F_z, as a function of the vertical contact pressure.

$$F_z = b\int_0^{l_p} p_z(\zeta)d\zeta$$

$$= b\int_0^{l_p} P_{\max}\left(1 + A_1 s\left(\zeta - \frac{l_p}{2}\right)\right)\sqrt{1 - \frac{\left(\zeta - \frac{l_p}{2}\right)^2}{\left(\frac{l_p}{2}\right)^2}}d\zeta \tag{3.12}$$

$$= \frac{\pi b l_p P_{\max}}{4}$$

Equation (3.12) yields the same result as shown by Salaani [35] and Lee [36] for the vertical force, ensuring that the shape change parameter, A_1 only changes the shape of the elliptic curve, but retains the area under the curve. We can determine the value of $P_{\max}$ as a function of the normal force as shown in equation (3.13) and express equation (3.11) as a function of F_z.

$$\therefore P_{\max} = \frac{4}{\pi b l_p} F_z \tag{3.13}$$

$$p_z(\varsigma) = \frac{4F_z}{\pi b l_p}\left(1 + A_1 s\left(\zeta - \frac{l_p}{2}\right)\right)\sqrt{1 - \frac{\left(\zeta - \frac{l_p}{2}\right)^2}{\left(\frac{l_p}{2}\right)^2}} \tag{3.14}$$

Using the relation we developed in equation (3.14) we can compute the vertical contact pressure for a tire during three operational modes of interest, namely acceleration, rolling, and deceleration. To illustrate the shift in the tire contact pressure discussed earlier, in Figure 3-5, we present the corresponding vertical contact pressure plots for these three driving scenarios for a Continental Contitrac SUV P265/70/R17 tire with a vertical load of 6672N.

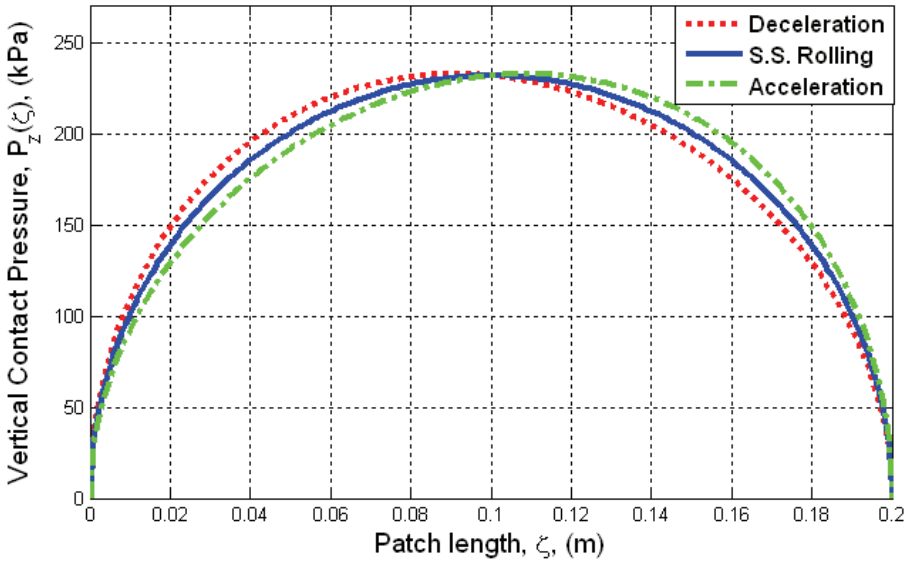

Figure 3-5. Qualitative plot depicting the calculated shift of tire contact pressure for a Continental Contitrac SUV P265/70/R17 tire with a vertical load of 6672N for deceleration (negative s), rolling (s=0), and acceleration (positive s). The value of A_1 used for creating this plot is assumed to be 1.

Equation (3.14) provides a way for the slip ratio to interact with the normal pressure distribution. This relationship will prove to be important when we derive the slip conditions for the tire model because of the tendency of the vertical contact pressure to shift forwards or backwards with change in longitudinal slip, as shown in Figure 3-5, changes the area integrated to calculate the sliding forces. That being said, we want to emphasize that the tire normal force is an integral part of the model, since it is the primary component of all the other forces. In addition, the normal force is also a component to be used for the estimation of the contact patch length, l_p, and is related to the tire deflection, δ, as shown by equation (3.15).

$$F_z = K_z \delta \tag{3.15}$$

In Figure 3-6 we introduce the terms unloaded tire radius, R_u, (which is the radius of the undeformed tire), loaded tire radius, R_l, (the distance from the center of the wheel to the point of the tire in contact with the ground), and the tire deflection (the difference between the unloaded and the loaded tire radii), δ.

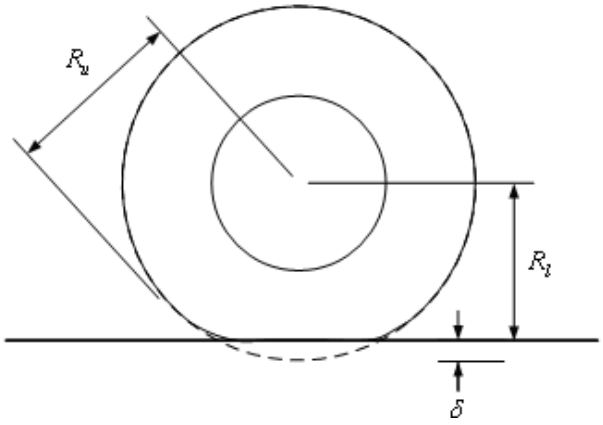

Figure 3-6. Relationship between the loaded radius R_l and the tire deflection δ.

The tire vertical stiffness, K_z is usually taken as a constant value, but recent experimental testing [37] have shown that the dynamic loaded radius decreases as the slip angle increases. This trend of behavior is highly dominant especially when the tire is subjected to dynamic vertical loads. It is reasonable to presume that the lateral deformation of the tire during cornering decreases the tire vertical stiffness and also the loaded radius. This effect can be incorporated into the tire vertical stiffness by modeling the stiffness as shown in equation (3.16). Note that the scaling factor is a bounded function, hence limiting the change in stiffness with respect to the slip angle. Figure 3-7 shows an example of the model output vs. the experimental data collected by NHTSA for the Contitrac SUV P265/70/R17. Similar trends have been observed in [37].

$$K_z = \left(C_{z1} + (1 - C_{z1}) \operatorname{sech}\left(C_{z2} \frac{|\tan(\alpha_c)|}{1 - |\tan(\alpha_c)|} \right) \right) K_{z0} \tag{3.16}$$

Where

C_{z1}, C_{z2} = Stiffness shape adjustment factors which are function of δ
K_{z0} = Dynamic stiffness at zero camber and slip angle
α_c = Contact patch slip angle

At higher slip angles, the stiffness values calculated from the model seems to stay a constant value while the data seems to drift away in different directions. It is hypothesized that this transient phenomenon is caused by the fact that the slip angle is

continuously swept at a certain rate (in this case 3 degrees/second) during testing and the tread did not have time to relax.

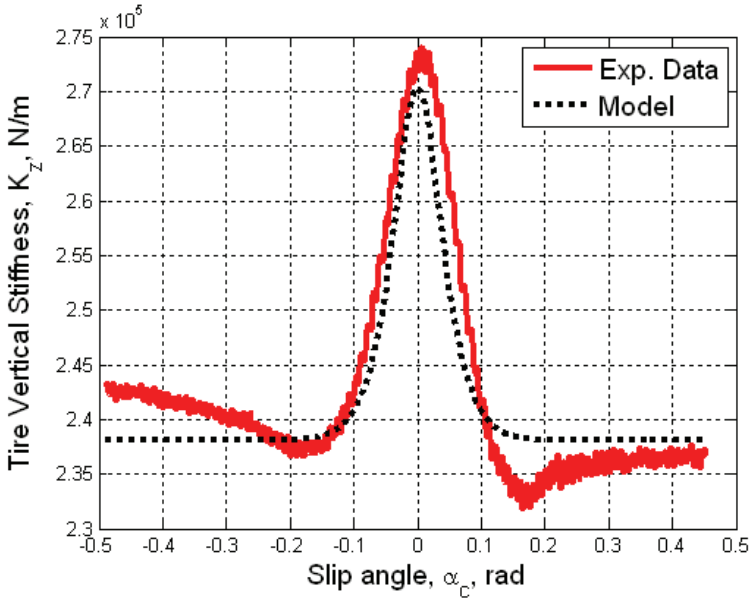

Figure 3-7. An example of the tire vertical stiffness data vs. the model for the Contitrac SUV P265/70/R17 tire.

A simplified method to estimate the contact patch length can be developed using following Gim and Nikravesh's method ([48] ,[39]). The relationship between R_u, l_p, and δ can be expressed using the Pythagorean Theorem as:

$$R_u^{\,2} = \left(\frac{l_p}{2}\right)^2 + \left(R_u - \delta\right)^2 \tag{3.17}$$

The tire deflection and the length of the contact patch can then be approximated as shown in equation (3.18).

$$\begin{aligned} l_p &= 2\sqrt{2R_u\delta - \delta^2} \\ \because \delta &= \frac{F_z}{K_z} \\ \therefore l_p &\approx 2\sqrt{2R_u\frac{F_z}{K_z} - \left(\frac{F_z}{K_z}\right)^2} \end{aligned} \tag{3.18}$$

Equation (3.18) represents one of the more simplified methods that can be used to estimate the contact patch length. In chapter 4, we will explore another method to

calculate the contact patch length by using a model that attempts to capture the enveloping properties of the tire as it transverses the terrain.

3.4 Longitudinal and Lateral Force: Tread and Belt Mechanics

The modeling of the rolling of the contact patch has been an active area of study by various researchers as shown by Clark [39] and Gent [1]. For pneumatic tires, the area of the tire circumference in contact with the road is defined as the contact patch. The mechanics of a contact patch in the lateral and longitudinal direction is a complex domain of interest and hence presents a very challenging phenomenon to understand and analyze.

For the development of the tire model in this dissertation, we first define the components of the velocities at the contact patch in terms of the longitudinal and lateral slip, as shown in Figure 3-8, based on the brush model developed originally by Pacejka [40]. Revisiting the original formulation, let V be the magnitude of the (effective) velocity of the center of the contact patch. We denote by V_x and V_y as the velocity components of the center of the patch in the longitudinal, respectively lateral directions with respect to the wheel plane. V_{slip} represents the slip velocity, which is further projected onto the longitudinal, respectively lateral directions, to obtain V_{slipx} and V_{slipy}.

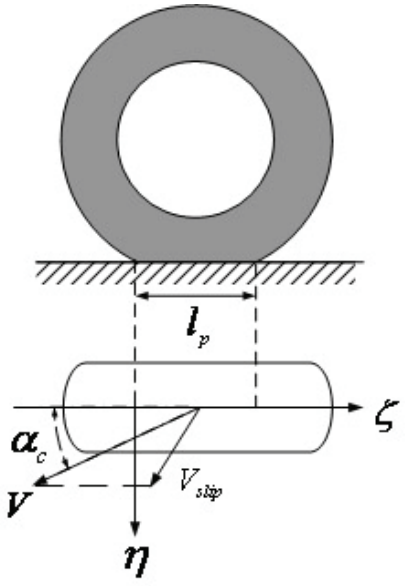

Figure 3-8. Depiction of the tire, contact patch geometry, and velocity components

$$V_x = V\cos(\alpha_c) \tag{3.19}$$

$$V_y = V\sin(\alpha_c) \tag{3.20}$$

$$V_{slipx} = sV_x \tag{3.21}$$

$$V_{slipy} = tan(\alpha_c)V_x \tag{3.22}$$

The rolling speed of the patch is then defined as:

$$V_r = V_x - V_{slip} = (1-s)V_x \tag{3.23}$$

The deflections of the individual elements of the tread in the adhesion region can then be defined as:

$$\lambda_\zeta = \frac{V_{slipx}}{V_r}\zeta = \frac{s}{1-s}\zeta \tag{3.24}$$

$$\lambda_\eta = \frac{V_{slipy}}{V_r}\zeta = \frac{\tan(\alpha_c)}{1-s}\zeta \tag{3.25}$$

For the entire length of contact patch, the longitudinal force and the lateral force per unit length of the circumference can be defined as given by the equations (3.26) and (3.27), respectively.

$$\sigma_x = k_x\lambda_\zeta = k_x\frac{s}{1-s}\zeta \tag{3.26}$$

$$\sigma_{yt} = k_y\lambda_\eta = k_y\frac{\tan(\alpha_c)}{1-s}\zeta \tag{3.27}$$

Where k_x and k_y are defined as the stiffnesses per unit length of the circumference for the tread elements in the x and y directions, respectively. The longitudinal stiffness and the cornering stiffness can then be evaluated by computing the value of the forces at

low values of lateral and longitudinal slip, where approximately the entire contact patch is in adhesion.

$$C_s = \frac{d}{ds}\left(b\int_0^{l_p} k_x \frac{s}{1-s}\zeta d\zeta \right)\Bigg|_{s=0} = \frac{k_x b l_p^{\,2}}{2} \tag{3.28}$$

$$C_{\alpha_c} = \frac{d}{d\alpha_c}\left(b\int_0^{l_p} k_y \frac{\tan(\alpha_c)}{1-s}\zeta d\zeta \right)\Bigg|_{s=0,\alpha_c=0} = \frac{k_y b l_p^{\,2}}{2} \tag{3.29}$$

Equations (3.28) and (3.29) will prove to be very important in determining the values of the element stiffnesses at low values of lateral and longitudinal slip. Note that equations (3.26) and (3.27) represent the deflection of the elements of the tread within the adhesion region only. Figure 3-9 is the graphical representation of the stresses in the lateral and longitudinal direction, projected along perpendicular planes to show the difference in the tire shear stresses when the tire model is operating in pure slip (top and bottom), and combined slip (middle). Within the adhesion region, the individual elements of the tread still deform following Hooke's Law, up to the maximum allowable lateral and/or longitudinal stress, which is limited by the assumed elliptical normal stress, depicted in Figure 3-9. Once the compliant stresses exceed the elliptical envelope, the elements of the trailing edge of the contact patch will start to go into sliding and the tire will start to lose grip.

When the tire loses traction completely, the area of the sliding region dominates the total force generated by the tire stresses. The total force generated then will be equivalent to the area calculated from the integration of the area under the ellipsoidal limit curve.

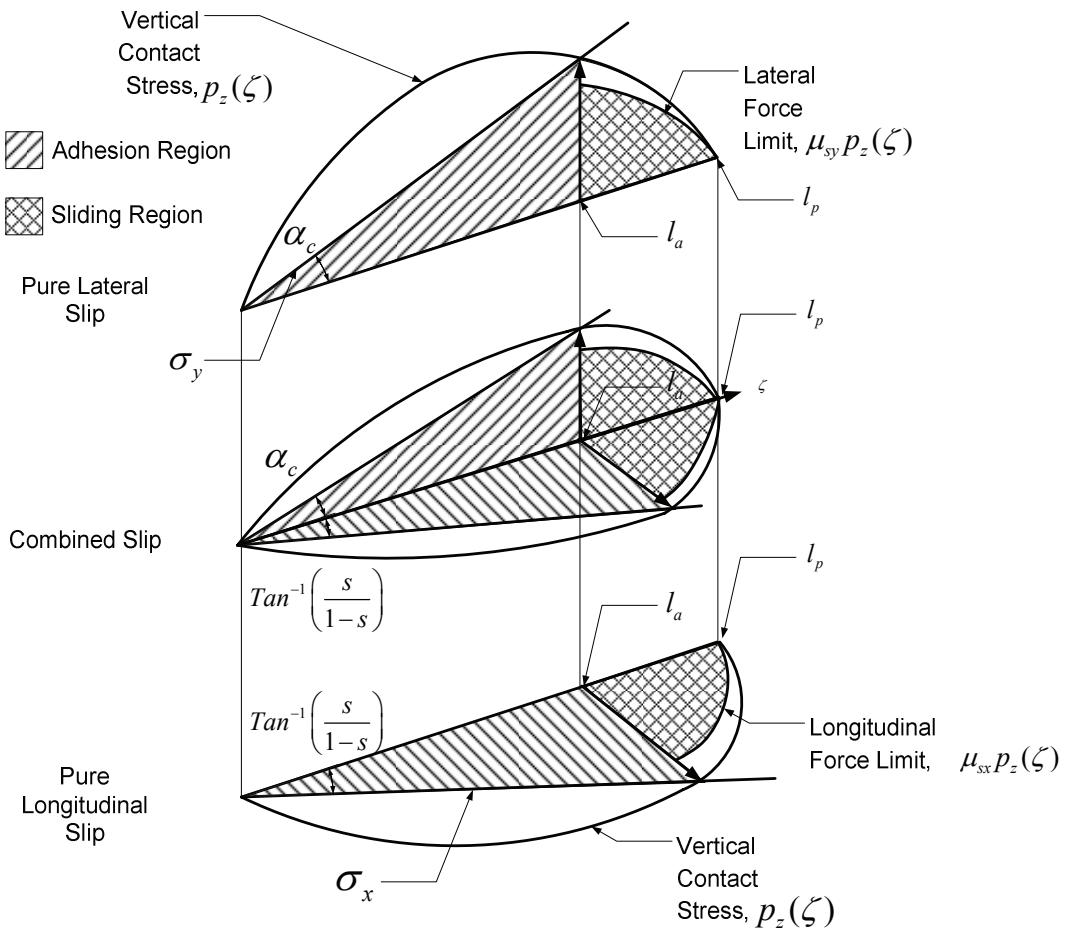

Figure 3-9. The contact patch force distribution from the front to the rear of the contact patch in pure lateral slip, pure longitudinal slip, and combined slip [Adapted from NHTSA report STI-TR-1227 [44] under the FOIA].

Even though the tread mechanics is essential to the efforts toward characterizing the behavior of the pneumatic tire, the lateral traction behavior of a passenger car tire is not just governed by the tread contact mechanics. Today, most passenger car and SUV tires in the market are radial-ply tires, used, as discussed in earlier chapters, mainly because they have a longer service life compared with the bias-ply tires. The construction of a radial ply tire yields a stiffer belt, wrapped around the tire in the circumferential direction, resulting in the entire contact patch to be deformed as shown in Figure 3-10. This phenomenon affects the lateral force generation because the additional deformation of the belt and carcass changes the shape of the stress distribution in the lateral direction. It has been experimentally shown that, in general, a radial tire is stiffer in the lateral

direction than a bias-ply tire because the radial tire requires a smaller slip angle input to produce the same lateral force ([51], [39], [1]). Since the cornering stiffness is a combination of lateral belt/carcass stiffness and tread stiffness, the force contribution of the belt and carcass deformation must be included in the calculation of the total lateral stress.

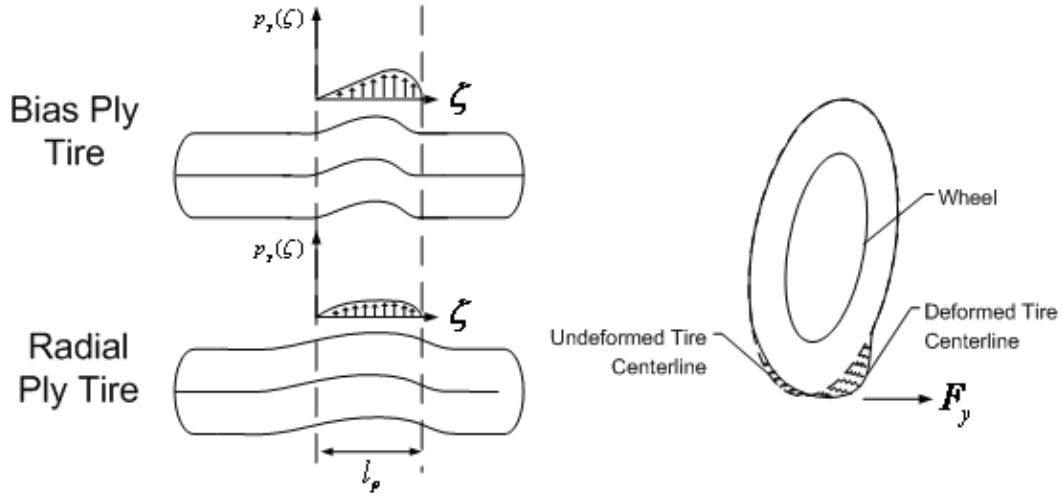

Figure 3-10. Comparison between the tire lateral deflection of a bias-ply tire and of a radial-ply tire. Note that the stress in the radial ply tire is more evenly distributed across the entire patch.

The interaction of the tread belt and the sidewall is treated as a beam on elastic foundation, as depicted in Figure 3-11 , in a similar manner to [50] and [47]. This approach was shown to be an adequate model for the sidewall-tread interaction for the radial-ply tire compared with the string on elastic foundation, as discussed by Clark [39].

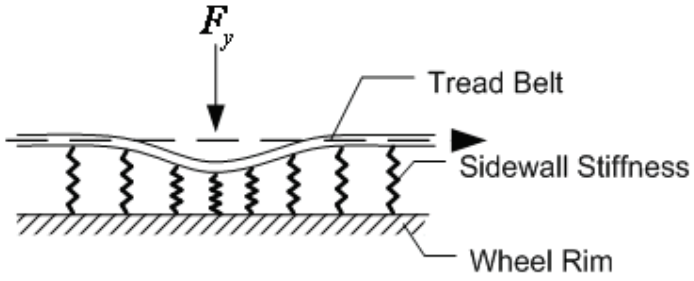

Figure 3-11. The tread belt and sidewall, modeled as a beam on elastic foundation with a point force applied.

Note that since the beam on elastic foundation is developed based on the assumption that the tire, modeled as a radial-ply tire, closely represents the majority of tires used by on-road vehicles today. This fact is primarily because of the tremendous advantages of the radial ply tire over the bias-ply tire, as discussed in the introduction.

In his simplified tire model, Fiala [47] approximated the deflection of the belt by uing a quadratic parabola. This method has been shown to yield reasonable results for simplified tire models in various other studies by Fromm [49], Gim ([37], [50]) and Kabe ([52], [53]). In our study, the deflection of the belt is expressed as a quadratic polynomial, as illustrated by equation (3.30).

$$\sigma_{yb} = \frac{F_y \zeta}{K_b l_p}\left(1 - \frac{\zeta}{l_p}\right) \tag{3.30}$$

The K_b term in equation (3.30) is used to approximate the combined stiffness of the belt and the sidewall. The total lateral shear stress generated in the adhesion region of the contact patch can then be computed as the sum of the lateral shear stress from the tread minus the relaxation of the belt by the deformation of the sidewall.

$$\sigma_y = \left[k_y \frac{\tan(\alpha)}{1-s}\zeta - \frac{F_y \zeta}{K_b l_p}\left(1 - \frac{\zeta}{l_p}\right)\right] \tag{3.31}$$

The belt deformation has a more dominant effect on the lateral force generation mechanism than in the longitudinal force generation mechanism. With the inclusion of the belt and carcass deformation, we can finally define the lateral and longitudinal forces as functions of the stresses acting across the contact patch in the fashion described by equations (3.1)-(3.6).

$$F_{xp} = -\left[\underbrace{b\int_0^{l_a} \sigma_x d\zeta}_{adhesion} + \underbrace{\mu_{sx} b\int_{l_a}^{l_p} P_z(\zeta) d\zeta}_{sliding} \right] \tag{3.32}$$

$$F_{yp} = -\left[\underbrace{b\int_0^{l_a} \sigma_y d\zeta}_{adhesion} + \underbrace{\mu_{sy} b\int_{l_a}^{l_p} P_z(\zeta) d\zeta}_{sliding} \right] \tag{3.33}$$

Equations (3.32) and (3.33) form the basis of the force generation mechanism within the contact patch. In the following subsection, we will use the combined slip limiting condition to compute the length of the contact patch in adhesion, l_a, to ensure that we do not exceed the total amount of physically available traction force, as well as modify equations (3.32) and (3.33) to ensure that the magnitude of the forces generated from the sliding region are consistent with the physical laws.

3.5 Longitudinal and Lateral Force: Adhesion and Force Limit

Figure 3-9 shows how, when the tire is operating in combined longitudinal and lateral slip, the effective force distribution will be reduced in both the longitudinal and the lateral directions. As either the slip angle or the slip ratio increase, the length of the contact patch in adhesion decreases, as shown in Figure 3-12 (b), thereby simultaneously reducing the contribution of the force from the adhesion region and increasing the contribution of the force from the sliding region.

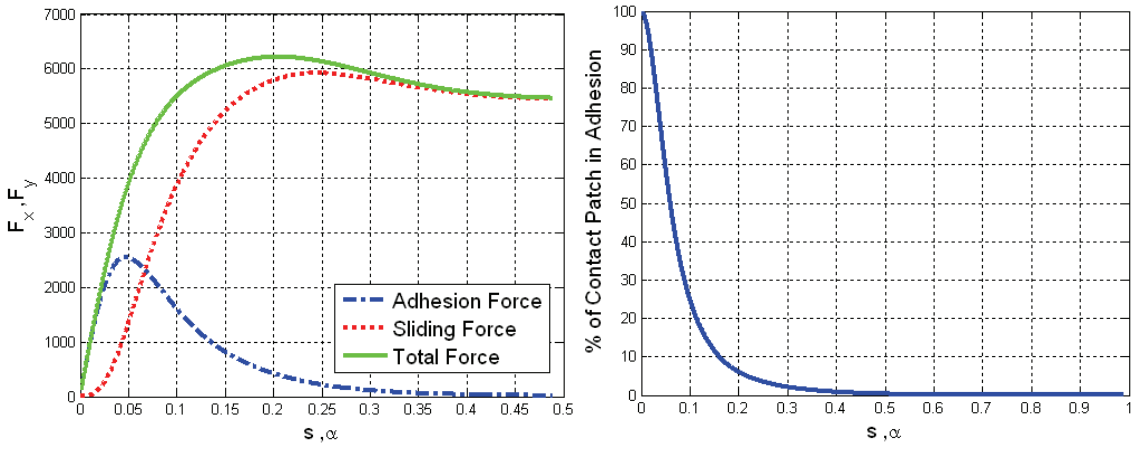

(a) (b)

Figure 3-12. (a) Qualitative plot of lateral and longitudinal force variation with slip ratio and slip angle. (b) Typical percentage of region of contact patch in adhesion with increase in either the slip ratio or the slip angle.

l_a provides us with the coordinate of the point where the contact patch transitions from adhesion to sliding. However, as mentioned earlier, the computation of l_a must be consistent with the physical laws, hence we will employ the elliptical boundary defined by equation (3.34) to limit the effective tire force. The forces $F_{xa}(\zeta)$ and $F_{ya}(\zeta)$ are the longitudinal and the lateral forces in the adhesion region, respectively.

$$\left(\frac{\frac{dF_{xa}(\zeta)}{d\zeta}}{\mu_{px}\frac{dF_z(\zeta)}{d\zeta}}\right)^2+\left(\frac{\frac{dF_{ya}(\zeta)}{d\zeta}}{\mu_{py}\frac{dF_z(\zeta)}{d\zeta}}\right)^2\le 1 \tag{3.34}$$

The limit curve of this the boundary constraint is then defined as:

$$\begin{aligned}
&\frac{1}{\left(\frac{dF_z(\zeta)}{d\zeta}\right)^2}\left[\left(\frac{\frac{dF_{xa}(\zeta)}{d\zeta}}{\mu_{px}}\right)^2+\left(\frac{\frac{dF_{ya}(\zeta)}{d\zeta}}{\mu_{py}}\right)^2\right]=1\Bigg|_{\zeta=l_a}\\
&\Rightarrow\left(\frac{\frac{dF_{xa}(\zeta)}{d\zeta}}{\mu_{px}}\right)^2+\left(\frac{\frac{dF_{ya}(\zeta)}{d\zeta}}{\mu_{py}}\right)^2=\left(\frac{dF_z(\zeta)}{d\zeta}\right)^2\Bigg|_{\zeta=l_a}\\
&\Rightarrow\left(\frac{\sigma_x}{\mu_{px}}\right)^2+\left(\frac{\sigma_y}{\mu_{py}}\right)^2=\left(P_z(\zeta)\right)^2\Bigg|_{\zeta=l_a}
\end{aligned} \tag{3.35}$$

$$\therefore\left(\frac{k_x\frac{s}{1-s}l_a}{\mu_{px}}\right)^2+\left(\frac{k_y\frac{\tan(\alpha)}{1-s}l_a-\frac{F_y l_a}{K_b l_p}\left(1-\frac{l_a}{l_p}\right)}{\mu_{py}}\right)^2=\left(\frac{4F_z}{\pi b l_p}\left(1+A_1 s\left(l_a-\frac{l_p}{2}\right)\right)\sqrt{1-\frac{\left(l_a-\frac{l_p}{2}\right)^2}{\left(\frac{l_p}{2}\right)^2}}\right)^2$$

$$\Rightarrow l_a \sqrt{\left(\frac{k_x \frac{s}{1-s}}{\mu_{px}}\right)^2 + \left(\frac{k_y \frac{\tan(\alpha)}{1-s} - \frac{F_y}{K_b l_p}\left(1-\frac{l_a}{l_p}\right)}{\mu_{py}}\right)^2} = \frac{4F_z}{\pi b l_p}\left(1 + A_1 s\left(l_a - \frac{l_p}{2}\right)\right)\sqrt{1 - \frac{\left(l_a - \frac{l_p}{2}\right)^2}{\left(\frac{l_p}{2}\right)^2}} \tag{3.36}$$

By solving the 4th order polynomial equation resulting from equation (3.36) for l_a, where $0 \le l_a \le l_p$, $l_a \in \mathbb{R}$, it can be assured that the force generated by each element of the tread will always be within the boundary of the friction ellipse. The solution of l_a for equation (3.36) has to be a non-zero and real expression which is valid for $l_a \le l_p$.

However, even with this method of determining the ratio of the adhesion/sliding region, there is one more part that needs to be taken into account with the sliding force component of the lateral and longitudinal forces. Currently, the tire model developed here has the capability to account for anisotropic friction characteristics; hence, some mechanics treatment will have to be applied so that the tire model sliding forces are modeled correctly. Figure 3-13 shows the difference between the Friction Circle in a system with isotropic friction ($\mu_{sx} = \mu_{sy}$) and the friction ellipse, which is more commonly associated with the anisotropic friction conditions ($\mu_{sx} \neq \mu_{sy}$).

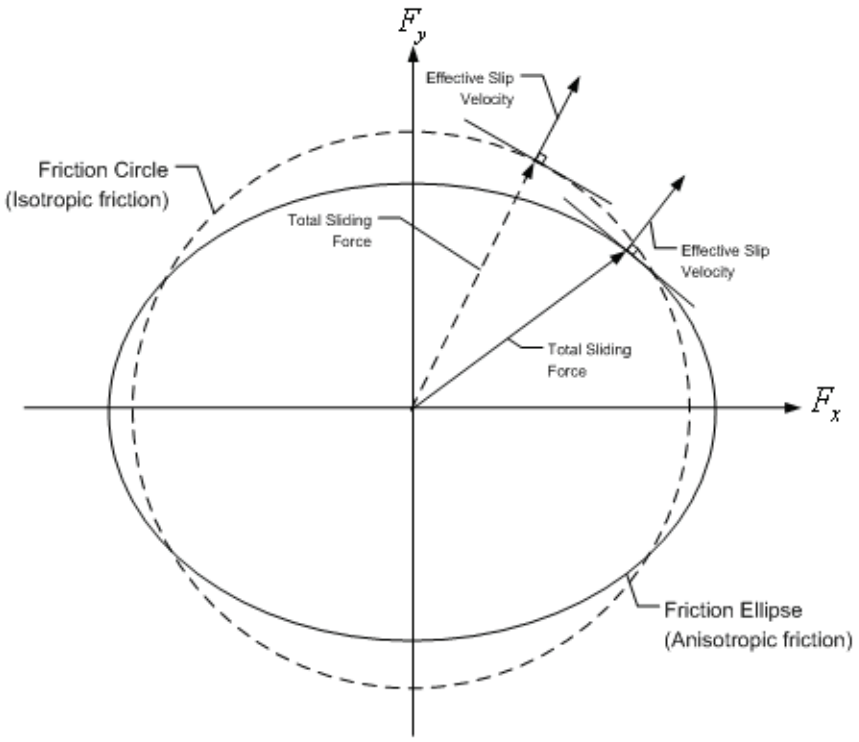

Figure 3-13. A conceptual comparison between the sliding force generated by an isotropic friction law and the sliding force generated by an anisotropic friction law based on equation (3.35) for $\mu_{sx} = \mu_{sy}$ vs $\mu_{sx} \neq \mu_{sy}$.

In a system with isotropic friction characteristics, the line of action of the sliding force is always collinear with the effective sliding velocity, thus maximizing the power dissipated, as noted in Figure 3-13. However, in a system with anisotropic friction, we can see that the generated sliding force does not act in the same direction as the sliding velocity, hence it does not obey the principle of Maximum Energy Dissipation Rate presented by Goyal [54]. This theory has been applied to vehicle dynamics analysis by Dimaggio [55] and to tire modeling by Svendenius [38] and has been used widely in the formulation of friction laws for robotics haptic interface because of its consistency with friction laws that are normal to the limit curve. According to the theory, the power dissipated can be computed using a product of the maximum allowable sliding lateral/longitudinal force and the lateral/longitudinal sliding velocity, following the method of virtual work.

$$W_{x\max} = -F_{x\max} \cdot V_{slipx} \tag{3.37}$$

$$W_{y\max} = -F_{y\max} \cdot V_{slipy} \tag{3.38}$$

Hence, we can calculate the direction of the sliding velocity, denoted as ϕ, knowing that the maximum allowable sliding force is the product of the normal force and the sliding coefficient of friction.

$$\tan(\phi) = \frac{W_{y\max}}{W_{x\max}} = \frac{-F_{y\max} \cdot V_{slipy}}{-F_{x\max} \cdot V_{slipx}} = \frac{\mu_{sy} \cdot F_z \cdot V_{slipy}}{\mu_{sx} \cdot F_z \cdot V_{slipx}} = \frac{\mu_{sy} \cdot V_{slipy}}{\mu_{sx} \cdot V_{slipx}} \tag{3.39}$$

Using the Pythagorean Theorem, the resultant magnitude of the sliding velocity can be expressed as:

$$V_{slip} = \sqrt{\left(\mu_{sy} \cdot V_{slipy}\right)^2 + \left(\mu_{sx} \cdot V_{slipx}\right)^2} \tag{3.40}$$

Then, by projecting the forces in the sliding region of the tire to the direction of the sliding velocity, which is always normal to the limit surface, we get the sliding forces as:

$$\begin{aligned} F_{sxp} &= \mu_{sx} \cos(\phi) b \int_{l_a}^{l_p} P_z(\zeta) d\zeta \\ &= \frac{{\mu_{sx}}^2 \cdot V_{slipx}}{\sqrt{\left(\mu_{sy} \cdot V_{slipy}\right)^2 + \left(\mu_{sx} \cdot V_{slipx}\right)^2}} b \int_{l_a}^{l_p} P_z(\zeta) d\zeta \end{aligned} \tag{3.41}$$

$$\begin{aligned} F_{syp} &= \mu_{sy} \sin(\phi) b \int_{l_a}^{l_p} P_z(\zeta) d\zeta \\ &= \frac{{\mu_{sy}}^2 \cdot V_{slipy}}{\sqrt{\left(\mu_{sy} \cdot V_{slipy}\right)^2 + \left(\mu_{sx} \cdot V_{slipx}\right)^2}} b \int_{l_a}^{l_p} P_z(\zeta) d\zeta \end{aligned} \tag{3.42}$$

The formulation of equations (3.41) and (3.42) means that now the force contribution from the sliding region in equations (3.32) and (3.33) has to be modified to include the effects of anisotropic friction. Thus, with the inclusion of the forces arising from the camber inclination stiffness, equations (3.32) and (3.33) can be rewritten as:

$$F_{xp} = \underbrace{-b\int_0^{l_a} \sigma_x d\zeta}_{adhesion} \underbrace{- \frac{\mu_{sx}{}^2 \cdot V_{slipx}}{\sqrt{\left(\mu_{sy} \cdot V_{slipy}\right)^2 + \left(\mu_{sx} \cdot V_{slipx}\right)^2}} b\int_{l_a}^{l_p} P_z(\zeta) d\zeta}_{sliding}$$

$$= \underbrace{-b\int_0^{l_a} \sigma_x d\zeta}_{adhesion} \underbrace{- \frac{\mu_{sx}{}^2 \cdot s}{\sqrt{\left(\mu_{sy} \cdot \tan\left(\alpha_c\right)\right)^2 + \left(\mu_{sx} \cdot s\right)^2}} b\int_{l_a}^{l_p} P_z(\zeta) d\zeta}_{sliding} \tag{3.43}$$

$$F_{yp} = \underbrace{-b\int_0^{l_a} \sigma_y d\zeta}_{adhesion} \underbrace{- \frac{\mu_{sy}{}^2 \cdot V_{slipy}}{\sqrt{\left(\mu_{sy} \cdot V_{slipy}\right)^2 + \left(\mu_{sx} \cdot V_{slipx}\right)^2}} b\int_{l_a}^{l_p} P_z(\zeta) d\zeta}_{sliding} + \overbrace{C_\gamma \tan\left(\gamma\right)}^{Camber\ Thrust, F_{y\gamma}}$$

$$= \underbrace{-b\int_0^{l_a} \sigma_y d\zeta}_{adhesion} \underbrace{- \frac{\mu_{sy}{}^2 \cdot \tan\left(\alpha_c\right)}{\sqrt{\left(\mu_{sy} \cdot \tan\left(\alpha_c\right)\right)^2 + \left(\mu_{sx} \cdot s\right)^2}} b\int_{l_a}^{l_p} P_z(\zeta) d\zeta}_{sliding} + \overbrace{C_\gamma \tan\left(\gamma\right)}^{Camber\ Thrust, F_{y\gamma}} \tag{3.44}$$

The projection of the sliding force in the direction that is always normal to the limit surface ensures that the model exhibits the behavior that concurs with the Principle of Maximum Dissipation Rate. Similar analysis has been done by Schuring et. al [56], Bakker et. al. [57], Gim [48] and Svendenius [38] on the forces of tire models in the sliding region. The incorporation of the camber thrust into the model enables us to account for the thrust generated by the cambering of the tire as a result of suspension travel.

With the incorporation of the effect of the combined sliding in the contact patch and camber thrust, we have developed a model that has the capability to simulate the operation of a tire under combined slip conditions. However, even though we can now compute the tire forces, without the associated moments, our model will be missing components integral to the vehicle handling simulations. Consequently, the development of the aligning and the overturning moment will be presented in the following section.

3.6 Aligning and Overturning Moment: Formulation

The aligning moment and the overturning moment are two of most important moments for vehicle simulations involving electronic stability control [58]. The aligning moment strongly influences the handling (steering) stability of the vehicle while the overturning moment plays an important role in characterizing the behavior of the vehicle in dynamic rollover simulations. Historically, purely analytical models of the aligning moment have been unsuccessful, primarily because of the fact that they often fail to predict that the aligning moment becomes negative at higher slip angles as demonstrated by the studies in [39] and [47].

The advantage of the model developed in our study is that the aligning moment and the overturning moment are a based on a combined empirical-analytical formulation where the moments are a result of the effective moment arms of the forces acting on the contact patch of the tire. The overturning moment is a result of the lateral and vertical forces, resulting from either a slip angle input or a camber angle input. The models proposed in this study to compute the aligning moment and the overturning moment are developed based on our analysis of empirical data from various sources ([39], [1], [51], [3]) with some insight from theoretical mechanics. The inclination moment has two components, one resulting from the camber angle, resulting in a static shift in the overturning moment and another, resulting in the change of the shape due to steering. Pottinger [1] and Genta [51] noted this phenomenon in tire testing data and hypothesized that this behavior in the overturning moment is consistent assuming small changes in camber (±10°). By using the expression for the overturning moment given in equation (3.10) as a start, we can develop the model for the overturning moment as shown in equation (3.45).

$$M_{xp} = \underbrace{C_{mx\gamma}\left(-\overbrace{C_\gamma \tan(\gamma)}^{F_\gamma} R_l \cos(\gamma) - F_{zp} R_l \sin(\gamma)\right)}_{\text{Inclination moment}} - \underbrace{C_{mx\alpha} F_{yp}}_{\text{Slip angle moment}}$$
$$= \underbrace{-C_{mx\gamma}\left(C_\gamma + F_{zp}\right) R_l \sin(\gamma)}_{\text{Inclination moment}} + \underbrace{C_{mx\alpha} F_{yp}}_{\text{Slip angle moment}} \tag{3.45}$$

Where

$$C_{mxs}, C_{mx\alpha} = \text{empirical shape factors}$$

The aligning moment, shown in equation (3.46), is formulated as a semi-empirical model, accounting for the change in the tire pneumatic trail with respect to the tire lateral force, as illustrated in Figure 3-14. The pneumatic trail represents the effective shift in the point of application of the lateral force with respect to slip angle input. Since the model is developed with lateral slip as the input, and tire testing data collected often has just lateral slip as the input (the longitudinal slip is forced to be zero during testing) the contribution from the longitudinal stress term is considered negligible.

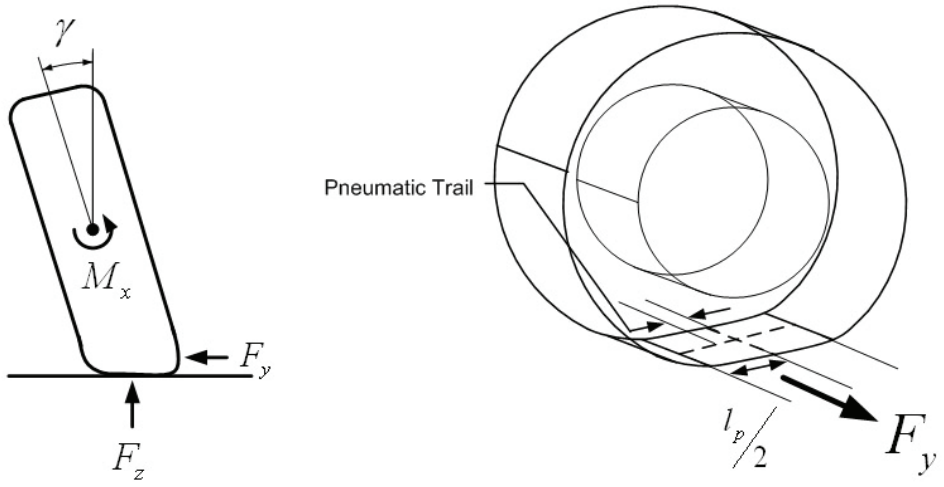

(a) (b)

Figure 3-14. (a) The lateral force, the vertical force, and the generation of the overturning moment. (b) Pneumatic trail of a tire rolling on a road.

$$\begin{aligned} M_{zp}(\alpha_c) &= \int_A \left(p_x \cdot y - p_y \cdot x \right) dA = \int_A \left(x \cdot p_y \right) dA \\ &= \underbrace{\left(C_{mz1} + \left(C_{mz2} - C_{mz1} \right) \operatorname{sech}\left(C_{mz3} \frac{\left| \tan\left(\alpha_c \right) \right|}{1 - \left| \tan\left(\alpha_c \right) \right|} \right) \right)}_{\text{Pneumatic Trail}} \left(F_{yp} \cos\left(\gamma \right) + C_\gamma \tan\left(\gamma \right) \right) \end{aligned} \quad (3.46)$$

Where

$$C_{mz1}, C_{mz2}, C_{mz3} = \text{empirical shape factors}$$

The methods of identifying the empirical factors of $C_{mxs}, C_{mx\alpha}, C_{mz1}, C_{mz2}$ and C_{mz3} will be presented in Chapter 5, since they are load dependent and require some post-processing of tire data before they can be acquired by analyzing the trends.

3.7 Transient Steering Properties: Relaxation and Time-delay

When a tire is steered with a certain slip angle α at the wheel center, the viscoelastic properties of the sidewall change the behavior of the slip angle at the contact patch, α_c. It was shown by Clark [39] that there is an increase in phase difference between the steering wheel input and the lateral force with increase in steering frequency. Recently, it has been proposed by researchers that the slip angle at the contact patch can then be modeled as a first order differential equation (Pottinger [1], Lee [36]) or a second order differential equation as shown in [37] with the slip angle at the wheel as the input to the system. Capturing this behavior is very important for vehicle simulations such as double lane change and single lane change maneuvers. Second order models are better at capturing the yaw rate overshoot for vehicle dynamics simulations, since a set of tires that have large overshoot may cause the vehicle to lose directional stability and spin out due to a sudden change in the steering input [59]. By modeling the time-delay behavior using the second order differential equation, we can empirically obtain the data and determine the appropriate constants to characterize the tire lateral force generation behavior.

Although first order tire dynamics models improve simulations, it has been demonstrated by studies conducted by NHSTA that tire side force dynamics exhibits a behavior more consistent with a second order model [59]. At higher speeds, the tire side force increases with frequency before rolling off, which is more characteristic to an underdamped system. Since the aligning moment (equation (3.46)) depends on the lateral force, the lagging of the slip angle input of the patch with respect to slip angle at the center of the wheel causes the lateral force and all associated moments (overturning moment, aligning moment) to be lagged simutaneously. The fact that this approach achieves a dual-purpose underscores the appropriateness of modeling tire dynamic behavior in this fashion.

The relationship between the slip angle at the center of the wheel and the slip angle at the contact patch can then expressed as:

$$\ddot{\alpha}_c + \rho_1 \dot{\alpha}_c + \rho_2 \alpha_c = \alpha \tag{3.47}$$

Where

ρ_1, ρ_2 = Empirical constants

α = Slip angle at the center of the wheel

α_c = Contact patch slip angle

In Figure 3-15 (a) we illustrated the accuracy of approximation of the first and second order models for the normalized lateral force with respect to the slip angle at the center of the wheel versus the frequency, by comparing the simulation results for the two models with experimental data. In Figure 3-15 (b), the models are compared with experimental data in terms of phase versus frequency. Although the first order lag fits the magnitude of the experimental data better, the second order lag fits the phase better. The second order lag also provides the model with the capabilities to account for lateral force overshoot, which is an important factor in modeling spinouts.

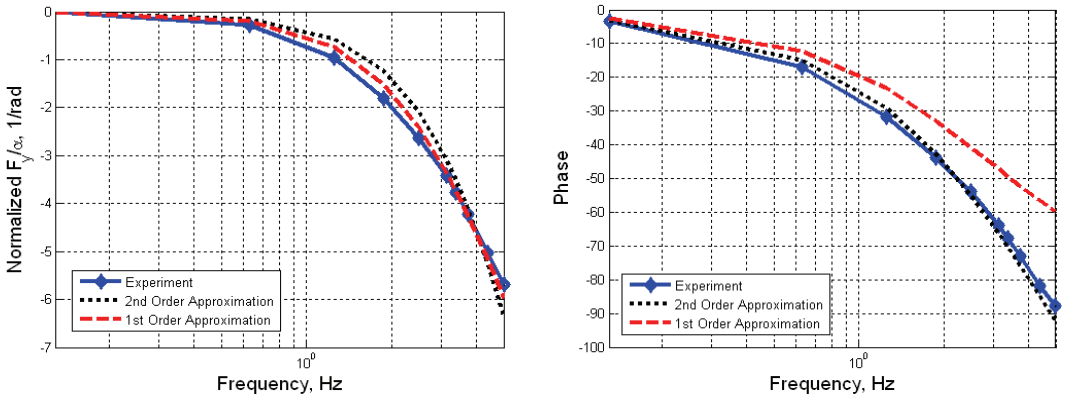

(a) **(b)**

Figure 3-15. A comparison of an example of experimental lateral tire dynamic behavior with first and second order models. (a) Magnitude plot (b) Phase plot.

In addition to the time delay, this viscoelastic property of tires also changes the stress relaxation tire properties. The effect of this stress relaxation is then reflected in the change in the effective peak coefficient of friction during change in slip ratio or slip angle. This effect is shown in Figure 3-16 (a) and can be modeled using equations (3.48)

and (3.49). In Figure 3-16 (b) we illustrate the fit of the proposed normalized lateral force model, for both positive and negative sweep, with experimental data.

The phenomenon of friction decay is a very complex one and thus, for the purpose of our study, the methodology used in the development of this tire model is developed on an approximation based on observations of empirical data.

$$\begin{aligned}\mu_x &= \mu_{xs} + \Delta\mu_{xp\max} + \Delta\mu_{xp\min} \\ &= \mu_{xs} + \left((\mu_{xp\max} - \mu_{xs})\right)\operatorname{sech}\left(S_x \frac{|s - s_p|}{1 - |s|}\right) + \left((\mu_{xp\min} - \mu_{xs})\right)\operatorname{sech}\left(S_x \frac{|s + s_p|}{1 - |s|}\right)\end{aligned} \tag{3.48}$$

$$\begin{aligned}\mu_y &= \mu_{ys} + \Delta\mu_{yp\max} + \Delta\mu_{yp\min} \\ &= \mu_{ys} + \left((\mu_{yp\max} - \mu_{ys})\right)\operatorname{sech}\left(S_y \frac{|\tan(\alpha_c) - \tan(\alpha_{cp})|}{1 - |\tan(\alpha_c)|}\right) \\ &\quad + \left((\mu_{yp\min} - \mu_{ys})\right)\operatorname{sech}\left(S_y \frac{|\tan(\alpha_c) + \tan(\alpha_{cp})|}{1 - |\tan(\alpha_c)|}\right)\end{aligned} \tag{3.49}$$

Where

α_{cp} = Slip angle at μ_{yp}

s_p = Slip ratio at μ_{xp}

μ_{xs} = Sliding Coefficient of friction (longitudinal direction)

μ_{ys} = Sliding Coefficient of friction (lateral direction)

S_y = Rate of decay for friction in the lateral direction

S_x = Rate of decay for friction in the longitudinal direction

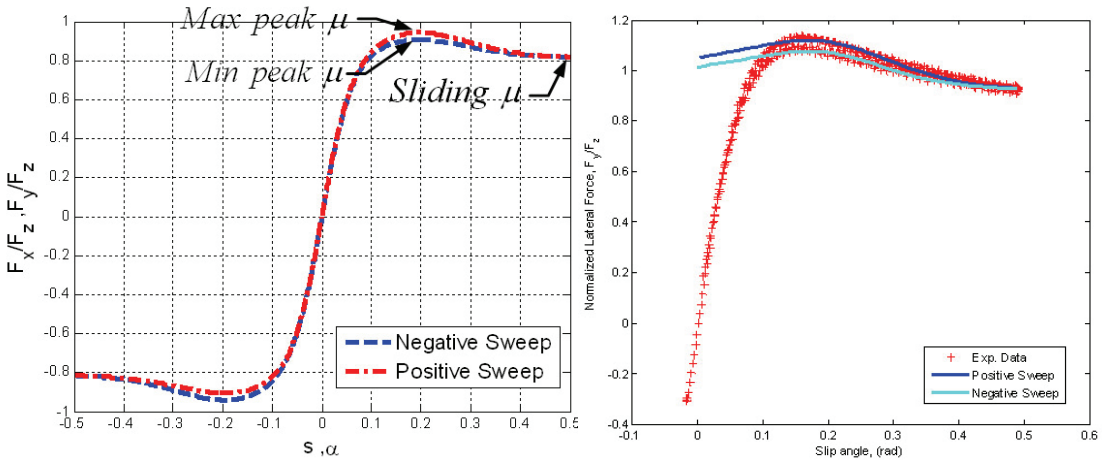

(a) (b)

Figure 3-16. (a) The relaxation properties of the tire for different slip angle and slip ratios. (b) An example of the coefficient of friction fits for a set of experimental data.

3.8 Rolling resistance: Steady State Handling

The rolling resistance is a very important part of vehicle dynamics modeling. Rolling resistance happens because of the fact that the tire deforms when it rolls on a flat surface. A steel wheel on a railroad vehicle will definitely have less rolling resistance than a tire rolling on a tarmac/asphalt road, when the magnitudes or relative deformation are noted. For practical simulation purposes, the rolling resistance data for a tire is collected at zero camber and zero slip. In our formulation, the rolling resistance force is taken as an offset in the slip ratio of the tire model, as shown in equation (3.50).

$$s = s + s_0 \tag{3.50}$$

Typically, the tire rolling resistance is taken as a percentage (~1%-2%) from the tire vertical force for the purpose of real-time vehicle dynamics simulations ([58], [51]).

3.9 Conicity and Plysteer: Steady State Handling

When a passenger vehicle is driven on the road, it will experience a “pulling” force to either left or right, depending on the conicity and plysteer characteristics of the tire. Conicity effect is defined as a constant lateral force acting on the wheel that has a direction which is independent of direction. Conicity is caused by tire manufacturing defects such as incorrect positioning of tire belts and off-center belts [39]. Plysteer

effects happen when the tire "pull" direction changes with the direction of rotation and is usually caused by the different behavior of symmetrical and asymmetrical laminates under tensile stress within the contact patch of a tire ([39], [1]). Conicity and plysteer effects result in the passenger vehicle deviating from a straight-line trajectory even when the steering angle is zero. The driver of the vehicle will have to maintain a constant torque to keep the vehicle moving in the intended direction.

Both of these effects are known as "pseudo-slip" and are included in this formulation by using a small off-set value of slip angle of the lateral forces. The small offset can be determined by measuring the value of α when the lateral force is zero, and denoting that value as α_0. Hence, the effective slip angle is:

$$\alpha_c = \alpha_c + \alpha_0 \tag{3.51}$$

With the inclusion of conicity and plysteer effect, the model now has now been given the capability to account for all the important effects of an on-road tire model for vehicle dynamics purposes, and hence we can move on to finalize the details of the implementation of this model.

3.10 Summary

In this chapter, an on-road tire model which incorporates many of the insights from recent experimental and theoretical work has been developed. The analytical modeling, although developed and applicable under certain assumptions as stated, provides users with the capability to perform dynamic simulations with a tire model that is consistent with the physical laws, correlates well with experimental results, and is augmented by empirical tire testing data.

An implementation diagram for this model is shown in Figure 3-17. The lateral forces calculated are fed back to compute other forces and moments in the system because the tire force and moment generation mechanics are heavily coupled to the belt mechanics and we believe that this is a more realistic representation of the tire behavior.

The contributions of the on-road model to the tire modeling community are:

1. The integration of a method to include the slip angle in the calculation of the vertical stiffness. This development allows for the change in the loaded radius with change in slip angle input.

2. Development of a tire model that uses data from pure slip testing to account for a theoretically developed combined slip tire traction behavior.
3. The augmentation of the analytical modeling approach with empirical characteristics allows us to account for phenomena that we did not model physically into the system.
4. The model developed has the capabilities for dynamic simulations, with the inclusion of tire relaxation properties and slip angle delay.

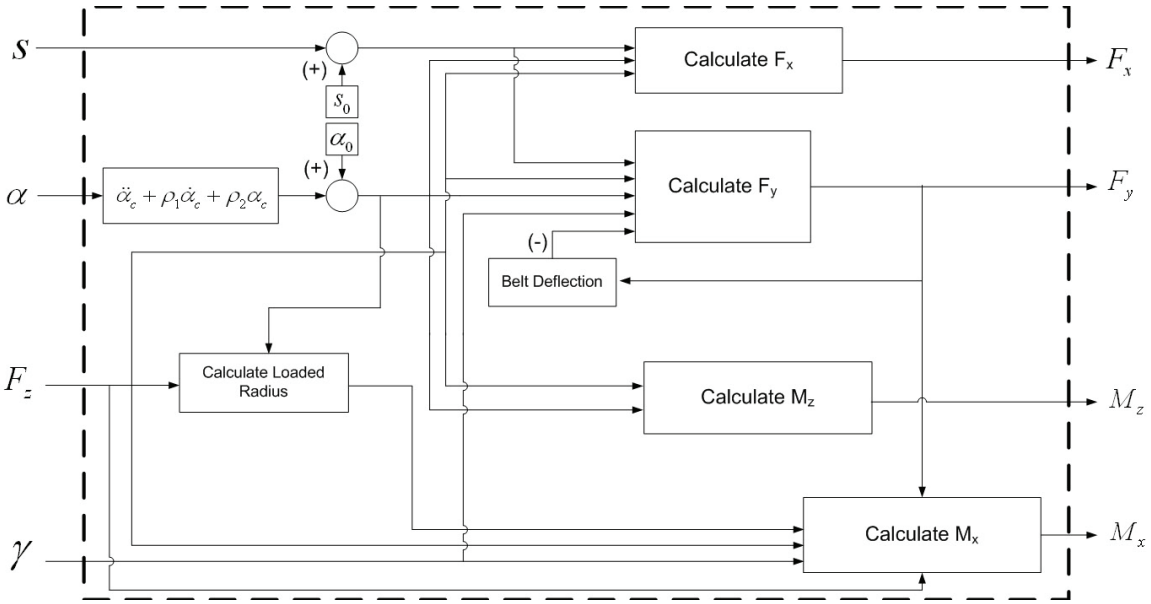

Figure 3-17. A block diagram implementation of the on-road tire model developed in this chapter.

In chapter 4, the model will be expanded upon to enable it to handle vehicle dynamics simulations for off-road simulations. The parameter identification for this tire model is presented in chapter 5. The main subroutine for this tire model is included in the appendix.

4. Tire Model Mechanics: Off-road

4.1 Tire Model: Rigid Wheel Model

The interaction between a rigid wheel and soft soil has been explored extensively by many researchers ([60],[7],[6],[20]). Sometimes, the tire, rather than being assimilated to a flexible body, can be approximated to a rigid wheel. This assumption can be made especially when the tire is transversing over terrain that is extremely soft, resulting in a more significant deformation of the terrain compared with the deformation of the tire. This phenomenon can happen also when the tire is inflated to a pressure where the combined pressure of the carcass rigidity and the inflation pressure exceed the load bearing capacity of the terrain.

The variables that will be used in the modeling are defined as shown in Figure 4-1**.**

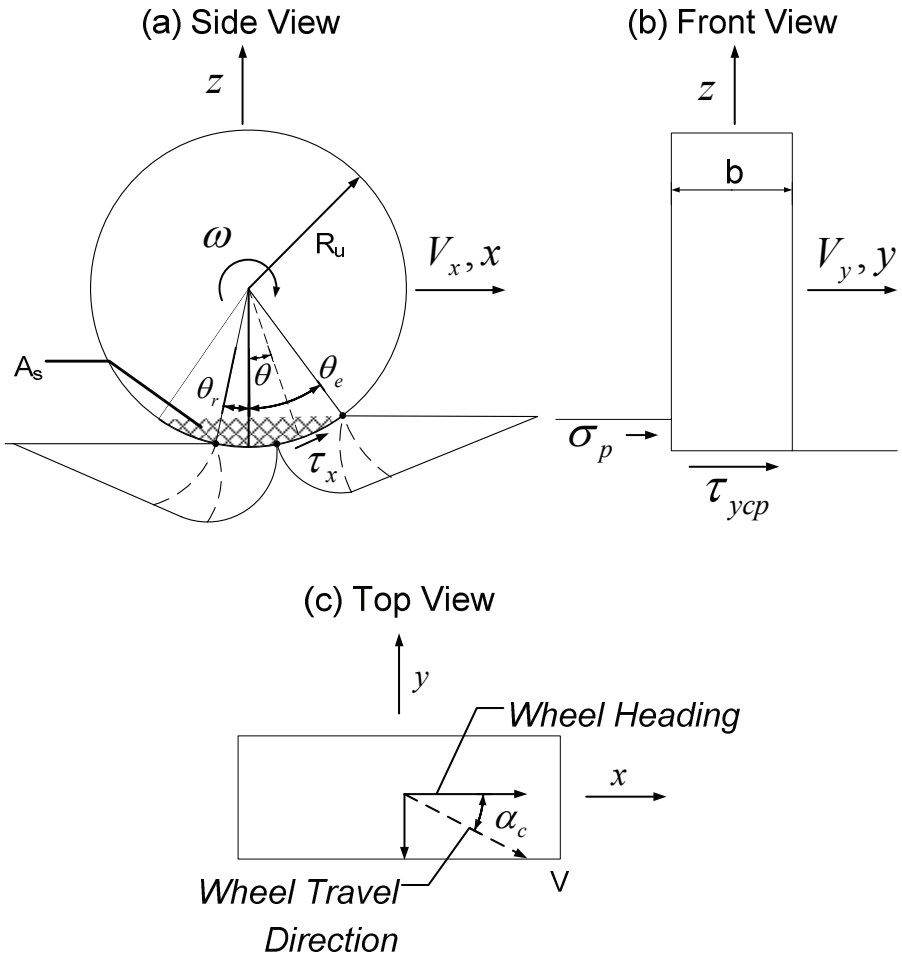

Figure 4-1. Rigid off-road tire model variables relative to the direction of wheel travel.

The variables introduced in Figure 4-1 will be revisited throughout the chapter; however, the definitions for some of the most important variables are given here:

R_u = Undeformed radius of the wheel
θ_e = Entry angle
θ_r = Exit angle
θ = Angle on the wheel relative to a fixed frame
V_x = Longitudinal velocity
V_y = Lateral velocity
ω = Angular velocity of the wheel
b = Width of the wheel
α_c = Slip angle relative to the center of the wheel
A_s = Area of the wheel sunk in soil in the plane of the wheel
σ_p = Lateral bulldozing pressure acting on side of the wheel
τ_{ycp} = Shear stress acting in the lateral direction of the wheel
τ_x = Shear stress acting in the longitudinal direction of the wheel

The assumptions involved in the development of the off-road tire model has been stated in the introduction and are revisited for clarification purposes:

1. When the ground becomes very hard/rigid, the tire model switches to the behavior of a flexible tire operating on road. This will limit the stresses imposed on the soil by the tire when it starts deforming.
2. The soil is mechanically modeled as a plastic material using the quasi-static equilibrium plate sinkage equations based on strip load analysis.
3. The tire model has its roots in analytical mechanics and is augmented with empirically obtained information to account for effects otherwise not possible to be captured.
4. The tire model should revert to a pure longitudinal model or to a pure lateral slip model when either the lateral, or respectively the longitudinal slip is zero.

5. The tire inflation pressure and the temperature remain constant or change at a very slow rate during the entire simulation.

4.1.1 Rigid Wheel Model: Stationary Vertical Loading

For any vehicle simulation, the most basic of all scenarios is the dynamic settling of the wheel on a flat, deformable surface. When the wheel sinks in the soil, the radial and the shear stresses acting on the surface of the soil will tend to achieve a sense of buoyancy. The shear and the radial stresses acting on the wheel will increase with sinkage until the wheel in a state of equilibrium. For vehicles, the static load of the wheels, w_0, when the vehicle is at standstill can be used for this purpose.

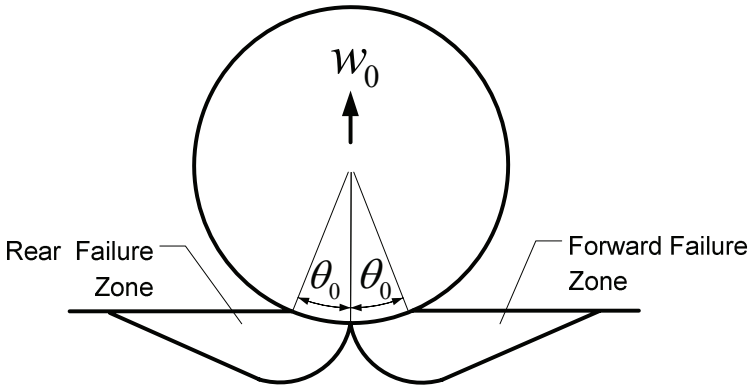

Figure 4-2. A non-rotating wheel in equilibrium conditions on flat, soft soil.

The shear displacement of the soil underneath the wheel for the stationary loading case can be written as a function of the stationary central angle, θ_0 as shown in equation (4.1). This relation will be important when we will calculate the shear stress acting on the surface of the wheel from the soil because of the symmetry of the stresses acting on the wheel. The main assumption for using this method for modeling the initial loading of soil is because the soil failure mode under the wheel can be assumed to be in the general shear failure mode in the longitudinal direction and the local failure mode in the lateral direction. When the soil is in the general shear failure mode, soil developed a distinct rupture surface and is pushed up on the sides of the tire. This is different than the local shear failure mode, where the rupture of the soil is confined to the surfaces immediately under the tire, and the soil bulge on the sides of the tire are less distinct. When the tire is

loaded on the soil, shear displacement of the soil should move in opposite directions on different sides of the wheel as shown in Figure 4-2.

$$j_0 = R_u\left[(\theta_0 - \theta) - \left(\sin\theta_0 - \sin\theta\right)\right] \tag{4.1}$$

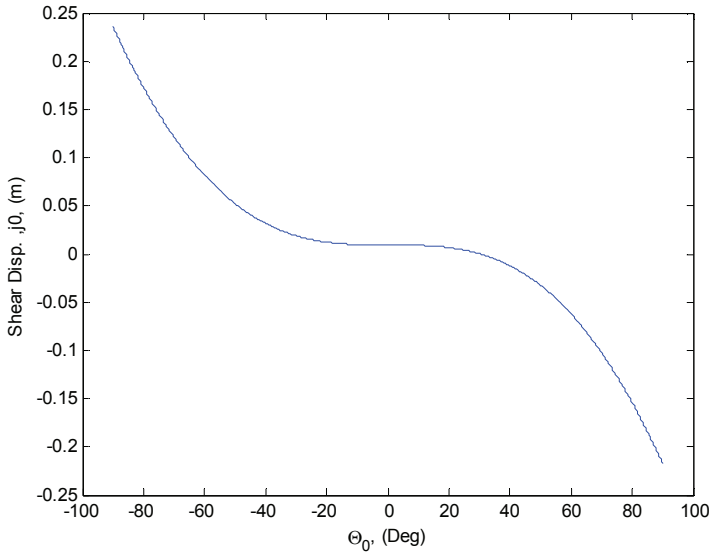

Figure 4-3. Shear displacement at a function of θ for an assumed angle of θ_0=30°.

The vertical support force acting on the wheel can be calculated from the normal stress as:

$$w_0 = R_u b\left(\int_{-\theta_0}^{\theta_0} \sigma_n(\theta)\cos\delta\cos\theta + \tau(\theta)\sin\delta\sin\theta d\theta\right) \tag{4.2}$$

Where

$\sigma_n(\theta)$ = stresses acting in the radial direction of the wheel

$$\delta(\theta) = \tan^{-1}\left(\frac{\tau(\theta)}{\sigma_n(\theta)}\right)$$

$$\tau(\theta) = \tau_{\max}\left(1 - e^{-j0/K_x}\right)$$

Note that the shear stress calculations show that the shear stress will increase from the point where the edge of the wheel makes contact with the ground until it reaches a point where the soil experiences shear failure, in which the shear stresses generated will

be limited by the failure envelope of the soil. The proposed implementation of this method involves incrementally increasing the sinkage until equation (4.2) is satisfied for a certain angle of θ_0. We can now proceed to the next section where the analysis will focus on modeling the forces and the moments resulting from the rolling of the wheel on soft terrain.

4.1.2 Rigid Wheel Model: Slip and Shear Displacement

The next step for a vehicle simulation is to provide the framework for a quasi steady-state simulation scenario from which computing the shear stress is an essential component. Naturally, the development of the model will first focus on wheel performance modeling for rigid wheels, as a general case.

To use the shear stress relation, we must first derive an expression for the shear displacement of the soil directly underneath the wheel. Let us recall the definition used in this dissertation for the longitudinal slip, which is defined in a manner consistent with the SAE convention. The longitudinal slip ratio for a moving wheel has been defined as:

$$s_d = 1 - \frac{V_x}{R_u \omega} \tag{4.3}$$

Where

V_x = Longitudinal velocity of center of wheel
ω = Angular velocity of wheel
s_d = Longitudinal slip in driven state

For a rigid wheel, Wong ([3], [61], [62]) has demonstrated that the soil shear displacement for a driven rotating wheel, j_d, can be calculated for any arbitary angle θ on the wheel using the interface velocity of the wheel. That means that we can also, in a similar manner, derive the shear displacement as shown in (reference) and equation (4.5) for the slip definitions we have specified in chapter 2. For a rigid wheel, we can assume that the radius is constant. In Figure 4-4 , we can note that a wheel of radius R_u, which moves with a forward velocity, V_x, and has an angular velocity, ω, the tangential slip velocity at the interface can be expressed as:

$$
\begin{aligned}
V_{sd} &= R_u\omega - V_x\cos\theta \\
&= R_u\omega\left[1-\left(1-s_d\right)\cos\theta\right]
\end{aligned}
\tag{4.4}
$$

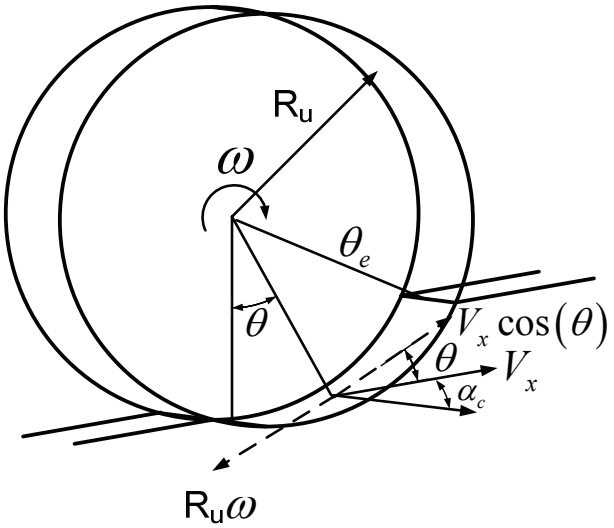

Figure 4-4. Some of the angles and velocities associated with the slip of the rigid wheel defined in 3-D.

The tangential soil shear displacement for a driven rigid wheel can then be calculated as shown in equation (4.5). The slip velocity tends to have a maximum value at the angle of entry, and decreases as we sweep across the angles to a minimum at the bottom center of the wheel, where it will start to increase again as we approach the exit angle, θ_r. In the terramechanics community, it has been common practice to avoid the use of slip to directly calculate the shear deformation of the soil and use the interface velocity instead. The whole concept of using the interface velocity originates from the fact that any given slip can produce significantly different slip rates, which is an important factor to be considered when modeling wheel-soil interaction on rate-dependent soil [63].

$$
\begin{aligned}
j_{dx} &= \int_0^t V_{sd}\,dt \\
&= R_u \int_0^t \left[1-\left(1-s_d\right)\cos\theta\right]\omega\,dt \\
&= R_u \int_{\theta}^{\theta_e} \left[1-\left(1-s_d\right)\cos\theta\right]d\theta \\
&= R_u\left[\left(\theta_e-\theta\right)-\left(1-s_d\right)\left(\sin\theta_e-\sin\theta\right)\right]
\end{aligned}
\tag{4.5}
$$

The amount of soil shear displacement continuously increases from the front to the rear of the entire region of contact. At the first point of contact, the amount of soil shear displacement is zero. As the wheel rotates, the shear displacement increases very rapidly towards the rear of the contact region. After a certain amount of shear displacement, the amount of stress in the soil underneath the wheel will be limited by the ultimate failure stress of the soil. However, as noticed, s_d approaches infinity when ω approaches zero in the driven state (skidding locked wheel) and similarly, when V_x approaches zero in the braking state (wheel spinning from standstill), s_d approaches infinity as well. Hence, when any of the velocities approaches zero, the longitudinal slip becomes ill-defined. Bernard et. al.[64] presented an approach for calculating the longitudinal slip ratio and the slip angle for elastic tires using the equilibrium relaxation lengths of the tread material of a tire to overcome the numerical stability problem arising from this behavior for vehicle dynamics simulations.

To define the lateral shear deformation under the wheel, we first revisit the definition of the slip angle. For the off-road rigid wheel, the slip angle, defined in term of the slip velocities is:

$$
\alpha_c = \tan^{-1}\left(\frac{V_y}{V_x}\right) \tag{4.6}
$$

Hence, the lateral slip velocity can be defined as:

$$
V_y = V_x \tan\left(\alpha_c\right) \tag{4.7}
$$

Similar to equations (4.5), we can now define the lateral soil shear displacement for driving operations as shown in equation (4.8).

$$\begin{aligned} j_{dy} &= \int_0^t V_y dt \\ &= \int_{\theta}^{\theta_e} V_x \tan(\alpha_c) dt \\ &= \tan(\alpha_c) \int_{\theta}^{\theta_e} \frac{V_x}{\omega} d\theta \\ &= R_u (1 - s_d)(\theta_e - \theta) \tan(\alpha_c) \end{aligned} \tag{4.8}$$

The soil shear displacement according to equations (4.8) assumes that the shear stress along the region of contact starts with zero at the point of initial contact and increases rapidly at the same rate with the longitudinal soil shear displacement as we progress from the front to the rear of the contact region. In summary, we can express the longitudinal and the lateral soil shear displacement for rigid wheels during different operating situations (driving or braking) as:

$$j_x = R_u \left[(\theta_e - \theta) - (1 - s_d)(\sin\theta_e - \sin\theta) \right] \tag{4.9}$$

$$j_y = R_u (1 - s_d)(\theta_e - \theta) \tan(\alpha_c) \tag{4.10}$$

4.1.3 Rigid Wheel Model: Stresses and Forces

The first step toward determining the stresses and the forces from the wheel-terrain interaction is to compute the stresses acting from the soil surface on the wheel, in the radial direction. The normal stress distribution should ideally be zero at the start of the contact region, reaching a maximum somewhere between the entry and the exit angles.

Bearing capacity theories have been central to the development of pressure-sinkage relationships for land locomotion studies [63]. However, it is necessary to emphasize the difference between the paradigm employed by soil mechanics and by vehicle mobility researchers. The soil mechanics expert is more concerned with the settlement of the foundation and the vehicle mobility researcher is preoccupied with the sinkage and the

traction of the vehicle. The relative magnitude and deformation rate for the soil is the main difference between the two different perspectives. Relatively speaking, the stress and strain experienced by a soil mass within the realm of the mobility researcher would be devastating to a soil mechanist.

The vehicle mobility researcher studies the behavior of the soil from the plasticity perspective to ensure that the model adheres to empirical observations and common sense. If the pressure acting against a loading plate is measured, and a bearing capacity equation is used to calculate the pressure acting on the surface of the plate, both solutions must provide the same pressure or else either one or both solutions are inaccurate. Terzaghi [65] was the first researcher to propose the solution of the plasticity equation for the load bearing capacity of soils using logarithmic spirals and straight lines. Meyerhof [10] then proposed a bearing capacity theory that can be applied to both deep and shallow foundations. The connection between the work done by Terzaghi and the work done by Meyerhof is that Meyerhof included the effect of depth as a significant part of his formulation. The only main drawback of the work done by Meyerhof from the mobility researcher's perspective is that he assumed that the soil mass is an incompressible material, which is a significantly limitative assumption. Even so, the work of Meyerhof is important in the sense that it inspired the development of a new plasticity-based pressure-sinkage relationship by Reece [9], which is supported by experimental evidence. The equation proposed by Meyerhof for the bearing pressure of the soil mass under a foundation is shown in equation (4.11).

$$\begin{aligned} q &= \overbrace{cN_c}^{\text{Cohesion Term}} + \overbrace{\frac{b\gamma}{2}N_\gamma}^{\text{Weight and Friction Term}} + \overbrace{pN_q}^{\text{Surcharge Term}} \\ &= \underbrace{cN_{cq}}_{\text{Cohesion+Surcharge}} + \underbrace{\frac{b\gamma}{2}N_{\gamma q}}_{\text{Weight+Friction+Surcharge}} \end{aligned} \tag{4.11}$$

The foundation problem represents a successful application of the theory of plasticity, since it has led to the development of bearing capacity theory, which has been used everyday in the construction of buildings, dams, and retaining walls. The sinkage problem has been approached primarily using empirical methods which have weak

connections to physical modeling. The most widely used equation to determine the pressure-sinkage relationship is the one developed by Bekker [7], which is revisited as shown in equation (4.12).

$$p = \left(\frac{k_c}{b} + k_\phi \right) z^n \tag{4.12}$$

Where k_c', k_ϕ' and n are termed as pressure-sinkage parameters and are usually acquired by sinkage plate tests, and b represents the main dimension of the plate.

As pioneer work in the development of vehicle terrain interaction, equation (4.12) represents a monumental step in the modeling of vehicle terrain interaction, expanding upon the work of Bernstein and Goraitchkin. However, like most empirical solutions, it is formulated as a "black box" model and may not have sound theoretical support. Reece [9] and Karafiath [20] argued that equation (4.12) is inconsistent with the insight from bearing capacity theory. By closely examining equations (4.11) and (4.12), we can surmise from (4.12) that the amount of load that a plate will support decreases with increase in plate width using the pressure-sinkage relation. This contradicts equation (4.11), where the bearing capacity of a plate will increase with an increase in plate loading area. From the common sense point of view, we can see that equation (4.11) makes more physical sense, as the method to get out of a quicksand pit entails spreading your weight across a larger area. Because of the fact that the stress behavior in this study will be based on a lot of analysis from the theory of plasticity, slip lines, and bearing capacity theory, the pressure-sinkage relation from Reece will be utilized to calculate the radial stresses acting on the wheel. The pressure-sinkage relation developed by Reece is revisited as equation (4.13), which bears a resemblance to equation (4.11).

$$\begin{aligned} p &= ck_c' \left(\frac{z}{b} \right)^n + \frac{\gamma_s b}{2} k_\phi' \left(\frac{z}{b} \right)^n \\ &= \left(ck_1 + \gamma_s b k_2 \right) \left(\frac{z}{b} \right)^n \end{aligned} \tag{4.13}$$

Unlike the coefficients from Bekker's pressure-sinkage equation, by definition, the parameters k_c' and k_ϕ' are truly non-dimensional and do not depend on the units of the

exponent n [9]. k_c' and k_ϕ' are variables that are related to the cohesion and to the angle of internal friction, respectively. n is the sinkage exponent and γ_s is the soil unit weight, which can be measured in the laboratory. In the computation of the radial tire stresses, it has been shown that the maximum point for the radial stress distribution under rigid wheels is not directly under the center of the wheel ([62], [61], [20]), and the general trend is that the maximum radial stress is shifted forward and moves further forward of the wheel with increase in slip. Equation (4.13) can be used to compute the radial shear stresses acting on the surface of the wheel from the front to the maximum radial stress by substituting equation (4.22) to get equation (4.14) as shown by Wong [62].

$$\begin{aligned}\sigma_{nf}(\theta) &= \left(ck_1 + \gamma_s b k_2\right)\left(\frac{R_u\left(\cos\theta - \cos\theta_e\right)}{b}\right)^n \\ &= \left(ck_1 + \gamma_s b k_2\right)\left(\frac{R_u}{b}\right)^n \left(\cos\theta - \cos\theta_e\right)^n\end{aligned} \tag{4.14}$$

For the region from the maximum radial stress to the rear of the contact region, where θ_N is the angle where the radial stress is maximum, we can compute the radial stresses for the tire from θ_N to θ_r using equation (4.15).

$$\sigma_{nr}(\theta) = \left(ck_1 + \gamma_s b k_2\right)\left(\frac{R_u}{b}\right)^n \left(\cos\left(\theta_e - \left(\frac{\theta - \theta_r}{\theta_N - \theta_r}\right)\left(\theta_e - \theta_N\right)\right) - \cos\theta_e\right)^n \tag{4.15}$$

Hence, we can summarize that the radial stresses acting on the surface of the wheel can be calculated according to equation (4.16). A plot depicting the radial stresses calculated using equation (4.16) is shown in Figure 4-6.

$$\sigma_n(\theta) = \begin{cases}\sigma_{nf}(\theta) & \theta_N \le \theta < \theta_e \\ \sigma_{nr}(\theta) & -\theta_r < \theta \le \theta_N\end{cases} \tag{4.16}$$

The methodology developed for computing the angle of maximum radial stress is based on the theory of plastic equilibrium for the soil. The soil failure is governed by the

plastic flow of soil under the wheel. As such, referring to Figure 4-5, there exists a point N on the surface of the wheel where the front and rear slip lines meet. At this point N, the sign of the shear stress changes and the maximum principle stress occurs. In order to calculate the radial stress from equation (4.16), we have to find point N along the circumference of the wheel. According to the Mohr-Coulomb Failure Criterion and the theory of plastic equilibrium, there has to be two slip lines on the axis of the major principle stress with an angle of $\mu = \frac{\pi}{4} - \frac{\phi}{2}$ on either side of the axis. It has been visually verified that the trajectory of soil particles traveling tangent to the surface of the wheel at the point N coincides approximately with the direction of the effective instantaneous velocity of the point on the rim in contact with it [61]. In civil engineering practice, it is often stipulated that the soil particle trajectory represents one set of slip lines in the failure zone. Using the kinematics of the wheel, we can determine the angle that the effective instantaneous velocity of a point on the surface of the wheel makes with a vector that is normal to the surface of the wheel. Figure 4-5 (a) shows the derivation of the angle κ for a driven wheel with the instantaneous center of rotation. Figure 4-5 (b) shows the derivation of the angle κ for a braked/towed wheel with the instantaneous center of rotation. This method has been used by Wong for braked/towed wheels with very good results [61]. In this study, we used the same method to derive the same expression for a driven wheel.

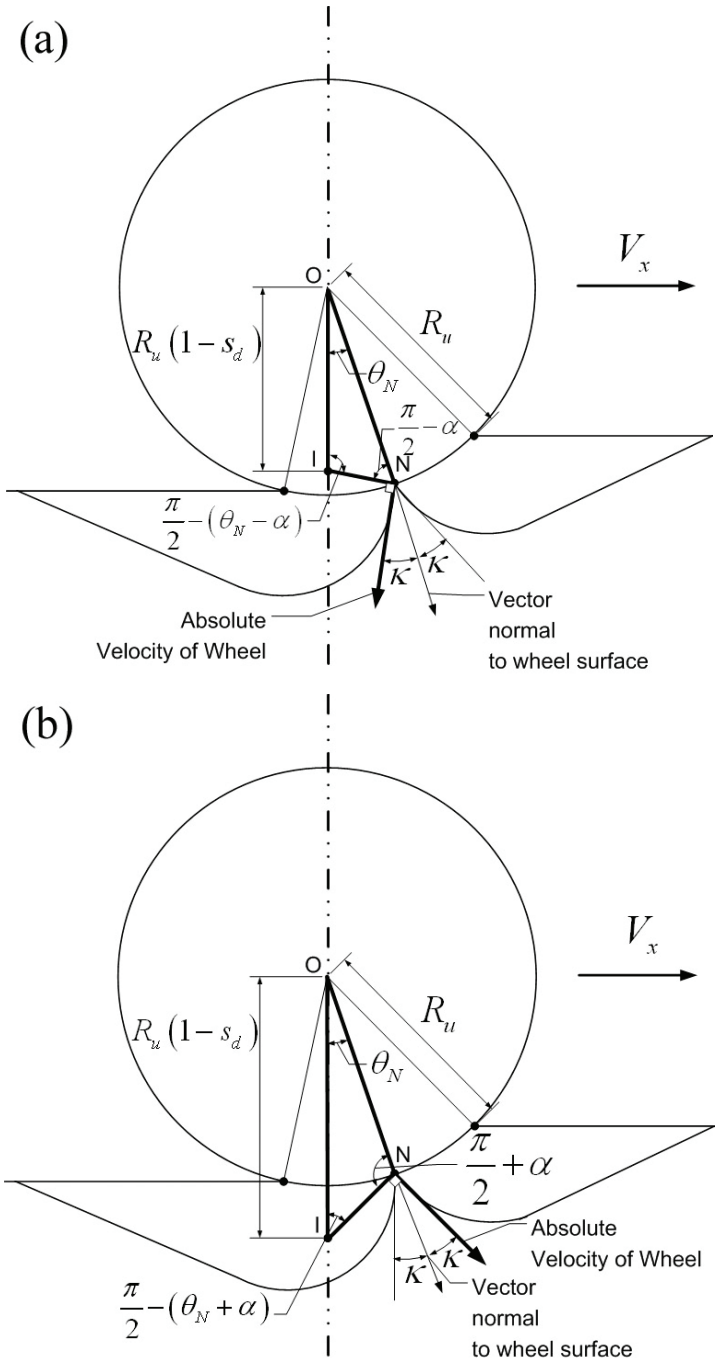

Figure 4-5. Diagrams used for deriving the angle where the front and rear slip lines meet (a) Driving (b) Braking.

For the rigid wheel, using the law of sines, we can derive the angle κ as:

$$
\begin{aligned}
&\frac{R_u}{\sin\left(\frac{\pi}{2}-\left(\theta_N-\kappa\right)\right)}=\frac{R_u\left(1-s_d\right)}{\sin\left(\frac{\pi}{2}-\kappa\right)}\\
&\Rightarrow\frac{R_u}{\cos\left(\theta_N-\kappa\right)}=\frac{R_u\left(1-s_d\right)}{\cos\left(\kappa\right)}\\
&\Rightarrow\frac{1}{\left(1-s_d\right)}=\frac{\cos\left(\theta_N-\kappa\right)}{\cos\left(\kappa\right)}\\
&\Rightarrow\tan\left(\kappa\right)=\frac{\frac{1}{1-s_d}-\cos\left(\theta_N\right)}{\sin\left(\theta_N\right)},\ 0\le\theta_N\le\frac{1}{3}\phi
\end{aligned}
\tag{4.17}
$$

The angle where the maximum radial stress occurs can then be computed from equation (4.17) by substituting $\kappa=\mu=\frac{\pi}{4}-\frac{\phi}{2}$. The mode of failure assumed for this calculation is the general shear failure mode, and hence the angle is limited to $1/3\,\phi$ based on the solutions of the retaining wall problem.

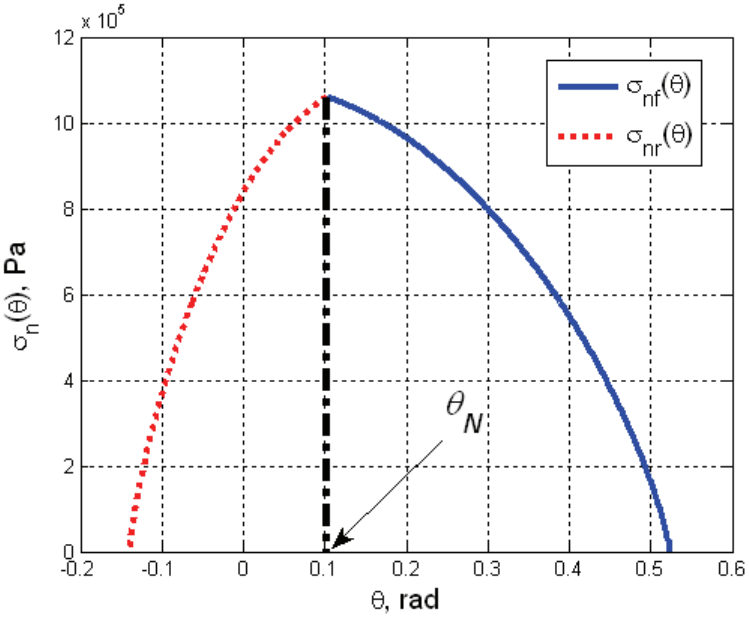

Figure 4-6. An example of the calculated radial stress acting acting on a tire in sandy terrain, where θ_N is point where the radial stress reaches a maximum.

The shear stresses in the longitudinal direction can then be calculated for loose soils using the Janosi-Hanamoto equation, with the shear displacement being calculated using equation (4.9). Figure 4-7 shows an example of the longitudinal stresses calculated for braking and driving situations. Similar results have been obtained by Onafeko [66], Wong [61], and Muro [6] for experimental data collected from testing on rigid wheels on soft soil.

$$\tau_x = (c + \sigma_n \tan(\phi))(1 - e^{\frac{-j_x}{K_x}}) \tag{4.18}$$

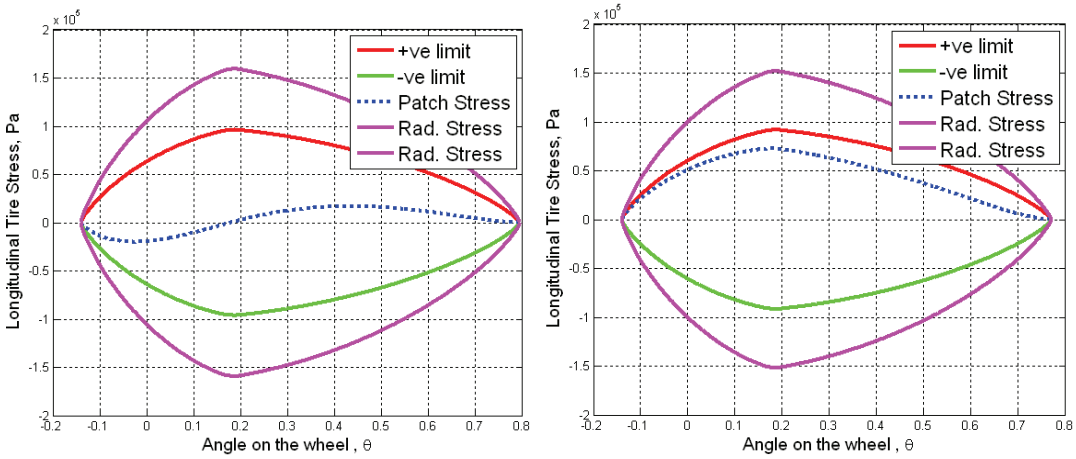

(a) (b)

Figure 4-7. Shear stresses computed from the model for sandy terrain in (a) braking (-10% slip) (b) driving (10% slip).

For the terramechanics community, equations (4.19), (4.20), and (4.21) provide the framework for the calculation of the drawbar pull (DP), the vertical force (W), and the angular torque (T). The radial and tangential stresses can then be integrated across the entire length of contact and projected along the direction vertical and longitudinal to the wheel, as shown in equations (4.19) - (4.21). For a given entry angle and exit angle, the integral evaluated for equation (4.20) has to match the wheel load exerted by the vehicle on the terrain for each wheel on the vehicle. Hence, for a given wheel load, the entry and the exit angles can be determined by iteratively solving for the stress that balances the applied vertical load.

$$DP = R_u b \left(\underbrace{\int_{-\theta_r}^{\theta_e} \tau_x(\theta)\cos\theta d\theta}_{\text{Shear Thrust}} - \underbrace{\int_{-\theta_r}^{\theta_e} \sigma_n(\theta)\sin\theta d\theta}_{\text{Compaction Resistance}} \right) \tag{4.19}$$

$$W = R_u b \left(\int_{-\theta_r}^{\theta_e} \sigma_n(\theta)\cos\theta d\theta + \int_{-\theta_r}^{\theta_e} \tau_x(\theta)\sin\theta d\theta \right) \tag{4.20}$$

$$T = R_u^2 b \int_{-\theta_r}^{\theta_e} \tau_x(\theta) d\theta \tag{4.21}$$

Where

b = width of the wheel
$\tau_x(\theta)$ = Shear stress as function of θ
$\sigma_n(\theta)$ = Normal stress as function of θ

The normal stress and the shear stress on a wheel are illustrated in Figure 4-7 as the radial and tangential stresses, respectively.

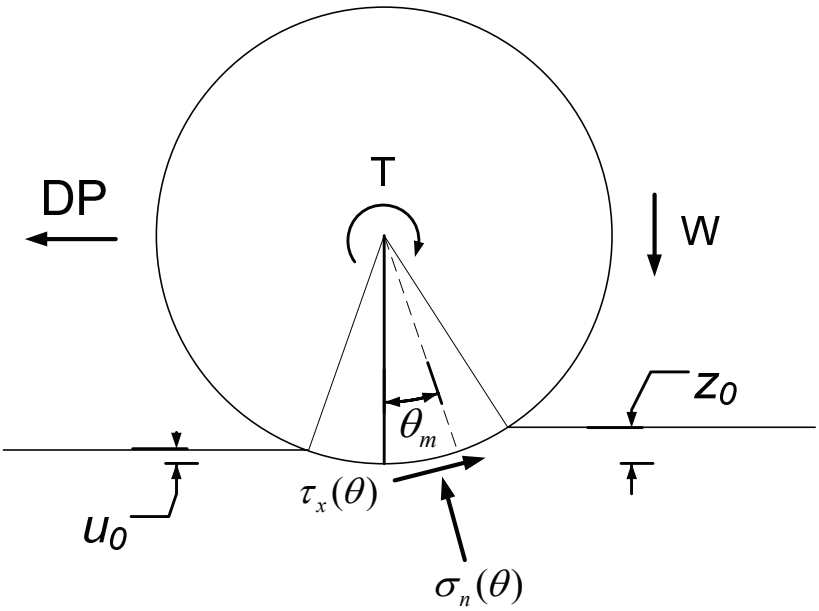

Figure 4-8. Definition of the normal stress and the shear stress on a wheel as the radial and tangential stresses, respectively.

Equations (4.19) - (4.21) are only applicable to rigid wheels, since the equations assume that the wheel radius has a constant value. Wong [62] assumes a linear

distribution of the shear stress, as a function of the normal stress and utilizes a curve-fitting method to determine θ_N, the angular position of the wheel where the soil pressure acting radially from the surface of the wheel reaches a maximum value. The vertical position of a soil particle anywhere along the circumference of the wheel can then be calculated as:

$$z = R_u\left(\cos\theta - \cos\theta_e\right) \tag{4.22}$$

The sinkage, z_0 and the unloaded terrain depth, u_0, as shown in Figure 4-8, can then be calculated in terms of the entry and exit angles as:

$$z_0 = R_u\left(1 - \cos\theta_e\right) \tag{4.23}$$

$$u_0 = R_u\left(1 - \cos\theta_r\right) \tag{4.24}$$

Equations (4.23) and (4.24) are applicable even if r is a function of θ, by replacing the constant value with a variably changing r, which we will use for the modeling for flexible tires later in this dissertation. The integrals in equations (4.19) - (4.21) are usually evaluated numerically because of the complexity of estimating the radial and tangential stresses. For simulations, the equations that relate the forces originating from the body of the vehicle to the forces arising from the load bearing capacity of the soil are shown in equations (4.25) - (4.27).

$$F_z - W = 0 \tag{4.25}$$

$$F_x - DP = 0 \tag{4.26}$$

$$T_{dr} - T = 0 \tag{4.27}$$

Where

F_z = Tire Vertical Force
F_x = Longitudinal Tire Force
T_{dr} = Driving Torque

Since equations (4.25) - (4.27) are contained within equations (4.19) - (4.21), their evaluation is done numerically in order to be applied to vehicle dynamics simulations.

Whilst this section of the paper presents the development of longitudinal traction modeling for a rigid wheel, the equations and figures will form the basis for the development of the new formulation later in the dissertation.

Although Bekker's equations, used in tandem with the Janosi-Hanamoto equation can be used to calculate the tangential and radial stresses reasonably well on rigid wheels, with simplifying assumptions as shown in [3], the application of the mentioned equations may need some adaptations for computing the stresses acting on flexible tires because the tire deformation changes the wheel radius. The wheel/tire model developed in this dissertation will compute the radial stresses based on Reece's equation, since it has been shown that the theoretical development of the equation is more consistent with the theory of plastic equilibrium.

4.1.4 Rigid Wheel Model: Lateral Force Generation

The lateral forces acting on the wheel in off-road terrain can be decomposed into two sources. The first source of the lateral force is the shear stresses resulting from the average shear force across the contact patch in the lateral direction. The second source is the bulldozing effect acting on the side of the embedded wheel. From Section 4.1.2, we have already determined the soil shear displacement at the bottom of the wheel with equation (4.10), shown here again in equation (4.28).

$$j_y = R_u\left(1-s_d\right)\left(\theta_e-\theta\right)\tan\left(\alpha_c\right) \tag{4.28}$$

Combining the Janosi-Hanamoto equation and equation (4.28), we get the expression for the lateral shear stress across the contact patch, τ_{ycp}.

$$\tau_{ycp} = (c+\sigma_n\tan(\phi))\left(1-e^{\frac{-j_y}{K_y}}\right) \tag{4.29}$$

The forces acting on the wheel from the lateral shear forces at the bottom of the wheel can then be calculated by integrating the shear stresses across the entire contact area, as shown in equation (4.30). It is assumed that the width of the contact region remains constant throughout the entire simulation.

$$F_{ycp} = R_u b \int_{-\theta_r}^{\theta_e} \tau_{ycp} d\theta$$
$$= R_u b \int_{-\theta_r}^{\theta_e} (c + \sigma_n \tan(\phi))(1 - e^{-\frac{j_y}{K_y}}) d\theta \quad (4.30)$$

Where

K_y = Empirical shear parameter for the tire in the lateral direction

For the analysis of lateral forces resulting from the bulldozing of the soil during cornering, Schwanghart has shown in [19] that the Hettiaratchi-Reece equation can be used to calculate the resultant force, F_{ybd}. First, let us recall from [67] and [68] that the passive ground resistance equation for a wall moving into a body of soil can be written as:

$$\sigma_p = \left(\gamma_s z^2 N_\gamma + czN_c + qzN_q\right)\cos\delta_f \quad (4.31)$$

Where

N_γ = Soil specific weight coefficient
N_c = Soil cohesion coefficient
N_q = Soil surcharge load coefficient
δ_f = Angle between the normal to the surface of the wall and the direction of motion
q = Surcharge load from accumulated bulldozed soil
z = Sinkage
γ_s = unit weight of soil

For the sake of simplicity, the bulldozing effect can be expressed as a function of the slip angle. Basically, the concept for calculating the bulldozing stress starts from the fact that we can assume that the volume of soil displaced in the lateral direction on each side of the wheel to be the same as the volume of soil accumulated for the surcharge load, especially for loose, uncompacted soil. The soil buildup will be less at the forward region of the wheel, compared with the rear region of the wheel. Then, as mentioned earlier, the second source of the cornering force, the bulldozing component, can be

calculated by substituting equation (4.22) into equation (4.31) and integrating across the entire sinkage area, A_s, as defined in Figure 4-1. Note that the wheel in our model is a circular rotating disc, not a flat wall or tine; hence the force resulting from the bulldozing stress has to be calculated by integrating across the sinkage area.

$$\begin{aligned} F_{ybd} &= \left(\int_0^{2\sin(\theta_e)} \sigma_p d\lambda \right) \tan(\alpha_c) \\ &= \left(\int_0^{2\sin(\theta_e)} \left(\gamma_s \left(R_u \left(\cos\theta - \cos\theta_e \right) \right)^2 N_\gamma \cos\gamma_t \right. \right. \\ &\quad + c \left(R_u \left(\cos\theta - \cos\theta_e \right) \right) N_c \cos\gamma_t \\ &\quad \left. \left. + q \left(R_u \left(\cos\theta - \cos\theta_e \right) \right) N_q \cos\gamma_t \right) d\lambda \right) \tan(\alpha_c) \end{aligned} \tag{4.32}$$

We propose that the surcharge load, q be approximated by calculating the volume of soil displaced because of the slip angle.

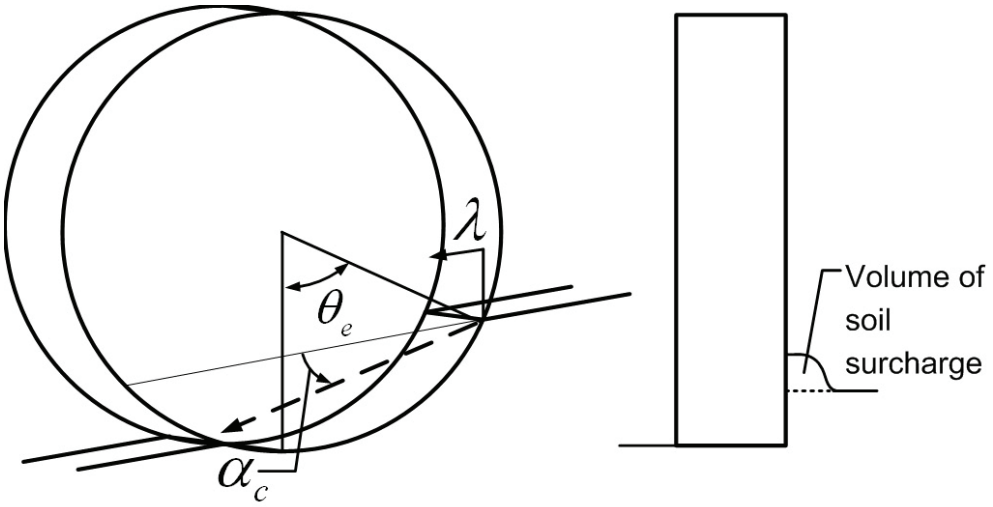

Figure 4-9. Graphical representation of the variables used for calculating the bulldozing force.

Similar to the expression for the lateral force arising from the shear stress, the bulldozing force starts with a value of zero at the entry angle and increases as we move towards the rear of the wheel, as depicted in Figure 4-9. The variable λ represents the linear distance from the front of the wheel, starting at the point corresponding to the entry angle.

$$q = \frac{\gamma_s V_{soil}}{mz} = \frac{\gamma_s V_{soil}}{mz} = \frac{\gamma_s \left(\int_{-\theta_e}^{\theta_e} z d\theta \right) \left(\int_{0}^{2\sin\theta_e} \lambda \tan(\alpha_c) d\lambda \right)}{mz} \tag{4.33}$$

Where

$$m \approx \tan\left(\frac{\pi}{4} + \frac{\phi}{2}\right)$$

$$z = \text{sinkage}$$

The applicability of equation (4.33) to mobility problems is estimated to be limited to slip angles under 45°. According to [19], this is due to the fact that at larger slip angles, the soil build-up on the side of the wheel becomes too rapid for the usage of equation (4.33).

Having computed the individual components of the later force coming from the two sources (the shear stress and the bulldozing effect), the total lateral force becomes.

$$F_y = -\left(F_{ycp} + F_{ybd}\right) \tag{4.34}$$

4.1.5 Rigid Wheel Model: Combined Slip

For combined traction/cornering and braking/cornering maneuvers, the complexity in defining the traction limit for off-road vehicles lies in the fact that the bulldozing force may still exist even if the contact patch is not in contact with the ground, as long as it is still below the sinkage. For on-road vehicles, the concept of the traction limit has been integral in defining the behavior in the combined maneuvers ([51], [69], [70]). To characterize the tractive behavior during combined maneuvers for traction resulting from the shear stresses in the lateral and longitudinal direction for off-road tires, we introduce a similar concept to limit the total traction generated by the soil shear strength. The limiting mechanism will not include the effect from the lateral bulldozing, but provides a starting point for the incorporation of the effect as an additional external lateral force.

The shear strength envelope of the soil is often defined by the Mohr-Coulomb Failure Criterion.

$$\tau_{\max} = c + \sigma_n \tan\left(\phi\right) \tag{4.35}$$

Hence, the shear stress will be bounded by an elliptical unilateral constraint such that inequality (4.36) is upheld.

$$\left(\frac{\tau_x}{\tau_{\max}}\right)^2+\left(\frac{\tau_{ycp}}{\tau_{\max}}\right)^2\le 1 \tag{4.36}$$

The limit curve to the constraint is then defined to be:

$$\begin{aligned}&\left(\tau_x\right)^2+\left(\tau_{ycp}\right)^2=\left(\tau_{\max}\right)^2\Big|_{\theta=\theta_a}\\ &\Rightarrow\left((c+\sigma_n\tan(\phi))\left(1-e^{\frac{-j_x}{K_x}}\right)\right)^2+\left((c+\sigma_n\tan(\phi))\left(1-e^{\frac{-j_y}{K_y}}\right)\right)^2=\left(c+\sigma_n\tan\left(\phi\right)\right)^2\Big|_{\theta=\theta_a}\end{aligned} \tag{4.37}$$

After some simplifications, the final expression for the limit curves are as shown as equation(4.38), where we can then solve numerically to find θ_a, the point on the wheel where the stresses transition from sticking to sliding.

$$\left(1-e^{\frac{-R_u\left[(\theta_e-\theta_a)-(1-s_d)(\sin\theta_e-\sin\theta_a)\right]}{K_x}}\right)^2+\left(1-e^{\frac{-\left(R_u(1-s_d)(\theta_e-\theta_a)\tan(\alpha_c)\right)}{K_y}}\right)^2=1 \tag{4.38}$$

Hence, the shear stress expressions to be integrated to find the longitudinal and lateral shear stress can be obtained as:

$$\tau_x=\begin{cases}\tau_{\max}\left(1-e^{\frac{-R_u\left[(\theta_e-\theta)-(1-s_d)(\sin\theta_e-\sin\theta)\right]}{K_x}}\right) & \theta_e>\theta\ge\theta_a\\ \tau_{\max} & \theta_a>\theta\ge-\theta_r\end{cases} \tag{4.39}$$

$$\tau_{ycp}=\begin{cases}\tau_{\max}\left(1-e^{\frac{-\left(R_u(1-s_d)(\theta_e-\theta)\tan(\alpha_c)\right)}{K_y}}\right) & \theta_e>\theta\ge\theta_a\\ \tau_{\max} & \theta_a>\theta\ge-\theta_r\end{cases} \tag{4.40}$$

Equations (4.38) ensure that the tangential stresses are limited by the soil failure criterion. With the inclusion of the bulldozing component, which contributes a significant portion of the bulldozing force, the lateral force generation from the effect of

sinkage is taken into account. The effect of sinkage is a necessary part of off-road tire modeling and requires more rigorous study as a limiting factor. Nonetheless, since the bulldozing effect is added on top of the shear-originating forces, if the sinkage (z) is zero, then according to equation (4.31), $\sigma_p = 0$.

The final equations used in the computation of the forces acting on the wheel are:

$$F_x = R_u b\left(\left(\int_{\theta_a}^{\theta_e} \tau_x(\theta)\cos\theta d\theta + \frac{\mu_x{}^2 \cdot s}{\sqrt{\left(\mu_y \cdot \tan(\alpha_c)\right)^2 + \left(\mu_x \cdot s\right)^2}} \int_{-\theta_r}^{\theta_a} \tau_{\max}(\theta)\cos\theta d\theta\right)\right) - \int_{-\theta_r}^{\theta_e} R_u \sigma_n(\theta)\sin\theta d\theta \tag{4.41}$$

$$F_y = \left(-R_u b\left(\left(\int_{\theta_a}^{\theta_e} \tau_{ycp}(\theta) d\theta + \frac{\mu_y{}^2 \cdot \tan(\alpha_c)}{\sqrt{\left(\mu_y \cdot \tan(\alpha_c)\right)^2 + \left(\mu_y \cdot s\right)^2}} \int_{-\theta_r}^{\theta_a} \tau_{\max}(\theta) d\theta\right)\right) - \left(\int_0^{2\sin(\theta_e)} \sigma_p d\lambda\right)\tan(\alpha_c)\right)\cos(\gamma_t) + F_z \sin(\gamma_t) \tag{4.42}$$

The moments acting on the wheel can then be approximately calculated based on the Figure 3-1 as:

$$M_x = -F_z R_u \sin(\gamma_t) - F_y R_u \cos(\gamma_t) \tag{4.43}$$

$$M_z = F_{ycp} \sin(\theta_N) + F_{ybd} R_u \sin(\theta_e) \tag{4.44}$$

Equations (4.41) - (4.44) are complicated expressions that must be solved numerically at each time-step to compute the forces acting on the center of the wheel. As mentioned before, the first step of every simulation is to ensure that the wheel vertical load is balanced by equation (4.20). This allows us to calculate the entry angle of the wheel. The exit angle can be assumed to be a small angle which cannot be greater than zero for the rigid wheel, such as -5°. This assumption has been shown to be acceptable when comparing measured stresses and calculated stresses for rigid wheels ([71], [66]) since it is within tolerance limits corresponding to the magnitude of the errors

propagating from the measurement of the soil properties (15-20%). The value of the friction coefficients in the case of off-road wheel/tire modeling can be computed as:

$$\mu_x = \mu_y = \min\left(\frac{\tau_{\max}(\theta)}{\sigma_n(\theta)}, 1\right) \tag{4.45}$$

The reason for which the implementation of the coefficients of friction had to be done in the form shown in equation (4.45) is because we have to limit the traction to the maximum allowable shear force available at the interface. When the soil is cohesive, there will be instances where μ_x and μ_y acquire a value larger than 1, which is very unrealistic since the traction is supposed to be limited by the failure envelope. In the case where that happens, the value of both coefficients μ_x and μ_y are numerically limited to 1 because the maximum generated stresses on the sliding section are then equals to the shear stress of the soil at failure. This method also allows the tire model to avoid the numerical convergence problems arising from the integration if the stresses because it allows the values of the sliding stresses to be bounded.

4.2 Tire model: Flexible Tire Model

In the previous section the soil interaction model has been applied to a mobility problem involving a rigid wheel. With some modification, the rigid wheel model can be extended to the modeling of flexible tires. Karafiath [20] presented an initial application of this method for mobility problems involving pneumatic tires, where the shortening radius at the front and rear of the contact patch is modeled using a logarithmic spiral. For a vehicle dynamics simulation, a tire model should be able to take the vertical wheel load, F_z, longitudinal slip, s_d, camber angle, γ and slip angle, α_c and be able to output the longitudinal force, F_x, lateral force, F_y, the overturning moment, M_x and the aligning moment, M_z, as shown in Figure 4-10.

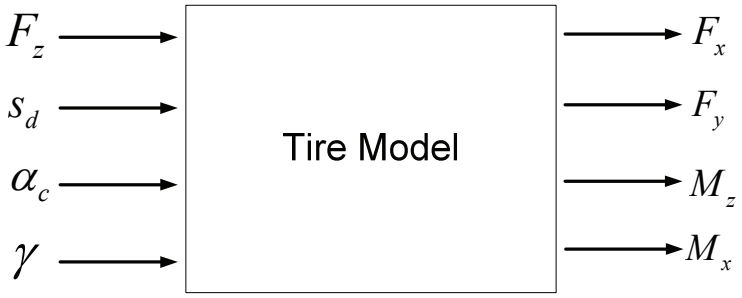

Figure 4-10. Minimum inputs/outputs to and from a tire model for vehicle dynamics simulation

4.2.1 Flexible Tire Model: Deformation Properties

In our study, the compliant behavior of the tire is developed based on a theoretical analysis and parameterized empirically. Where the tire meets the surface of the road, the beginning and ending of the contact patch are described by logarithmic spirals while the part of the tire in contact with the road is described by a straight line segment, as shown in Figure 4-15, which can be determined empirically by deflection tests, which is dependent on the vertical wheel load [39]. Figure 4-11 shows a mechanical schematic used in the theoretical development of the formulation for the radial deformation of the tire as a flexible ring tire model. The *raison d'etre* for this development is to provide the model with a more solid theoretical approach and to ensure that the flexible behavior of the tire model concurs with physical characterization tests.

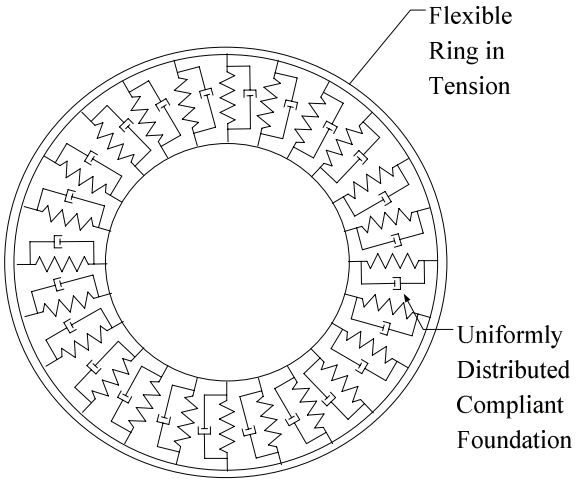

Figure 4-11. The analytical mechanical schematic of the tire model as a flexible ring on compliant foundation.

The theoretical analysis employed in the development of the tire model is similar to the method described by Loo [72], Yu [73], Gong[74], and Clark [39]. Consider a segment of the flexible ring as shown in Figure 4-12. The flexible ring is kept under constant tension T throughout the entire duration of simulation time span that we are interested in, the internal pressure is constant. There are several assumptions involved in this model, namely:

1. The amount of static tension in the ring, T, is much larger compared with the changes induced by the deflection.
2. The radial deflection, w, will always be smaller than the undeflected radius of the ring, R_u.
3. The tension in the ring, T can be defined as a function of the tire inflation pressure, where $T = p_0 R_u$.
4. $\dot{w}$, the rate of radial deflection vanishes with respect to time because of the equilibrium condition assumptions.
5. The ring is stiff enough in the circumferential direction to fulfill the inextensibility condition.

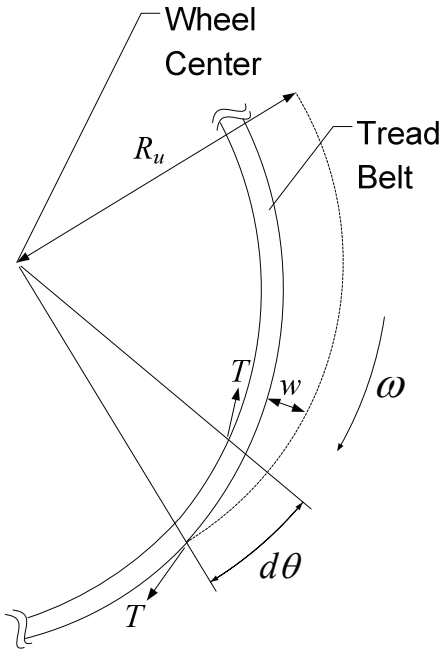

Figure 4-12. Diagram of the differential ring element used for derivation of the equations from equilibrium conditions.

By summing the forces in the radial direction of the wheel, we can express the equilibrium condition of the flexible ring as shown in equation (4.46), where w' represents the derivative of w with respect to θ.

$$T\left(\frac{w'+w''d\theta}{R_u}+d\theta\right)-T\frac{w'}{R_u}-p_0R_u d\theta=0 \tag{4.46}$$

Where

p_0 = Internal tire pressure

By adding the foundation stiffness, k, and damping, c, and after some basic mathematical manipulations, we arrive at equation (4.47), where $\dot{w}$ represents the derivative of w with respect to time.

$$\frac{T}{R_u}w''-\left(kR_u w+cR_u\dot{w}\right)=0 \tag{4.47}$$

Equation (4.47) can then be transformed to yield the differential equations from the fixed non- rotating coordinate θ to the new fixed non-rotating coordinate θ_1. Assuming that the model is rolling freely with the angular velocity ω, we can then express $\theta_1=\theta-\omega t=\theta-\theta_f$, which will then turn into a new version of equation (4.47). Note that this solution is for the shape of the tire in the leading edge of the tire.

$$\frac{T}{R_u}w''-cR_u\left(\dot{w}-\omega w'\right)-kR_u w=0 \tag{4.48}$$

When $\dot{w}\to 0$,

$$\frac{T}{R_u}w''+cR_u\left(\omega w'\right)-kR_u w=0 \tag{4.49}$$

Next, we want to express equation (4.49) in terms of the normalized variable z, where $z = w/R_u$. Thus, we finally arrive at the form of equation (4.49), where β and ζ are introduced as new dimensionless variables. The methods for determining β and

ζ will be discussed in the chapter on testing methodologies for characterizing the tire properties.

$$z''+2\zeta\beta z'-\beta^2 z=0 \tag{4.50}$$

Where

$$\zeta=\frac{R_u c\omega}{2\sqrt{kT}} \tag{4.51}$$

And

$$\beta=R_u\sqrt{\frac{k}{T}} \tag{4.52}$$

Equation (4.50) is solved analytically and obtained as

$$z=Ae^{-\beta\left(\sqrt{1+\zeta^2}+\zeta\right)\theta_1}+Be^{\beta\left(\sqrt{1+\zeta^2}-\zeta\right)\theta_1} \tag{4.53}$$

For the leading edge, the solution for *z* can be then be obtained for θ_1 by applying the boundary condition where $z\to 0 \;\; as \;\; \theta_1\to\infty$, thus giving us:

$$z=z(\theta_f)e^{-\beta\left(\sqrt{1+\zeta^2}+\zeta\right)(\theta-\theta_f)},\;\; \theta_f<\theta<\pi \tag{4.54}$$

Similarly, we can obtain the solution for the trailing edge as:

$$z=z(2\pi+\theta_b)e^{\beta\left(\sqrt{1+\zeta^2}-\zeta\right)(\theta-(2\pi+\theta_b))},\;\; \pi<\theta<2\pi+\theta_b \tag{4.55}$$

When the tire is in contact with a flat surface, such as in the situation shown in Figure 4-13 , the radial deflection of the ring is constrained to the geometry of the surface, which yields:

$$z=1-\frac{1-\delta/R_u}{\cos\theta},\;\; \theta_b\le\theta\le\theta_f \tag{4.56}$$

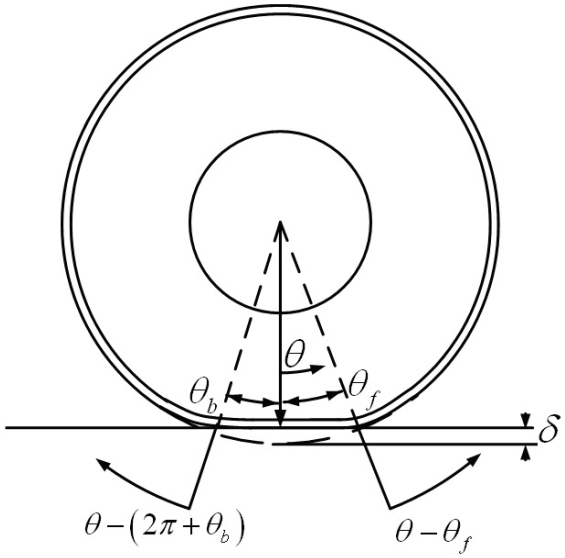

Figure 4-13. Angle and deflection variables in the tire model

The slope of z at each θ then can be calculated using equation (4.57):

$$z' = \frac{dz}{d\theta} = -\left(1-\frac{\delta}{R_u}\right)\frac{\sin\theta}{\cos^2\theta} \tag{4.57}$$

At θ_f, the slope of the curved logarithmic spiral has to match the slope of the straight-line segment, in addition to the value of the radius. Hence, we can express the constraint equation for the leading edge as:

$$\begin{aligned} & z'(\theta_f) = -\beta\left(\sqrt{1+\zeta^2}+\zeta\right)z(\theta_f) \\ & \Rightarrow z'(\theta_f) + \beta\left(\sqrt{1+\zeta^2}+\zeta\right)z(\theta_f) = 0 \\ & \Rightarrow -\left(1-\frac{\delta}{R_u}\right)\frac{\sin\theta}{\cos^2\theta} + \beta\left(\sqrt{1+\zeta^2}+\zeta\right)\left(1-\frac{1-\delta/R_u}{\cos\theta}\right) = 0 \end{aligned} \tag{4.58}$$

And for the trailing edge,

$$
\begin{aligned}
& z'(\theta_b) = \beta\left(\sqrt{1+\zeta^2} - \zeta\right) z(\theta_b) \\
& \Rightarrow z'(\theta_b) - \beta\left(\sqrt{1+\zeta^2} - \zeta\right) z(\theta_b) = 0 \\
& \Rightarrow -\left(1 - \frac{\delta}{R_u}\right)\frac{\sin\theta_b}{\cos^2\theta_b} - \beta\left(\sqrt{1+\zeta^2} - \zeta\right)\left(1 - \frac{1-\delta/R_u}{\cos\theta_b}\right) = 0
\end{aligned}
\tag{4.59}
$$

Equations (4.58) and (4.59) will allow us to determine the contact angles given all the parameters. When the tire is loaded on a flat surface with no rolling speed, the constraint equations are symmetrical because $\zeta = 0$ and become:

$$
\begin{aligned}
& z_0' + \beta z_0 = 0 \\
& \Rightarrow -\left(1 - \frac{\delta}{R_u}\right)\frac{\sin\theta_0}{\cos^2\theta_0} + \beta\left(1 - \frac{1-\delta/R_u}{\cos\theta_0}\right) = 0
\end{aligned}
\tag{4.60}
$$

So, the radius of the tire can be expressed using the piecewise expression shown in equation (4.61). An example of the deflected tire shape calculated using this method is shown in Figure 4-14.

$$
R_{eff}(\theta) = \begin{cases}
R_u - R_u\left(1 - \dfrac{1-\delta/R_u}{\cos\theta}\right) & \theta_b < \theta \le \theta_f \\
R_u - R_u\left(1 - \dfrac{1-\delta/R_u}{\cos\theta_f}\right) e^{-\beta\left(\sqrt{1+\zeta^2}+\zeta\right)(\theta-\theta_f)} & \theta_f < \theta \le \pi \\
R_u - R_u\left(1 - \dfrac{1-\delta/R_u}{\cos(2\pi+\theta_b)}\right) e^{\beta\left(\sqrt{1+\zeta^2}-\zeta\right)(\theta-(2\pi+\theta_b))} & \pi < \theta \le 2\pi + \theta_b
\end{cases}
\tag{4.61}
$$

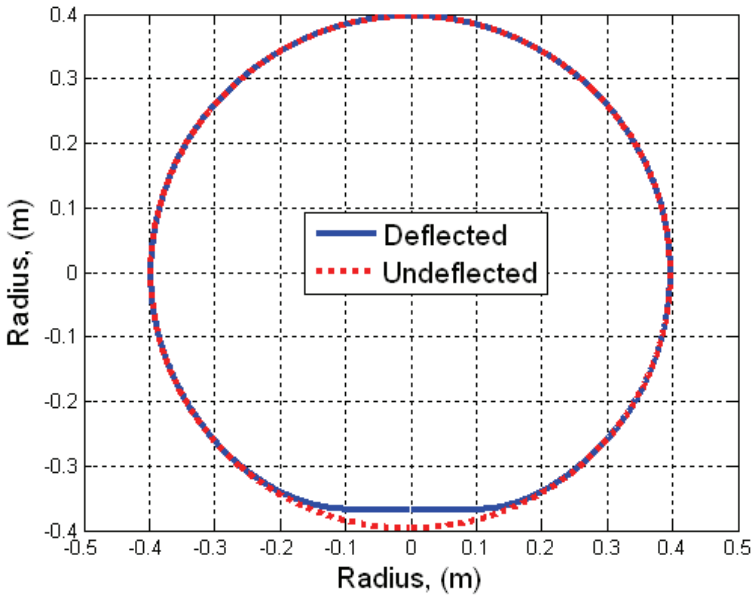

Figure 4-14. The calculated shape of a tire with $R_u = 0.397m$, $\delta = 0.0236m$, $\beta = 6.75$, and $\zeta = 0.1175$, loaded on a flat rigid surface.

The contact length of the flat region (straight-line segment in Figure 4-15) can also be determined. The contact length, l_p is then defined according to equation (4.62):

$$l_p = (R_u - \delta)\tan(|\theta_b|) + (R_u - \delta)\tan(\theta_f) \tag{4.62}$$

As the simulation progresses, l_p will change with speed, as shown in Figure 4-15 and as evident from equation (4.50). This evolution is expected, since the static loaded radius merely gives us an idea of the deflection when the tire is not rotating. Once the tire starts spinning, the centripetal effect from the mass of the rubber and tread material will increase the radius of the tire. This increase will change the tire curvature, hence affecting the tractive forces calculated. We expect that the usage of empirical data and theoretical analysis will be able to assist in capturing this phenomena. The main reason behind this is that the tire parameters used are dependent on many factors such as tire structural composition and inflation pressure. This model attempts to incorporate all these properties in a simplified manner to calculate the necessary tire geometry.

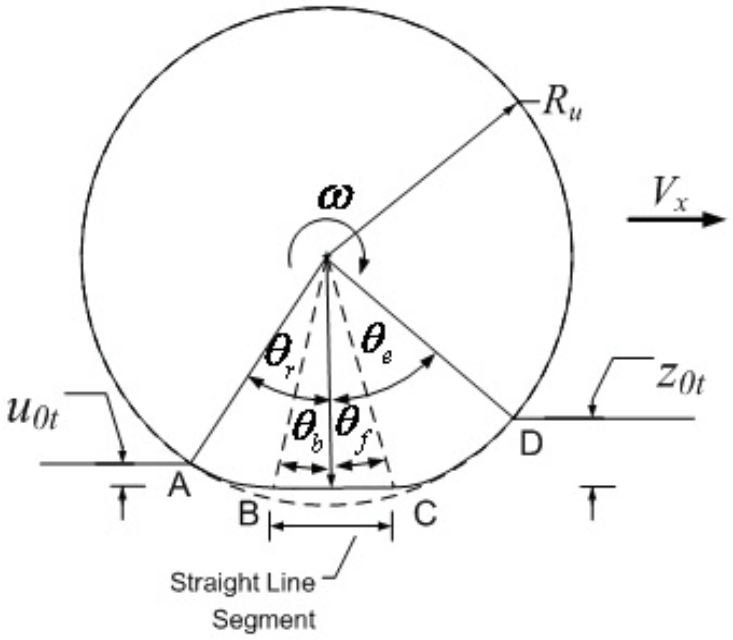

Figure 4-15. Definition of angles for the pneumatic tire model

In [39] it has been shown that the contact patch length has a dependency on the travel speed of the tire. It is estimated that, with the inclusion of the ω term, we can include this effect in our model. Based on Figure 4-15, we can also calculate the unloaded soil height, u_{0t} and the sinkage, z_{0t} for the flexible tire in a similar manner with the one employed for the rigid wheel where we used equations (4.23) and (4.24).

$$z_{0t} = R_{eff}(\theta)\left(\cos\theta_f - \cos\theta_e\right) \tag{4.63}$$

$$u_{0t} = R_{eff}(\theta)\left(\cos\theta_b - \cos\theta_r\right) \tag{4.64}$$

4.2.2 Flexible Tire Model: Stationary Vertical Loading

Any tire model must account for the effect due to a stationary vertical loading as a first step for any vehicle-terrain simulation. The same methodology used for modeling the vertical loading of the rigid wheel can be applied to the flexible wheel. Equation (4.2) can be modified to account for the deformed geometry of the flexible tire to yield equation (4.65).

$$w_0 = b\left(\int_{-\theta_0}^{\theta_0} R_{eff}(\theta)\sigma_n(\theta)\cos\delta\cos\theta + R_{eff}(\theta)\tau(\theta)\sin\delta\sin\theta d\theta \right) \quad (4.65)$$

4.2.3 Flexible Tire Model: Longitudinal Slip and Shear Displacement

Once the geometry of the flexible tire has been defined, we need to characterize the shear displacement for the three segments of the wheel that is in contact with the ground. The shear deformation of soil for a driven wheel can be calculated for any arbitrary angular position θ on the tire-soil interface by integrating the shear velocities as shown in [3] and [6], with minor modifications. s_d is calculated as shown in equation (4.3). For the entire region of the tire that is in contact with the ground, the shear displacement can be calculated, similar to the case of the rigid wheel, as shown in equation (4.66), by integrating the interface velocity across the entire contact area.

$$j_x(\theta) = \int_{\theta}^{\theta_e} R_{eff}(\theta)\left[1-(1-s_d)\cos\theta\right]d\theta \quad (4.66)$$

Having derived the shear deformation of the soil for a driven tire, the shear deformation of soil for a braked tire can be calculated similarly, for any arbitrary angular position θ on the tire-soil interface by integrating the velocities at the shearing interface.

4.2.4 Flexible Tire Model: Stresses and Forces

With the assumption that the sinkage is such that the width of the tire, b, remains constant, the drawbar pull, the wheel load, and the longitudinal force can be calculated from the stresses computed at the interface. The application of Reece's equation in this formulation requires us to determine the point where the maximum radial force acts on the tire. Based on the slip line theory, we can calculate the point where the front and the rear slip line fields meet. The radial stresses are calculated using equation (4.67).

$$\sigma_n(\theta)=\begin{cases}\left(ck_1+\gamma_s bk_2\right)\left(\dfrac{R_{eff}(\theta)}{b}\right)^n\left(\cos\theta-\cos\theta_e\right)^n & \theta_N\le\theta<\theta_e \\ \left(ck_1+\gamma_s bk_2\right)\left(\dfrac{R_{eff}(\theta)}{b}\right)^n\left(\cos\left(\theta_e-\left(\dfrac{\theta-\theta_r}{\theta_N-\theta_r}\right)\left(\theta_e-\theta_N\right)\right)-\cos\theta_e\right)^n & -\theta_r<\theta\le\theta_N\end{cases}$$

(4.67)

The radial stresses acting on the surface of the flexible tire are different compared with those computed for the rigid wheel. The deflection of the tire limits the amount of stress that the tire can exert on the soil surface. The maximum amount of radial stress that a tire can apply on the ground can be measured by pressing the tire against a rigid surface and measuring the contact pressure. This observation has been supported by work done by Karafiath [20], Wong [3], and Muro [6]. The contact pressure where the tire resorts to a flexible body is referred to as a limit pressure that can be defined as a function of the inflation pressure and the equivalent carcass stiffness. Referring to the flexible ring on compliant foundation model, we can approximate that limit pressure based on the stiffness of the compliant foundation. The limit pressure has to be equivalent to the stiffness of the deformed section of the tire, in order to be in equilibrium.

$$q_{\text{limit}}=kb=\frac{b\beta}{2R_u{}^2}\left(\alpha p_i+c\right) \tag{4.68}$$

Where

$c=$ Offset value of point-load stiffness

$p_i=$ Tire inflation pressure

$\alpha=$ Rate of change of point-load stiffness with respect to tire pressure

The methodology for acquiring equation (4.68) and its parameters are discussed in the chapter dedicated to tire testing. As the vertical load of the tire is increased, the tire will experience an increase in the radial stress as well. At one point, the tread will deform, and the radial stress of the tire will be limited by the stiffness of the compliant foundation. Figure 4-16 shows the radial stresses acting on the surface of the wheel for several wheel loads. For the tire modeled in this study, at a vertical load of 4000 N, the tire behaves as a rigid wheel, since the limit pressure has not been reached. However,

when the vertical load is increased past 8000N, the tire will reach the limit pressure and deform, causing all radial stresses developed at the contact patch to reach a constant value at the limit pressure. When the load is increased further to 10,000N, we can observe that, due to the limit pressure, a larger area of contact is needed to support the increased wheel load.

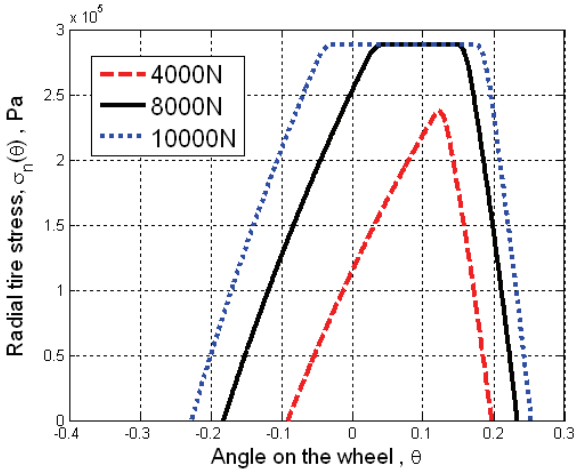

Figure 4-16. The calculated radial pressure acting on the surface of a tire for three different wheel vertical loads.

The point where the maximum stress occurs on the surface of the wheel is calculated the same way as shown for the rigid wheel, with the exception that the wheel-fixed frame is rotated by the angle of the maximum stress, such that the maximum deflection always occurs at the point of maximum tire radial stress as shown by the experiments by Freitag [75]. Hence, the radial stresses acting on the tire can now be computed as:

$$\sigma_n(\theta) = \min(\sigma_n(\theta), q_{\text{limit}}) \tag{4.69}$$

The longitudinal tire stresses can then be calculated by combining (4.18) and (4.66), such that the stresses computed account for the deformed radius of the wheel, as shown in equation (4.70).

$$\tau_x(\theta) = (c + \sigma_n(\theta)\tan(\phi))\left(1 - e^{\frac{-\left(\int_{\theta}^{\theta_e} R_{eff}(\theta)\left[1-(1-s_d)\cos\theta\right]d\theta\right)}{K_x}}\right) \tag{4.70}$$

The vertical wheel load can be calculated next by integrating the stresses across the entire contact area. Equation (4.71) is then used to calculate the entry angle needed to balance the wheel vertical load. The width of the tire in contact is assumed to be constant throughout the entire simulation. Similar to the rigid wheel, a small angle is first assumed for the exit angle, and then an iterative procedure is used to ensure that the calculated exit angle is past the lowest point on the tire.

$$W = b\left(\int_{-\theta_r}^{\theta_e} R_{eff}(\theta)\sigma_n(\theta)\cos\theta d\theta + \int_{-\theta_r}^{\theta_e} R_{eff}(\theta)\tau_x(\theta)\sin\theta d\theta\right) \tag{4.71}$$

Once the exit and entry angles have been determined, we can continue to determine other tire force components. By integrating the vertical and longitudinal stresses at the contact patch, the corresponding longitudinal and vertical forces can be computed from quasi-static equilibrium conditions. The stresses for the tire model on a firm Yolo loam soil with a vertical wheel load of 8,000 N are shown in Figure 4-17. The radial stresses for the flexible tire are saturated to the limiting pressure, causing the maximum limits to have the same shape.

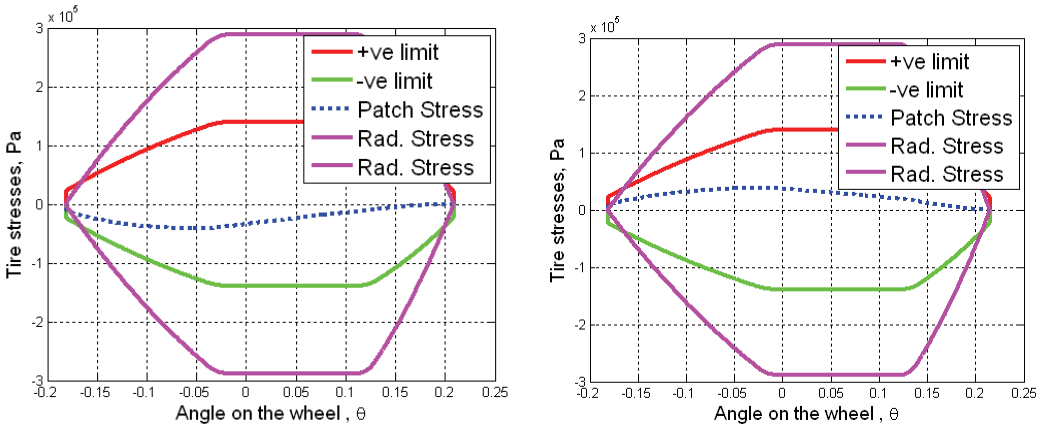

(a) (b)

Figure 4-17. Longitudinal shear stresses calculated from the flexible tire model for yolo loam terrain in (a) braking (-10% slip) (b) driving (10% slip).

The stresses at the interface can then be integrated to yield the longitudinal force, where similar to the forces computed for the rigid wheel, they are equivalent to the forces resisting the drawbar pull.

$$F_x = DP = b\left[\int_{-\theta_r}^{\theta_e} R_{eff}(\theta)\left(\tau_x(\theta)\cos(\theta) - \sigma_n(\theta)\sin(\theta)\right)d\theta\right] \tag{4.72}$$

Equation (4.72) has to be implemented numerically after the entry and exit angles are determined by equating the wheel vertical load with the supporting forces from the ground. Equation (4.72) will be expanded to account for the effect of combined slip by projecting the slipping stresses onto the direction that is normal to the limit surface of the tire forces.

4.2.5 Flexible Tire Model: Lateral Forces

The lateral force formulation for an off-road tire is more difficult to model than the lateral formulation for an on-road vehicle. However, we do know that according to [20], a significant portion of the tractive forces in the lateral direction for a tire are developed at the soil-tire interface and dependent on the soil failure at the interface. Schwanghart [19] had shown that the total lateral deformation for the soil-wheel interface is composed of the deformation of the tire and the deformation of the soil. The shear forces developed

at the interface are dependent on the change in tire stiffness with slip angle. In the on-road tire model developed earlier in this dissertation, the stiffness of the tire was modeled such that it decreases with non-zero slip angle. Hence, the effective tire deflection will decrease with increased slip angle.

As with the rigid wheel, the first step in computing the lateral force starts is the definition of the lateral shear displacement, which is obtained by integrating the velocity acting in the lateral direction across the contact patch. However, the radius of the tire is defined in the flexible tire case as the calculated deflected radius.

$$\begin{aligned} j_y &= \int_0^t V_y dt \\ &= \int_\theta^{\theta_e} V_x \tan(\alpha_c) dt \\ &= \tan(\alpha_c) \int_\theta^{\theta_e} \frac{V_x}{\omega} d\theta \\ &= R_{eff}(\theta)(1-s_d)(\theta_e - \theta)\tan(\alpha_c) \end{aligned} \tag{4.73}$$

The form of the shear displacement equation (4.73) is similar to the form presented for the lateral shear displacement by Grecenko [76] and Schwanghart [19]. However, the method for deriving the equation is not shown explicitly in either work. The lateral shear stresses can the be calculated as shown in equation (4.30):

$$\tau_{ycp} = (c + \sigma_n \tan(\phi)) \left(1 - e^{\frac{-j_y}{K_y}} \right) \tag{4.74}$$

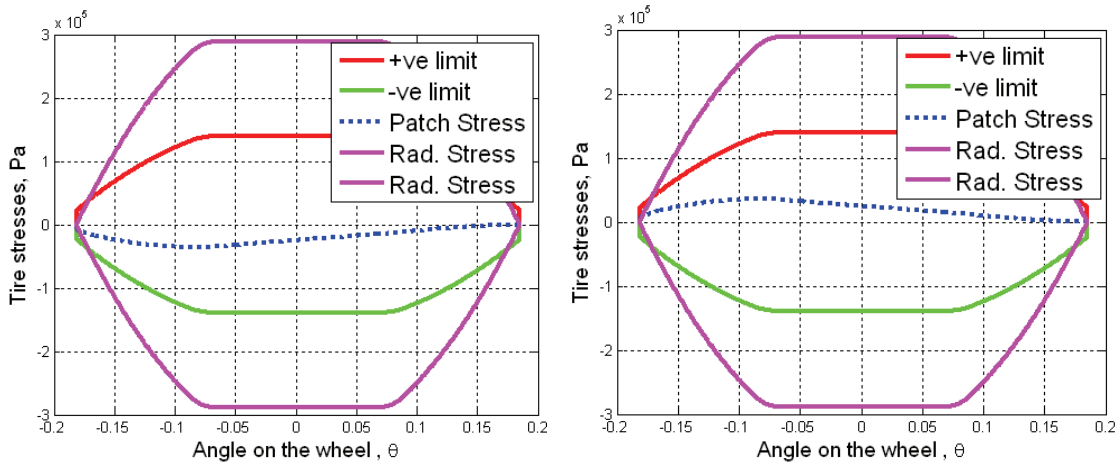

Figure 4-18. Calculated lateral stresses acting on the contact patch of the tire at zero longitudinal slip for Yolo loam (a) slip angle of -2 deg (b) slip angle of 2 deg.

The lateral forces can then be calculated, similar to the case of the rigid wheel. The lateral stresses are integrated across the entire contact patch. As shown in equation (4.75) , the radius of the wheel that was used for calculating the stresses is the deflected radius of the tire.

$$\begin{aligned} F_{ycp} &= b\int_{-\theta_r}^{\theta_e} R_{eff}(\theta)\tau_{ycp}\,d\theta \\ &= b\int_{-\theta_r}^{\theta_e} R_{eff}(\theta)(c+\sigma_n\tan(\phi))(1-e^{-\frac{j_y}{K_y}})\,d\theta \end{aligned} \tag{4.75}$$

As with the longitudinal stresses, the lateral force calculated using equation (4.75) does not account for combined slip. In the next section, we will apply the same projection method used in the rigid wheel formulation to ensure that the lateral and longitudinal shear forces are limited. The bulldozing force can be calculated using the same method shown for the rigid wheel, except for the fact that we have to include the deformation of the carcass in the calculation of the angle at which the force is acting on the side of the tire. The deformation is proportional to the slip angle, starting from zero at the entry angle, and achieving maximum deformation at the rear of the sunken section of the tire.

$$
\begin{aligned}
F_{ybd} &\approx \left(\int_0^{2\sin(\theta_e)} \sigma_p d\lambda \right) \tan(\alpha_c) \\
&\approx \left(\int_0^{2\sin(\theta_e)} \left(\gamma_s \left(R_{eff}(\theta) \left(\cos\theta - \cos\theta_e \right) \right)^2 N_\gamma \cos\left(\tan^{-1}\left(\left(\frac{\lambda}{K_b} \right) \frac{\tan(\alpha_c)}{R_u - R_w} \right) + \gamma_t \right) \right. \right. \\
&\quad + c\left(R_{eff}(\theta) \left(\cos\theta - \cos\theta_e \right) \right) N_c \cos\left(\tan^{-1}\left(\left(\frac{\lambda}{K_b} \right) \frac{\tan(\alpha_c)}{R_u - R_w} \right) + \gamma_t \right) \\
&\quad \left. \left. + q\left(R_{eff}(\theta) \left(\cos\theta - \cos\theta_e \right) \right) N_q \cos\left(\tan^{-1}\left(\left(\frac{\lambda}{K_b} \right) \frac{\tan(\alpha_c)}{R_u - R_w} \right) + \gamma_t \right) \right) d\lambda \right) \tan(\alpha_c)
\end{aligned}
\tag{4.76}
$$

4.2.6 Flexible Tire Model: Combined slip forces

The combined slip forces can be calculated similar to the rigid wheel case, where the limit stresses for the lateral and the longitudinal stresses are defined as the failure envelope of the soil. The modified equation for the limit boundary is presented as equation (4.77).

$$
\left(1 - e^{\frac{-\int_{\theta_a}^{\theta_e} R_{eff}(\theta)\left[1-(1-s_d)\cos\theta\right] d\theta}{K_x}} \right)^2 + \left(1 - e^{\frac{-\left(R_{eff}(\theta)(1-s_d)(\theta_e-\theta_a)\tan(\alpha_c) \right)}{K_y}} \right)^2 = 1 \tag{4.77}
$$

The longitudinal and lateral forces for the combined slip case, with the inclusion of the camber inclination stiffness, are next computed as:

$$
\begin{aligned}
F_x = b \left(\left(\int_{\theta_a}^{\theta_e} R_{eff}(\theta)\tau_x(\theta)\cos\theta d\theta + \frac{\mu_x{}^2 \cdot s}{\sqrt{\left(\mu_y \cdot \tan(\alpha_c) \right)^2 + \left(\mu_x \cdot s \right)^2}} \int_{-\theta_r}^{\theta_a} R_{eff}(\theta)\tau_{\max}(\theta)\cos\theta d\theta \right) \right) \\
- \int_{-\theta_r}^{\theta_e} R_{eff}(\theta)\sigma_n(\theta)\sin\theta d\theta
\end{aligned}
\tag{4.78}
$$

$$F_y = \left(-b\left(\left(\int_{\theta_a}^{\theta_e} R_{eff}(\theta)\tau_{ycp}(\theta)d\theta + \frac{\mu_y{}^2 \cdot \tan(\alpha_c)}{\sqrt{\left(\mu_y \cdot \tan(\alpha_c)\right)^2 + \left(\mu_y \cdot s\right)^2}} \int_{-\theta_r}^{\theta_a} R_{eff}(\theta)\tau_{\max}(\theta)d\theta \right) \right) \right.$$
$$\left. -\left(\int_0^{2\sin(\theta_e)} \sigma_p d\lambda \right) \tan(\alpha_c) \right) + C_\gamma \tan(\gamma_t) \tag{4.79}$$

Having calculating the forces, the moments can be obtained in the same fashion as was done in the case of the rigid wheel formulation, with the needed modifications to include the stiffness characteristics of the flexible tire from the on-road tire model. Note that both equations (4.80) and (4.81) include the lateral bulldozing effect into the total moments generated.

$$M_x = C_{mxg}(C_\gamma + F_z)R_l \sin(\gamma_t) + C_{mxa}F_{ycp} + R_l \cos(\gamma_t)F_{ybd} \tag{4.80}$$

$$M_z = -\left(C_{mz1} + \left(C_{mz2} - C_{mz1}\right)\operatorname{sech}\left(C_{mz3} \frac{\left|\tan(\alpha_c)\right|}{1 - \left|\tan(\alpha_c)\right|} \right) \right) \left(F_{ycp}\cos(\gamma) + C_\gamma \tan(\gamma) \right)$$
$$+ R_l \sin(\theta_e) F_{ybd} \tag{4.81}$$

4.3 Tire Model: Summary

In this chapter, a rigid wheel model for vehicle dynamics simulations has been developed. Next, the formulation has been extended to the flexible tire case, also incorporating in this model some of the most recent developments and insights of tire and tire-soil modeling. The analytical formulation for the flexible ring on elastic foundation is meant to provide a bridge between analytical modeling and experimental characterization of tire and soft soil interaction. The insight from the experimental work of various researchers in the terramechanics community ([77], [75], [8], [63], [9]) has been combined with some of the more recent developments in tire modeling in the vehicle dynamics community ([72], [78]) to characterize the tire deformation and tractive performance. The deformed section of the tread, as applied to the model, is meant to account for the bending and "snap through" buckling of the tread when the tire is loaded on the ground. The tire contact stress models, developed from observations of

photographic evidence and experimental data from various sources, is hoped to unify the gap between experimental and analytical work in off-road tire modeling. The main subroutine for this tire model is included in the appendix.

5. Experimental Tire Testing and System Identification

In this chapter, the identification of the various parameters required to characterize the tire model is described. The variables for the on-road tire model are introduced previously in chapter 3 and the variables for the off-road tire model were introduced in chapter 4. This chapter will also present a link between the tire deformation model developed in chapter 4 with some of the experiments conducted towards the completion of this dissertation. For a comprehensive understanding of the testing methodologies employed, it is recommended by the author of this dissertation that users explore chapter 8 of [1].

5.1 Tire Deformation Characterization: Theoretical Development

The determination of the tire parameters introduced in the previous chapter is essential to characterizing the enveloping/deformation behavior of the tire. To develop the testing method, we have to first establish the connection between the Deformation model and the empirical data to be collected. Tire deformation properties have been studied by Loo [72], Guan [78], and various other researchers outlined in the NHTSA report by Clark [39] and Gent [1]. The procedures described in this dissertation are developed based on similar analysis, with the difference that its results are not applied to finite element models.

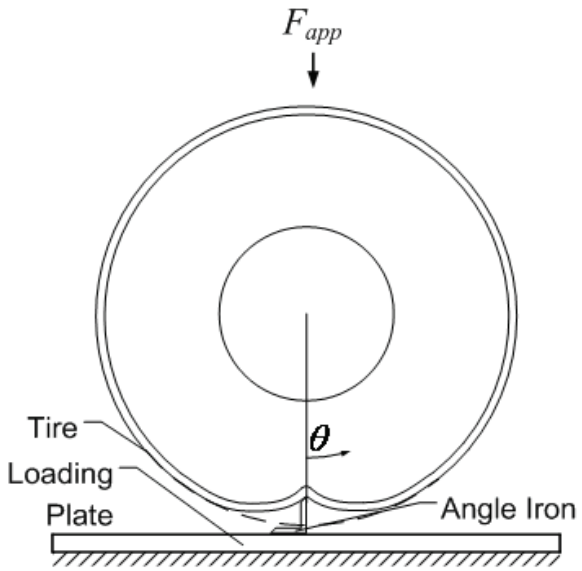

Figure 5-1. The tire loaded against a plate with a point load.

Figure 5-1 shows an experimental setup where the tire is loaded statically onto an angle iron with a point load F_{app} in the center of the contact patch. Since the tire is non-rotating in this situation, $\zeta = 0$, which then gives us the normalized deflection in the leading edge of the tire at the point of force application as:

$$z = z_{app} e^{-\beta\theta} \tag{5.1}$$

Where

z_{app} = Normalized deflection of tire resulting from applied force

β = Rate of deformation of the tire, as defined in chapter 4

θ = Angular position measured from a fixed reference frame on the tire

Differentiating equation (5.1) with respect to θ, we obtain:

$$z'_{app} = -\beta z_{app} \tag{5.2}$$

By employing the results from the analysis of a flexible ring tire model from Loo [72], we can obtain the normalized point load stiffness for the radial tire, q_{app}, in addition to physical parameters (such as the ring tension and the foundation stiffness).

$$q_{app} = \frac{F_{app}}{z_{app}} \tag{5.3}$$

The tension in the ring can then be defined as:

$$T = \frac{q_{app}}{2\beta} \tag{5.4}$$

From the analysis done in the previous chapter in similar fashion to Loo [72], we can then have the foundation (sidewall and carcass) stiffness, *k* be defined as:

$$k = \frac{\beta q_{app}}{2R_u^{\,2}} \tag{5.5}$$

Where

R_u = Undeformed radius of the tire

Equations (5.3) - (5.5) underline our need to acquire the parameters q_{app} and β to capture the deformation behavior of the tire and to compute the related physical parameters. The following subsections will illustrate how we intend to parameterize equations (5.3) - (5.5) using simple quasi-static empirical tests.

5.2 Tire Deformation Properties: Experiment Design

There are several methods that can be employed to acquire the data for the parameters needed. For the parameter β, the procedure proposed in this dissertation is based on the assumption that we can measure the tire contact length for a known deflection as shown in Figure 5-2. From equation (5.2), we can deduce that the parameter β is the slope of z'_{app} vs. z_{app}. In addition to that, from the analysis done in chapter 4, for a tire that is statically loaded, the deflection will be symmetrical from the leading edge of the tire to the trailing edge of the tire, resulting in a symmetrical deflection angle. From basic trigonometry, we can then calculate the angle , θ_{app} as:

$$\theta_{app} = \tan^{-1}\left(\frac{\frac{l_p}{2}}{R_u\left(1-\frac{\delta}{R_u}\right)}\right) \tag{5.6}$$

With that, we can calculate the normalized deflection z_{app} as;

$$z_{app} = 1 - \frac{1-\delta/R_u}{\cos\theta_{app}} \tag{5.7}$$

And z'_{app} can be computed as

$$z'_{app} = -\left(1-\frac{\delta}{R_u}\right)\frac{\sin\theta_{app}}{\cos^2\theta_{app}} \tag{5.8}$$

The length of the contact patch, l_p can be accurately measured by using the footprint data acquired with a Tekscan footprint pressure measurement system. The maximum tire deflection, δ, can be measured from the loading actuator, assuming we

start at a location just below the contact patch. The advantage of this method is that it is similar to the method used by the U.S. Army Waterways Experimental Station [75] for characterizing the centerline deflection of the pneumatic tire and provides the analytical support for the empirical method used by Karafiath [20], which has been used successfully for vehicle mobility analysis.

Hence, the steps needed for the procedure we developed to obtain the parameter β are as follows:

1. Load tire with a preset deflection.
2. Record footprint, tire normal pressure distribution, tire load, and deflection.
3. Increase tire deflection by preset increment.
4. Repeat step 2 and 3 for until load reaches 175% of static curb weight load in operating conditions.
5. Calculate θ_{app} for each test case and plot z'_{app} vs z_{app}.
6. Obtain best fit data for β. (Note that when the tire deflection is zero, the derivative of the deflection is zero as well)

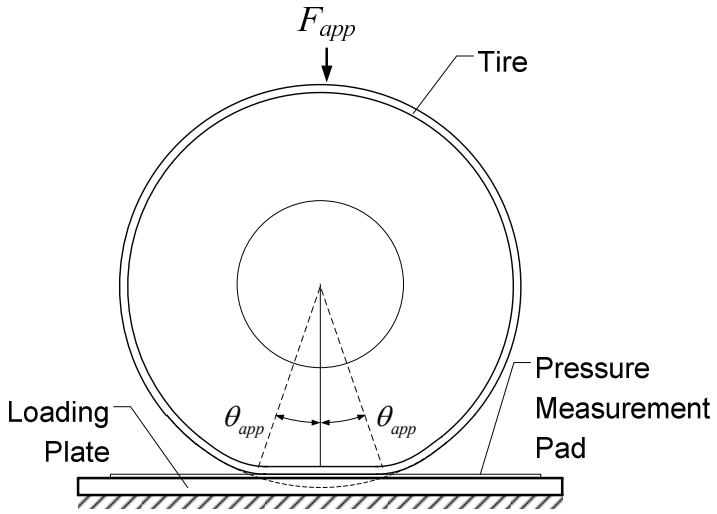

Figure 5-2. Tire testing by loading the tire against a flat plate with the pressure measurement pad.

For the purpose of testing, a controlled laboratory environment is needed to ensure that the tire was appropriately characterized. As part of this study, a tire mechanics attachment was developed for the purpose of tire testing. The tire mechanics attachment was used on the existing quarter-car rig available at CVeSS in the Performance

Engineering Laboratory (PERL) in Danville, VA. To illustrate the final configuration of the tire mechanics attachment, the CAD drawing of the setup is shown in Figure 5-3(a) and in Figure 5-3(b). Figure 5-3 (a) shows the setup where the tire was mounted on the wheel hub and loaded against an angle iron bolted on a flat plate to simulate a point-loading. This test was used to determine the point load normalized stiffness, q_{app}, a variable that will be discussed later in this section. Figure 5-3 (b) is the experimental setup where the angle iron is taken off the plate and replaced by the pressure measurement pad and the tire is loaded against a flat surface.

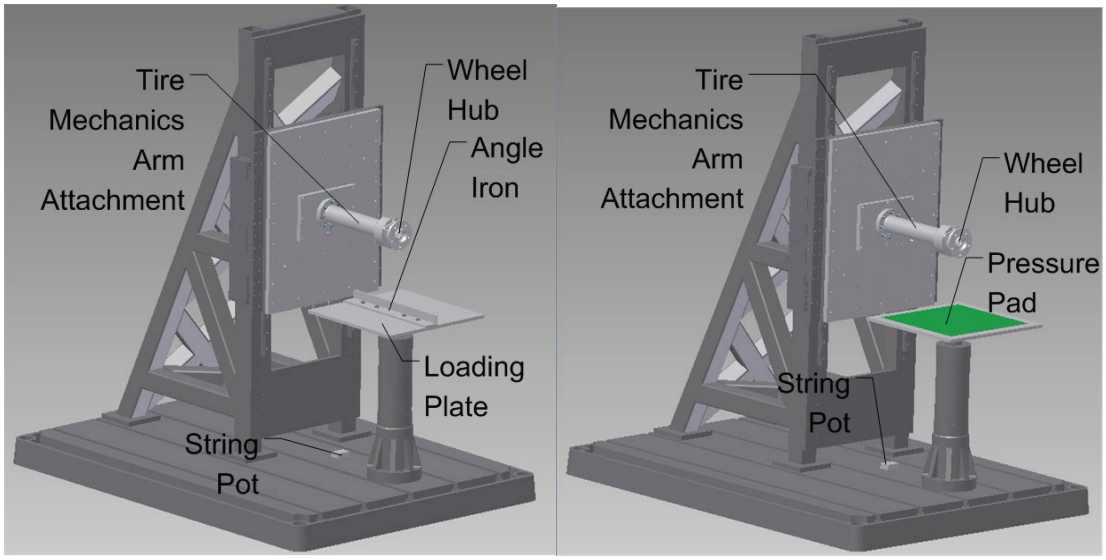

(a) **(b)**

Figure 5-3. 3-D Drawing of the proposed test setup with the tire mechanics attachment on the quarter-car rig. (a) Point load test setup (b) Flat surface test setup.

The quarter car-rig with its original setup is shown in Figure 5-4. The tire mechanics test setup was modified by removing the Porsche suspension shown mounted on the rig in Figure 5-4.

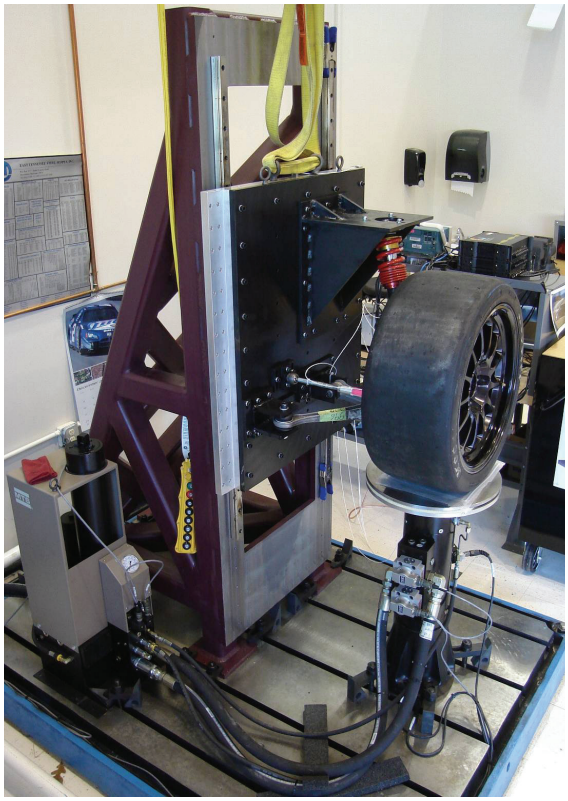

Figure 5-4. Original configuration of the quarter car setup with a Porsche Racing Suspension .

This arrangement was conceived as a cost effective way to attain the desired tire parameters and maximize lab resources. The arm was designed to withstand a maximum force of 3,000 lb-f of vertical loading with a factor of safety of 2 and have a maximum static deflection of 0.033 in at maximum load. The tire mechanics test setup is designed to have two setups as shown in Figure 5-5. The final test setup has been assembled for the purpose of testing for the point-load stiffness, as well as the flat tire loading characteristics. Figure 5-5 shows the rig configuration as used during final testing.

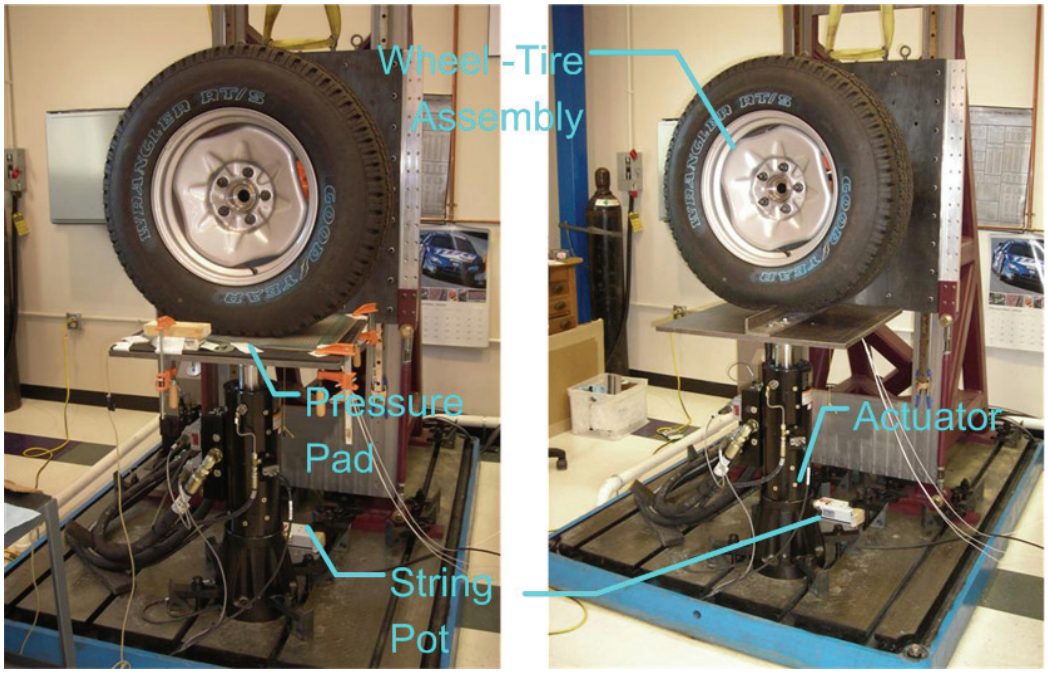

(a) **(b)**

Figure 5-5. Tire testing setup in final configuration as used in IALR at Danville, VA. (a) Flat surface loading testing (b) Point load testing.

The actuator used was an MTS Model 248.03 linear hydraulic actuator capable of 5.5 Kip force [79] with a dynamic stroke of approximately ±3 in. The piston was custom-made to be light and rigid enough to provide an actuation bandwidth of over 150 Hz at low amplitude displacements. The actuator has an inline linear-Voltage Differential transformer (LVDT) and a delta-pressure cell for position or force feedback to the controller respectively. The difference between the data from the LVDT and the spring pot mounted to the arm was used to determine the tire deflection. The delta pressure cell has been used to determine the force acting on the center of the contact patch. The pressure measurement pad has been used to measure footprint data for later analysis.

Figure 5-6 shows the signal conditioning and instrumentation used for controlling the actuator and collecting the data.

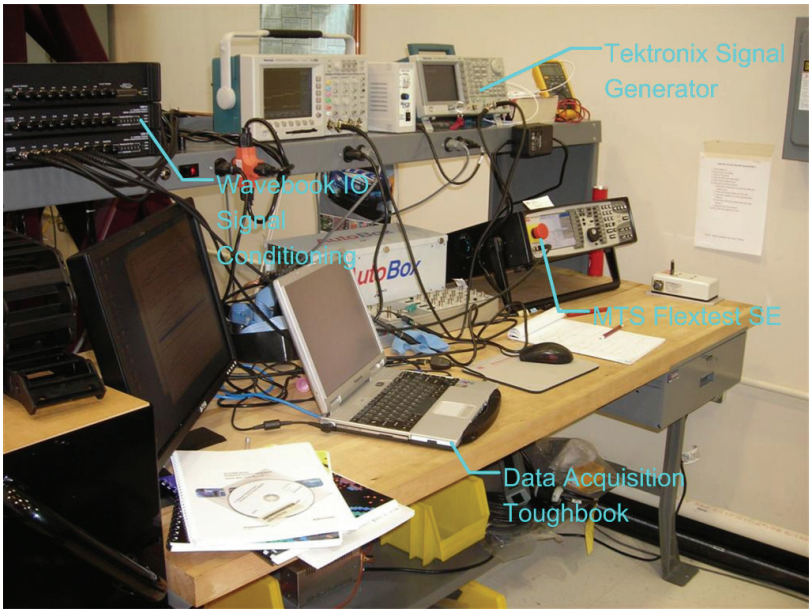

Figure 5-6. Data acquisition and instrumentation for actuator control and collection of data.

For the purpose of this testing, an adjustable lockout mechanism had to be designed and installed at the base of the plate the remove the unnecessary degrees of freedom on the rig. This mechanism is shown in Figure 5-7.

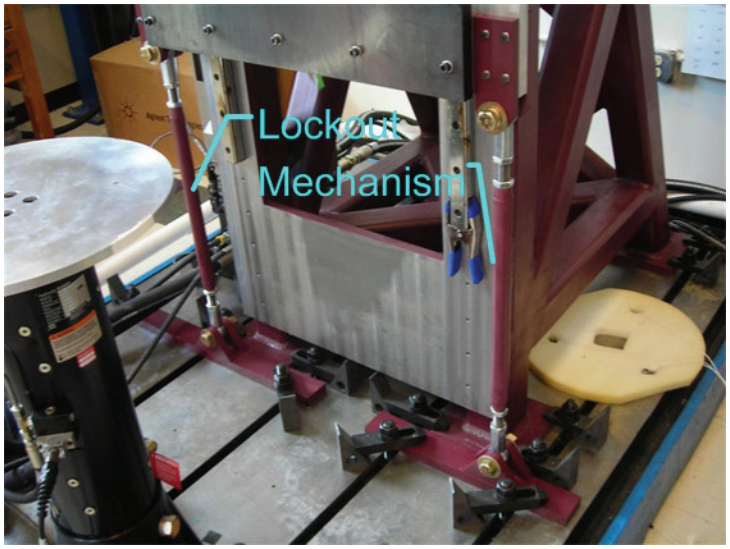

Figure 5-7 Lockout mechanism on the quarter car rig.

Figure 5-8 shows the data acquired from the tire mechanics rig using the flat loading setup for different inflation pressures to determine the value of β.

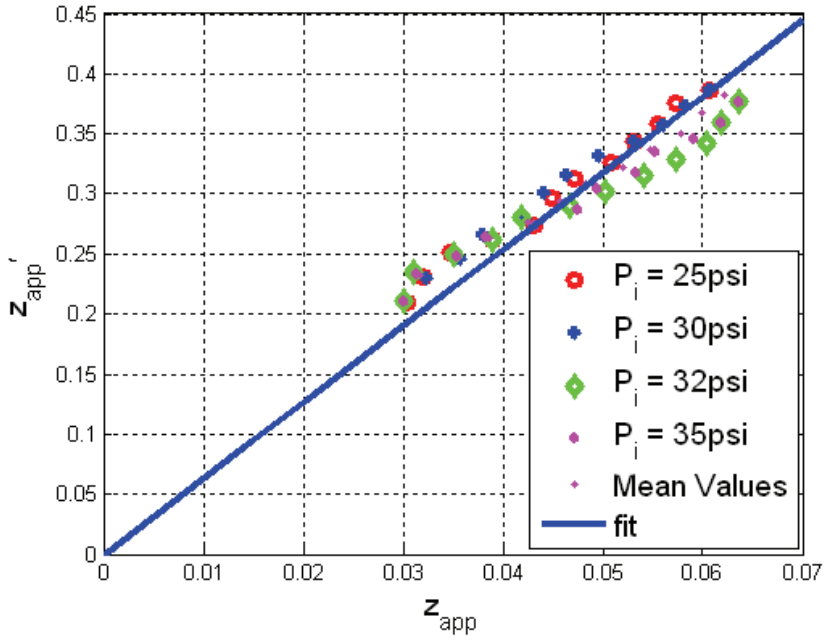

Figure 5-8. Data for estimation of β and the best fit line

The work by Loo [72] determined the parameter β by using just one inflation pressure. In this study we have collected data for a range of operating inflation pressures from 25 psi to 35 psi, which is the normal operating range of most tires. The parameter β is determined to be 6.3579 for the tire tested (Add again the tire type at the beginning of this chapter). This value of β is determined to be reasonable because it is within the range of the data found in [72].

Footprint data was also collected for the tire using this setup. An example of this data can be seen in Figure 5-9. It can be noted from the figure that the tire contact patch length decreases with increase in inflation pressure. This behavior is expected, and is useful for developing insight for analytical tire modeling. Although the data from the contact patch footprint is subjective and differs from tire to tire, the objective of collecting the data is to gain insight into the contact pressure and geometry. As such, from Figure 5-9, the modeling assumption that the contact patch is rectangular in shape does not seem to be that far off, after all.

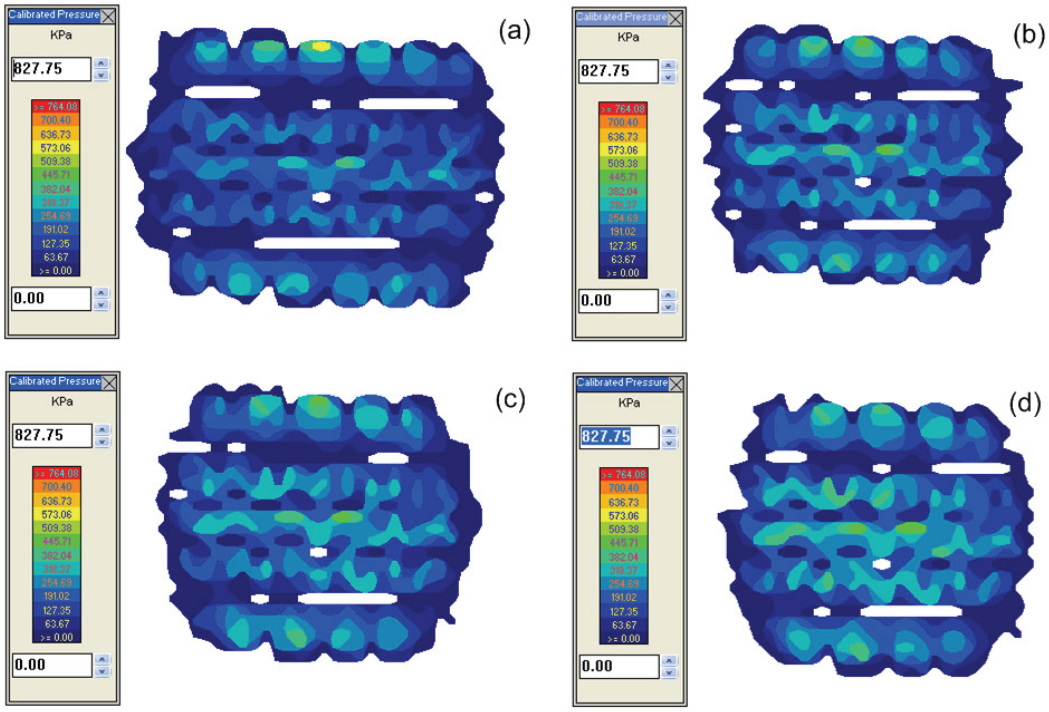

Figure 5-9. Footprint data for different inflation pressures at loads close to GVW - (a) 25psi (b) 30psi (c) 32psi (d) 35psi.

The point-load stiffness q_{app} is a necessary variable to calculate the values of T and k according to equations (5.4) and (5.5). Loo [72] has demonstrated that the point-load stiffness can be calculated as a linear function of the inflation pressure, as shown in equation (5.9).

$$q_{app} = \alpha p_i + c \tag{5.9}$$

Where

$c =$ Offset value of point-load stiffness

$p_i =$ Tire inflation pressure

$\alpha =$ Rate of change of point-load stiffness with respect to tire pressure

The experimental test setup designed for this procedure can be seen at Figure 5-3(b). The procedure for obtaining the value of q_{app} is as follows:

1. Infuse tire with air up to 15 psi.
2. Load tire against point-loading plate starting from 0 lbs.
3. Record tire radius, tire load, and deflection.
4. Increase load up till deflection reaches 0.1 inch from previous value.

5. Record tire load and deflection.
6. Repeat step 4 up till deflection reaches 1 inch from 0 deflection.
7. Unload the tire with increments of 0.1 inch.
8. Record tire load and deflection. Stop when tire is fully unloaded.
9. Increase pressure by preset increment (recommended 5 psi) and repeat testing starting from step 2 till tire pressure reaches 45 psi.
10. Plot 3-D plot of vertical load vs. deflection vs. tire pressure to check for validity of data.
11. Calculate the value of q at max δ at different inflation pressure using equation (5.3).
12. Plot the value of q vs. p_i to get the best fit line for equation (5.9).

In Figure 5-10 we present the experimentally obtained data for the normal load versus the tire deflection at the various tire inflation pressures used. If the transient peaks at low deflections are neglected, we can see that the curves closely resemble typical load deflection curves for tires.

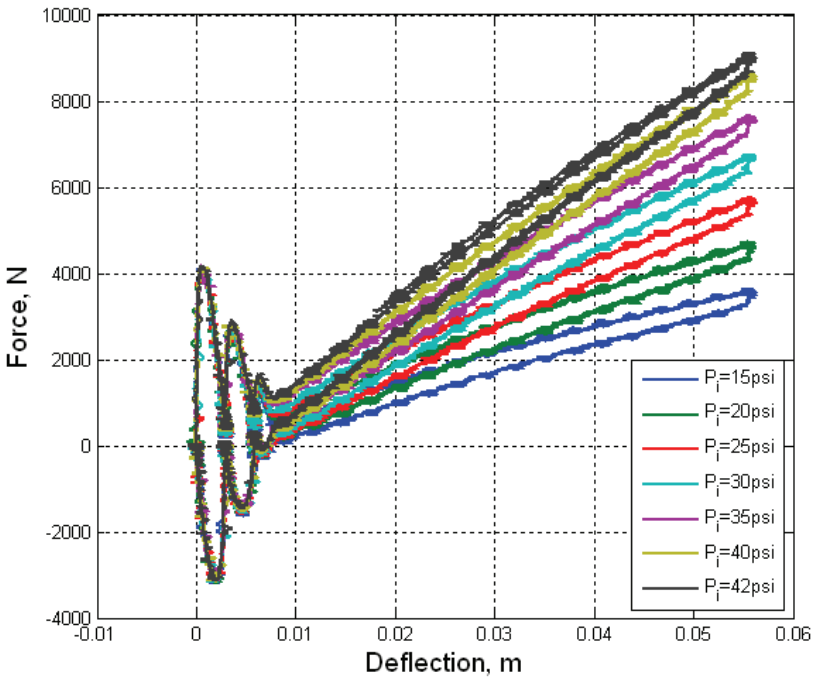

Figure 5-10. Raw data of the Load vs. Deflection Curve acquired using the tire mechanics rig.

In Figure 5-11 we present the experimentally obtained data versus the results obtained with the model we developed for the point load stiffness versus the tire inflation pressure.

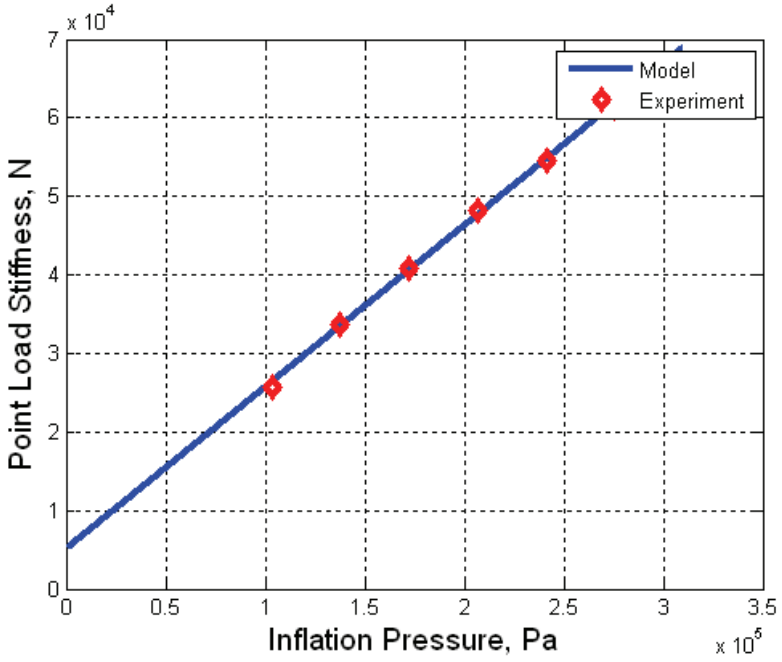

Figure 5-11. Point load stiffness acquired from testing on the Tire Mechanics Rig

The data from Figure 5-10 was processed to yield the parameters for equation (5.9). By using a nonlinear least squares algorithm, the parameters were determined as $c = 5024.4$ N and $\alpha = 0.2059$ m^2. Note that the force-deflection curve for low displacements seems to have large peaks that are not expected in the usual force-deflection curves. One probable reason why this is happening is fact that the static displacements are input as step ladder functions, which, when coupled with the fact that the use of an angle iron to apply the input, may seem as a wide-band excitation to the tire, similar to a cleat in a drum tester. However, the short dwells in between each increment still provide us with the necessary quasi-static data at the dwell of each step. These parameters were found to have reasonable values within the range of values found in [72].

With completion of the tests mentioned in the earlier parts of the chapter, we are left with the task of determining the parameter c_d used in equation (5.10), which is the internal damping of the tire in the radial direction. From the analysis done by Loo [72],

the total longitudinal force acting on a tire rolling at a steady state speed and zero camber and slip angle can be written as:

$$F_x = \left(1-\frac{\delta}{R_u}\right)\left(\sec\theta_f - \sec\theta_r\right)\left\{T + kR_u^2\left[1-\frac{1}{2}\left(1-\frac{\delta}{R_u}\right)\left(\sec\theta_f + \sec\theta_r\right)\right]\right\} + \frac{1}{3}c_d\omega R_u^2\left(1-\frac{\delta}{R_u}\right)^2\left(\tan^3\theta_f - \tan^3\theta_r\right) \quad (5.10)$$

Using this equation, since we know *k, T,* and R_c, we can measure the value of F_x, ω, and δ for a tire being tested on a flat-trac testing machine and use an optimization algorithm to calculate a value for c_d. Hence the testing method to acquire a value for the parameter c_d is as follows:

1. Run tire at certain angular velocity and deflection.
2. Record longitudinal force.
3. Run optimization algorithm to obtain a value of c_d.

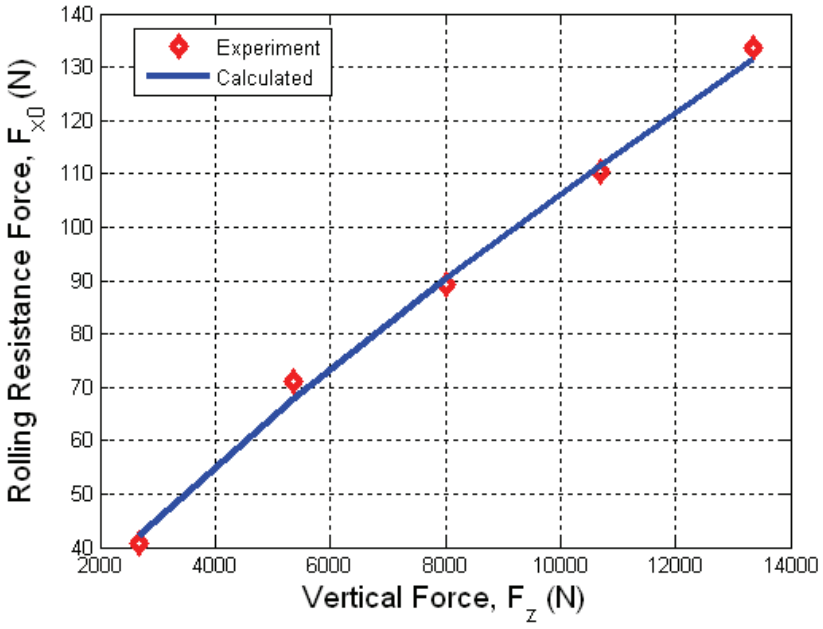

Figure 5-12. Comparison between the line that fits the rolling resistance of the model with the obtained value of damping and the collected experimental data.

The value of the damping constant c_d is found to be equal to 1476.78 Ns/m, which is within the reasonable range for tires [3]. For the value of c_d found, a plot of the rolling resistance, calculated with equation (5.10).

5.3 On-road Tire Model: Experiment Design

The work presented in this dissertation has been primarily focused on the development of the theoretical framework of a dynamic tire model which has roots in analytical mechanics modeling but which has been augmented with empirical relations. This augmentation is expected to provide a more realistic output for the simulation of pneumatic tires in the quasi-static and dynamic conditions for on-road simulations. There will be two parts for the testing of the tire for the on-road model. The first part will dwell upon the quasi-static testing, and the second part will explore the dynamic testing that is needed for characterizing some of the dynamics properties of the tire.

Quasi-static tire testing has been the primary method used to characterizing tire behavior. It can be done in the laboratory with testing machines [1], or outside with on-road tire testing rigs [39]. Currently, there is a rich amount of experimental work described in the literature on quasi-static testing of tires and many different experimental test matrices suggested. With that in mind, it must be mentioned that the recommended quasi-static tests presented in this subsection are inspired by the work of different samples of experimental design in the literature. However, the incremental steps presented for the loading of the tire tested are recommended by the author of this dissertation for increased accuracy in the determination of the quasi-static properties of the tire.

Dynamic tire testing has been a rather intensive area of research by various researchers, as discussed by Pottinger in [1]. The objective of dynamic testing is to ascertain the effect that an increase in the rate of change of the slip angle at the center of the wheel has on the slip angle at the contact patch. The dynamic testing procedures for the tire model in this formulation will be discussed in the further subsection. For the dynamic testing procedures, the lateral force generation dynamic behavior is of more interest than the longitudinal force generation dynamic behavior, since the transient effects resulting from the lateral tire force are important for limit handling studies.

5.3.1 On-road Tire Model: Quasi-static Testing

For the model presented in this dissertation, the first set of characterization tests are 4 sets of quasi-static tire tests. Quasi-static tire testing are standard bare minimum tests that have been recommended to be used for tire characterization [1]. The complete recommended test matrix developed is presented in Table 5-1, where we have:

a. Quasi-static steering tests
   - At discrete increments of the normal load and belt speed, with zero camber angle and zero slip ratio, the slip angle of the tire is swept at the rate of 1 deg/sec between ± 25º.

b. Quasi-static braking/driving tests
   - At discrete increments of the normal load and belt speed, with zero camber angle and zero slip angle, the slip ratio of the tire is swept with the ramp time of 3 sec. between ± 1.

c. Quasi-static steering/braking/driving tests
   - At discrete increments of the normal load, belt speed and discrete increments of slip angle from -10 º to 10 º with zero camber angle, the slip ratio of the tire is swept with the ramp time of 3 sec between ± 0.9.

d. Quasi-static steering/cambering tests
   - At discrete increments of the normal load, belt speed and discrete increments of camber angle from -9 º to 9 º with zero slip ratio, the slip angle of the tire is swept at the rate of 1 deg/sec between ± 25º.

The testing methodologies in Table 5-1 have been structured to be very flexible, in order to accommodate the capabilities of various tire testing machines that are currently used in industry. The reference tire vertical force, F_{zref} is taken as the maximum load on any of the 4 tires at Gross Vehicle Weight (GVW). The test matrix is designed for a belt testing machine, but there are methods developed to convert data from belt testers to drum testers [80]. The spacing between the discrete increments of the tire vertical load are left to the subjective choice of the tester, however, a minimum of data from three (3) vertical loads are recommended to acquire enough resolution for tire vertical testing. Measurements during each test should include, but are not limited to:

1. Slip angle

2. Slip ratio
3. Camber inclination angle
4. Belt speed
5. Spindle height/loaded radius
6. Lateral force
7. Longitudinal force
8. Vertical force
9. Overturning moment
10. Aligning moment

Table 5-1. Recommended complete quasi-static experimental test matrix

Test	Slip angle, α	Camber angle, γ	Slip Ratio, s	Vertical Force, F_{zref} (%N)	Belt Speed, (kph)
a. Quasi-static steering	-1º → 25º→-25º →1 º	0	0	Discrete increments from %50 F_{zref} → %200 F_{zref}	Discrete increments from 50 kph → 100 kph
b. Quasi-static braking/driving	0	0	-0.1→ 1→0.1 →-1	Discrete increments from %50 F_{zref} → %200 F_{zref}	Discrete increments from 50 kph → 100 kph
c. Quasi-static combined steering braking/driving	Discrete increments from -10 º → 10 º	0	-0.9→ 0.9	Discrete increments from %50 F_{zref} → %200 F_{zref}	Discrete increments from 50 kph → 100 kph
d. Quasi-static combined steering/cambering	-1º→ 25º→-25º →1 º	Discrete increments from -9 º → 9 º	0	Discrete increments from %50 F_{zref} → %200 F_{zref}	50kph

The tire parameters that are to be regressed from the quasi-static testing include the vertical stiffness, cornering stiffness, braking/driving stiffness, the peak coefficients of friction, as well as the sliding coefficients of friction. In addition, we can also determine the sensitivity coefficient that changes the shape of the normal pressure distribution if

the dynamic footprint data is collected. The conicity and plysteer offset for the lateral force can also be acquired from the quasi-static set of data.

5.3.2 On-road Tire Model: Dynamic Testing

The study of the dynamic lateral force generation mechanism of tires first started with the study of shimmying on aircraft wheels [49]. The lateral force and aligning moment will be lagging behind the steering input because of the viscoelastic properties of the tire structure. This lag is very important for transient maneuvers which approach the limit handling operation region of the tire [1]. This is because the lag creates a delay between the directional control input from the steering wheel, causing instability, and a reduction in lateral force, reducing vehicle controllability. Various models have been proposed to model the tire lag behavior at the contact patch. The STI model [43] approximates this behavior with two first order lags, resulting in a total lag with second order characteristics.

The dynamics tire test matrix is shown in Table 5-2. The test proposed for characterizing the tire dynamic lag in this study is a discrete sinusoidal steering test, similar to the one proposed by Heydinger [81]. Although it is recommended to run the test for various tire vertical loads to observe the effect of tire load on the lag, if the resources to obtain experimental data are limited, then the most important test load needed on the tire is the one for loading at GVW.

Table 5-2. Recommended complete dynamic experimental testing

Test	Slip angle, α	Camber angle, γ	Slip Ratio, s	Normal Force, F_{zref} (%N)	Belt Speed, (kph)
Discrete Sinusoidal Steering	Discrete increments of frequency from $0 \rightarrow 5$Hz with peak to peak of 1.5 º ~ 2 º of at least 4 cycles	0	0	Discrete increments from $\%50F_{zref} \rightarrow \%200F_{zref}$	50kph

The phase and magnitude of the measured force/aligning moment due to a slip angle input will be plot against the frequency of the input to acquire the second order phase and magnitude of the tire lag, and from here regress the parameters needed. By assuming the damping ratio of the second order equation to be 1 (critically damped system), we can then determine all the other parameters for the second order differential equation.

In Figure 5-13 we present experimental data from discrete sinusoidal steer tests for a P265/70R17 tire. Note that the loop becomes wider as the frequency is increased. This phenomenon is accounted for by the tire mechanics community by using a lagged filter on the slip angle at the center of the wheel.

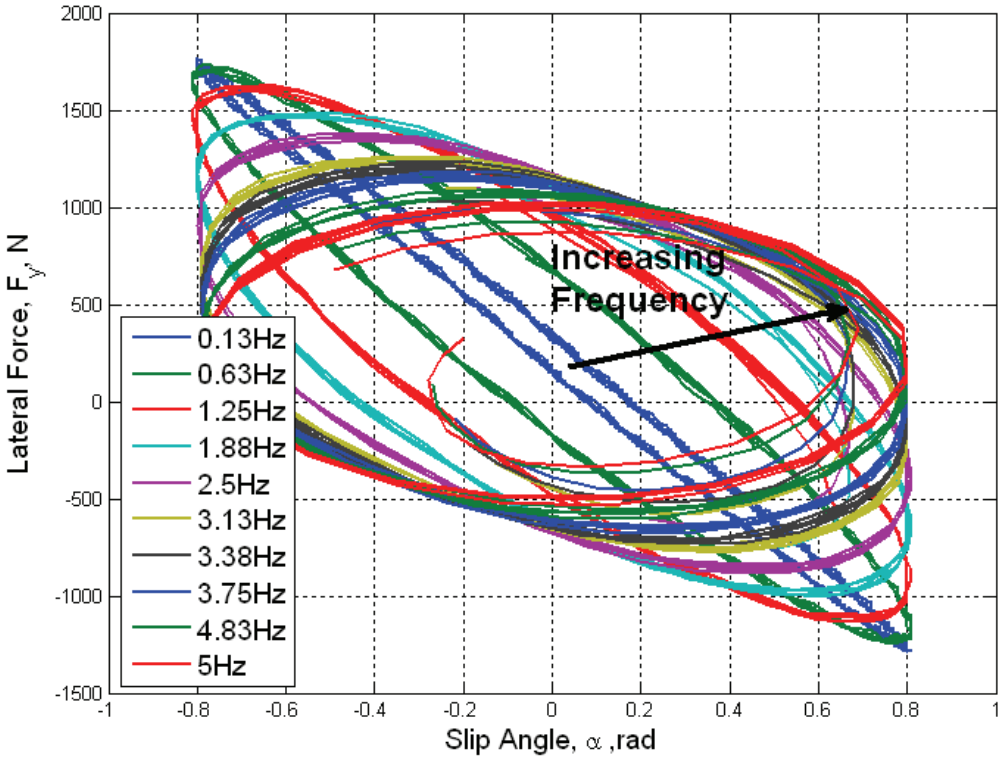

Figure 5-13. Data from discrete sinusoidal steer tests for a Continental Contitrac P265/70R17 tire. Note that the loop becomes wider as the frequency is increased, implying a reduction in the generated tire lateral force.

The second order approximation for the magnitude and the phase are shown together with the first order approximation and the actual experimental data used for

parameterizing the models developed in this dissertation in Figure 5-14 and respectively in Figure 5-15. It can be noticed that the second order approximation is a poorer fit for the magnitude of the lag, compared with the first order fit, but provides a better fit for the actual phase of the tire lag. In Table 5-3 we present the parameters regressed for the slip angle lag of the tire using the optimization routine.

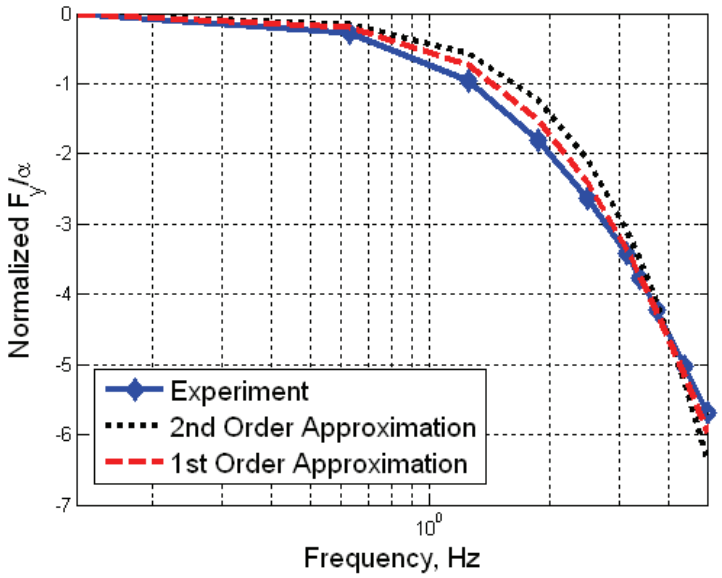

Figure 5-14. Comparison between the magnitudes of experimental data, first order approximation, and second order approximation

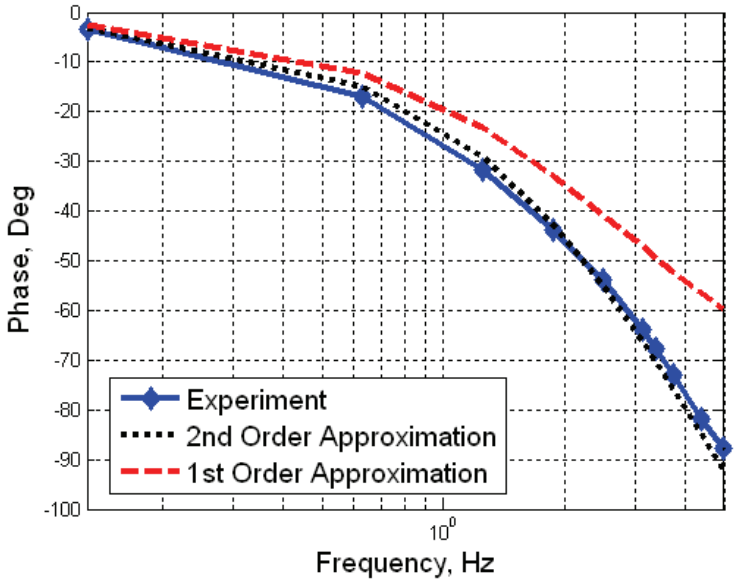

Figure 5-15. Comparison between the phase of experimental data, first order approximation, and second order approximation

The first order model for the tire dynamic lag can be defined in transfer function form as shown in equation (5.11) and the second order model for the tire dynamic lag can be defined as shown in equation (5.12).

$$\frac{\alpha_c(s)}{\alpha(s)} = \frac{\omega_0}{s + \omega_0} \tag{5.11}$$

$$\frac{\alpha_c(s)}{\alpha(s)} = \frac{\omega_n^{\,2}}{s^2 + 2\zeta\omega_n + \omega_n^{\,2}} \tag{5.12}$$

Where

$\alpha_c(s) = \text{Slip angle at contact patch}$
$\alpha(s) = \text{Slip angle at center of wheel}$
$\omega_n, \omega_0 = \text{Break Frequencies}$
$\zeta = \text{Damping Ratio}$

Table 5-3. Parameters regressed for the slip angle lag using the optimization routine for both the first order and second order lag.

Lag type	Parameter	Value
First Order Lag	ω_0	18.2261
Second order lag	ω_n	30.1335
	ζ	1

5.3.3 On-road Tire Model System Identification

The data acquired from the tire testing must to be processed to identify the tire parameters to be used for simulations. The tire testing data used for the regression in this section of the tire parameter identification comes from the National Highway Traffic Safety Administration (NHTSA) for the Continental Contitrac SUV P265/70R17 tire used in the 2003 Ford Expedition [82]. The regression of the parameters are done as a function of the tire vertical load since the data exhibits a larger sensitivity to increase in normal load, as opposed to other factors (e.g., speed, temperature). The system identification done in this section reflects the study of the trends observed in the data, and is based on a lot of experience and analysis of empirical tire data from primarily [39] and [1].

Figure 5-16 (b) and Figure 5-17 (b) show the gradual decrease of the tire longitudinal and lateral force, respectively, with change in tire vertical load. Aside from modifying the coefficients of friction to account for the effects of sliding as shown in chapter 3, accounting for the change in tire vertical load will enable us to change the friction behavior of the tire model in maneuvers that are caused by lateral load transfer of the vehicle.

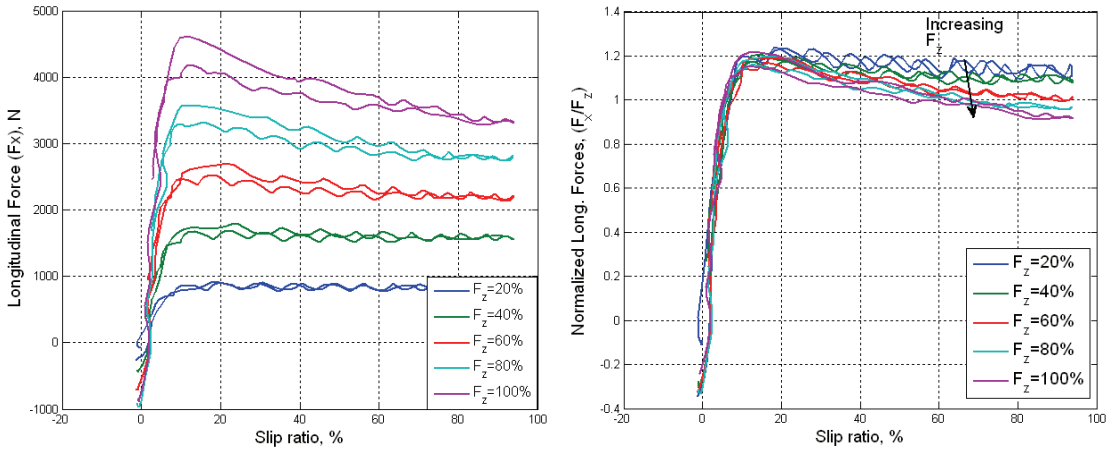

(a) **(b)**

Figure 5-16. Raw data (a) vs normalized data (b) for the longitudinal force for a driven tire.

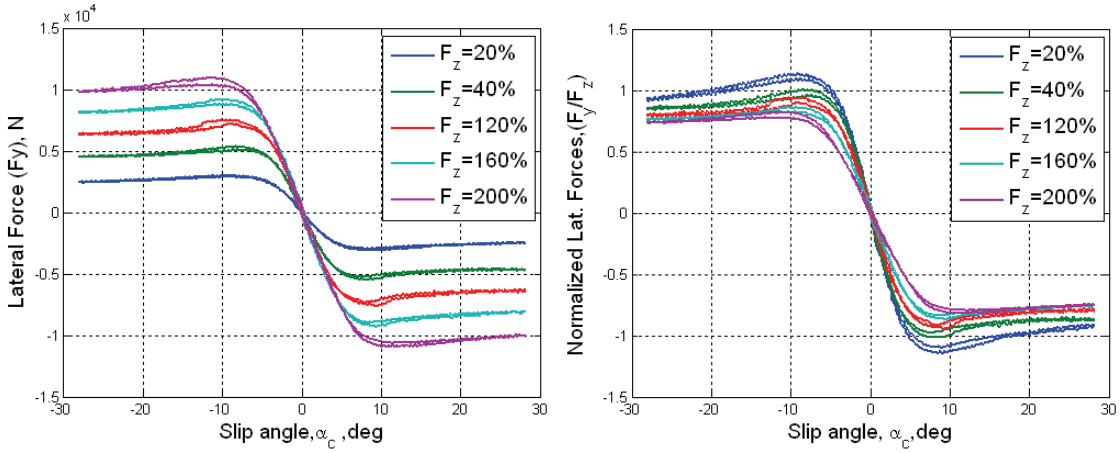

(a) **(b)**

Figure 5-17. Raw data (a) vs normalized data (b) for the lateral force.

If we model this decrease in lateral and longitudinal force with increase in vertical tire load, we can use the analysis from chapter 3 and the quasi-static experimental data to

extrapolate this change in the tire force generation characteristics for vehicle dynamics simulation purposes. The following subsection will demonstrate how we model this behavior by modifying the coefficient of friction of the tire with increase in tire vertical load.

5.3.3.1 On-road Tire Model System Identification: μ_{pmax}, μ_{pmin}, and μ_s.

From Figure 5-16 (b), we can see a reduction in the friction coefficients of the tire with increase in tire normal load. The friction coefficients are highly dependent on tire vertical load, speed, and temperature and the effect of these variables are very well documented in [39]. When acquiring experimental data during laboratory testing, the temperature and the speed are usually controlled for development of tire models, and the operating temperature is usually assumed to be the cold running temperature of the tire for tire models. The model proposed for capturing the load dependence of the coefficient of friction is shown in equation (5.13). This model is an entirely empirical function and was selected because of the fact that it has a lower bound and is intended to be used for wheel loads of 20% to 200% of GVW. It is reasonable to assume this range of wheel loads as the application load because loads beyond this range implies a spinout or rollover situation[37], which is beyond the range of operation that we are interested in. A function of similar form has been proposed in [39] to model the dependence of the coefficients of friction on speed.

$$\mu = \mu_0 \left(\frac{F_z}{F_0} \right)^n \tag{5.13}$$

For the tire used in this study, the parameters found for the coefficients of friction are shown in Table 5-4. Although the values of the coefficients of friction are not symmetrical for braking and driving, the values in Table 5-4 are optimized for braking. The reason to have the parameters optimized for braking is that most transient states for combined maneuvers happen while the vehicle is operated in braking situations. This is especially true during validation tests for vehicle ABS/ESP systems, where the vehicle is not driven, but rather braked while cornering. Figure 5-18 through Figure 5-23 show the fitting of equation (5.13) for lateral and longitudinal data. The fitting of equation (5.13)

is meant to provide users with the capabilities to extrapolate the rate of change of the coefficients of friction with respect to the tire vertical force, within the operating range of the GVW. The values of the lateral coefficient of frictions are almost symmetrical; hence it makes no difference whether the coefficients are taken from the positive or from the negative slip angle.

Table 5-4. Coefficients for the curve fit of the coefficients of friction as a function of the wheel vertical load.

	Longitudinal Coefficients			*Lateral Coefficients*		
	μ_0	F_0	n	μ_0	F_0	n
μ_{pmax}	*1.569*	*9.900*	*-0.062*	*2.901*	*20.010*	*-0.1903*
μ_{pmin}	*1.562*	*9.893*	*-0.067*	*2.990*	*20.010*	*-0.2042*
μ_s	*2.189*	*10.611*	*-0.173*	*1.903*	*20.000*	*-0.1455*
S_x, S_y	*3*			*6*		
s_p, α_{cp}	*10.00%*			*9.66Deg*		

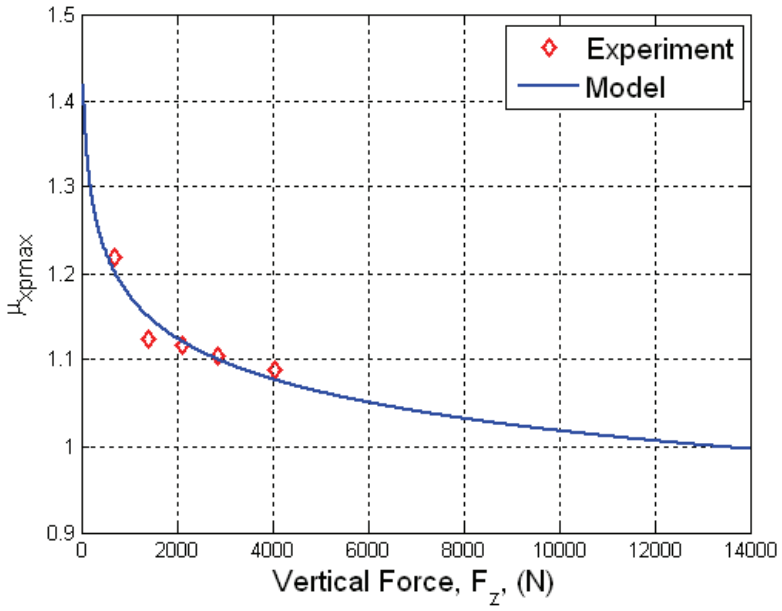

Figure 5-18. Longitudinal maximum peak coefficient of friction with change in tire vertical load.

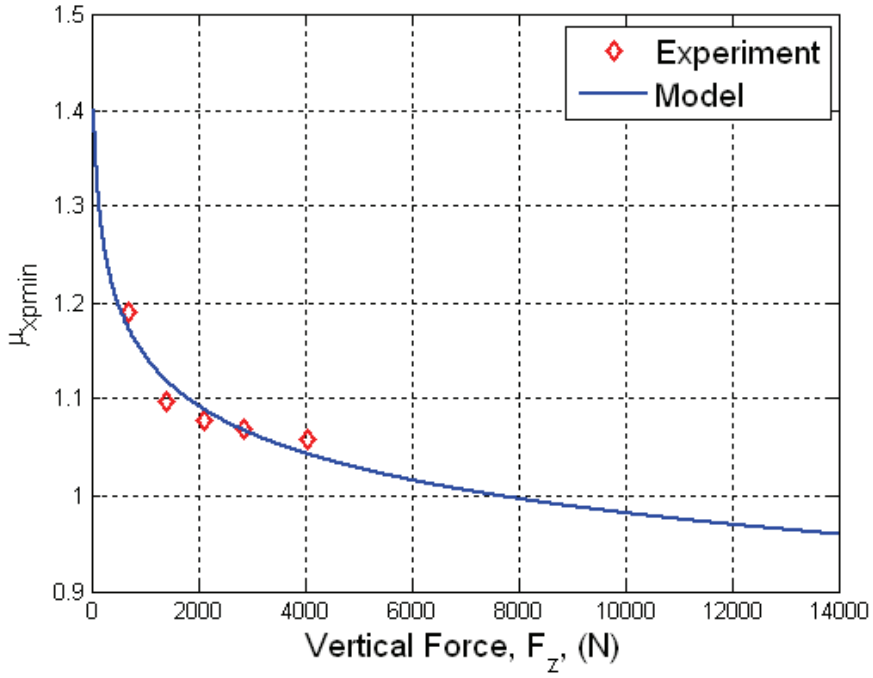

Figure 5-19. Longitudinal minimum peak coefficient of friction with change in tire vertical load.

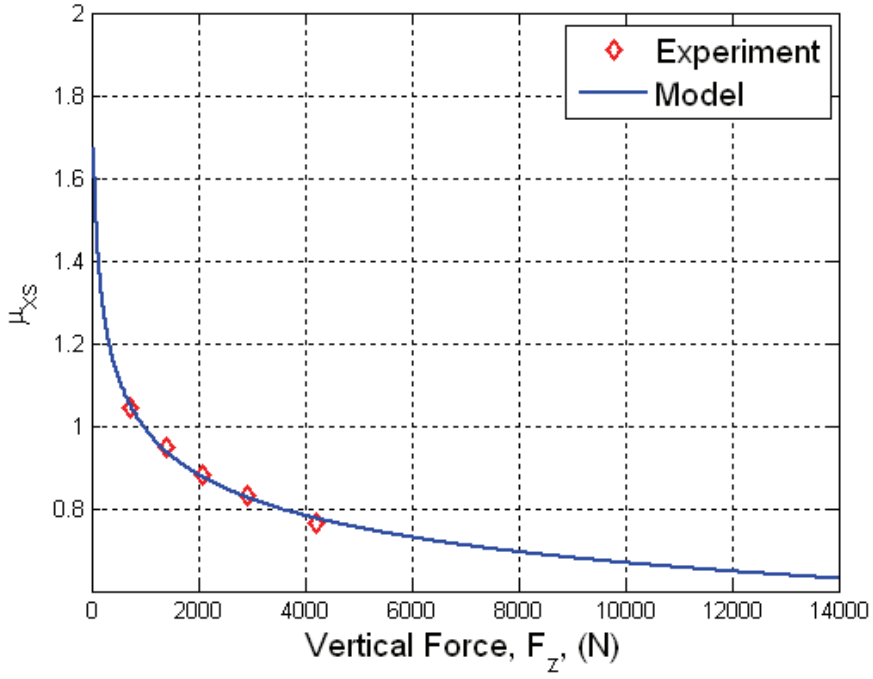

Figure 5-20. Longitudinal sliding coefficient of friction with change in tire vertical load.

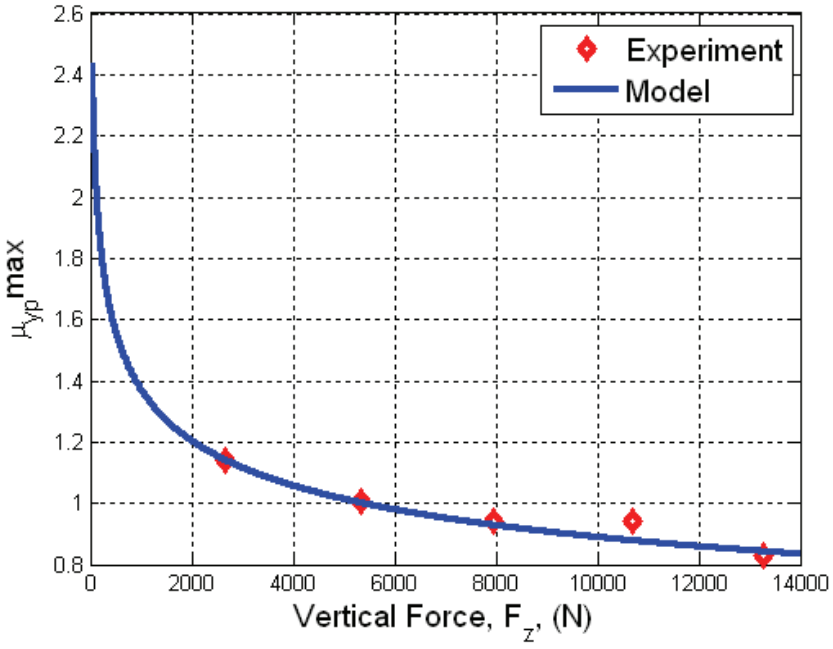

Figure 5-21. Lateral maximum peak coefficient of friction with change in tire vertical load.

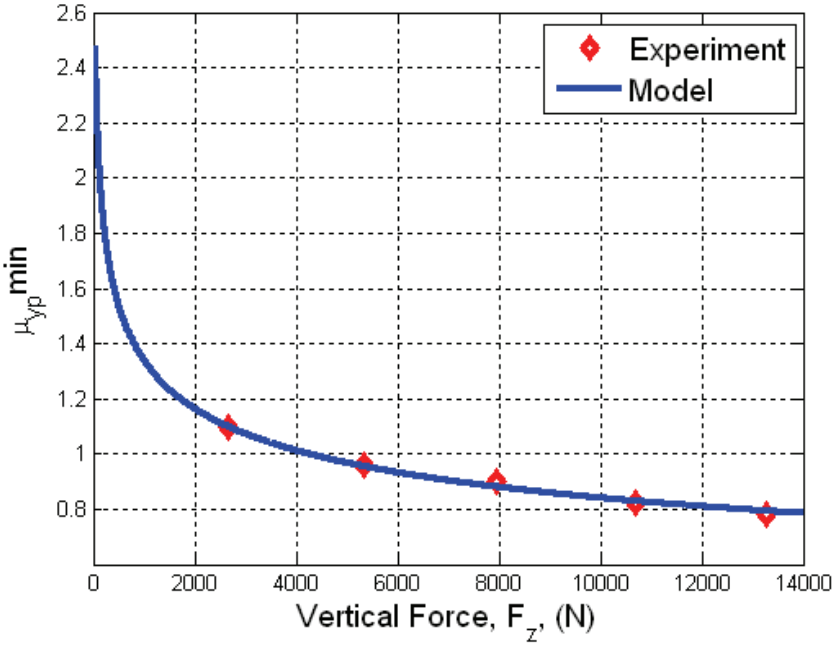

Figure 5-22. Lateral minimum peak coefficient of friction with change in tire vertical load.

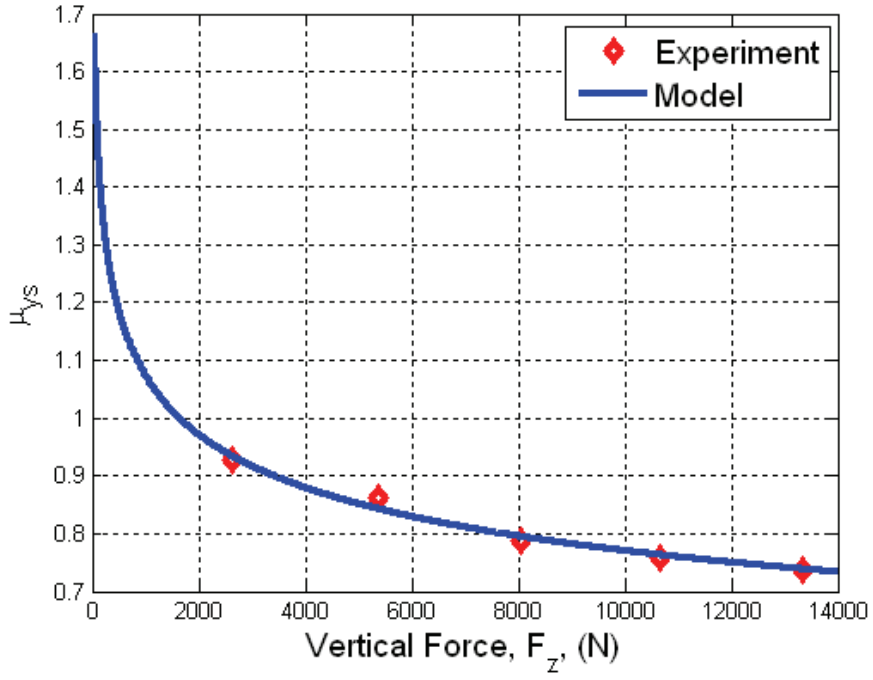

Figure 5-23. Lateral sliding coefficient of friction with change in tire vertical load.

In addition to accounting for the change in the tire vertical load, the effect of the longitudinal velocity of the tire and the nominal friction coefficient of the surface has to be included into the friction coefficient models. The rationale behind this modification is because tire testing is usually done on high friction coefficient silicon carbide surfaces in laboratory testing[1], which is different than the vehicle simulation road surface (ice road, asphalt) and at one reference speed for the operation of the tire. These factors may change the friction decay coefficient and value of all the coefficients of friction in both the lateral and longitudinal direction. Equation (5.13) can then be rewritten, with the inclusion of the effect of the scaling nominal friction coefficient as:

$$\mu = \mu_{nom}\mu_0\left(\frac{F_z}{F_0}\right)^n \tag{5.14}$$

Where

$$\mu_{nom} = \text{ Scaling coefficient for the friction coefficient } (\in[0,1])$$

To include the speed dependent coefficient, the friction decay coefficient S_x is modified as shown in equation (5.15).

$$S_x = S_x \frac{|V_x|}{V_{ref}}, V_x \in \left[V_{ref}, \infty\right) \tag{5.15}$$

The modification proposed in equation (5.15) increases the rate of decay of the friction coefficient with slip when the longitudinal velocity is increased. An example of the effect of changing the coefficients with equation (5.14) and (5.15) can be seen in Figure 5-24(a) and Figure 5-24(b), respectively.

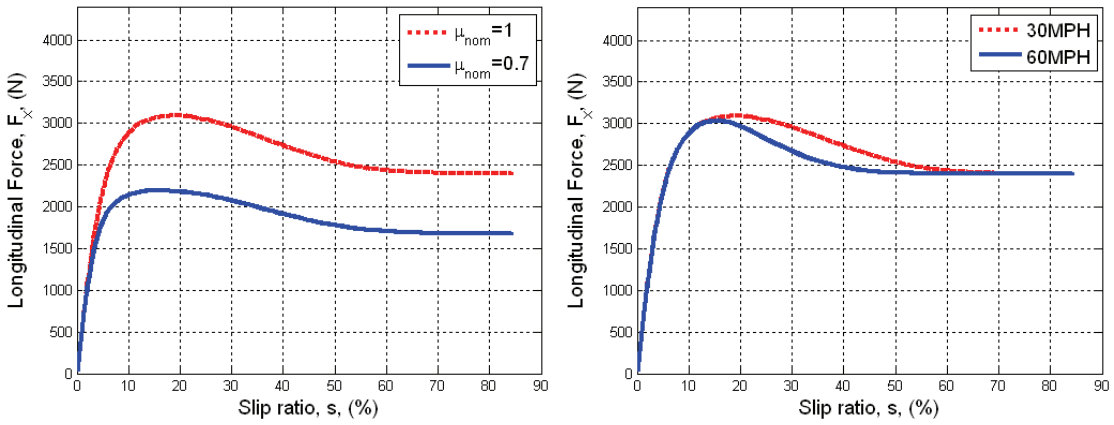

(a) (b)

Figure 5-24. (a) An example of the effect of reducing the nominal coefficient of friction on longitudinal force. (b) An example of the effect of increasing the velocity on the generated tire longitudinal force .

Note that reduction in the coefficient of friction reduces the generated longitudinal force in Figure 5-24(a), and an increase in velocity causes an increase in the rate of decay of the coefficient of friction. The parameters identified in this subsection will be used in the equations in section 3.7 of this dissertation.

5.3.3.2 On-road Tire Model System Identification: Vertical Stiffness

Figure 5-25 shows the tire vertical force vs. the tire deflection for several tire loads. The figure allows us to extrapolate and determine the nominal tire vertical stiffness, K_0. To assert the vertical stiffness of the tire during straight driving operations and during static loading, the nominal tire vertical stiffness has to be regressed from quasi-static zero slip and zero camber test data.

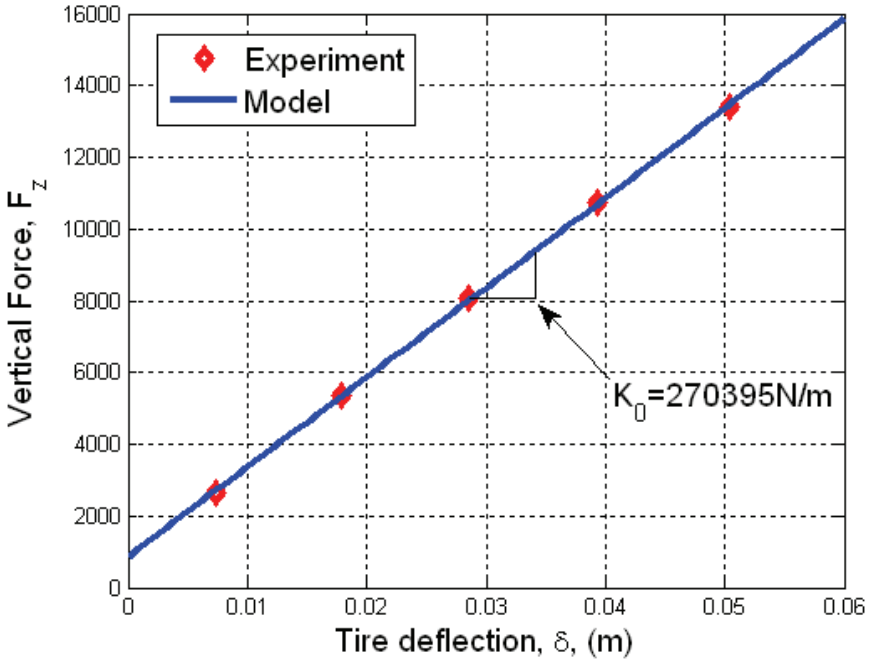

Figure 5-25. Vertical Stiffness at zero camber and slip angle

The shape modification factors C_{z1} and C_{z2} are then modeled as polynomial functions of the vertical deflection and of the slip angle. Note that the usage of polynomials requires some subjective judgment of the final result so that the final parameter estimation does not yield results exceeding realistic values. The value of C_{z1} at zero deflection has been set to 1 so that the stiffness at zero deflection is the same as the nominal stiffness. Figure 5-26 shows the results for the polynomial fit of the experimental data to identify the shape modification factors C_{z1} and C_{z2} with change in tire deflection for the tire used in this dissertation. The parameters for this polynomial fit are displayed in Table 5-5. The equation in which the shape modification factors C_{z1} and C_{z2} will be used is presented in chapter 3 in equation (3.16). Since the available data for determining the values of the parameters span from 20% GVW to 200% GVW, we can assume that the curve fit will produce model behaviors that adequately represent the tire within operating conditions. In a vehicle dynamics situation, in the case in which any of the one set of tires experience a load exceeding 200% GVW, vehicle rollover is imminent.

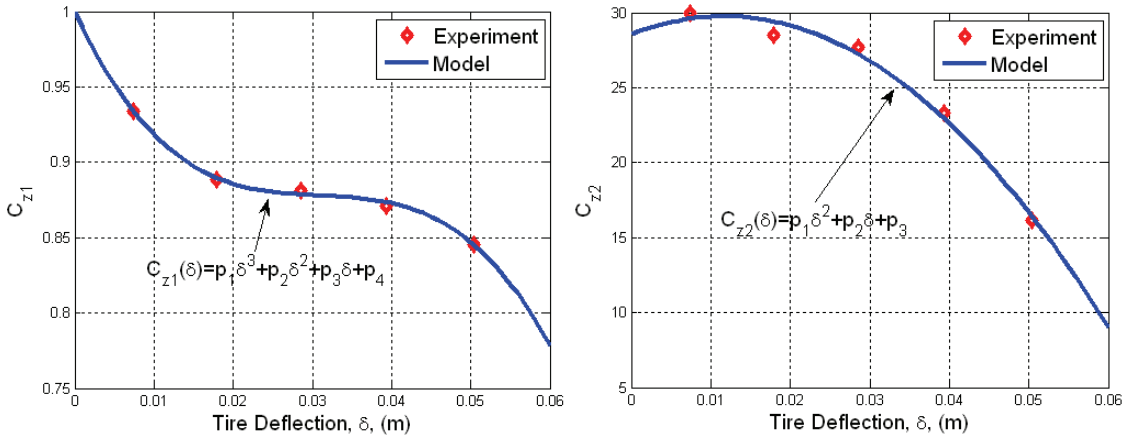

Figure 5-26. Polynomial fit of the data for the shape modification factors

Table 5-5. Parameters for the polynomial fit of C_{z1} and C_{z2}

	Parameters
$C_{z1}(\delta)=p_1\delta^3+p_2\delta^2+p_3\delta+p_4$	$p_1 = -3816$
	$p_2 = 355.2$
	$p_3 = -11.27$
	$p_4 = 0.9996$
$C_{z2}(\delta)=p_1\delta^2+p_2\delta+p_3$	$p_1 = -8893$
	$p_2 = 207.5$
	$p_3 = 28.56$

It is important to model tire vertical stiffness as accurately as possible. By accounting for the effect of tire input parameters such as the slip angle into the calculation of the vertical stiffness, the effect of the variation of the slip angle on the contact patch length can be accounted for.

5.3.3.3 On-road Tire Model System Identification: Cornering and Longitudinal Stiffness

The tire cornering and longitudinal stiffness is computed from quasi-static tire testing data at low slip angles and low slip. The tire cornering stiffness is a parameter dependent on the tire design. For best handling, it is desirable that the peak stiffness occur at loads

greater than the rated load [1]. Normally, the estimation of the cornering stiffness is done using a polynomial fit [43]. However, recent work [35] has shown that the polynomial model may yield erroneous estimations at higher vertical wheel load (reduction in stiffness values). As such, it has been proposed that a bounded function be used to fit the tire cornering and longitudinal stiffnesses[35]. The bounded exponential function used to produce the fit is shown in Figure 5-27.

The longitudinal stiffness of a tire arise as a result of the combined interaction of the tread band around the circumferential direction of the tire and the elastic properties of the tread rubber elasticity [39]. Since experimental data has shown that the longitudinal stiffness can range anywhere from 5 to 15 times the tire vertical load [39], and is about on the same order of magnitude as the cornering stiffness when expressed in N/deg, we can use the same bounded function to model the longitudinal stiffness. This is because similar to the cornering stiffness, the longitudinal stiffness cannot grow indefinitely with increase in wheel load. As with any physical system, both stiffnesses will saturate at some point. Considering that the available data does not provide us with the longitudinal stiffness values at higher vertical loads due to testing machine limitations, the model is fitted with available data. From the results of the fit, the graphs from Figure 5-27 seem reasonable from observations of available stiffness data [3] and the values used to fit the equations are tabulated in Table 5-6.

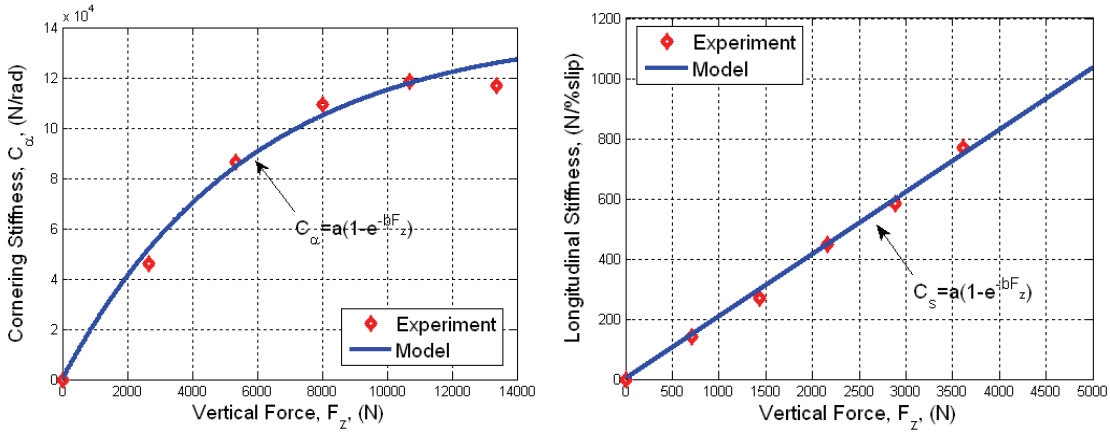

Figure 5-27. Cornering and Longitudinal Stiffness – Experiment and Model

In addition to the cornering and longitudinal stiffness, the tread belt elasticity in the lateral direction must be specified for the model. Due to lack of data for the tested tire, the tread belt elasticity is taken from a typical value of K_b=350253.67 [39] for a similar

sized radial tire. The coefficient of sensitivity for this tire, A_1, is set at the value of 0 because it cannot be measured without measuring the dynamic vertical contact stress.

Table 5-6. Parameters for longitudinal and cornering stiffness fit

	Parameters
$C_\alpha = a(1-e^{-bFz})$	$a = 139541$
	$b = 0.0001743$
$C_s = a(1-e^{-bFz})$	$a = 239800$
	$b = 8.6430 \times 10^{-7}$

The parameters shown in Table 5-6 are used in equations (3.28) and (3.29) in chapter 3.

5.3.3.4 On-road Tire Model System Identification: Camber Inclination Stiffness

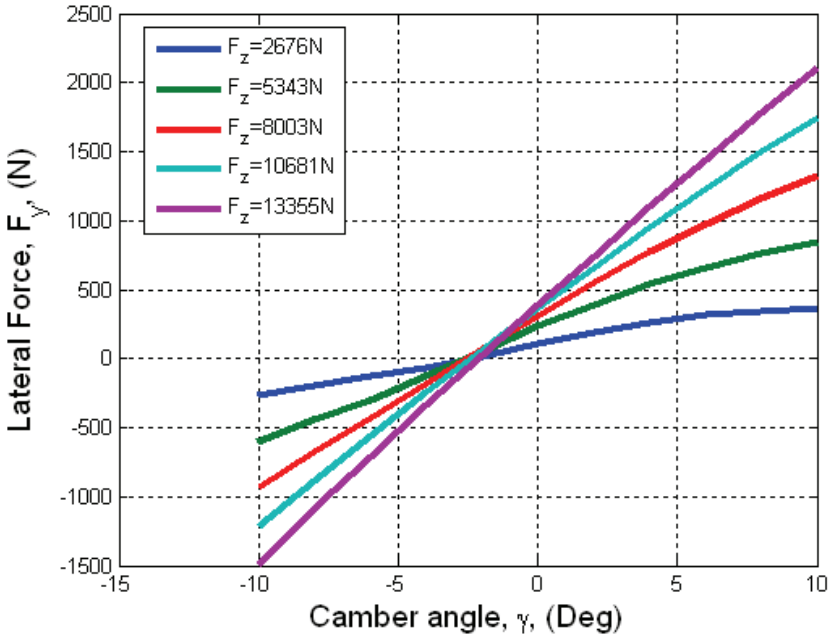

Figure 5-28. Available data for lateral force generation for increasing camber angle from NHTSA.

Figure 5-28 shows the available data for the lateral force generated from an input camber angle for different vertical forces. This force generation is caused by the camber inclination stiffness, which tends to saturate with increase in vertical tire force. As a rule of thumb, the camber inclination stiffness should be roughly 10% or less of the cornering

stiffness, when considered as force per degree [1] . A visual comparison of Figure 5-28 and Figure 5-27 verifies this characteristic in our model. It can also be noted that the slope of the inclination angle is positive, hence a positive change in inclination angle results in a positive increase in lateral force, which is shown in the fitted model. This inclination stiffness will also be one of the main contributors to the generation of the static overturning moment. The model chosen for the camber inclination stiffness is the same bounded exponential model used for the cornering and longitudinal stiffnesses. This is because the camber thrust will saturate after a certain camber inclination angle.The parameters regressed from fitting the equation to the experimental data is shown in Table 5-7.

Table 5-7. Parameters for the camber inclination stiffness model

	Parameters
$C_\gamma=a(1-e^{-bFz})$	$a = 70230$
	$b = 0.00001198$

The results of the fit are shown in Figure 5-28 and show good agreement with the data trend. The parameters shown in Table 5-7 are used in the calculation of the total lateral force in chapter 3.

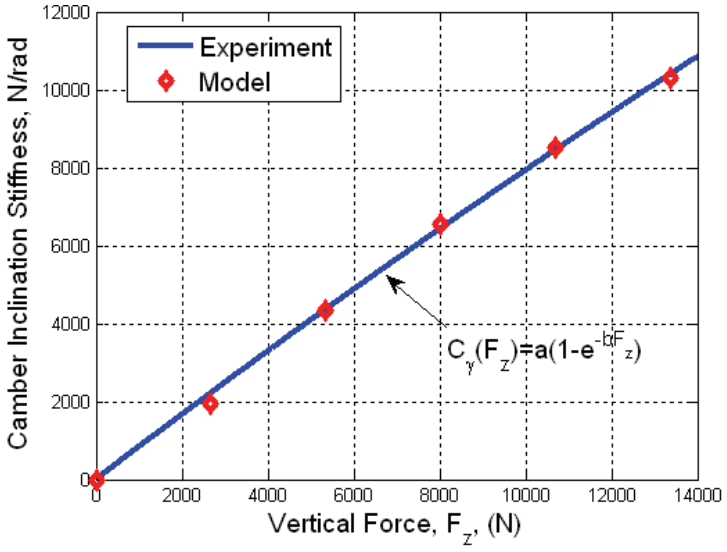

Figure 5-29. Experimental data and model for the camber stiffness

5.3.3.5 On-road Tire Model System Identification: Conicity and Plysteer Forces

As mentioned before, there are two factors that will induce a tire, when mounted on a vehicle, will pull to one side or the other. The two effects are conicity and plysteer, where conicity is indifferent to rolling direction and plysteer is not. When compared to data in [1], our model is close to the typical range of tire plysteer by the tire. Figure 5-30 shows the exponential bounded model, used for characterizing the tire pull behavior. When compared with the plysteer data of four different types of radial tires, we can see that the trend of change of the plysteer force with tire vertical load qualitatively matches our model.

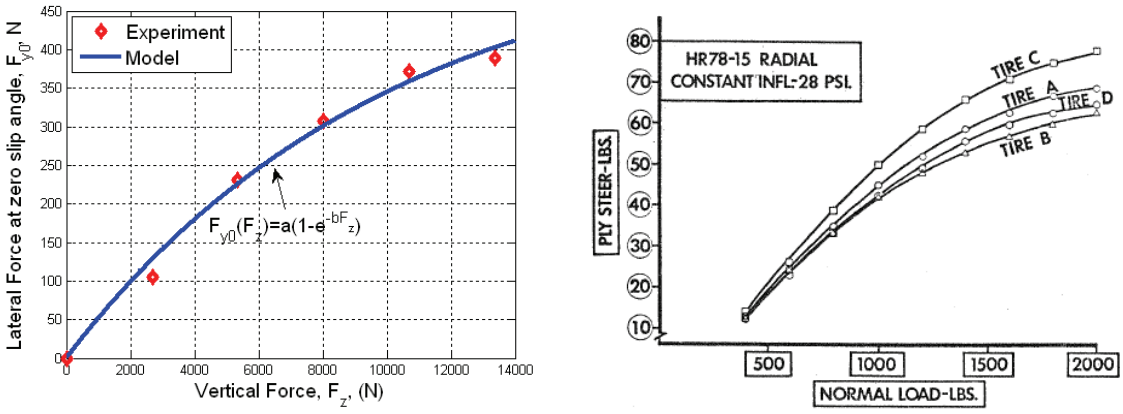

Figure 5-30. Model of the conicity and plysteer, compared with data from [39].

The lateral tire pull behavior can be included in the model as an offset in the lateral slip angle using equation (5.16), in the fashion shown in chapter 3.

$$\alpha_0 = -sign(V_y)\frac{F_{y0}}{C_\alpha} \tag{5.16}$$

The parameters regressed for the fit of lateral tire pull as a function of the vertical wheel load for the tire in this study is tabulated in Table 5-8.

Table 5-8. Parameters for tire pull identification

	Parameters
$F_{y0}=a(1-e^{-bFz})$	$a = 548.11$
	$b = 0.0001$

5.3.3.6 On-road Tire Model System Identification: Rolling Resistance Force

The rolling resistance forces from the test data that was used to determine the value of the foundation damping can also be used to empirically define the rolling resistance force. This approach can be used because analytical expressions may not be able to define the rolling resistance of a tested tire accurately.

The typical range of rolling resistance of a radial car tire is from 0.5% to 1.8% of the tire vertical force [39], up to 100 km/hr, which is within the range shown by our estimation in Figure 5-31. Note that the function used to characterize the rolling cresistance is a bounded function, and is applicable up to 200% of the GVW, which covers the realistic operating condition of the tire on a vehicle. Thus, we can assume that the model fit can be used to calculate the rolling resistance within reasonable range for vehicle simulations. Rolling resistance is an essential part of vehicle simulations because it determines the amount of resistance that the tires experience. With an accurate model resistance, we can be sure that the vehicle behavior within the region of zero slip is realistic for the specific tire, hence improving the prediction of braking distance.

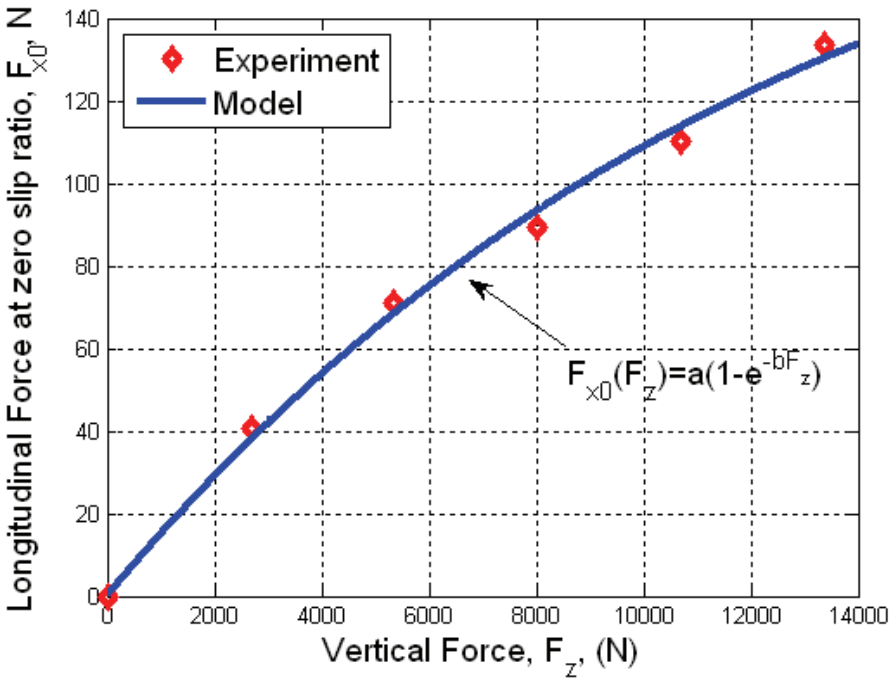

Figure 5-31. Bounded exponential model to include the load dependence in the rolling resistance, with the same data as used in Figure 5-12.

The parameters regressed for the fit of longitudinal tire rolling resistance force as a function of the vertical wheel load for the tire in this study is tabulated in Table 5-8

Table 5-9. Rolling resistance model parameters

	Parameters
$F_{x0}=a(1-e^{-bFz})$	$a = 202.86$
	$b = 0.000076$

The rolling resistance force can then be included in the model as an offset in the longitudinal slip using equation (5.17), in the fashion shown in chapter 3.

$$s_0 = -sign(V_x)\frac{F_{x0}}{C_s} \tag{5.17}$$

5.3.3.7 On-road Tire Model System Identification: Overturning Moment

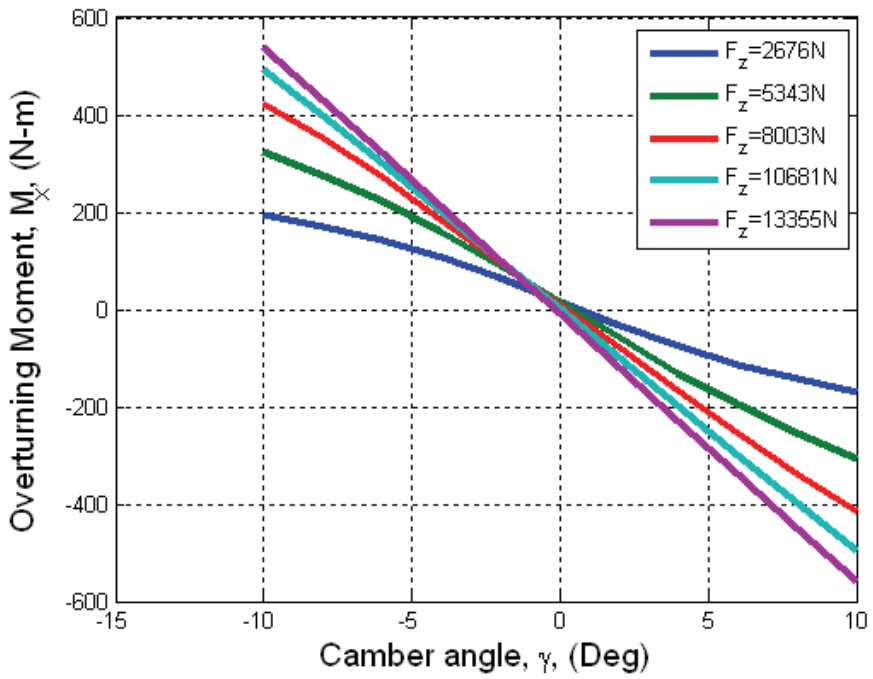

Figure 5-32. Available raw data for overturning moment vs. camber angle from NHTSA.

The raw data for the overturning moment vs. camber angle is shown in Figure 5-32. The moment generation is almost similar to the lateral force generation, hence a similar

model can be used to model the static change in the camber angle due to the loaded radius and the pneumatic scrub.

The fit for the model is shown in Figure 5-33, where the load dependence is accounted for in the parameter. As with the other parameters, fitting for a range from 20% to 200% of GVW is deemed to be sufficient for vehicle simulations. The inclusion of the camber inclination stiffness and the tire vertical force with an empirical scaling factor for the moment arm represents a development that is consistent with the observations of experimental data ([1],[51]). For the range of camber angle that we are interested in for on-road vehicles, this model seems to be valid.

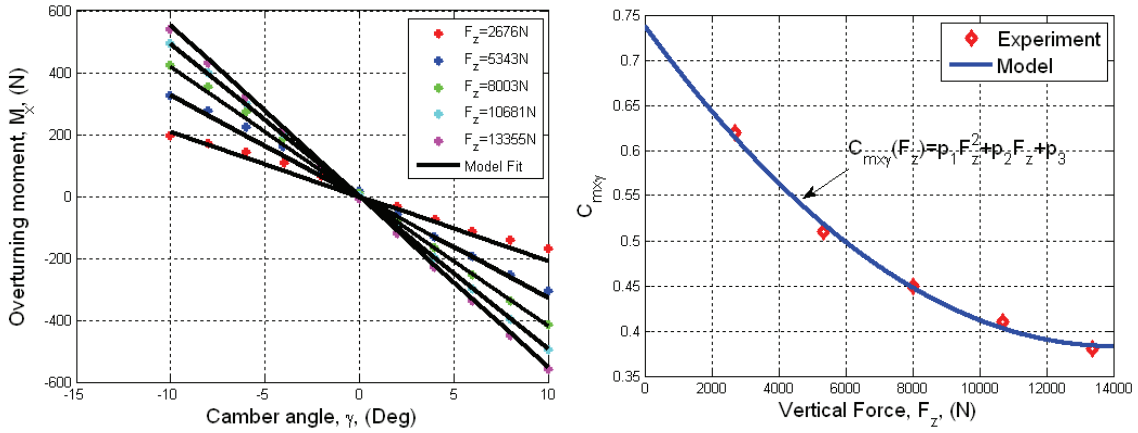

Figure 5-33. The static pneumatic scrub parameter with change in camber angle and a proposed empirical representation of the model based on the equation in Chapter 3.

However, the overturning moment does not just change with change in camber angle. The overturning moment also changes with slip angle as well. The relation between the slip angle and the overturning moment is highly complex and can be modeled with a second order polynomial fit. This ensures that the contribution of the slip angle is taken into account for the calculation of the overturning moment. The physical meaning of the relation is that it represents the moment arm acting between the lateral force and the generated overturning moment. The same relation is used in [35] and similar trends have been observed in tires of different sizes and applications.

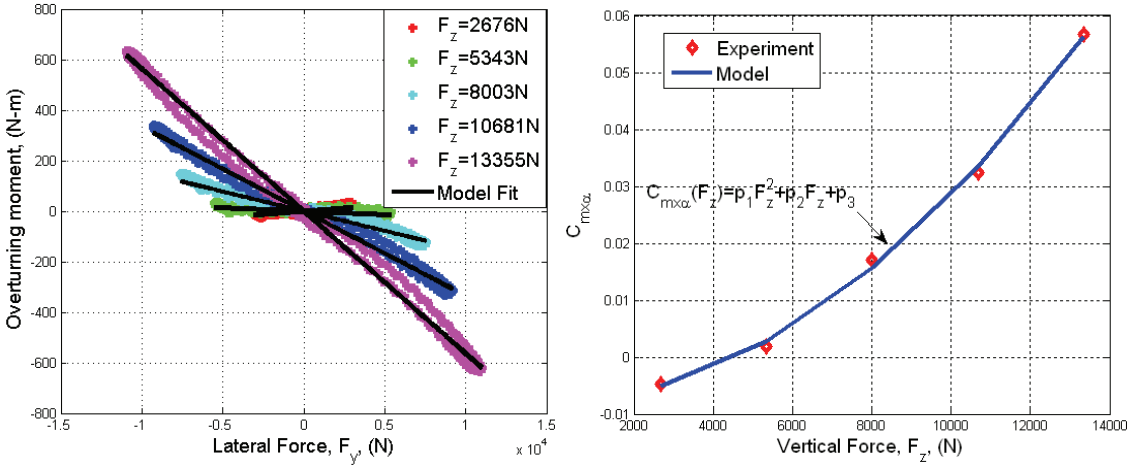

Figure 5-34. Overturning moment arm as a function of the tire vertical load.

The parameters regressed for the fit of the overturning moment empirical factors as a function of the vertical wheel load for the tire in this study is tabulated in Table 5-10. The parameters are derived in chapter 3 in section 3.6.

Table 5-10. Parameters for camber angle overturning moment identification

	Parameters
$C_{mx\gamma}= p_1F_z^2+ p_2 F_z+ p_3$	p_1 = 1.809e-009
	p_2 = -5.074e-005
	p_3 = 0.7387
$C_{mx\alpha}= p_1F_z^2+ p_2 F_z+ p_3$	p_1 = 3.544e-010
	p_2 = 6.726e-008
	p_3 = -0.007734

5.3.3.8 On-road Tire Model System Identification: Aligning Moment

In a moving vehicle, the aligning moment provides an important source of force feedback that informs the driver about the magnitude of tire steering forces at the wheels. In vehicle dynamics simulations where there is no human drivers, this moment is not of great importance, but when the model is used in driving simulators, the moments needs to be accurate to elicit the correct response from drivers. The formulation of the aligning moment in this dissertation is dependent on the pneumatic trail of the tire, and based on observations of empirical data for typical tires ([37]). For the sake of

simplicity, the pneumatic trail is formulated as an empirical function which has a maximum value and decays as the tire approaches the slip angle where sliding begins. Figure 5-35 shows the pneumatic trail and the aligning moment computed from the model presented. The aligning moment shows good agreement with experimental data.

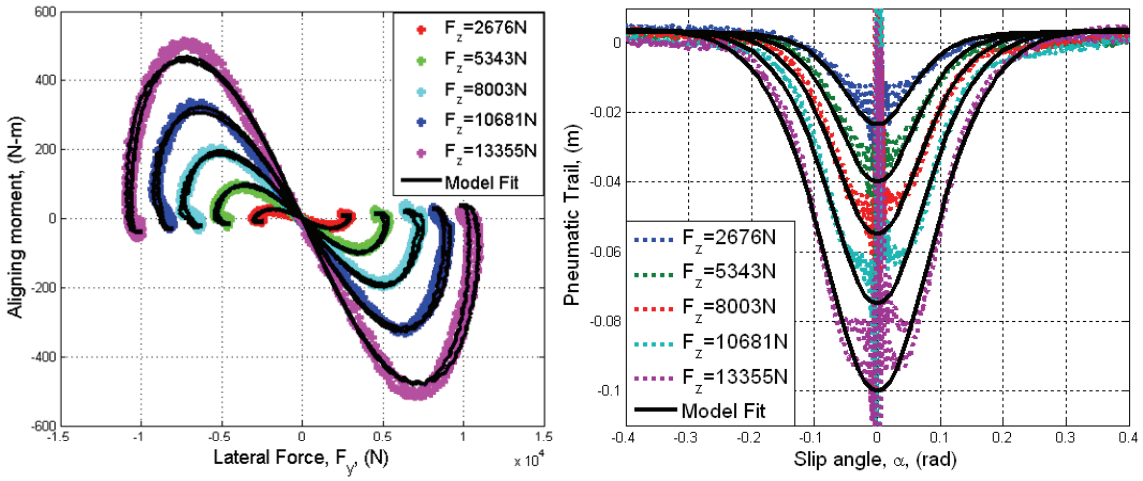

Figure 5-35. Aligning moment and pneumatic trail

Since the model is formulated in terms of 3 load dependent parameters, as shown in chapter 3, it is essential that the shape modification factors be formulated as a function of the vertical tire load as shown in Table 5-11. The choice of polynomials as the function for the shape factors are entirely based on observations of the trend in the data.

Table 5-11. Parameters for the aligning moment shape modification parameter identification

	Parameters
$C_{z1}= p_1 F_z^2 + p_2 F_z + p_3$	p_1 = 4.377e-015
	p_2 = 7.484e-008
	p_3 = 0.0028
$C_{z2}= p_1 F_z^2 + p_2 F_z + p_3$	p_1 = -2.309e-010
	p_2 = -3.304e-006
	p_3 = -0.01421
$C_{z3}= p_1 F_z^2 + p_2 F_z + p_3$	p_1 = 1.64e-008
	p_2 = -0.0009414
	p_3 = 21.08

Table 5-11 also shows the parameters regressed from the polynomial fits of the data. The results of the polynomial curvefit for the shape modification factors are shown in Figure 5-36.

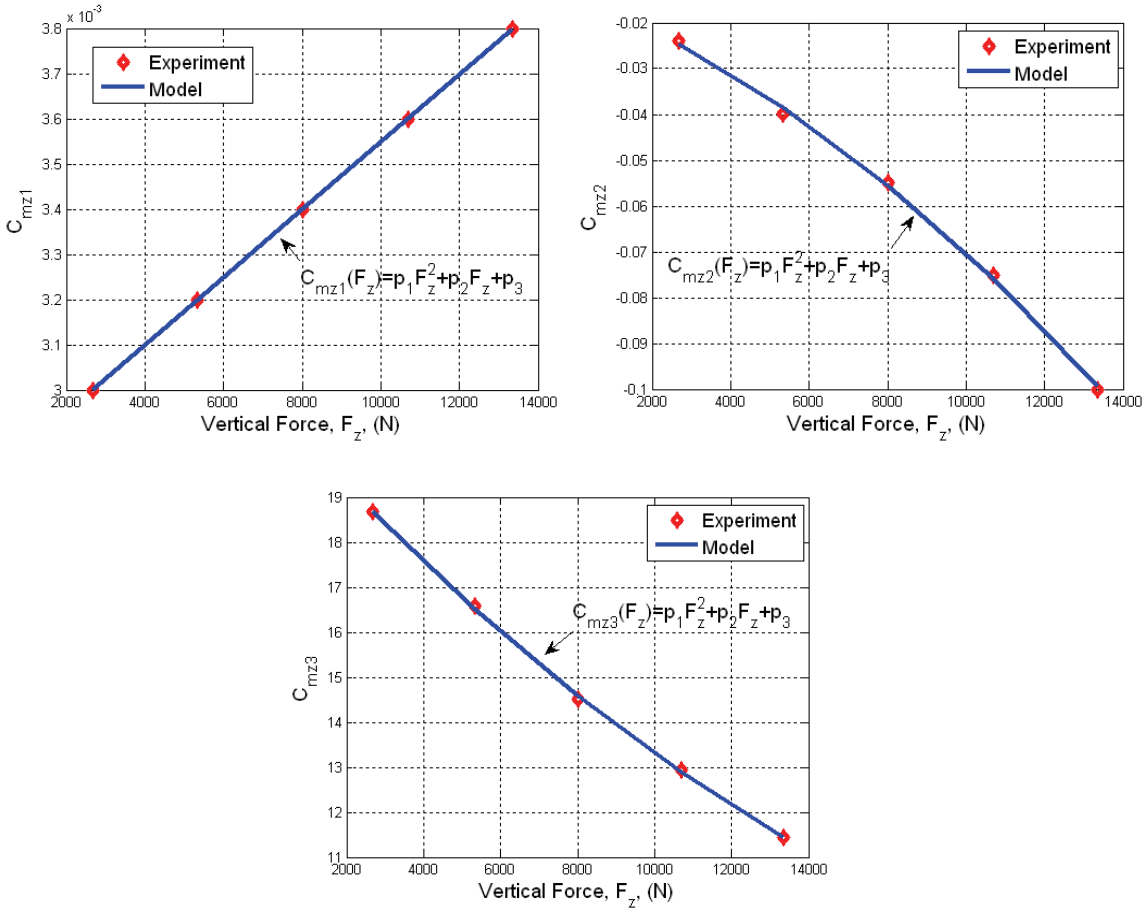

Figure 5-36. Fit for all the shape modification factors C_{mz1}, C_{mz2} and C_{mz3} as a function of load.

5.4 Off-road Tire Model: Recommended Experiment Design

The tests discussed in this section provide insight into the testing needed to characterize, refine, and validate the models developed for wheeled off-road locomotion. Without accurate soil, tire, or soil-tire parameters, the tire model developed in this study will not provide sufficient insight into the behavior of the actual tire in off-road conditions. Since the tractive limit is dependent on the failure conditions of the soil at the surface, it is of the utmost importance that the soil strength is determined adequately.

5.4.1 Soil Parameters: Recommended Experiments

The primary assumption of the off-road tire model is that a significant part of the tractive force is generated by the failure of the soil. Hence, it is essential that the soil strength of the terrain be accurately determined using the empirical methods. It has been suggested by Liston[63], Karafiath[20], and Bekker[7] that a ring-shaped shearing device can be used to characterize the soil strength parameters and the slip shear parameters for land locomotion purposes. However, there has been a disagreement on how the tests should be done, or whether the shearing ring method is applicable for determining the soil-wheel/soil-tire characteristics. The reason for which this apparatus is recommended in this study is because it can be designed such that it has a dual purpose. The apparatus can be used to:

1. Collect plate sinkage data for Reece's equation. This can be done by applying a vertical load at a constant rate until the soil reaches plastic equilibrium. However, a surcharge load has to be applied to the center of the annulus and the area outside of the shearing annulus (black colored part in Figure 5-37) to prevent the development of oblique failure planes [20]. In this setup, only a vertical load will be applied onto the plates.
2. Collect data for shear displacement constant, K. For both K_x and $K_{y,}$ the collection of the shear constant has to be done by attaching the pieces of the tread to the bottom of the annulus in the different directions. The shear deformation constants are highly dependent on the soil moisture, tread geometry, and the frictional contact between the soil and the rubber, which needs to be obtained experimentally. In this setup, a combined torsional and vertical load is applied on the annulus while the same vertical load is applied onto the center plate and the outer ring to provide a static surcharge load.

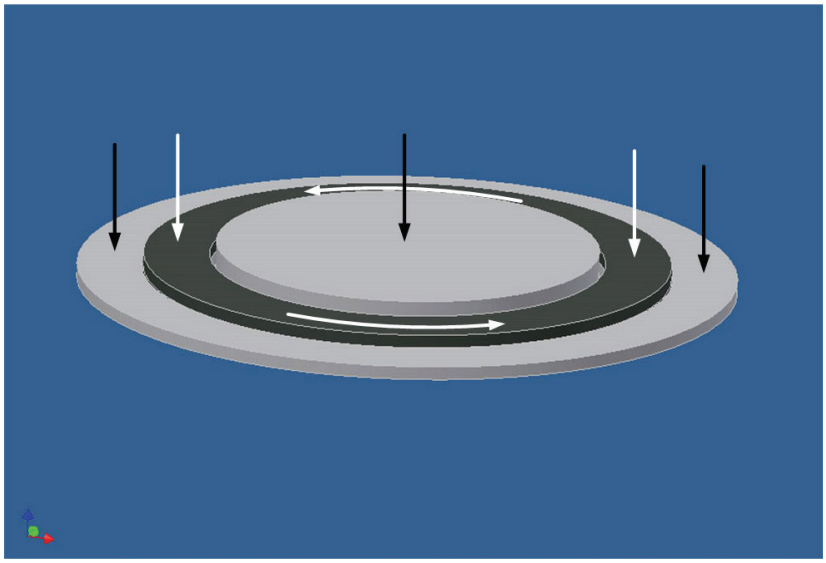

Figure 5-37. Shearing ring apparatus with the center annulus and the outer and inner surcharge plates. Black arrows shows the surcharge load and white arrows show the shearing annulus load.

The property of the shear ring test that makes it particularly attractive is that the area of soil loaded remains constant throughout the entire process of loading and hence requires no area correction of the data obtained. The processing of the data can then be done by utilizing the method proposed by Wong for analyzing data obtained using the bevameter [83]. For the soil weight, the unit soil weight can be measured relatively easily in a laboratory after collected using a drive cylinder. The methods for determining the unit weights are described in the ASTM standards D-1556 and D-2167.

The shear strength parameters can be determined using the triaxial test apparatus in Unconsolidated Undrained (UU) configuration, since the undrained conditions closely match field conditions, compared with the Consolidated Undrained (CU) or the Consolidated Drained (CD) configuration.

5.4.2 Tire Testing: Recommended Experiment on the Terramechanics Rig

Another test setup that can be used to refine and validate the off-road tire model is the collection of data from the terramechanics rig developed in the Advanced Vehicle Dynamics Laboratory at Virginia Tech. A terramechanics rig is an experimental setup that will enable researchers to apply known loading conditions to a tire under known

terrain conditions, hence enabling the researcher to gather data such as forces, moments, and states of the tire in the presence of known terrain data such as soil type, density, and moisture content. Such an experimental facility has been developed at Virginia Tech to support the research on developing and analyzing off-road tire models, which requires new tools in order to be able to generate off-road conditions in a controlled laboratory environment.

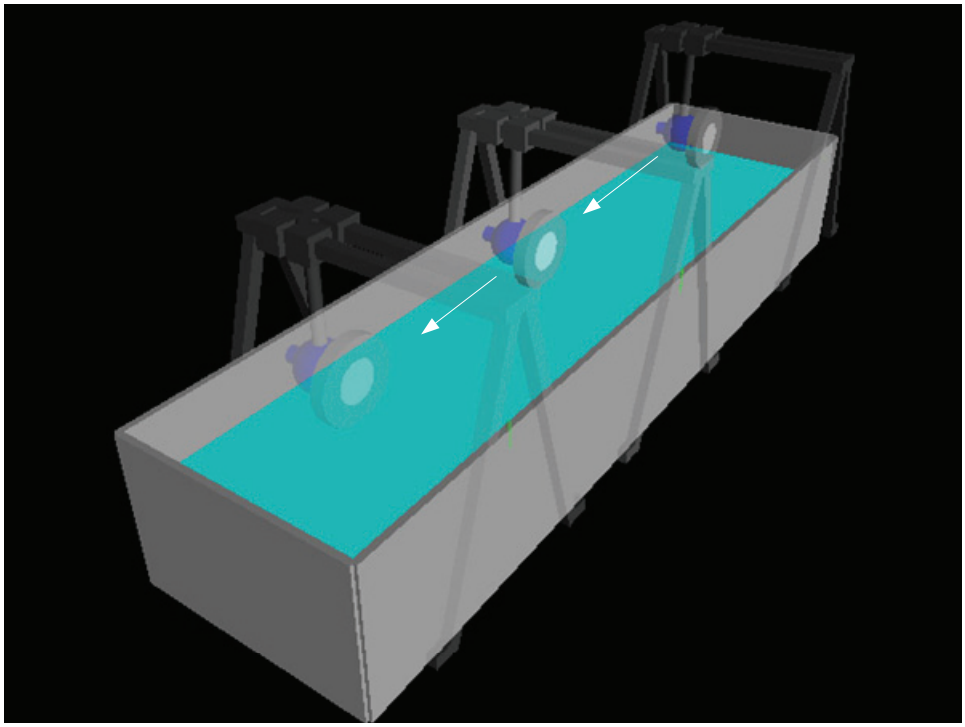

Figure 5-38. Longitudinal testing of the tire by moving it forward and varying the slip ratio.

Figure 5-38 shows a snapshot of a simulation of a virtual terramechanics rig for a test setup where the carriage of the rig is moved forward but the rotational velocity of the wheel is varied to achieve varying slip. The proposed steps for doing this test are:

1. Rotate the tire a certain distance to achieve proper tire-soil relaxation.
2. Start varying slip after certain distance, and measure longitudinal forces
3. Stop wheel carriage before it reaches the end.

The test can also be used to study different vertical wheel loads on different types of soil. The proposed steps for performing such tests are:

1. Start from 20% of GVW load on wheel
2. Run variable slip test
3. Increase load by 20%
4. Repeat step number 2 until 200% of GVW load has been tested
5. Stop carriage.

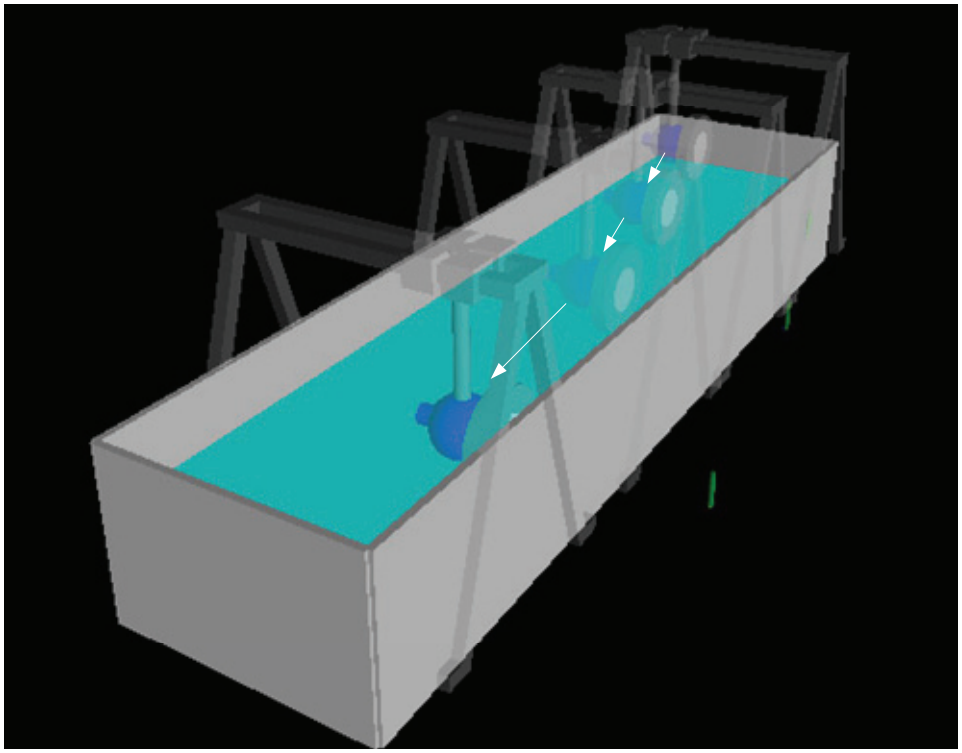

Figure 5-39. Lateral/combined testing of the tire by moving it forward and measuring the forces at different slip angles.

In addition to varying the longitudinal slip, the terramechanics rig also allows us to test the tires for lateral forces generated during cornering. This phase of the testing can be done by varying the longitudinal slip at different slip angles.

5.5 Summary

In this chapter, the method of acquiring of the parameters involved in tire modeling for chapter 3 has been presented. A recommended set of tire test for getting the data is also presented so that the tests can be standardized in the event that tire testing equipment is

available. Some initial results were presented in this chapter, as well, but a more comprehensive collection of results will be presented in chapter 6. In addition to that, the preliminary version of a set of recommended tests for acquiring data for the off-road tire model are presented. For future work, the parameters acquired from the recommended test in section 5.4, may be further studied to include their dependence on loading rates and varying vertical loads. The values of the parameters used for the off-road tire simulation in this dissertation are derived from readily available resources, pending the completion of the terramechanics rig in the Center for Vehicle Systems and Safety at Virginia Tech.

6. Results and Discussions

6.1 On-road Tire Model

The on-road tire model developed in this study has been parameterized with tire testing data from the National Highway Traffic Safety Administration (NHTSA) for the Continental Contitrac SUV P265/70R17 tire used in the 2003 Ford Expedition [82]. The parameters were derived from the system identification listed in the chapter 5 for the various parameters. Aside from the dynamic steering behavior of the tire, none of the parameters were acquired directly, but they were obtained using optimization methods and curvefits. All the plots shown in this chapter come from a model that has been parameterized from the physical tire testing data. Some of the information that was unavailable from the test data acquired from NHTSA was acquired using a tire of similar size and application. Given the fact that tire testing is a complex process, the comparison between the simplified tire model and the test data is to be taken from a more qualitative perspective rather than a quantitative point of view.

6.1.1 Pure Slip: Quasi-static Lateral Slip

Pure lateral slip corresponds to testing conditions where the tire is given a slip angle input with zero camber, and the slip ratio is held constant at zero. The reference tire load for this test case is set at 100% GVW load and is 6,672 N. The testing speed is 30 mph.

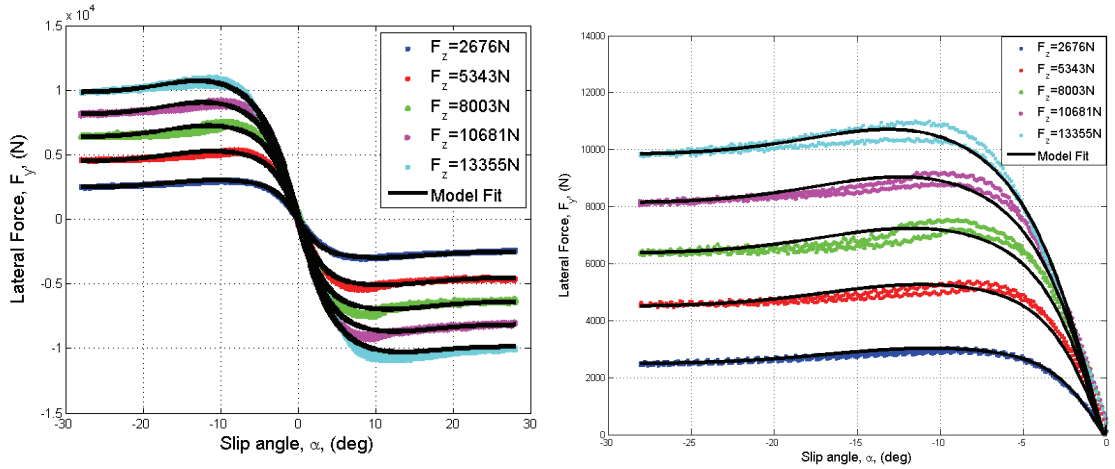

(a) **(b)**

Figure 6-1. (a) Lateral force vs. slip angle for the on-road tire model. (b) A zoomed-in look of the lateral force vs. slip angle plot.

With the lateral coefficients determined from the physical data in Chapter 5 and theoretical development in chapter 4, the physical model was parameterized and the output was calculated for 40%, 80%, 120%, 160%, and 200% of the reference load. For each load, the slip angle is varied from -28° to 28° at the rate of 3°/sec at the speed of 30mph. Figure 6-1 shows the output of the lateral force produced by the model for the five different test loads. The results of the model output seem to be in close agreement and bounded by the test data. However, there seems to be a peak in the lateral force that is underpredicted in the model for the higher vertical loads. The likely cause of this discrepancy could be the inaccuracy in the value of the carcass and belt stiffness. A higher value of carcass stiffness will generate a higher value of the adhesion force component.

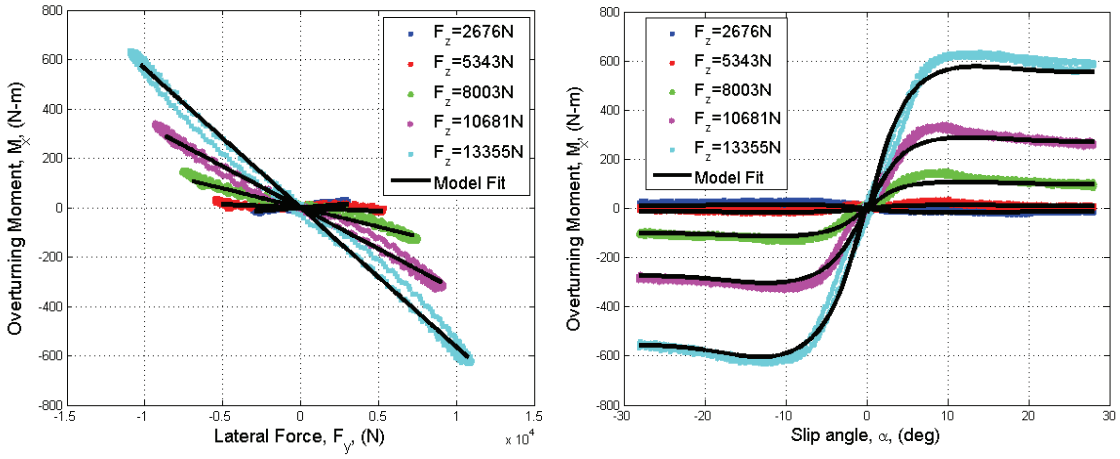

(a) **(b)**

Figure 6-2. (a) Overturning moment vs. lateral force (b) Overturning moment vs. slip angle

Figure 6-2 and Figure 6-3 show the results for the overturning moment and the aligning moment for the pure slip input, respectively. The overturning moment and the aligning moment also agree quite closely with the test data. Since the lateral forces agree closely with the test data, the formulation will therefore generate aligning moment behavior that closely resembles it.

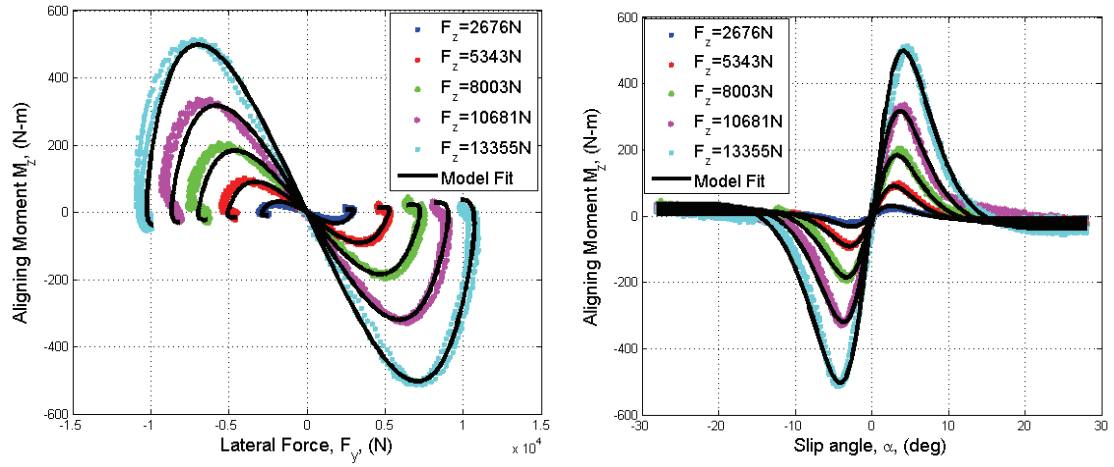

(a) **(b)**

Figure 6-3. (a) Aligning moment vs. lateral force (b) Aligning moment vs. slip angle

6.1.2 Pure Slip: Quasi- static Longitudinal Slip

Pure longitudinal slip test case corresponds to testing conditions where the tire is given a slip ratio input with zero camber, and the slip angle is held constant at zero. The reference tire load for this test case is set at 100% of the maximum allowable testing load of the machine, which is 4,155.5N.

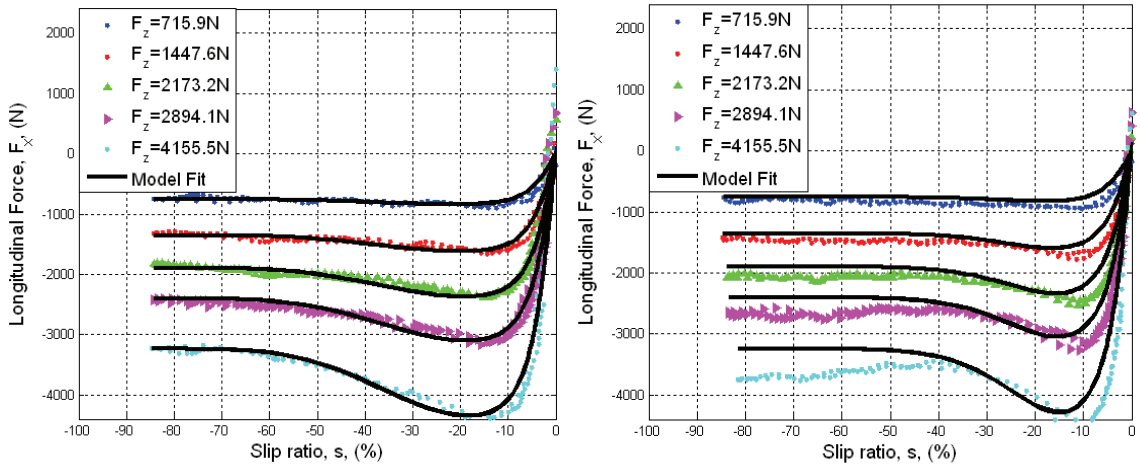

(a) **(b)**

Figure 6-4. Longitudinal force vs. slip ratio for a maximum vertical force of 4,155.5N (a) 30 mph (b) 60 mph

Figure 6-4 shows the longitudinal force for pure slip for a range of slip ratio during braking for 30 mph and 60 mph for various vertical loads. For this tire, it can be noticed

that the longitudinal decay in the friction coefficient happens at a higher rate as the speed is increased. Although there was also a slight but noticeable increase in the peak and sliding coefficient of friction in the data with increase in speed, the cause of this phenomenon is unknown and certainly warrant future in-depth studies. The speed dependence of the decay of the coefficients of friction seem to be typical for various types of tires from the observation of tire data [35]. For typical vehicle dynamics simulation studies, it is often a common acceptable practice to use the lower value of the coefficient of friction to err on the side of caution.

6.1.3 Quasi- static Combined Slip

The quasi-static combined steering lateral and longitudinal forces have been plot for quasi-static braking input in Figure 6-5. The tire load at which this test was done is 4,200 N for a slip ratio that is varied from -80% to 0% with a ramp time of 1.5 sec. The testing case consists of tests done at 30 mph and 60 mph, where most of the parameterization was done by using the data from the 30 mph test case. The only modification to the model for the 60 mph test case is that a velocity dependent term is used to scale the longitudinal coefficient of friction.

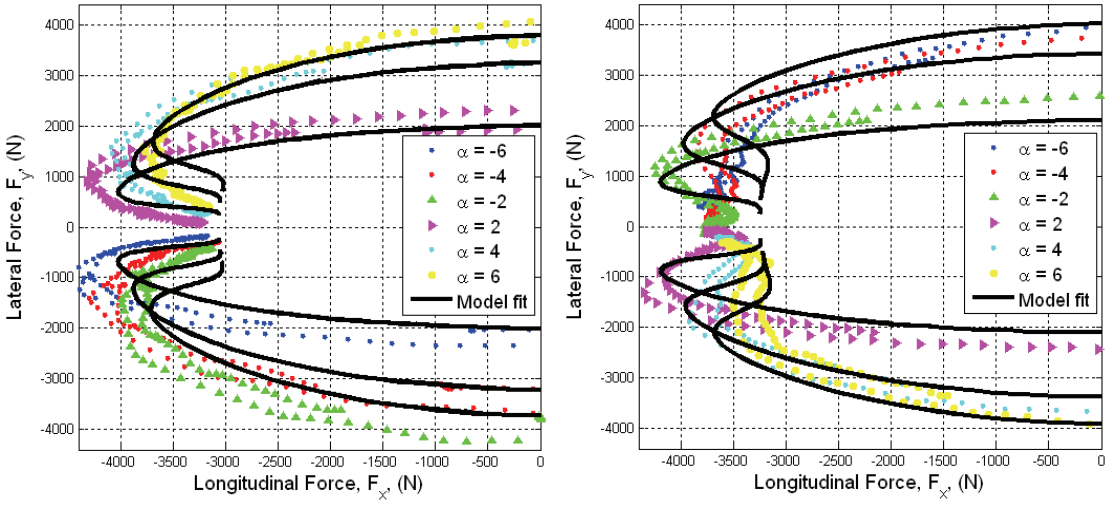

Figure 6-5. Lateral force vs. longitudinal force plots for a vertical force of 4,200 N during combined steering/driving (a) 30 mph (b) 60 mph

Figure 6-5 shows the lateral force vs. longitudinal force plots for a vertical force of 4,200 N during combined steering/driving at the two different speeds. The model shows a close and better bounded agreement with the test data when compared with the STI tire model [82], even at higher speeds.

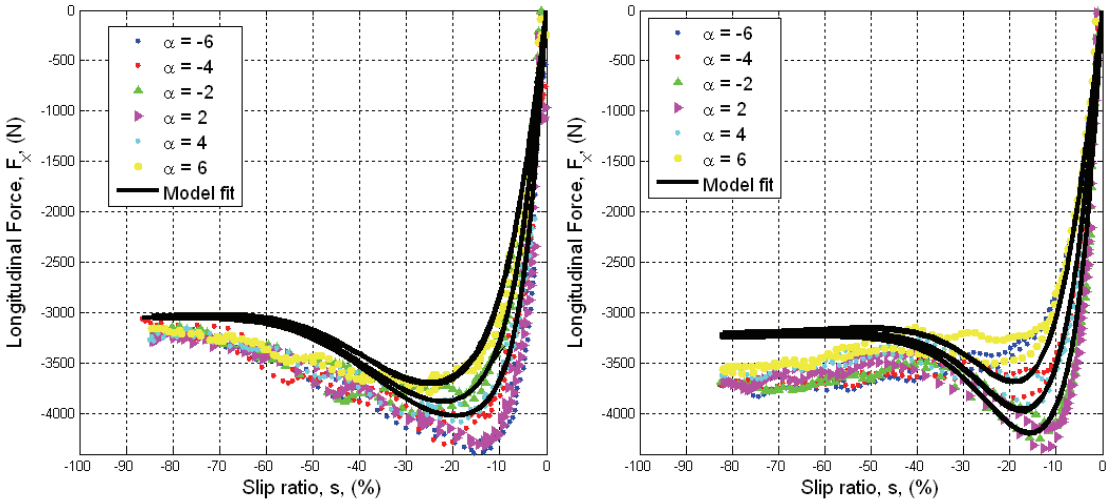

(a) **(b)**

Figure 6-6. Longitudinal force vs. slip ratio plots for a vertical force of 4200N during combined steering/driving (a) 30mph (b) 60mph

The longitudinal forces for the different lateral slip angles are shown in Figure 6-6. The difference in the rate of decay of the longitudinal force with slip is evident when Figure 6-6(a) and Figure 6-6(b) are compared.

The lateral force is plot vs. the slip ratio in Figure 6-7. For both speeds, it can be noted that the model has reasonable agreement up till about -20% slip. Beyond that, the trend of the behavior remains the same but the model tends to overpredict the forces. Within this region (-20% to -80% slip ratio), the contribution of the lateral force almost completely comes from the sliding component. Most likely a more detailed investigation into the dynamic sliding coefficient of friction for the tire can address that issue. Nonetheless, most anti-lock brake (ABS) algorithms and Electronic Stability Control algorithms are designed to operate around the peak coefficient of friction, which is less than -20% slip. Hence, the tire model developed here is still suitable for simulations of vehicles with ABS/ESP systems for on-road locomotion.

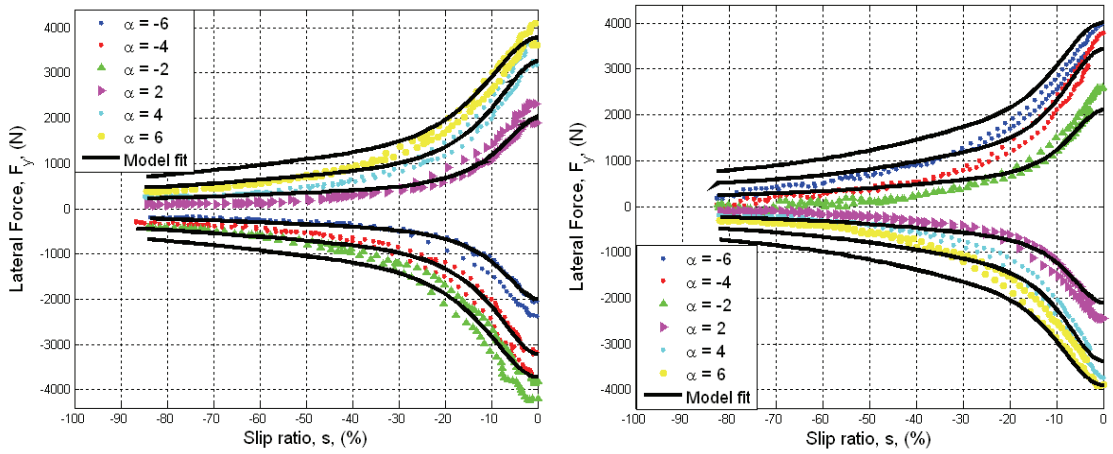

(a) **(b)**

Figure 6-7. Lateral force vs. slip ratio plots for a vertical force of 4200N during combined steering/driving (a) 30mph (b) 60mph

6.2 Off-road Tire Model

The off-road tire model has two modes of operation, the rigid wheel mode and the flexible tire mode. If the maximum pressure exerted at the interface exceeds the critical carcass stiffness pressure, the flexible tire model is used.

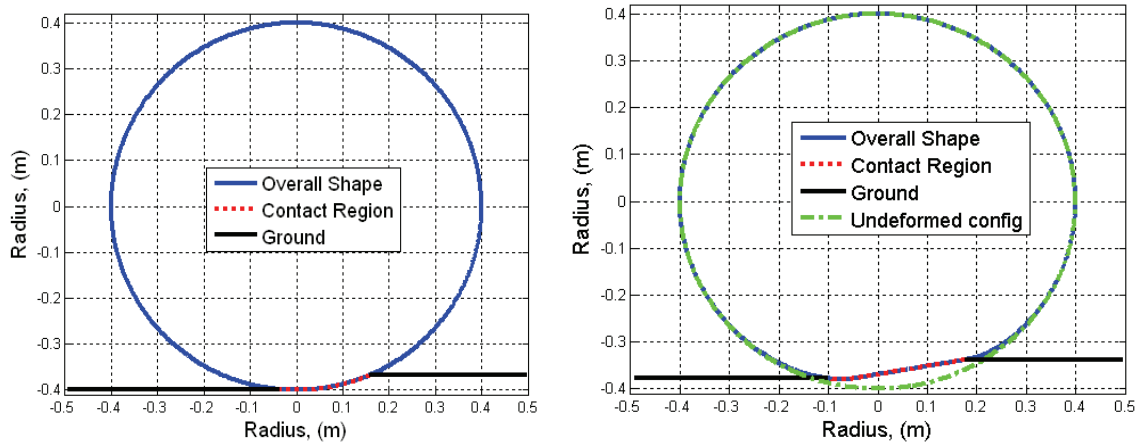

(a) (b)

Figure 6-8. The two operating modes of the off-road tire model developed in this dissertation. (a) Rigid wheel model (b) Flexible wheel model.

The reason why two different models are developed for this study is that on extremely deformable soils, the tire can be assimilated to a rigid wheel, hence saving

computational time for simulations. Using the rigid wheel model ensures that the computer does not have to solve for the shape of the flexible wheel and the value of the radius can be assumed to be constant. The shape of the stresses calculated using this model concurs with experimental data collected by various researchers ([66], [6], [20], [61]), as shown in Figure 6-9. Figure 6-9 illustrates the shape and stresses for the wheel/tire model on sand braking with a slip of -15% and being driven at 15% slip at zero slip angle. Although the sinkage and the contact length are approximately the same in the two cases, the stresses at the contact patch are very different.

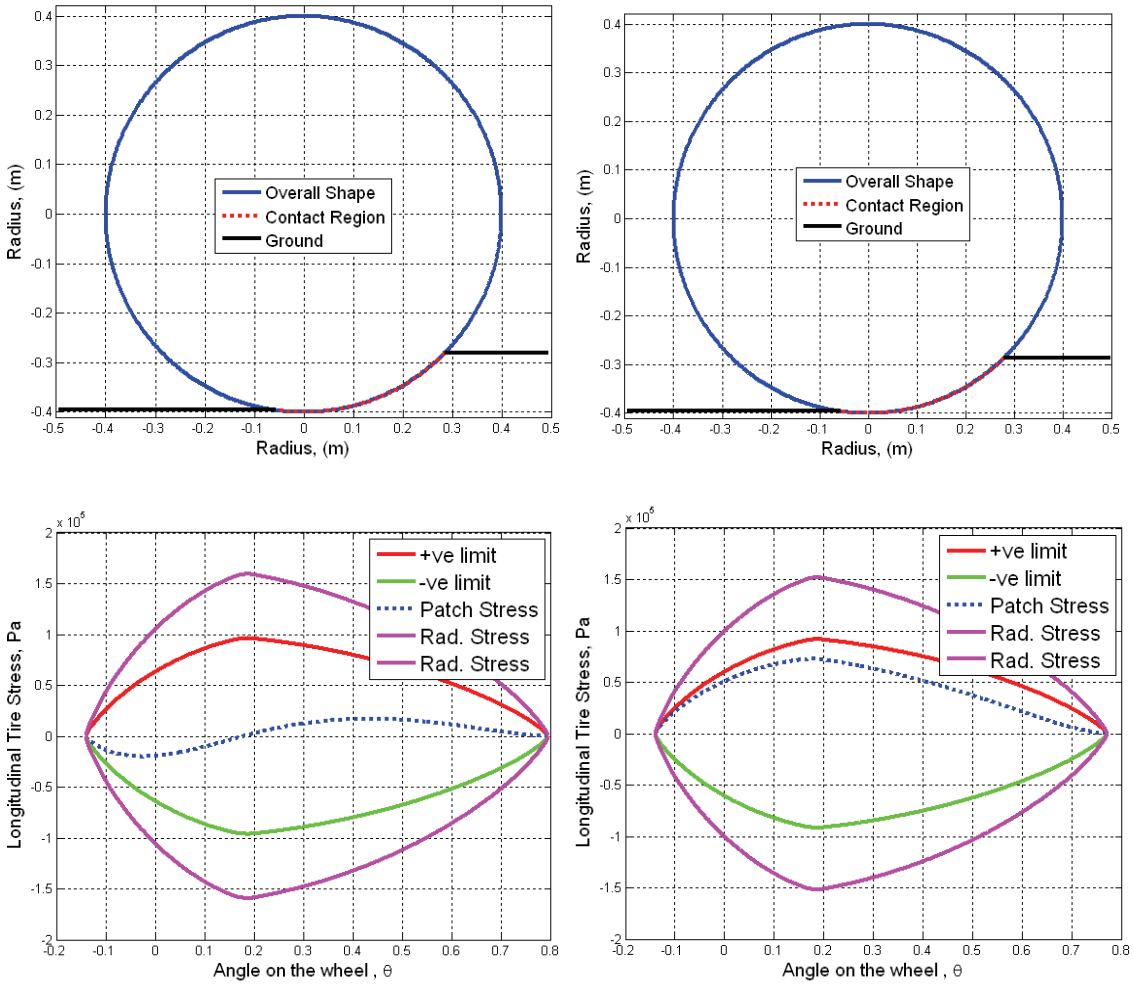

Figure 6-9. (a) Shape and tire longitudinal stress of a braking tire in sand at zero slip angle. (b) Shape and tire longitudinal stress of a driving tire in sand at zero slip angle.

The data used to parameterize the tire model was derived from various sources available for off-road traction calculations in the literature. The two types of soil for which data was readily available are sandy terrain and moist Yolo loam. The two soils are selected because sand is an example of a frictional soil with weak cohesive properties and Yolo loam is a firm soil composed of sand, silt, and clay which has a stronger cohesive behavior than sand. The difference between the two types of soil provides insight into the capabilities of the model for purely frictional soils and frictional cohesive soils. The shear displacement constants K_x and K_y were set to be the same value for both the lateral direction and the longitudinal direction due to the fact that the parameters where acquired under the same conditions as the other soil parameters for rubberized surfaces. The soil parameters used to compute the tire forces are presened in Table 6-1.

Table 6-1. Soil parameters used to compute the tire forces (Regressed from data from [83] and [18]).

Soil	k_1	k_2	n	C, **(Pa)**	ϕ, **(°)**	K_x / K_y, **(m)**	γ_s, **(kg/m^3)**
Sandy terrain	2	17658.75	0.77	130	31.1	0.038	1600
Yolo loam terrain	3.25	4600	0.99	22670	22	0.015	1258

6.2.1 Pure Slip: Quasi-static Lateral Slip

Similar to the on-road tire model, in the off-road case we had to study the behavior of the model for pure slip to understand whether the behavior follows physical understanding of expected behavior of a wheel/tire on off-road terrain. For this section, the quasi-static pure lateral slip input was varied from -30 degrees to 30 degrees with an increment of 1 degree, while the lateral forces were calculated. The lateral forces were plot for sandy terrain in Figure 6-10 and for Yolo loam terrain in Figure 6-11. Since the approach used in this dissertation for the wheel/tire model has not been used in any other off-road tire model, the discussion of the results presented in this section will be more

qualitative in nature, with the results being compared against empirical evidence collected by various researchers.

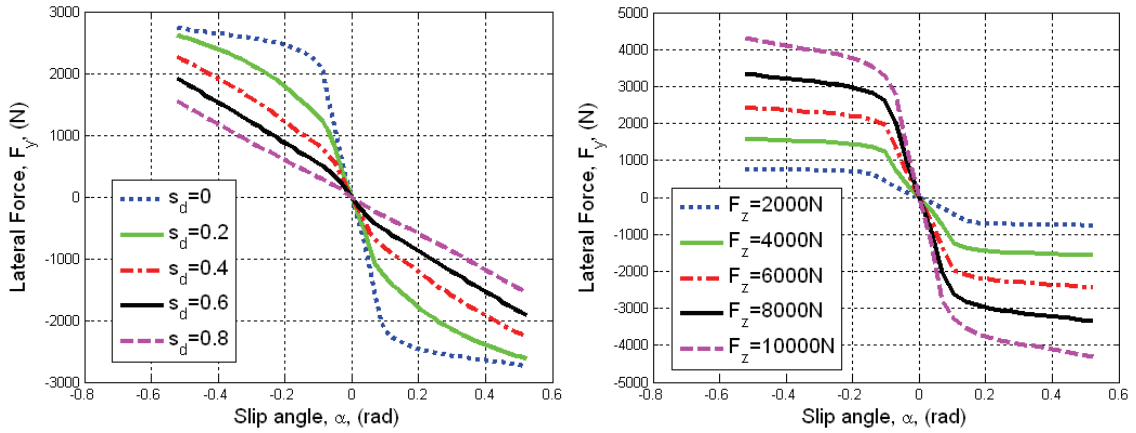

(a) (b)

Figure 6-10. Lateral forces for sandy terrain. (a). Lateral force vs. slip angle for different slip ratio with a reference load of 6672N (b). Lateral force vs. slip angle for different vertical loads at zero slip ratio.

For sandy terrain, the tire limit pressure was never exceeded; hence the tire remained a rigid wheel for all tire vertical loads from 2,000 N to 10,000 N. However, sinkage was calculated for the sandy terrain to be about 12 cm, which is comparable to sinkage data for tire of approximately the same size tested at CRREL [84]. As expected, in Figure 6-10 (a), there is a reduction in tire lateral forces with increase in longitudinal slip. For sandy terrain, almost all of the lateral force comes from the shear forces at the interface. The bulldozing force component does not contribute much to the total lateral force component because of the lack of cohesion in the soil mass even though the sinkage experienced by the tire on sandy terrain is larger than the sinkage in Yolo loam by a factor of 10. However, with increase in the vertical load, as shown in Figure 6-10 (b), there is an increase in sinkage and the contribution of the bulldozing force to the total force becomes larger, leading to an increase in the rate of lateral force increase at higher slip angles. For the Yolo loam terrain, at low slip angles, the lateral forces for varied longitudinal slip, as seen in Figure 6-11 (a), seem to have the same trend as the lateral forces on sandy terrain.

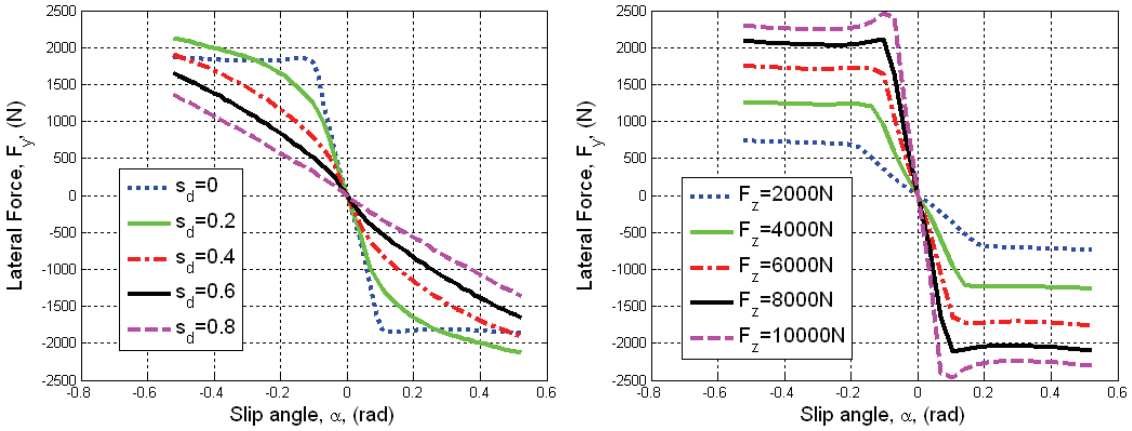

(a) (b)

Figure 6-11. Lateral forces for Yolo loam terrain. (a). Lateral force vs. slip angle for different slip ratio with a reference load of 6,672 N (b). Lateral force vs. slip angle for different vertical loads at zero slip ratio.

However, since the cohesion is higher in Yolo loam compared to sandy terrain, the rate of buildup of bulldozing force is higher and hence the lateral forces for non-zero slip ratio at higher slip angles will exceed the lateral forces at zero slip ratio. When the wheel vertical loads are increased, the tire remained a rigid wheel up to a wheel load of 6,000 N. At the wheel load of 8,000 N and 10,000 N, the tire is modeled as a flexible tire. There seems to be a distinctive peak as the slip angle is increased for Figure 6-11(b) at zero slip ratio. Past the slip angle where this peak occurs, the lateral forces will decay to a constant value. It is presumed that, for a soil this firm, sinkage will not increase much even with increase in vertical wheel load, hence reducing the influence of the lateral bulldozing force on the total lateral force, which results in the peak and the decay of the lateral forces at 8,000 N and 10,000 N as shown in Figure 6-11 (b).

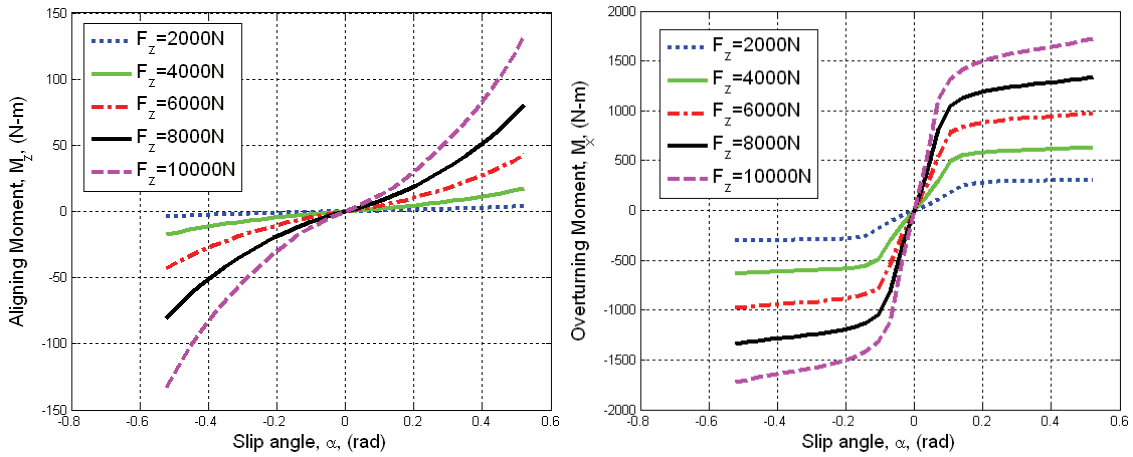

(a) (b)

Figure 6-12. Moments for sandy terrain. (a). Aligning moment vs. slip angle for different vertical loads at zero slip ratio. (b). Overturning moment vs. slip angle for different vertical loads at zero slip ratio.

The aligning moment and the overturning moment for the lateral forces shown in Figure 6-10 are illustrated in Figure 6-12. It can be noticed that the aligning moment in Figure 6-12 (a) for the off-road tire does not necessarily drop down to zero and become negative with increase in slip angle as it has been shown to happen for the on-road tire model in Figure 6-3 (b). The increase in sinkage causes the increases of the component of the aligning moment due to the bulldozing force for sandy terrain. The same argument can be made for the overturning moment shown in Figure 6-12 (b). The overturning moment has the same general shape as the overturning moment for the on-road tire model shown in Figure 6-2 (b).

For the wheel/tire on Yolo loam, the moments shown in Figure 6-13 are slightly different than those shown in Figure 6-12. The aligning moment, shown in Figure 6-13 (a) is similar in shape to Figure 6-12 (a) for the load range of 2,000 N – 6,000 N. However, once the tire snaps into the flexible tire mode (vertical load of 8,000 N and 10,000 N) the moments are calculated with the flexible tire formulation, yielding to a behavior similar to the on-road tire aligning moment shown in Figure 6-3 (a) (with the exception of higher slip angles) the moment decays to the values for the rigid wheel.

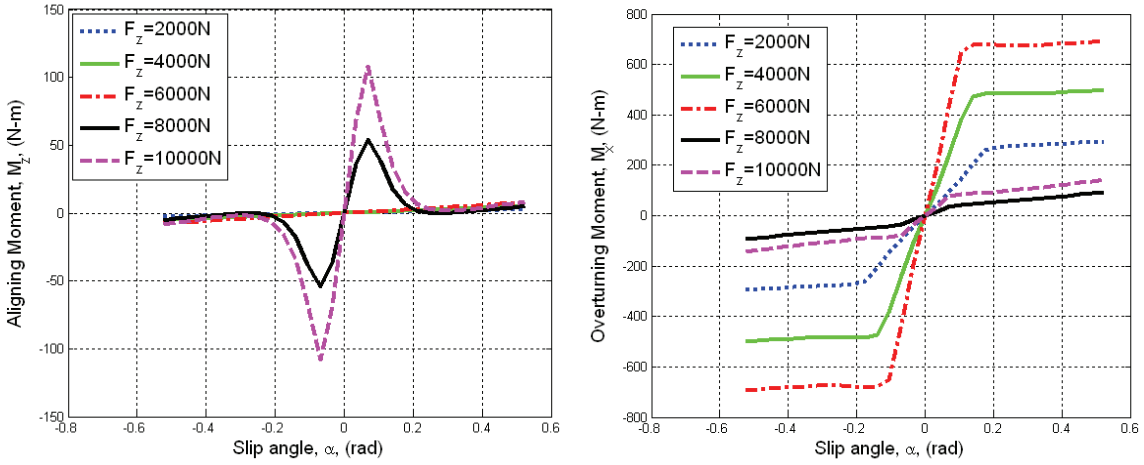

(a) (b)

Figure 6-13. Moments for Yolo loam terrain. (a). Aligning moment vs. slip angle for different vertical loads at zero slip ratio. (b). Overturning moment vs. slip angle for different vertical loads at zero slip ratio.

The incorporation of the bulldozing force in the model is the cause of this phenomenon. Since the sinkage for this soil is not deep, the bulldozing force contribution to the total moment is small, compared to the contribution by the shear forces at the patch. The overturning moment, depicted in Figure 6-13 (b), shows the same trend of behavior as in Figure 6-12 (b), with the exception that the moments for the flexible tire are much lower than the moments computed in the rigid wheel cases. The cause of this phenomenon is attributed to the reduced radius because of the deflection, reduced sinkage and the deflection of the carcass reducing the lateral bulldozing component of the total lateral force.

6.2.2 Pure Slip: Quasi-static Longitudinal Slip

The longitudinal tractive force of a tire is the most important part of the tire model. The modeling of the longitudinal force in this tire model accounts for the effect of a non-zero slip angle on the total longitudinal force. For this section of our study, the slip was varied from -80% to 80% with increments of 1%, while the longitudinal forces were calculated. In Figure 6-14 (a), the increase in the slip angle causes a reduction in the total longitudinal forces, as predicted by the experiments done by the US Army

Waterways Experimentation Station (WES) in Figure 6-16. Refering to Figure 6-14 (a), at 0.1% slip, there is a slight drop in the rate of increase of the force for the case of a 20 degree slip angle. This decrease is attributed to the fact that the point of maximum pressure moves to the front of the tire with increase in forward slip. After the radial stress shift to that point and reaches the maximum value it can attain, the shear forces start building up again and continue to increase until it saturates. Note that for both Figure 6-14 (a) and Figure 6-14 (b), the forces for braking are much larger than the forces for driving because of the sinkage. At the point where the tire's longitudinal force saturates, the wheel cannot move forward anymore without any external force input at the axle because the wheel is just slipping on the sand.

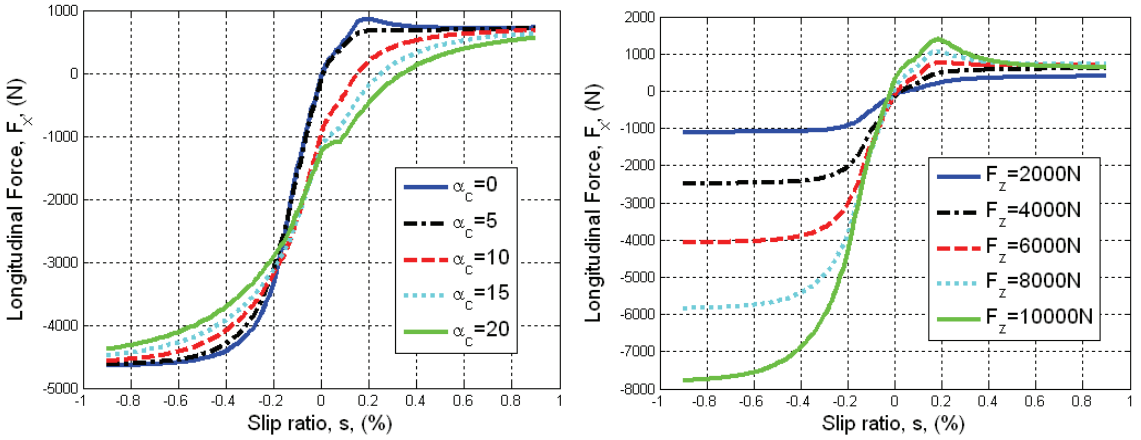

(a) (b)

Figure 6-14. Longitudinal forces for sandy terrain. (a). Longitudinal force vs. slip ratio for different slip angle with a reference load of 6,672 N (b). Longitudinal force vs. slip ratio for different vertical loads at zero slip angle.

This behavior has been shown to be consistent with experimental data collected by Shmulevich [85] and Muro [6]. When the tire is being driven forward, slip sinkage and compaction resistance cause the longitudinal force at positive slip to saturate at one point, particularly for deep sinkage situations. As the tire is braked, it plows into the ground, and additional stopping force is gained by adding compaction resistance. This observation is evident in real-life driving situations, where it is recommended that drivers turn off their Anti-lock Brake System (ABS) when transversing on off-road terrain.

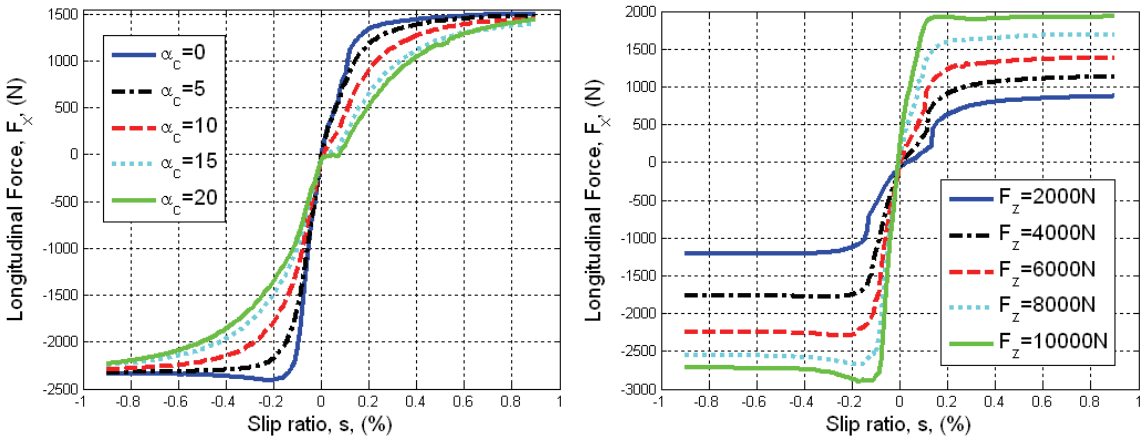

(a) (b)

Figure 6-15. Longitudinal forces for Yolo loam terrain. (a). Longitudinal force vs. slip ratio for different slip angle with a reference load of 6,672 N (b). Longitudinal force vs. slip ratio for different vertical loads at zero slip angle.

Figure 6-15 (a) shows the same trend for decrease in force for the tire on Yolo loam with increase in slip angle. However, the longitudinal forces calculated seem to be more symmetrical than in Figure 6-14 (a), although the same cusp in the longitudinal force happens at ~0.1% slip. Figure 6-15 (b) shows the longitudinal forces corresponding to the different vertical loads. Compared to Figure 6-14 (b), Figure 6-15 (b) shows closer equivalence for longitudinal forces across positive and negative slip. The cause of this difference in behavior between Figure 6-14 and Figure 6-15 is the fact that there is less sinkage in Yolo loam compared to sand. The reduction of sinkage in Yolo loam means that compaction resistance is reduced in its role as a limiting factor in traction generation compared with sandy terrain. In this sense, the tire will behave more like an on-road tire model on firmer terrain, except for the fact that the traction limit is defined by the soil failure under the tire-soil interface. The traction limit curves have significantly less area than the on-road tire model in yolo loam, but retain the same conical shape (relatively) as the on-road tire model, as evident in the following subsection of this dissertation.

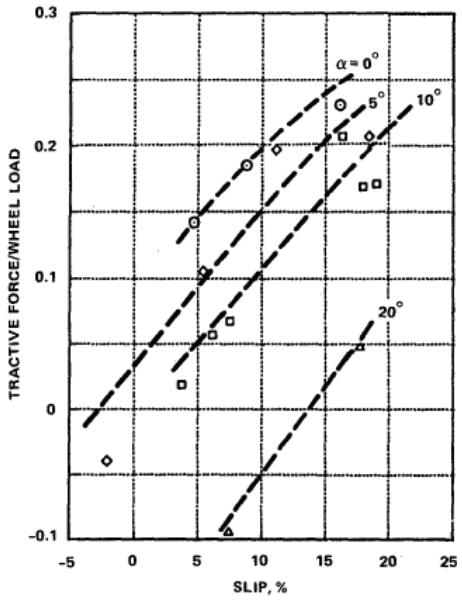

Figure 6-16. Tire data collected by the US Army WES for longitudinal force vs. slip for different slip angles on sand (reproduced from DOD WES report M-76-9 [77], under the FOIA)

In addition to having the forces matching with the intuition of everyday driving, the shear stresses calculated by the model can be clearly seen to show correlation with the measured experimental data shown by Oida [86], Krick [87] and Onafeko [66] in Figure 6-9 for sandy terrain. The differences in the longitudinal slip behavior between the model running on sandy terrain and on Yolo loam can be attributed to tire deflection and the sinkage, shown in Figure 6-17.

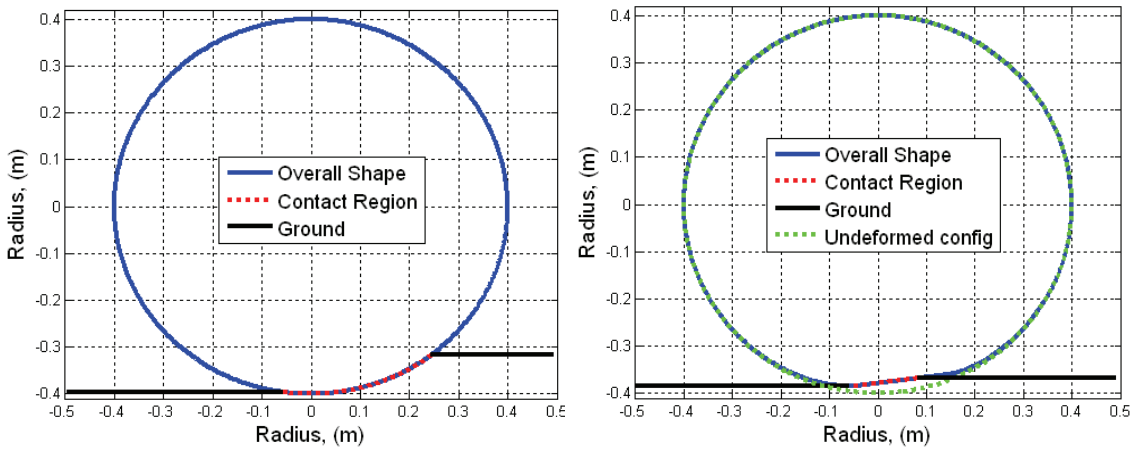

(a) (b)

Figure 6-17. Tire shapes and sinkage at a vertical wheel load of 6672N, 40% slip and zero slip angle. (a) Sandy terrain (rigid wheel) (b) Yolo loam terrain (flexible tire).

6.2.3 Quasi- static Combined Slip

The model was also evaluated for quasi-static combined slip operation by sweeping the longitudinal slip from -80% to 80% for different slip angles, just to determine the envelope of traction and determine the effects of sinkage on combined slip forces.

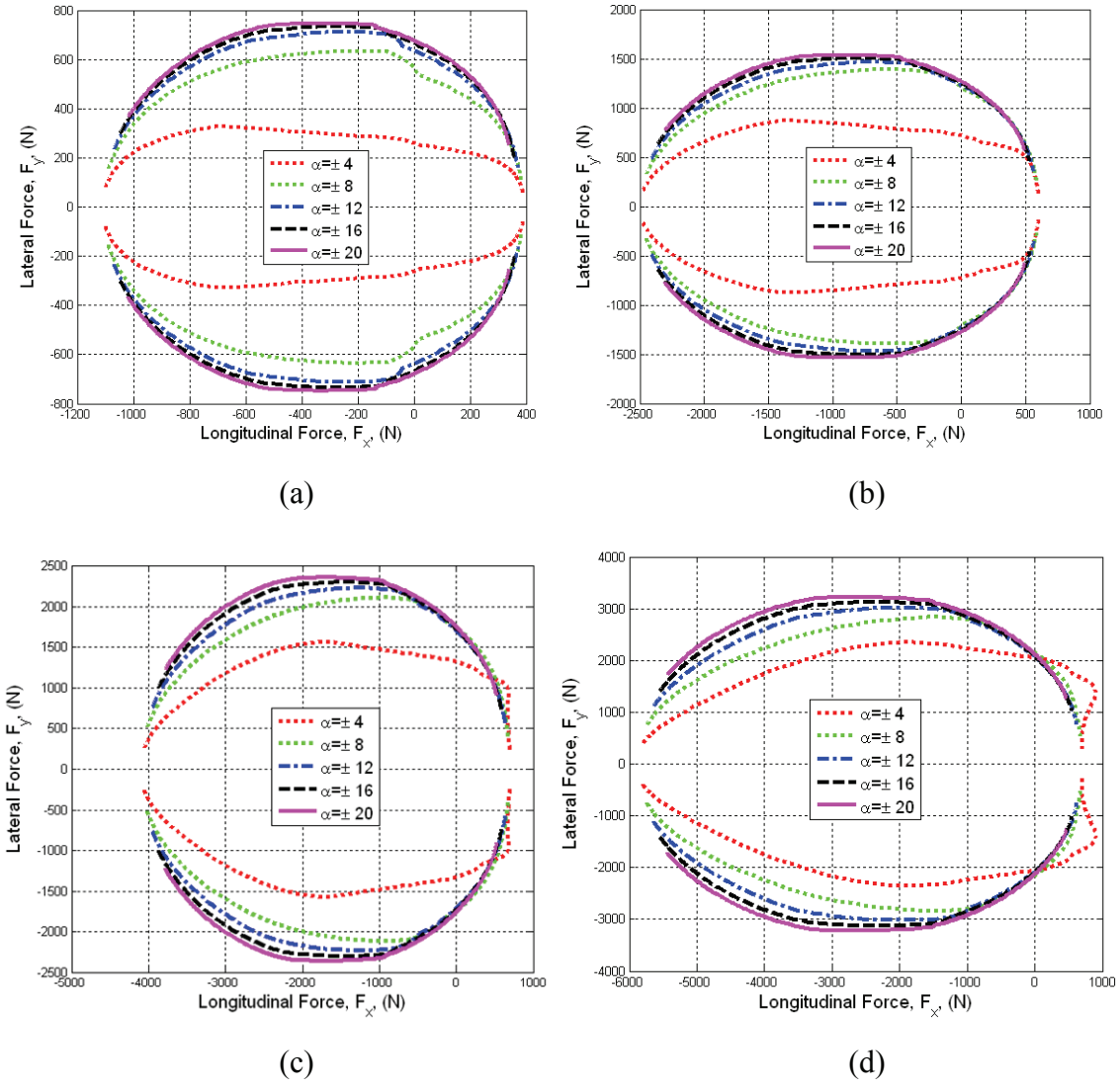

Figure 6-18. Combined slip forces for sandy terrain. (a) Forces for a vertical tire load of 2,000 N. (b) Forces for a vertical tire load of 4,000 N. (c) Forces for a vertical tire load of 6,000 N. (d) Forces for a vertical tire load of 8,000 N.

Figure 6-18 shows the combined slip behavior for different wheel loads for sandy terrain. At a wheel load of 2,000 N, the lateral and longitudinal forces tend to have a traction envelope that resembles the envelope for on-road tire models. As the wheel load is increased, the maximum sinkage is increased, as shown in Figure 6-19, causing compaction and bulldozing contribution to the forces to have more significance.

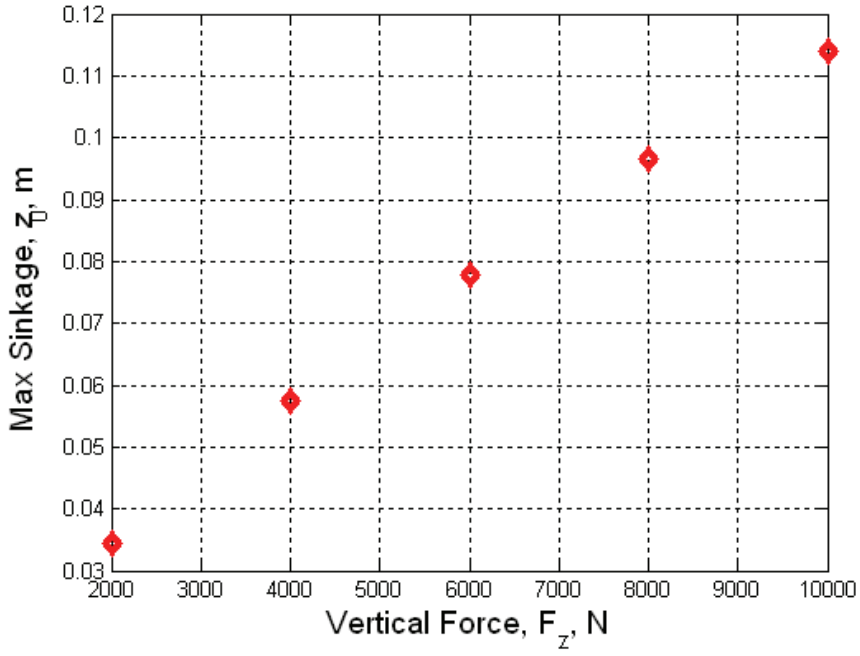

Figure 6-19. Calculated maximum sinkage as a function of the vertical load for the wheel on sand for a longitudinal slip of 10%.

When sinkage becomes an important contributor in the total lateral and longitudinal forces, the longitudinal forces for high positive slip ratio at low slip angles may exceed the envelope, as shown in Figure 6-18 (c) and (d). However, once the slip angle is increased, the total shear force generated is reduced in either direction and falls back into the general envelope. The only force components that are projected into the Mohr-Coulomb failure criteria envelope are the forces from the shear stresses acting on the wheel-soil interface. The bulldozing and compaction resistance forces are not bounded, since there is no experimental data collected extensively to determine the limits of those forces, but are determined as a function of sinkage, hence with increased sinkage, the effect of those forces are taken into account.

The combined slip forces for Yolo loam are shown in Figure 6-20. The first thing that can be noticed about this plot is the fact that the envelope appears to be more symmetric about the y-axis, compared with Figure 6-18. All the plots shown in Figure 6-20 (a), (b), (c) and (d) are approximately the same shape, except for the fact that there is a cusp right about where the longitudinal slip is zero. We stipulate that the reason for which this phenomenon happens is that at low slip the lateral force grows faster than the longitudinal force due to the higher cohesion in the soil.

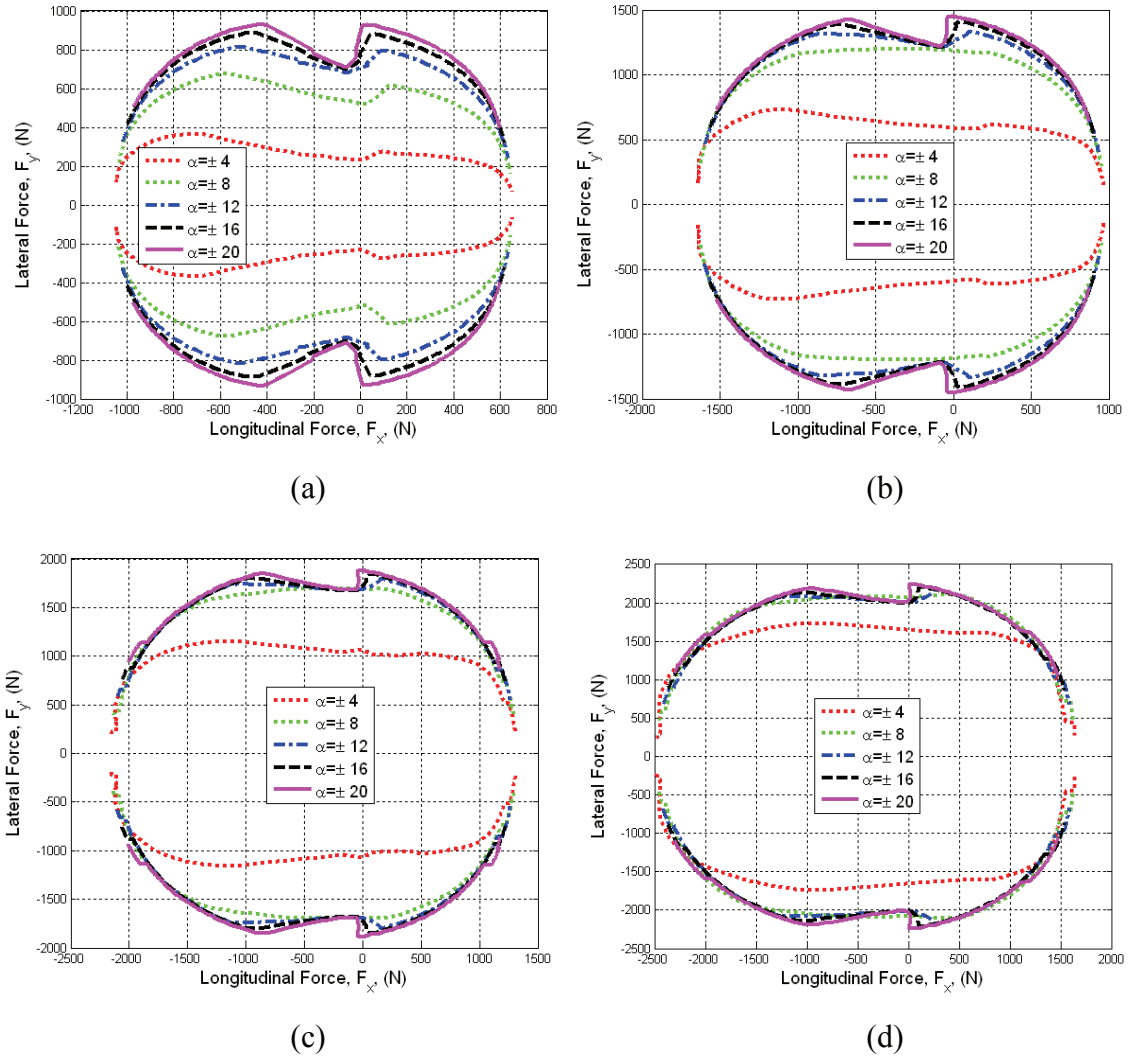

Figure 6-20. Combined slip forces for Yolo loam terrain. (a) Forces for a vertical tire load of 2,000 N. (b) Forces for a vertical tire load of 4,000 N. (c) Forces for a vertical tire load of 6,000 N. (d) Forces for a vertical tire load of 8,000 N.

Higher values for the cohesion term in the soil make the lateral bulldozing force increase a lot faster with increase in slip angle, compared with the case of running the wheel/tire on sandy terrain. However, past certain values of slip, the value of the lateral force reaches a maximum as there is only so much thrust you can get from light bulldozing at certain slip angles. From Figure 6-21, we can see that once the tire model switches to the flexible tire model, the maximum sinkage decreases because of the increase in contact area. This explains why the cusps formed by the lateral bulldozing force seem to have a similar magnitude although the wheel load is increased. The area of soil pushed aside laterally remains approximately the same.

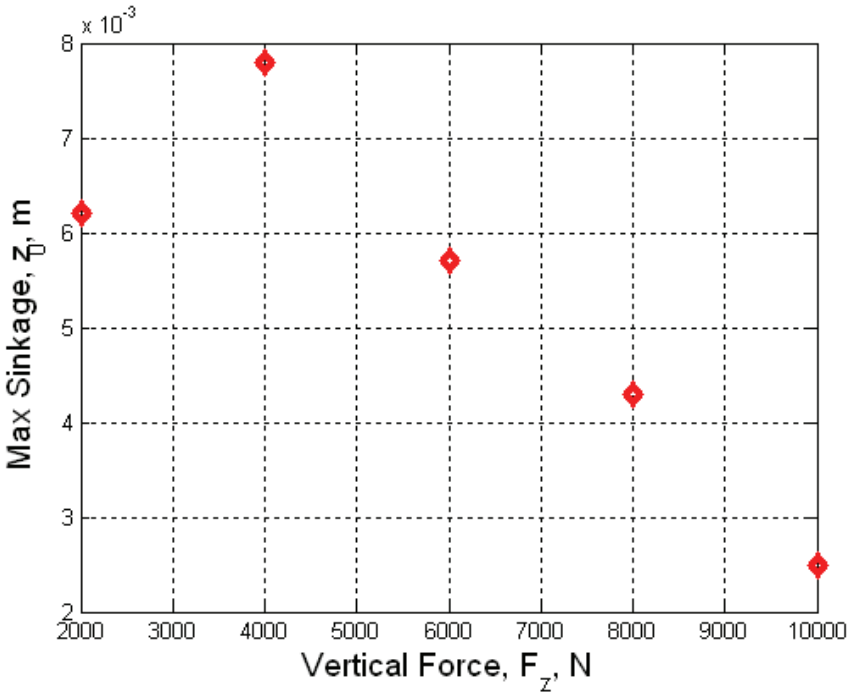

Figure 6-21. Calculated maximum sinkage as a function of the vertical load for the wheel on Yolo loam for a longitudinal slip of 10%.

The model shows behavior for combined slip that can be explained from observations of common phenomenon of tire rolling on off-road terrain. Both Figure 6-18 and Figure 6-20 show a similar trend with the data collected by the US Army Waterways Experimentation Station [77], as shown in Figure 6-22. There seems to be a higher lateral force generated in braking compared to driving. These results should be

taken from a qualitative perspective since due to the testing conditions, the tire types, and the wheel loads are not identical to the ones used in this study.

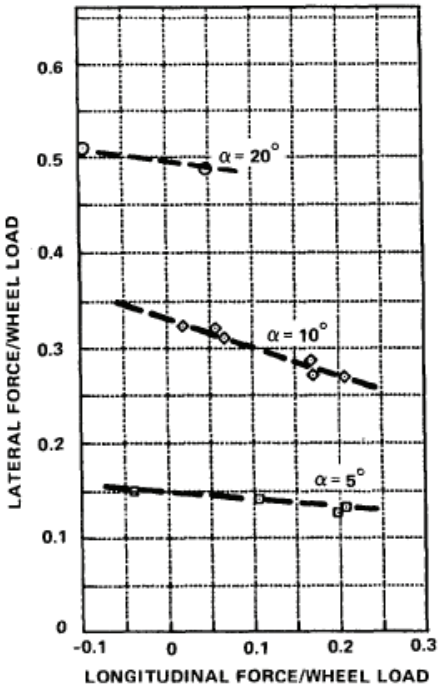

Figure 6-22. Lateral force vs. longitudinal force tire data for sand, collected by the US Army Waterways Experimentation Station in report M-76-9 [77], reproduced under the FOIA.

6.3 Results Summary

The main results discussed in this chapter can be summarized using a mobility map, shown in Figure 6-23, for the three different terrains analyzed.

For soils on which there is a lot of sinkage, such as sand, there is not a lot of increase in driving force with increase in slip, but there is a significantly larger braking force than driving force in the longitudinal direction, as shown in Figure 6-23. Hence, as the vertical wheel load is increased in sand, there will be a shift of the envelope towards the braking side.

For firmer soils, such as the Yolo loam, the mobility envelope is more conical in shape because of a more symmetric distribution for forces between driving and braking. It must be noted that the conical shape shown in Figure 6-23 (b) looks like a scaled version of the one shown in Figure 6-23 (c) for the on-road tire. The insight to be derived from this is that softer soils offer more braking capability because of the sinkage,

but reduced forward mobility. Firmer soils provide more balance between forward mobility and braking, but still have less tractive capabilities compared to on-road operation, which agrees closely with behavior seen in off-road tires such conditions.

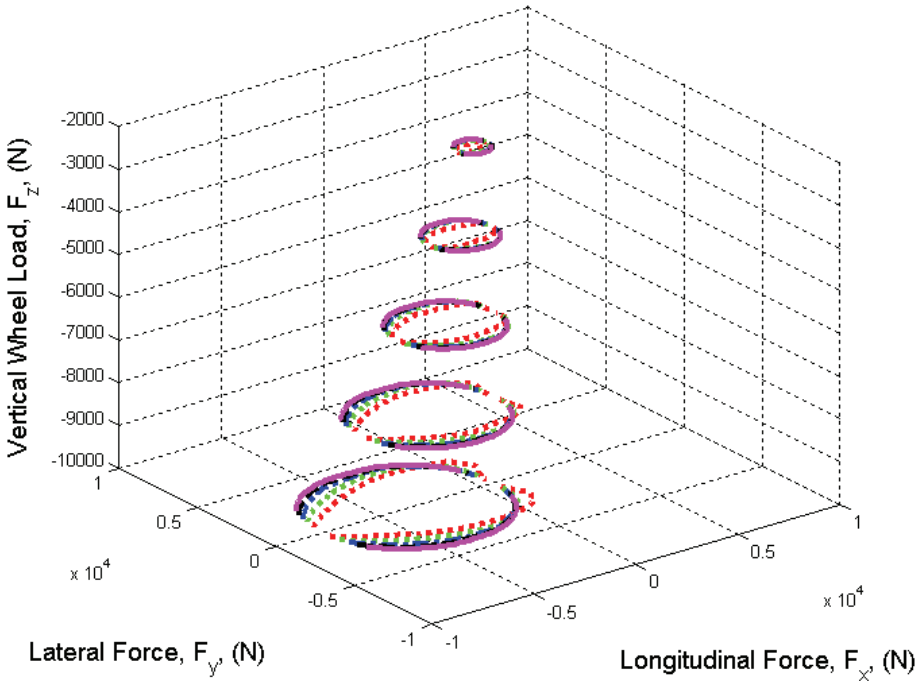

(a)

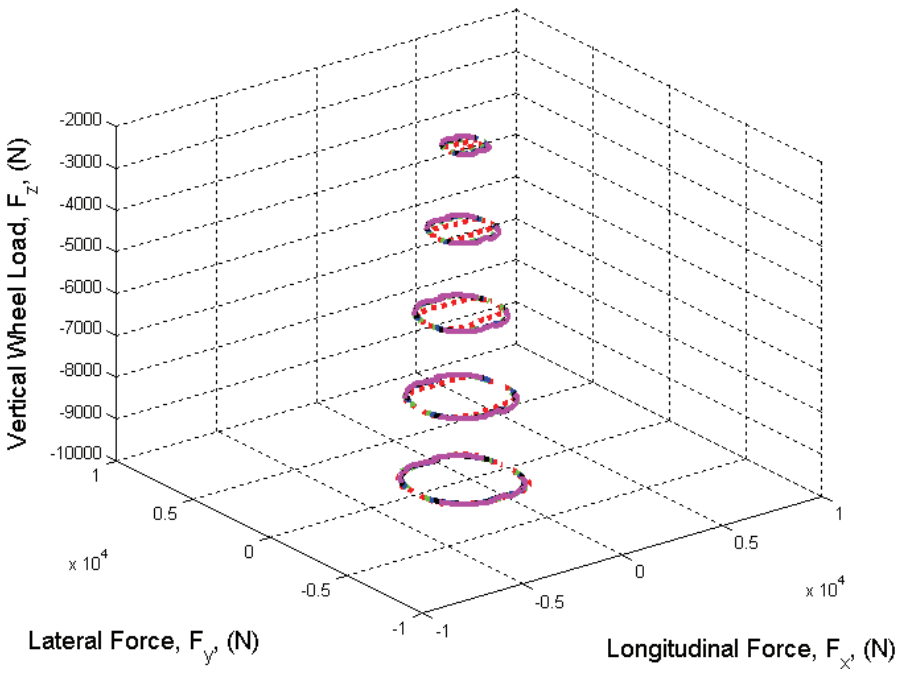

(b)

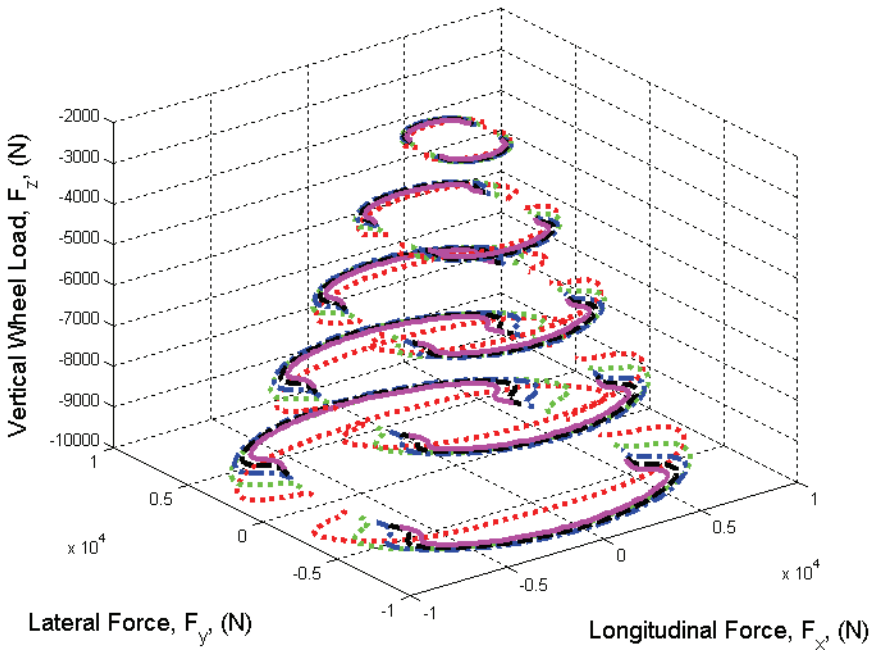

(c)

Figure 6-23. Mobility Map - The lateral and longitudinal forces of the tire model vs. the vertical wheel load on different terrains. (a) Sandy terrain (b) Yolo loam terrain (c) On-road tire model.

7. Alternative Multibody Mechanics-Based Approach to Wheel-Soil Interaction Modeling

The performance prediction of wheeled vehicles depends on accurate estimation of the forces developed at the interface between the tire and the running support. These forces are responsible for the vehicle tractive and braking capabilities, its behavior during steering maneuvers, and, in a more general sense, for the overall vehicle mobility.

Current tire modeling techniques can be classified in analytical, semi-analytical, empirical, and computational (finite element methods). The application for which the model is intended to be used defines, in general, the level of details and the complexity of the tire model. Numerous tire models have thus been developed, ranging from simple linear spring models for ride dynamics applications, for example, to complex finite element models for tire design purposes. While finite element models simulate with the tire in details, their use in vehicle dynamics applications is not feasible, due to the extremely large computational time.

Looking at the tire as a vehicle component, one needs to consider in the modeling process the type of environment for which a specific tire model is to be developed. There is currently an extensive literature dedicated to models designed to simulate the tire for on-road applications, where the tire is the only deformable/flexible body, in contact with a rigid, undeformable surface. Nevertheless, the majority of the existing on-road tire models are either static, or developed for steady-state conditions. On the other side, for off-road applications, the soil under a running vehicle undergoes processes of compaction and shearing, with implications in the dynamics of the tire. Thus, in addition to capturing the behavior of the tire, one needs to also account for the soil dynamics. Accurate mathematical representation of the dynamic interaction between a body that suffers elastic deformations and one that sustains changes in the plastic domain is non-trivial. Additional conditions, such as intermittent contact, and unpredictable changes in the system parameters increase the complexity of the problem. Computational requirements for real-time simulations also add to the challenging task of modeling off-road tires.

While collecting experimental data will continue to be an essential element in tire-ground interaction, especially for validation purposes, a critical step in the advancement

of tire modeling techniques is to develop comprehensive, mathematically consistent, and generic analytical models that capture, at the abstract level, all tire/wheel-road/soil possible situations. Thus, in this chapter we propose an analytical lumped parameter approach for dynamic modeling of off-road tires. The methodology used was to develop consistent and gradually more complex models, and to simulate the tires as rigid wheels on rigid and flexible surfaces. The work presented in this chapter has been performed by the author of this dissertation under the supervision of Dr. Corina Sandu and in cooperation with Dr. Harry Dankowicz, and Mrs. Noelani Laney. Part of this work has been published in the Proceedings of the 15th ISTVS Conference in Hayama, Japan.

The goal of the work presented in this chapter is to develop an alternative lumped parameter model for the dynamic contact between a flexible tire and deformable terrain which is capable of: (1) offering more physical insight into the mechanical behavior of the wheel-soil interaction than those based on Bekker's method, and (2) more computationally efficient than the finite element method models.

7.1 Modeling Approach

In this chapter we develop a two-dimensional rigid wheel with a deformable soil contact model, and their dynamic interaction. The methodology used to model the soil is similar to the dynamic lumped-mass approach [88] and the tire considered in this study is a large agricultural tire with straight lugs, where the soil deformation is significantly more than the tire deformation most of the time. The models have been developed under the following assumptions:

1. The tire and the soil are operating in the elastic region when the wheel is in the state of "stick".
2. The soil is considered to be 'plastic' when the tire starts to slip.
3. The lugs are fully or partially embedded in the soil during the time of rolling.
4. The tire inflation pressure remains constant during the entire simulation.
5. The deflection of the tire is small compared to the deflection of the soils used in this study.

It has been shown by Bekker [60] that the propelling power from walking can be computed, assuming that walking is kinematically identical to the rolling of a polygon

with the side length equal to the length of a step. As the steps become smaller, the polygon approximates the continuous surface of a wheel. Hence, it was hypothesized that walking with very short steps was kinematically identical to a rigid wheel rolling with practically no resistance. Based on the same hypothesis, we can assume then, that it is possible to sum the forces at the tip of the lugs to create a lumped parameter discretized wheel model.

7.2 Tire-Terrain Interaction: Physical Phenomena

Figure 7-1 illustrates a variety of scenarios that can possibly happen to a tire operating on off-road conditions. In Figure 7-1(1), the wheel is rolling on the surface of the ground with an angular velocity, ω , and the center of the wheel is moving with the linear velocity V. However, in Figure 7-1(2), we see that the wheel hits a bump and the tire loses contact with the ground, as seen in Figure 7-1(3). The whole assembly eventually starts to descend toward the ground and comes back into contact with the ground as shown in Figure 7-1(4) and continues rolling forward. Consequently, the contact mechanics are very difficult to model and FEM is often the method of choice to describe the interaction of the soil and the tire. The main reason for this is because the traction generated by the tire-soil interaction is largely attributed to the combined deformation of the soil and tire, which is captured in great detail by FEM. Even so, the difficulty of capturing this phenomenon is further exemplified by the fact that during off-road locomotion the tire does not necessarily stay in contact with the ground.

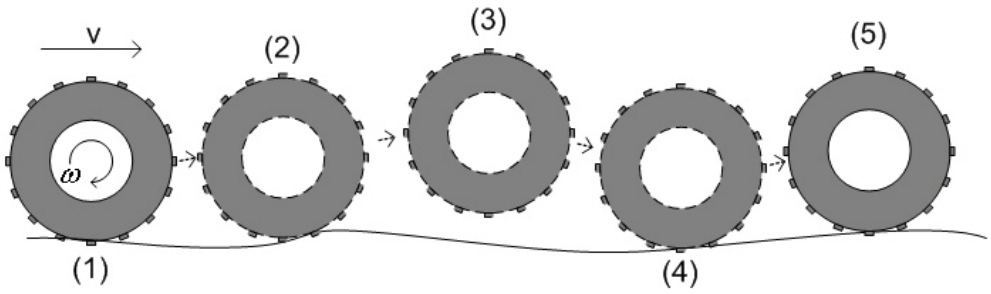

Figure 7-1. Possible Progression of a Tire Rolling on Soft Soil

7.3 Contact Force Modeling: A look at an individual lug (R-C model)

Let, for the moment, the tire be considered as a rigid body interacting through a discrete set of body-fixed contact points with the deformable terrain as shown in Figure 7-2. Specifically, denote by R_i, $i = 1, \ldots, N$, the points on the tire at which reaction forces representing contact with the environment are applied. For each such body-fixed contact point, suppose that nonzero forces result only in the case of nonzero penetration of the contact point through a surface representing the terrain boundary.

Denote by $\mathcal{W}$ a reference frame, relative to which the terrain boundary is stationary and let $\mathbf{r}^{WR_i}$ denote the position vector from the reference point W of $\mathcal{W}$ to the point R_i. Then, the boundary surface is locally captured by the zero-level surface of an *event function* h_{contact}, such that $-h_{\text{contact}}\left(\mathbf{r}^{WR_i}\right)$ equals the penetration of the i-th contact point through the terrain boundary. It follows that nonzero forces result only in the case when

$$h_{\text{contact}}\left(\mathbf{r}^{WR_i}\right) < 0. \tag{7.1}$$

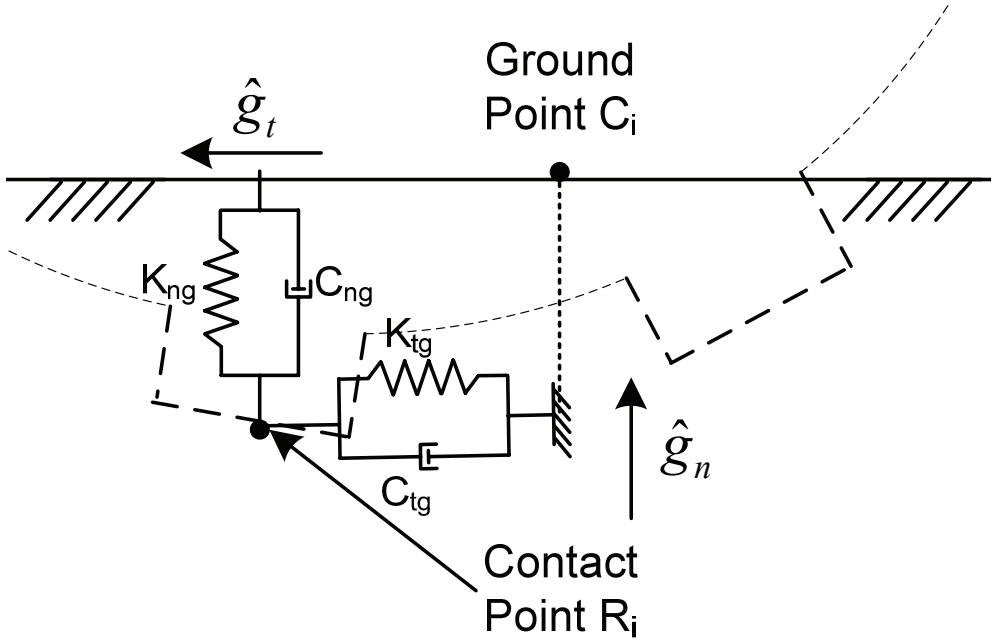

Figure 7-2. Springs and dampers acting on the body's contact point; C_i = Point R_i 's initial contact point with ground, R_i = Point on rigid body.

In the case of nonzero penetration of R_i with the terrain boundary, we seek to model the force interactions between the terrain and the tire transmitted through R_i using spring-damper elements. For this purpose, we associate with each body-fixed contact point R_i a boundary contact point C_i, such that

$$h_{\text{contact}}\left(\mathbf{r}^{WC_i}\right) = 0. \tag{7.2}$$

In particular, we envision that the position of the boundary contact point C_i is initialized to coincide with that of the corresponding R_i at the moment that contact is established.

The elastic component of the force interactions is given by a restoring force that seeks to bring the body-fixed contact point toward the boundary contact point. In contrast, the dissipative component of the force interactions is given by a damping force that is a function of the body-fixed contact point's speed relative to the terrain. Specifically, let $\hat{\mathbf{g}}_t\left(C_i\right)$ and $\hat{\mathbf{g}}_n\left(C_i\right)$ be two unit vectors which are tangential and normal, respectively, to the boundary surface at the point C_i, such that $\hat{\mathbf{g}}_n\left(C_i\right)$ points in the direction of increasing values of h_{contact}. Then, for $h_{\text{contact}}\left(\mathbf{r}^{WR_i}\right) < 0$, the force applied to the tire at R_i is given by

$$f_t\hat{\mathbf{g}}_t\left(C_i\right) + f_n\hat{\mathbf{g}}_n\left(C_i\right), \tag{7.3}$$

where

$$\begin{aligned} f_t &= -K_{tg}\hat{\mathbf{g}}_t\left(C_i\right)\bullet\mathbf{r}^{C_iR_i} - C_{tg}\hat{\mathbf{g}}_t\left(C_i\right)\bullet^{\mathcal{W}}\frac{dR_i}{dt}, \\ f_n &= -K_{ng}\hat{\mathbf{g}}_n\left(C_i\right)\bullet\mathbf{r}^{C_iR_i} - C_{ng}\hat{\mathbf{g}}_n\left(C_i\right)\bullet^{\mathcal{W}}\frac{dR_i}{dt}, \end{aligned} \tag{7.4}$$

where K_{tg}, K_{ng}, C_{tg}, and C_{ng} are material parameters representing the terrain compliance and dissipation and $\dfrac{^{\mathcal{W}}dR_i}{dt}$ is the velocity of the body-fixed contact point R_i relative to the reference frame $\mathcal{W}$. Note that it may be appropriate for certain contact models to envision using different material parameters when the motion of R_i is in the direction of increasing or decreasing penetration.

In the case of nonzero penetration of the body-fixed contact point R_i through the boundary surface, three different contact conditions can occur corresponding to three different motion constraints on the point C_i. In particular, the body-fixed contact point R_i is said to be in *stick* relative to the boundary surface when the boundary contact point C_i is stationary relative to the environment, i.e., when

$$ {}^{\mathcal{W}}\frac{dC_i}{dt} = \mathbf{0} \tag{7.5} $$

and in *slip* relative to the boundary surface otherwise. In the latter case, the body-fixed contact point R_i is *slipping to the right* when

$$ \hat{\mathbf{g}}_t\left(C_i\right) \bullet {}^{\mathcal{W}}\frac{dC_i}{dt} > 0 \tag{7.6} $$

and *slipping to the left* otherwise.

Stick is maintained as long as the point C_i is located within an interval P that is centered around the position of R_i (as shown in Figure 7-3), i.e., as long as $h_{\text{slip}\pm}\left(\mathbf{r}^{WC_i}, \mathbf{r}^{W\partial P_{\mp}}\right) < 0$, where ∂P_- and ∂P_+ are the end points of the interval P for some suitably defined event functions $h_{\text{slip}+}$ and $h_{\text{slip}-}$. A transition to slip to the right/left occurs when $\partial P_{\mp}$ crosses C_i in the direction of $\pm\hat{\mathbf{g}}_t\left(C_i\right)$ corresponding to a zero-crossing of the event function $h_{\text{slip}\pm}$.

During slip to the right/left, the motion of the point C_i is constrained such that it coincides with $\partial P_{\mp}$. Slip is maintained as long as the velocity of $\partial P_{\mp}$ points in the direction of $\pm\hat{\mathbf{g}}_t\left(\partial P_{\mp}\right)$, i.e., as long as

$$ h_{\text{stick}\pm}\left({}^{\mathcal{W}}\frac{d\partial P_{\mp}}{dt}\right) = \mp {}^{\mathcal{W}}\frac{d\partial P_{\mp}}{dt} \bullet \hat{\mathbf{g}}_t\left(\partial P_{\mp}\right) < 0. \tag{7.7} $$

A transition back to stick occurs when the velocity of $\partial P_{\mp}$ changes direction corresponding to a zero-crossing of the event function $h_{\text{stick}\pm}$.

The functions $h_{\text{stick}+}$ and $h_{\text{stick}-}$ are also useful in determining whether the transition from the absence of contact to the presence of contact results in an initial state of stick or slip. In particular, stick occurs if, at the moment of contact, $h_{\text{stick}\pm} > 0$. In contrast, if $h_{\text{stick}+} < 0$ and $h_{\text{stick}-} > 0$ then slip to the right ensues. Finally, if $h_{\text{stick}+} > 0$ and $h_{\text{stick}-} < 0$ then slip to the left ensues.

Consider, for example, a contact model inspired by Coulomb-Amonton dry friction. In this case, and assuming that the terrain boundary is flat, the interval P is bounded by the points ∂P_- and ∂P_+, such that

$$\pm K_{tg}\hat{\mathbf{g}}_t \bullet \mathbf{r}^{\partial P_\mp R_i} + \mu K_{ng}\hat{\mathbf{g}}_n \bullet \mathbf{r}^{\partial P_\mp R_i} = 0. \tag{7.8}$$

and stick is maintained as long as $h_{\text{slip}\pm} < 0$, where

$$h_{\text{slip}\pm} = \pm K_{tg}\hat{\mathbf{g}}_t \bullet \mathbf{r}^{C_i R_i} + \mu K_{ng}\hat{\mathbf{g}}_n \bullet \mathbf{r}^{C_i R_i} \tag{7.9}$$

corresponding to an upper limit on the ratio of the absolute values of the compression and shear forces in the terrain, given by a local coefficient of friction μ.

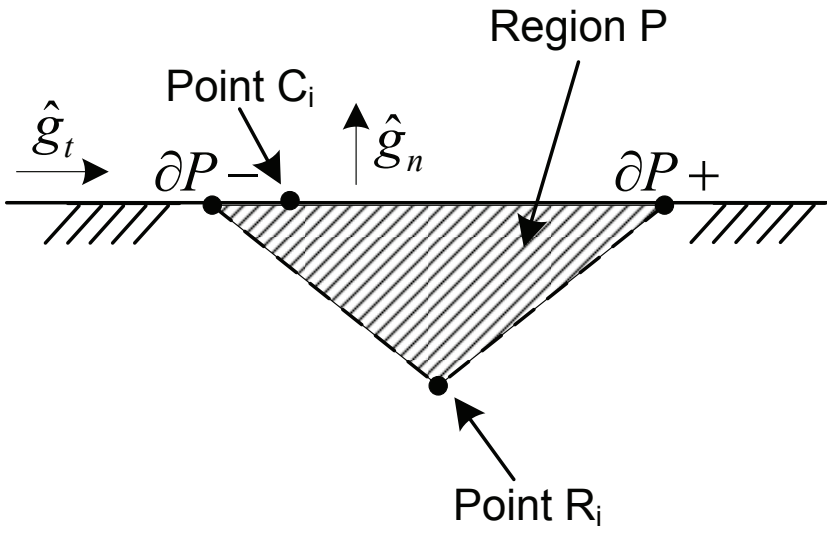

Figure 7-3. Friction triangle: R_i = Point on rigid body, C_i = Initial point of contact of boundary surface with point R_i

Multiple simultaneous transitions between different phases of motion may occur under special circumstances. For example, the body-fixed contact point R_i may transition from slip to stick and from contact to no contact at the same time, provided that at the moment of transition R_i coincides with the boundary contact point C_i. Although such simultaneous transitions should be intuitively straightforward to deal with, they may pose numerical challenges as the detection of one such transition may interfere with the processing of subsequent transitions.

7.3.1 Soil Stiffness Modeling

As stated earlier, we assume that the soil can be modeled as a combination of springs and dashpots, similar to the Winkler foundation model and the Vlasov soil model as described by Vallabhan [89] for shallow foundations. Since the vertical stiff ness of the soil, K_{zg}, is directly related to the shear deformation of the soil, G, as proven by McQuillan [90] and Verruijt [91], we can initially calculate the ground's stiffness and damping coefficients in terms of Poisson's ratio, γ, density, ρ, and contact patch areas as shown in equation (7.10).

$$\begin{aligned} K_{ng} &= \frac{4GA_z}{1-\nu}, C_{ng} = \frac{3.4GA_z^2}{1-\nu}\sqrt{G\gamma}, \\ K_{tg} &= \frac{32(1-\nu)GA_x}{7-8\nu}, C_{tg} = \frac{4.6GA_x^2}{2-\nu}\sqrt{G\gamma}, \end{aligned} \tag{7.10}$$

where contact areas are $A_x = H_i\, b_t$ *and* $A_z = b_t\, l$, as depicted in Figure 7-4.

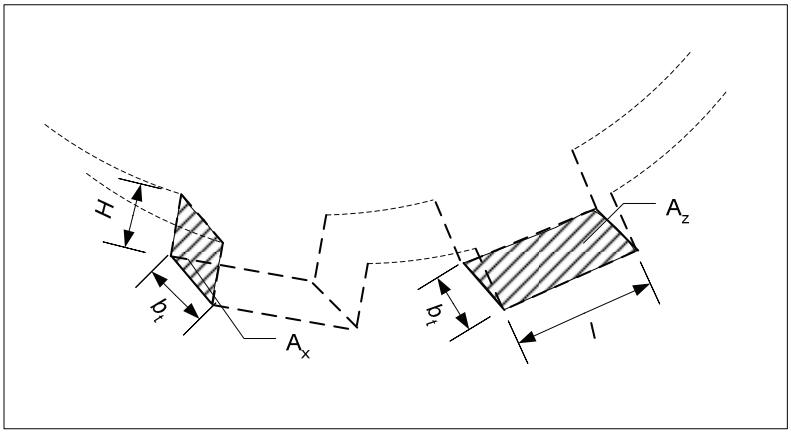

Figure 7-4. Lug Dimensions and Areas

Using soil dynamics theories, it has been proven in [92] that we can use in-situ techniques to measure the velocity of propagation of stress waves through the soil, in order to determine the mechanical behavior of the soil. However, since compression waves are dominated by the response of the pore fluid in saturated soils, most techniques measure the S-waves or shear waves. Thus, if the velocity of the shear wave is denoted by V_s, we can determine the shear modulus of the soil as:

$$G = \rho V_s^2 \tag{7.11}$$

Where ρ is the density of the soil. Using this shear modulus K_{zg}, K_{xg}, C_{xg} *and* C_{zg} can be determined and used to calculate the forces on the tire.

7.3.2 Stick-slip Conditions

In the present study, a modified version of the Coulomb-Amonton contact model is employed to determine conditions for stick and slip. Assuming again that the terrain boundary is flat, the interval P is bounded by the points ∂P_- and ∂P_+, such that

$$\pm K_{tg}\hat{\mathbf{g}}_t \bullet \mathbf{r}^{\partial P_\mp T_i} + \mu K_{ng}\hat{\mathbf{g}}_n \bullet \mathbf{r}^{\partial P_\mp T_i} - F_{EP,i} = 0 \tag{7.12}$$

and stick is maintained as long as $h_{\text{slip}\pm} < 0$, where

$$h_{\text{slip}\pm} = \pm K_{tg}\hat{\mathbf{g}}_t \bullet \mathbf{r}^{C_i T_i} + \mu K_{ng}\hat{\mathbf{g}}_n \bullet \mathbf{r}^{C_i T_i} - F_{EP,i}. \tag{7.13}$$

Here, the contribution of the lug to the maximum sustainable shear force applied to the ground is described by the earth pressure force

$$F_{EP,i} = [K_p(\sigma_{r,i} + \gamma d_i) + 2c\sqrt{K_p}]d_i b_t, \tag{7.14}$$

where $d_i = \left|\vec{\mathrm{r}}^{CT_i} \bullet \mathbf{w}_3\right|$ is the lug-tip sinkage, K_p is a passive earth pressure coefficient (REF), γ is the bulk unit weight of the soil, c is Mohr's cohesion variable, and

$$\sigma_{r,i} = \begin{cases} 0 & h_{\text{contact}}\left(\mathbf{r}^{WS_i}\right) \geq 0 \\ \dfrac{K_{ng} h_{\text{contact}}\left(\mathbf{r}^{WS_i}\right)}{2\pi R_u \dfrac{b_t}{n}} & h_{\text{contact}}\left(\mathbf{r}^{WS_i}\right) < 0 \end{cases} \tag{7.15}$$

captures the vertical pressure originating in the loading of the tire carcass. In addition to the constraints on the points C_i and T_i introduced previously, the rate of change of the lug-tip sinkage is set to zero as long as $\sigma_{r,i}$ exceeds a critical value σ_{crit}.

7.4 Simulation Results and Analysis

Figure 7-5 shows the visualization of two simulations that were done on the wheel model with our methodology.

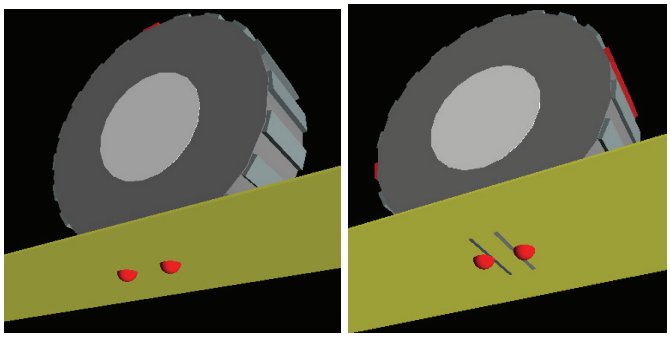

(a) Saturated Clay (b) Saturated Beach Sand

Figure 7-5. Results of Simulation Running on Different Terrain at Low Velocities

For the purpose of simulation, we used an agricultural tire with 20 straight lugs, running with constant torques. The soil data for the simulation is attached in the appendix. The model was implemented in Matlab and was coded with the help of the Mambo Toolbox [93], a set of multibody dynamics procedure developed by Dr. Harry Dankowicz. The visualization for the model is generated by Mambo, the accompanying software for Mambotoolbox [94]. The test scenarios for this model are:

Table 7-1. Test Case Scenarios

	Saturated Sand	Saturated Clay
Low Torque (Case(a))	1 Nm	1 Nm
Intermediate Torques (Case (b) and (c))	3 Nm	3 Nm
	7 Nm	7 Nm
High Torque (Case (d))	10 Nm	10 Nm
Drop Test(with Torque)	20 Nm	20 Nm

The parameters for this simulation are available in the Appendix. For clay the stiffnesses are $K_{rt} = 2.1695e5, K_{tt} = 1.1393e5, K_{tg} = 1.9792e8, K_{ng} = 4.6878e8 \frac{\text{kg}}{\text{s}^2}$ and $C_{tg} = 1.0786e4, C_{ng} = 5.9710e4, C_{rt} = C_{tt} = 500 \frac{\text{kg}}{\text{s}}$. For sand the stiffnesses and damping are $K_{rt} = 2.1695e5, K_{tt} = 1.1393e5, K_{tg} = 1.7355e8, K_{ng} = 3.8554e8 \frac{\text{kg}}{\text{s}^2}$ and $C_{tg} = 1.1539e4, C_{ng} = 5.9911e4, C_{rt} = C_{tt} = 500 \frac{\text{kg}}{\text{s}}$. The wheels are unloaded, except for the effect of the gravitational field on the mass of the wheel.

7.4.1 Analysis: Vertical Position

Figure 7-6 shows the vertical position of the center of gravity of the wheel running on saturated clay and sand, with different torques applied on them. Comparing the figures, we can see that at lowest applied torque, which is 1 Nm, in the test case of clay compared with the test case of sand has a longer dwelling time during the acceleration phase of the simulation. Since the inputs to the models are different torques, we hypothesize that the main difference in the behavior of both cases will be the transient response. As seen from Figure 7-6, as the simulation is run, the responses of both test cases tend to approach the same trend, with the lug impacts increasing in frequency, regardless of applied torque.

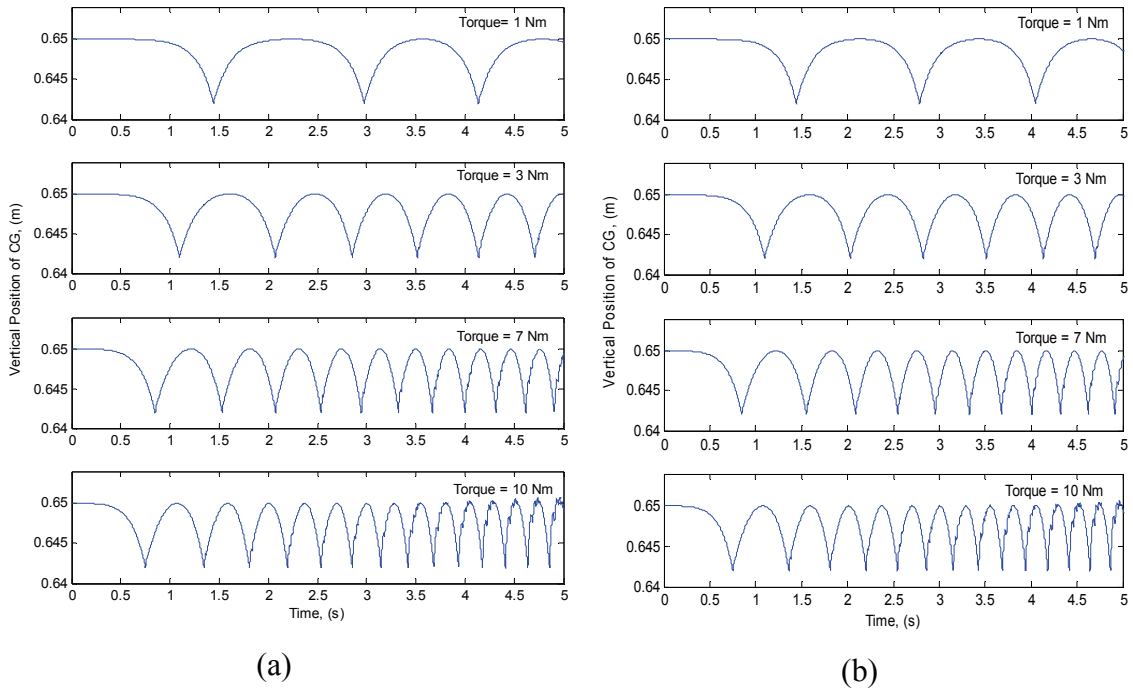

Figure 7-6. Vertical Position of the Center of Gravity of the Wheel Running with Different Torques on Saturated Clay (a) and Sand (b).

7.4.2 Analysis: Vertical Force

Figure 7-7 shows the net vertical force acting on the center of gravity of the wheel during simulation. We can noticed from this figure that the initial net vertical force acting on the tire is equivalent to the weight of the assembly. Also, from the results, it can be observed that the net vertical force decreases at a faster rate for higher applied torques for both sand and clay. The sharp peaks in the plots are actually effects of the lug impacting against the surface of the ground.

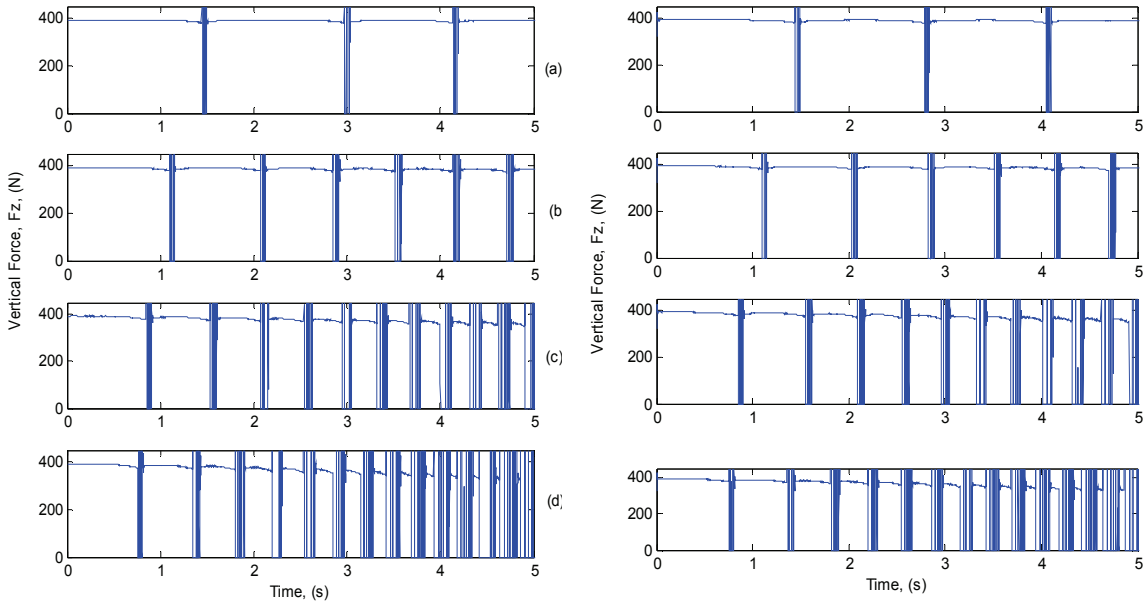

(a) (b)

Figure 7-7. Net Vertical Force Acting on the Center of Gravity of the Wheel Running with Different Torques on Saturated Clay (a) and Sand (b).

7.4.3 Analysis: Longitudinal Forces

Figure 7-8 illustrates the net longitudinal forces acting on the center of gravity of the wheel with different applied torques.

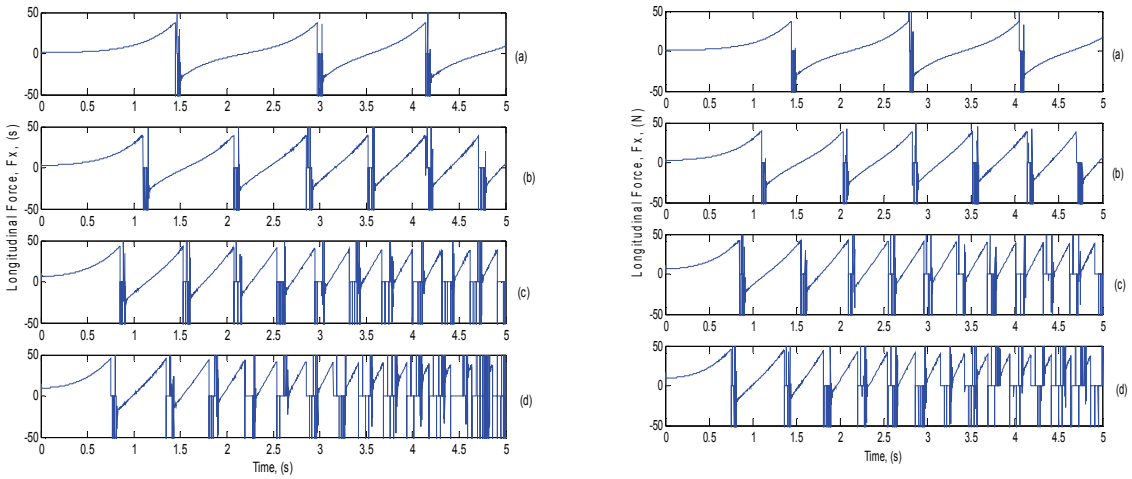

(a) (b)

Figure 7-8. Net Longitudinal Force Acting on the Center of Gravity of the Wheel Running with Different Torques on Saturated Clay (a) and Sand (b).

The instances that this force is zero on the plots depict that the system is in 'slip' condition. These results suggest that the system approaches the 'slip' regime at a faster rate when the applied torque is increased. As expected if the torque is increased, the system will spend more time slipping as compared to when the applied torque is low.

7.4.4 Analysis: Velocities

Figure 7-9 shows how the longitudinal and angular velocities vary for all constant torque test cases. The sharp peaks in the 'wave-like' plot are caused by the impact of the lugs coming into the ground, and the slow dip in velocity represent when more than one lug is in contact with the ground and as the lug slowly exits the ground, the velocity starts to increase again. Taking into consideration that we are driving the assembly with a torque, the increase in velocity is due to the fact that the damping modeled into the system was unable to dissipate all the energy being put into the system by the applied torque. In the event that the system reaches a steady state velocity, then the rate of the energy being put into the system is equals to the rate that the energy is being dissipated.

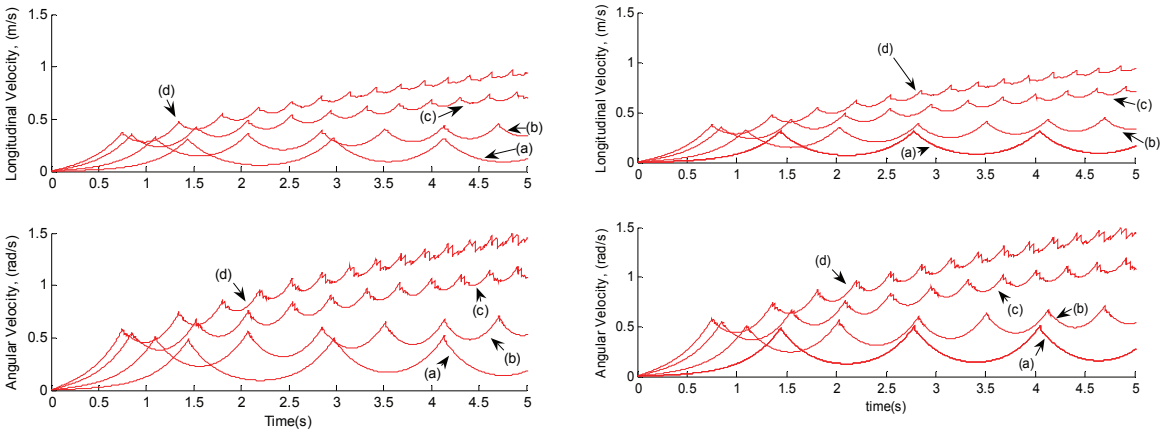

(a) (b)

Figure 7-9. Angular and Longitudinal Velocities of the Wheel Running on Different Torques on Saturated Clay (a) and Sand (b).

7.4.5 Analysis: Drop Test with Constant Torques

Figure 7-10 shows the result of dropping the tire from 1m above the ground and at the same time torquing the whole assembly with 20 Nm of torque. From the two plots, we can see that in both sand and clay, the tire will lose some velocity as it is impacts the

ground and settles out. However, since we are applying a constant torque to the system, the velocities will start increasing after a while. Consequently, since this is a tire with just a torque applied to it and no other external loads, the system will naturally start to bounce when it reaches higher angular and longitudinal velocities.

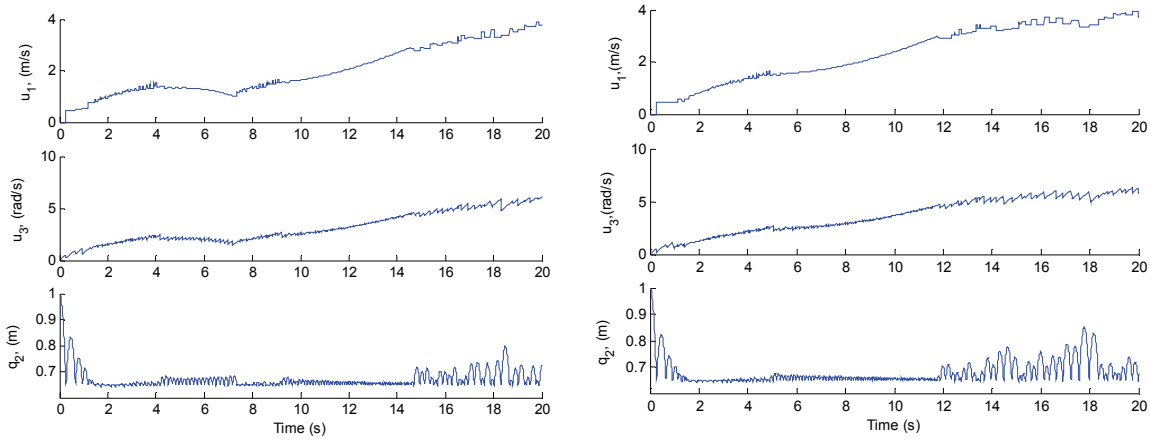

(a) **(b)**

Figure 7-10. Angular Velocities, Longitudinal Velocities and Vertical Position of the Center of Gravity of the Wheel Running on 20Nm of Torque on Saturated Clay (a) and Sand (b).

7.5 Chapter Summary

In conclusion, our simulation results show that it is possible to model tire-soil interaction using soil-dynamics formulation to capture the traction behavior. The results of the simulation with this contact model also fall within our expectation for the behavior of a lugged tire at the tested scenarios. Unlike other models in the literature, the developed contact model is formulated to handle transient behavior like braking and acceleration, as well as loss of contact with the ground, and is not limited to steady state rolling at constant velocities.

Work is already well on the way to developing a 3-D traction model for the tire so that it can be used in full vehicle models for steering and other transient maneuvers. The revised and improved model will also enable us to look at the compliance of the lug, in addition to the compliance of the terrain, to enhance the accuracy of the model. The model presented in this study has shown great potential in many other applications in addition to agricultural tires. However, more work will have to be done to expand the

model from a 2-D model to a 3-D model. Also, the non-linear effects of the tire-soil interaction can be incorporated into the model to effectively capture the behavior of the soil when subjected to large strains and high-velocity loading. In addition to that, our model has been developed to simulate the behavior of traction with no need for the assumption of the homogeneity of the soil transversed, by basing the force calculations on the mechanical behavior of the terrain. This material is partially based upon work supported by the National Science Foundation under Grant No. 0237370 for Dr. Harry Dankowicz. The work of Corina Sandu is supported in part by an AdvanceVT faculty development grant from Virginia Tech's NSF ADVANCE Award 0244916.

There has been a more recent development of this work by Dr. Harry Dankowicz, where the model has been improved and refined. The author of this dissertation and Dr. Corina Sandu have been involved in the development of this newer work from the aspect of specifying numerical simulation scenarios and acquiring simulation parameters of realistic values. The newer and better models that have since been developed include models of rigid wheels on compliant incline, compliant wheels on rigid inclines and compliant wheels on compliant incline. Results of this more recent work are in the process of being prepared for publication.

8. Conclusion and Future Work

This chapter summarizes the results stemming from the work conducted in this study. The primary results are highlighted and suggestions are made for the extension of this work and for future development of the tire model presented in this study.

8.1 Research Summary and Contribution

This research explored the development of an on-road, off-road capable tire model for vehicle dynamics simulation purposes. From the time that tires were first put on motor vehicles, the quest to design better tires have actively spurred the efforts to understand them as mechanical systems.

The on-road tire model seek to extend the work of Pacejka [40] on the brush-based models, while incorporating the observations of some of the latest effort to collect experimental data on tire behavior ([1], [39]) into the modeling process. The fact that the results for combined slip simulations show that the new model has better correlation with respect to the state-of-the-art models such as the STI tire model [82] with the improved systems identification of load-dependent coefficients. Hence, it can be said that the on-road tire model developed is successful because of the fact that the parameter identification is supported by experimental data. In addition to that, the model utilizes a mechanics based approach to calculate the traction limit, which can be parameterized using data from pure slip testing, and used for combined slip maneuvers.

The development of the off-road tire model has been the primary focus of the work represented in this dissertation. The application of Reece's equation [9], Hettiaratchi and Reece formulation [67] and the theory of instantaneous center of rotation to determine the point where the maximum principle stress act on the wheel is an application of plasticity theory and mechanical modeling on the development of this tire model. The model was designed to be one that applies a mechanics based approach, where the tractive forces are calculated from the integration of the shear stresses at the tire contact interface. Plus, similar to the on-road tire model, the off-road tire model uses the same approach to calculate the traction limit as the on-road tire model. This method was conceptualized by observations of contact stress data by Schwanghart[19] and Krick[87]. For soils that are extremely deformable, the tire reverts to a rigid wheel, as per

observations of experimental data by Shoop[29], Fujimoto[95], Muro[6] and Wong[3] to save computational resources.

The application of the flexible ring tire model to model the tire deformation is an improvement over the empirical method used by Karafiath [20] and the current methods ([85], [6]) in the terramechanics community to characterize the tire deflected geometry. The method in which the model was applied integrates the observations by Freitag [75] on how the method should be used, and allows for a better way to compute the tire interface stresses. The application of the Principle of Maximum Dissipation rate [54] to project the forces in the sliding region into the directions collinear with the slip velocities ensure that once soil failure occurs at the interface, the sliding forces are projected into directions that are normal to the limit surface of traction. Finally, the inclusion of forward compaction resistance and lateral bulldozing resistance ensures that the tire model accounts for the effect of sinkage when determining the traction performance.

This research was initiated to study the state of the art of tire modeling and develop a tire model that does not only have the capability to work on-road, but off-road as well by making use of the latest developments in tire mechanics and soil mechanics. The work developed in this dissertation produced an on-road tire model, consistent with the principles of mechanics and enhanced with expressions developed from the observation of experimental data collected throughout the years. Moreover, two models were developed for the off-road wheel/tire tractive modeling based on numerous empirical studies and observations by terramechanics experts throughout the years. The off-road wheel/tire model incorporates elements from the on-road tire model to ensure that it produces results that are consistent with experimental measurements from various terramechanics researchers. Obviously, the stresses generated at the tractive interface are far from being uniform across the width of the tire/wheel. Even so, the development of a (relatively speaking) simplified tire-soil interaction model for combined slip operation of a wheel/tire that uses minimal number of readily available input parameters to yield sufficiently useful results represents a forward step in this area of off-road vehicle dynamics. Results from the output of the model clearly show that the off-road tire model results which reflect the insight corresponding to the empirical data collected by various

terramechanics researchers throughout the years. This fact suggests that the model is a good starting point for a terramechanics-based tire model but may still warrant further refinement, as will be suggested in the next section.

8.2 Recommendations for Future Research

Throughout the course of this research, several topics, beyond the scope of the current study, were encountered. In the following subsections, a brief discussion of the possible future directions of research is provided.

- **Experimental refinement of the off-road tire model**

  The model was developed based on photographic evidence and insight from experimental data accumulated by researchers in the terramechanics area throughout the years. There are many simplifications done in the modeling of the tire for this study. Other tire characteristics can be incorporated into the off-road modeling of the tire by analyzing experimental data. Usage of the AVDL terramechanics rig is suggested for the application of tire modeling fine-tuning and refining. Amongst the studies that can be done include studies on the soil unloading mechanism for rolling of deformable tires on soft soil. Currently, much work has been done in the analytical development of the soil unloading mechanism of soil implements but little has been done to study the soil unloading mechanism of a rolling wheel/tire.

- **Extension of the model over different terrain types.**

  The current model has been formulated in terms of frictional-cohesive soil models, where the Mohr-Coulomb failure criteria has been used as the traction limit and the Reece's plasticity-based plate sinkage equation has been used for calculating the stresses acting on the radial surface of the wheel. Wong has developed pressure-sinkage equations for snow and muskeg in [3] which has shown to have good correlation with experimental data. A new model of the tire for snow and other terrains may be developed from these alternative pressure-sinkage relationships. These other tire models can be developed based on those equations with other suitable failure theories for the different terrain types in a similar fashion with the one used for this tire model.

- **Improved system identification of the on-road tire model.**

  The system identification of the on-road tire model did not include much of the effect of speed on the forces. Many researchers have studied and collected data on the effect of velocity ([39], [1]) on coefficients of friction and on the tire stiffness but they are still in the process of developing expressions to include such effects in tire models. The effect of speed, tread design and hydroplaning on the system parameters represent some of the possible future directions of research.

- **Collection of pressure-sinkage data to characterize Reece's equation.**

  Pressure-sinkage data for Reece's equation, which has been shown to be more appropriate than Bekker's equation, can be collected using a bevameter, or an annular ring setup. In order to study the effect of velocity on the pressure measured from the plate sinkage test, data with varying deformation rates have to be collected so that an accurate model of the plate-sinkage dynamic behavior can be characterized. This study will also have the additional benefit of creating a better way to calculate the point of maximum radial/normal pressure along the direction normal to the circumference of the wheel.

- **Studies on the effect of the limitation of the factors μ_x and μ_y to the numerical value of 1 for the off-road tire model.**

  The limitation of the value of μ_x and μ_y to the numerical value of 1 for the off-road tire model is a limiting approximation, imposed upon the model because of the unknown nature of the variation of these coefficients with soil strength and cohesion. As seen in chapter 5, the variation of the coefficients with tire load for the on-road values of μ_x and μ_y seems to, at time, increase the value of the coefficients. It is possible that the same phenomenon may occur for these parameter for off-road tires, but due to lack of information, the safe assumption of limiting the factors are necessary to ensure the numerical integration of the stresses converge to a finite value. In the future, this assumption might be modified or removed one the variation of these factors with speed and tire load are better studied, from the experimental point of view.

- **Application of the tire model to vehicle models with validation.**

The application of the tire model to a vehicle model will be an excellent use of the tire model. However, it is recommended that the tire data parameters be extracted from the recommended test set suggested in chapter 5.

- **System identification of the tire model with different types of tires for different vehicles.**

  The on-road tire model has been parameterized using test data for one set of tires. System identification of other tire models are also possible to ensure that the on-road tire model is parameterized for various tires in order to develop better simulation models for a larger set of vehicles.

- **Usage of the terramechanics rig to study and develop theories to include the slip-sinkage effect on the off-road tire model.**

  When combined vertical and tangential loading of plates was performed on soils, it has been noticed that the plate continued to sink with applied shear stress even though no vertical load was applied. This phenomenon is called slip-sinkage. Bekker[7], Liston [63], and Soltynski [96] studied the concept of slip-sinkage from the mobility perspective, and put forth suggestions on how slip-sinkage should be addressed in mobility modeling. However, no researcher has developed a comprehensive analytical slip-sinkage theory that works for both cohesive and frictional soils. As with further pressure-sinkage testing, it is very important to look into characterizing the slip-sinkage phenomenon in tire-terrain interaction as a direction of future research.

- **Development of a closed-form analytical solution for the constraint inequality used to calculate the adhesion/sliding region of the contact patch.**

  The limit surface calculation in the off-road tire model requires the solving of non-linear equations to determine the value of θ_a. The implementation of the model done in this dissertation, which serves as a proof of concept solution, utilizes a numerical implementation to solve the equations. This method subjects the model to the possibility of numerical issues arising from the "jumping" of the solution, under various initial guesses. As with the on-road tire model, in which

the calculation of l_a was done analytically, devising a method to compute the solution of θ_a will greatly improve the simulation efficiency of the model.

The programs provided in the appendix are meant to provide an idea on how this model is implemented in this dissertation, and may need further optimization. However, they serve to demonstrate how the proof of concept of the model is implemented, and are meant to be used with caution. It is recommended that any party interested in using the tire models follow the parameter identification method outlined in chapter 5 before attempting to blindly apply the model to a vehicle. As has been stated before, the work presented in this dissertation is meant to provide a unified framework between vehicle dynamics and terramechanics, which has been traditionally disjointed. It is hoped that the work done in this dissertation can provide a unifying insight into the two different disciplines, and provide insight into the engineering problem of off-road vehicle dynamics.

9. References

[1] Gent, A. N., Walter, J. D., 2005, "The Pneumatic Tire," Washington, D.C.

[2] Shearer, G. R., 1977, "The Rolling Wheel - The Development of the Pneumatic Tire " Proceedings of the Institution of Mechanical Engineers (IMECHE), 191.

[3] Wong, J. Y., 2001, Theory of Ground Vehicles, John Wiley and Sons.

[4] SAE, 1978, "Vehicle Dynamics Terminology," Society of Automotive Engineers, Warren, PA.

[5] SAE, "Vehicle Dynamics Terminology," Society of Automotive Engineers, Warren, PA.

[6] Muro, T., O'Brien, J., 2004, Terramechanics: Land Locomotion Mechanics, A.A. Balkema, Lisse.

[7] Bekker, M. G., 1969, Introduction to Terrain-Vehicle Systems, University of Michigan Press, Ann Arbor.

[8] Janosi, Z., Hanamoto, B., 1961, "The Analytical Determination of Drawbar Pull as a Function Of Slip for Tracked Vehicles," 1st ISTVS Conference Torio.

[9] Reece, A. R., 1964, "Problems of Soil-Vehicle Mechanics," Land Locomotion Laboratory (USATACOM), Warren, MI.

[10] Meyerhof, G. G., 1951, "The Ultimate Bearing Capacity of Foundations " Geotechnique, 2(301).

[11] El-Gawwad, K. A., Crolla, D.A., Soliman, A.M.A., El-Sayed, F.M., 1999, "Off-Road Tyre Modelling I: The Multi-Spoke Tyre Model Modifed To Include The Effect Of Straight Lugs," Journal of Terramechanics, 36, pp. 3-24.

[12] El-Gawwad, K. A., Crolla, D.A., Soliman, A.M.A., El-Sayed, F.M., 1999, "Off-Road Tyre Modelling II: Effect Of Camber On Tyre Performance," Journal of Terramechanics, 36, pp. 25-38.

[13] Knight, S. J., Rula, A. A., 1961, "Measurement and estimation of the trafficability of fine-grained soils.," Proceedings of the 1st International ISTVS Conference, ISTVS, Torino, Italy, pp. 371-384.

[14] Brixius, W., 1987, "Traction Prediction Equations for Bias-ply Tires," Transactions of the ASAE (871622), ASAE, St. Joseph, MI.

[15] Upadhyaya, S. K., Wulfsohn, D. , 1990, "Review of traction prediction equations," ASAE, ASAE, St. Joseph, Michigan.

[16] Wismur, R. D., Luth, H.J. , 1973, "Off-road traction prediction for wheeled vehicles," Journal of Terramechanics, 10, pp. 49-61.

[17] Wismur, R. D., Luth, H.J. , 1974, "Off-road traction prediction for wheeled vehicles," Transactions of the ASAE 7, pp. 8-14.

[18] Upadhyaya, S. K., Wulfsohn, D. , 1993, "Traction prediction using soil parameters obtained with an instrumented analog device," Journal of Terramechanics, 30(2), pp. 85-100.

[19] Schwanghart, H., 1968, "Lateral Forces on Steered Tyres in Loose Soil," Journal of Terramechanics, 5(1), pp. 9-29.

[20] Karafiath, L. L., E. A. Nowatzki, 1978, Soil Mechanics for Off-Road Vehicle Engineering, Trans Tech Publications.

[21] Karafiath, L. L., 1971, "Plasticity theory and the stress distribution beneath wheels," Journal of Terramechanics, 8(2), pp. 49-60.
[22] Sokolovskii, V. V., 1965, Statics of granular media, Pergamon Press, New York.
[23] Karafiath, L. L., Nowatzki, E. A. , 1974, "General yield conditions in a plasticity analysis of soil-wheel interaction," Journal of Terramechanics, 11(1), pp. 29-44.
[24] Lee, J., Liu, Q., 2006, "Interfacial Forces between Tire and Snow under Different Snow Depths," 2006 SAE World Congress, SAE, Detroit, MI.
[25] Lee, J., Liu, Q., Mourelatos, Z., 2006, "Simulation of Tire-Snow Interfacial Forces for a Range of Snow Densities with Uncertainty," 2006 SAE World Congress SAE, Detroit, MI.
[26] Ridha, R. A., 1980, "Computation of stresses, strains and deformation of tires," Rubber chemistry and technology, 53(4), pp. 849-902.
[27] Shoemaker, P., 1984, "Tire engineering by finite element modelling," SAE 840065, SAE.
[28] Rothert, H., Gebbeken, N., Jagusch, J., Kaliske, M., 1994, "Recent developments in the numerical tire analysis.," Proc. Int. Rubber Conf. IRCMoscow, Russia, pp. 246-252.
[29] Shoop, S., 2001, "Finite Element Modeling of Tire-Terrain Interaction," University of Michigan, Ann Arbor.
[30] Fervers, C., 2002, "Improved FEM Simulation Model for Tire-soil Interaction.," Proceedings of the 14th ISTVS Conference, ISTVS, Vicksburg, MS.
[31] Schlotter, V., Kutzbach, H. D., 2002, "Investigation on the Soil-Tyre Interaction of Agricultural Tyres With Respect to the Influence of Dynamic Tyre Load," Proceedings of the 14th ISTVS Conference ISTVS, Vicksburg, MS.
[32] Nakashima, H., Oida, A., 2002, "Algorithm and Implementation of Soil-Tire Contact Analysis Code Based on Dynamic FE-DE Method," Proceedings of the 14th ISTVS Conference ISTVS, Vicksburg, MS.
[33] Pan, W., Solis, D.,, 2002, "High Fidelity Tire-soil Interaction Modeling and Simulation for VPG Applications," Proceedings of the 14th ISTVS Conference, ISTVS, Vicksburg, MS.
[34] Chan, B. J., Thompson, N., Sandu, C. and Dankowicz, H., 2005, "A Novel Tire-soil Interaction Model for Simulation of Off-road Vehicles," ISTVS Proceedings of the 15th International Conference of the ISTVS Hayama, Japan.
[35] Salaani, M. K., 2007, "Analytical Tire Forces and Moments Model with Validated Data," SAE World Congress, SAE, Detroit.
[36] Lee, S., 1994, "Development of a New Dynamic Tire Model for Improved Vehicle Dynamics Formulation," Ohio State University, Columbus.
[37] Gim, G., et. al., 2005, "A Semiphysical Tire Model for Vehicle Dynamics Analysis of Handling and Braking," Vehicle System Dynamics, 43, pp. 267-280.
[38] Svendenius, J., 2003, "Tire Models for Use in Braking Applications," Lund Institute of Technology, Lund.
[39] Clark, S. K., 1981, "Mechanics of Pneumatic Tires," NHSTA, Washington D.C.
[40] Pacejka, H. B., 2002, Tyre and Vehicle Dynamics, SAE.
[41] Jurkat, M. P., Brady, P. M., 1981, "On a Lateral Force tire model for both highway and soft-soil conditions," Proc. of the 7th int. Conf. ISTVS ISTVS, Calgary.

[42] Del Rosario, C. R., 1980, "Lateral Force Investigations On Steered, Pneumatic Tyres Operating Under Soil Conditions ", Cranfield Insitute of Technology, Silsoe.
[43] Allen, R. W., Rosenthal, T. J., Chrstos, J. P., 1997, "A Vehicle Dynamics Tire Model for Both Pavement and Off-Road Conditions " SAE International Congress and Exposition, SAE, Detroit, Michigan.
[44] Szostak, H., Allen, R. W., Rosenthal, T. J. , 1988, "Analytical Modeling of Driver Response In Crash Avoidance Maneuvering: Volume II: An Interactive Tire Model for Driver/Vehicle Simulation," Department of Transportation, Washington, D.C.
[45] Liang, C., Allen, R. W., Rosenthal, T. J., Chrstos, J., Nunez,P. , 2004, "Tire Modeling for Off-Road Vehicle Simulation," Proceedings of the 2004 SAE Automotive Dynamics, Stability & Controls Conference, SAE, Detroit, Michigan.
[46] Metz, L. D., 1993, "Dynamics of Four-wheel Steer on Off-road Vehicles ", SAE International 930765.
[47] Fiala, E., 1964, "Seitenkrafte am Rollenden Luftreifen," VDI-Zeitschrift p. 96.
[48] Gim, G., 1988, "Vehicle Dynamic Simulation with a Comprehensive Model for Pneumatic Tires," The University of Arizona, Tucson.
[49] Fromm, H., 1965, "Seitenschlupf und Fuhrungswert des Rollenden Rades."
[50] Gim, G., Kang, N., 1996, "Requirements of a tire model for Practical Cornering Simulations of Vehicles," SAE International Congress and Exposition SAE, Detroit, Michigan.
[51] Genta, G., 2003, Motor Vehicle Dynamics: Modeling and Simulation, World Scientific Publishing Co. Pte. Ltd, Singapore.
[52] Kabe, K., Miyashita, N., 2006, "A New Analytical Tire Model for Cornering Simulation. Part I: Cornering Power and Self-Aligning Torque Power," Tire Science and Technology, 34(2), pp. 84-99.
[53] Kabe, K., Miyashita, N., 2006, "A New Analytical Tire Model for Cornering Simulation. Part II: Cornering Force and Self-aligning Torque," Tire Science and Technology, 34(2), pp. 100-118
[54] Goyal, S., 1989, "Planar Sliding Of A Rigid Body With Dry Friction:Limit Surfaces And Dynamics Of Motion.," Cornell University, Ithaca.
[55] DiMaggio, S. J., Bieniek, M. P., 1998, "Vehicle dynamics using a limit surface treatment of the tyre±road interface," Proceedings of the Institution of Mechanical Engineers (IMECHE), 212(D).
[56] Schuring, D. J., Pelz, W., Pottinger, M. G. , 1996, "A model for combined tire cornering and braking forces," Investigations and Analysis in Vehicle Dynamics and Simulation, SAE International.
[57] Bakker, E., Pacejka, H. B., Lidner, L., 1989, "A new tire model with an application in vehicle dynamics studies," SAE International.
[58] Pan, W., Papelis, Y. E., 2005, "Real-time dynamic simulation of vehicles with electronic stability control: modelling and validation," Int. J. Vehicle Systems Modelling and Testing, Vol. 1(Nos. 1/2/3), pp. 143–167.
[59] Heydinger, G. J., Garrott, W. R., Chrstos, J. P. , 1991, "The Importance of Tire Lag on Simulated Transient Vehicle Response," Proceedings of the 1991 SAE International Congress and Exposition, SAE, Detroit, Michigan.
[60] Bekker, M. G., 1960, Off-the-road Locomotion, University of Michigan Press, Ann Arbor.

[61] Wong, J. Y., Reece, A.R., 1967, "Prediction of rigid wheel performance based on the analysis of soil-wheel stresses - Part II," Journal of Terramechanics, 4(2), pp. 7-25.
[62] Wong, J. Y., Reece, A. R., 1967, "Prediction of rigid wheel performance based on the analysis of soil-wheel stresses - part I," Journal of Terramechanics, 4(1), pp. 81-98.
[63] Liston, R. A., 1973, "The Normal and Tangential Loading of Soil," Michigan Technological University, Houghton.
[64] Bernard, J., Clover, C.,, 1995, "Tire Modeling for Low-speed and High-Speed Calculations," SAE
[65] Terzaghi, K., 1943, Theoretical soil mechanics, J. Wiley and Sons, New York.
[66] Onafeko, O., Reece, A. R., 1967, "Soil stresses and deformations beneath rigid wheels," Journal of Terramechanics, 4(1), pp. 59-80.
[67] Hettiaratchi, D. R. P., Reece, A.R. , 1974, "The Calculation of Passive Soil Resistance," Geotechnique, 3, pp. 289-310.
[68] Hettiaratchi, D. R. P., Reece, A.R., 1967, "Symmetrical Three-Dimensional Soil Failure," Journal of Terramechanics, 4(3), pp. 45-67.
[69] Gillespie, T. D., 1992, Fundamentals of Vehicle Dynamics, SAE.
[70] Milliken, W. F. a. M., D. L. , 1995, Race Car Vehicle Dynamics, SAE, Warrendale, PA.
[71] Karafiath, L. L., 1973, "An Application of Plasticity Theory to the Solution of the Rigid Wheel - Soil Interaction Problem," Grumman Aerospace Corp., Research Dept. , Bethpage, NY.
[72] Loo, M., 1985, "A model Analysis of Tire Behavior Under Vertical Loading and Straight-Line Free Rolling," Tire Science and Technology, 13(2), pp. 67-90.
[73] Yu, Z., Tan, H., Du, X., Sun, L., "A Simple Analysis Method for Contact Deformation of Rolling Tire," Vehicle System Dynamics, 36(6), pp. 435 - 443.
[74] Gong, S., 1993, " A Study of in-plane Dynamics of Tires," T.U. Delft, Delft.
[75] Freitag, D. R., Smith, M. E., 1966, "Centerline Deflection of Penumatic Tire Moving in Dry Sand," Journal of Terramechanics, 3(1).
[76] Grecenko, A., 1992, "The Slip and Drift Model of a Wheel with Tyre Compared to Some Other Attempts in this Field," Journal of Terramechanics, 29(6), pp. 599-604.
[77] Durham, G. N., 1976, "Powered Wheels in the Turned Mode Operating on Yielding Soils," US Army Waterways Experiment Station, Vicksburg.
[78] Guan, D., Fan, C., 2003, "Tire Modeling for Vertical Properties Including Enveloping Properties Using Experimental Modal Parameters," Vehicle System Dynamics, 40(6), pp. 419–433.
[79] Langdon, J. D., 2007, "Design and Adaptive Control of a Lab-based, Tire-coupled, Quarter-car Suspension Test Rig for the Accurate Re-creation of Vehicle Response," Virginia Polytechnic Institute and State University, Danville, VA.
[80] SAE, 1975, "Laboratory Testing Machines and Procedures for Measuring the Steady state Force and Moment Properties of Passenger Car Tires," SAE, Warrensdale, PA.
[81] Heydinger, G. J., 1990, "Improved Simulation and Validation of Road Vehicle Handling Dynamics ", Ohio State University, Columbus.

[82] SEA, i., 2003, "Vehicle Inertia Measurement Facility, Suspension Kinematics and Compliance, Shock Absorber, Suspension Component, Geometric and Inertia, and Tire Test Measurement Results," Columbus.
[83] Wong, J. Y., 1980, "Data Processing Methodology In the Characterization of the Mechanical Properties of Terrain," Journal of Terramechanics, 17(1), pp. 13-41.
[84] Coutermarsh, B., 2007, "Velocity effect of vehicle rolling resistance in sand," Journal of Terramechanics, 44, pp. 275-291.
[85] Shmulevich, I., Osetinsky, A., 2003, "Traction performance of a pushed/pulled drive wheel," Journal of Terramechanics, 40(1), pp. 33-50.
[86] Oida, A., Satoh, A., Itoh, H., Triratanasirichai, K., 1991, "Three-dimensional stress distributions on a tire-sand contact surface," Journal of Terramechanics, 28(4), pp. 319-330.
[87] Krick, G., 1969, "Radial and shear stress distribution beneath rigid wheels and pneumatic tyres on yielding soils with regard to tyre deformation," Journal of Terramechanics, 6(3), pp. 73-98.
[88] Das, B. M., 1983, Fundamentals of Soil Dynamics, Elsevier Science Publishing, Amsterdam.
[89] Vallabhan, C. V. G., Daloglu, A. T., , 1999, "Consistent Fem-Vlasov Model For Plates On Layered Soil," Journal Of Structural Engineering.
[90] McQuillan, J., 2002, "Modeling Dynamic Ground Reaction to Predict Motion of and Loads on Stranded Ships in Waves," Virginia Tech, Blacksburg.
[91] Verruijt, A., 2001, Soil Mechanics, Delft University of Technology, Delft.
[92] Engineers, U. A. C. o., 1997, "Soil Dynamics and Special Design Aspects.."
[93] Dankowicz, H., 2005, Multibody Mechanics and Visualisation, Springer-Verlag.
[94] Dankowicz, H., 2005, "Mambo and the Mambo Toolbox," https://netfiles.uiuc.edu/danko/www/Mambo/MamboHome.htm.
[95] Fujimoto, Y., 1977, "Performance of elastic wheels on yielding cohesive soils," Journal of Terramechanics, 14(4), pp. 191-210.
[96] Soltynski, A., 1965, "Slip sinkage as one of the performance factors of a model pneumatic-tyred vehicle," Journal of Terramechanics, 2(3), pp. 29-54.

10.Appendix

A. Main Subroutine For On-Road Tire Model

```
function [ Fx,Fy,Mx,Mz ] =
chanmodel(mu0,Fz,gammat,sd,sdd,alphac,alphacd,omega,speed)

% Brendan J. Chan 2007
% Code for the on-road tire model
% Vectorized
% limits the input to bounded conditions
% Use with caution!


sd=min(abs(sd),0.99).*sign(sd);
alphac=min(abs(alphac),1.56).*sign(alphac);

%%%%%%%%%%%%%%%%%%%%%%%%%% Parameters %%%%%%%%%%%%%%%%%%%%%%%%%%%%%%%%

% Insert tire/soil param here
tireparam


%%%%%%%%%%%%%%%% Program starts here %%%%%%%%%%%%%%%%%%
% Inline Functions
funsat=@(coeff,x) coeff(1).*(1-exp(-coeff(2).*x));
funmu =@(coeff,x) coeff(1).*(x./coeff(2)).^coeff(3);
funcubic =@(coeff,x)
coeff(1).*x.^3+coeff(2).*x.^2+coeff(3).*x+coeff(4);
funquad =@(coeff,x) coeff(1).*x.^2+coeff(2).*x+coeff(3);
funkz=@(coeff,x) coeff(1)+(coeff(2)-
coeff(1)).*(sech(coeff(3).*(abs(tan(x))./(1-abs(tan(x))))));

% Vertical Stiffness modeling
initdel=Fz./Kz0;
Cz1=funcubic(Cz1prm,initdel) ;
Cz2=funquad(Cz2prm,initdel) ;
Kz=funkz([Cz1,1,Cz2],alphac).*Kz0;

% Contact patch length
[lp,tr,tf] = patchlength(Ru,beta,Fz./Kz,ccons,alp,p_i,omega,cdamp);

% Rolling Radius
Rl=Ru-Fz./Kz;

% Longitudinal and lateral element stiffness
Cs=funsat(Csparam,Fz);
Calph=funsat(Calphparam,Fz);
Cgamma=funsat(Cgammaparam,Fz);

% Calculates coefficient of friction
mupmaxx=funmu(mupmaxxprm,Fz);
mupminx=funmu(mupminxprm,Fz);
```

```
musx=funmu(musxprm,Fz);
mupmaxy=funmu(mupmaxyprm,Fz);
mupminy=funmu(mupminyprm,Fz);
musy=funmu(musyprm,Fz);

% Friction decay modification
if speed<vref,
    speed=min(abs(speed),vref);
    Sx=Sx*(abs(speed)/vref);
else
    speed=speed;
    Sx=Sx*(abs(speed)/vref);
end

% Calculate simulation stiffness element parameters
kx=(2.*Cs./(b.*lp.^2));
ky=(2.*Calph./(b.*lp.^2));

% Calculate the coefficient of friction
mux=musxfun(musx, mupmaxx, mupminx, Sx, Sx, sp, sd, sdd);
muy=musyfun(musy, mupmaxy, mupminy, Sy, Sy, alphacp, alphac, alphacd);

% Calculate camber thrust
Fygamma=Cgamma.*tan(gammat);

% Calculate Rolling Resistance Force
Fx0=funsat(Fx0prm,Fz);
s0=-sign(sd).*(Fx0./Cs);
sd=sd+s0;

% Calculate Conicity and Plysteer Force
Fy0=funsat(Fy0prm,Fz);
alph0=-sign(alphac).*(Fy0./Calph);
alphac=alphac+alph0;

% Initial estimate of contact length
la=0.64e2 .* Fz .^ 2 ./ pi .^ 2 ./ b .^ 2 ./ lp .^ 3 ./ ((kx .^ 2 .*
abs(sd) .^ 2 ./ (1 - abs(sd)) .^ 2 ./ mux .^ 2) + ky .^ 2 .*
tan(alphac) .^ 2 ./ ((1 - abs(sd)) .^ 2) ./ muy .^ 2 + 0.64e2 .* Fz .^
2 ./ pi .^ 2 ./ b .^ 2 ./ lp .^ 4);

% Initial estimate of Lateral force
if isempty(find(isnan(la)>0.5))> 0,

    % Lateral Forces
    Fya=(0.3e1 .* b .* (la .^ 2) .* ky .* tan(alphac) .* Kb .* (lp .^
     2) ./ (-6 .* Kb .* lp .^ 2 + 6 .* Kb .* lp .^ 2 .* sd - 2 .* b .*
     la .^ 3 + 2 .* b .* la .^ 3 .* sd + 3 .* b .* la .^ 2 .* lp - 3 .*
     b .* la .^ 2 .* lp .* sd));
    Fys=(muy .^ 2 .* tan(alphac) .* Fz .* lp ./ pi ./ abs(lp) .* (muy
     .^ 2 .* tan(alphac) .^ 2 + mux .^ 2 .* sd .^ 2) .^ (-0.1e1 ./
     0.2e1) .* sign(lp) .* pi ./ 0.2e1 - 0.4e1 .* muy .^ 2 .*
     tan(alphac) .* Fz ./ lp ./ pi ./ abs(lp) .* (muy .^ 2 .*
     tan(alphac) .^ 2 + mux .^ 2 .* sd .^ 2) .^ (-0.1e1 ./ 0.2e1) .*
     sqrt((la .* lp - la .^ 2)) .* la + 0.2e1 .* muy .^ 2 .*
```

```
    tan(alphac) .* Fz ./ pi ./ abs(lp) .* (muy .^ 2 .* tan(alphac) .^
    2 + mux .^ 2 .* sd .^ 2) .^ (-0.1e1 ./ 0.2e1) .* sqrt((la .* lp -
    la .^ 2)) + muy .^ 2 .* tan(alphac) .* Fz .* lp ./ pi ./ abs(lp)
    .* (muy .^ 2 .* tan(alphac) .^ 2 + mux .^ 2 .* sd .^ 2) .^ (-0.1e1
    ./ 0.2e1) .* asin((-2 ./ abs(lp) .* la + 1 ./ abs(lp) .* lp)) +
    0.8e1 ./ 0.3e1 .* muy .^ 2 .* tan(alphac) .* Fz ./ pi ./ abs(lp)
    .* (muy .^ 2 .* tan(alphac) .^ 2 + mux .^ 2 .* sd .^ 2) .^ (-0.1e1
    ./ 0.2e1) .* A1 .* sd .* la .* sqrt((la .* lp - la .^ 2)) - 0.8e1
    ./ 0.3e1 .* muy .^ 2 .* tan(alphac) .* Fz ./ lp ./ pi ./ abs(lp)
    .* (muy .^ 2 .* tan(alphac) .^ 2 + mux .^ 2 .* sd .^ 2) .^ (-0.1e1
    ./ 0.2e1) .* A1 .* sd .* (la .^ 2) .* sqrt((la .* lp - la .^ 2)));
    Fyp=-(Fya-Fys);
    Fyb=Fyp+Fygamma;

else

    Imax=find(isnan(la)>0.5);
    if length(lp)>1,
        la(Imax)=lp(Imax)-0.0000001;
    else
        la(Imax)=lp-0.0000001;
    end
    mux=muxt;
    muy=muyt;
    % Lateral Forces
    Fya=(0.3e1 .* b .* (la .^ 2) .* ky .* tan(alphac) .* Kb .* (lp .^
    2) ./ (-6 .* Kb .* lp .^ 2 + 6 .* Kb .* lp .^ 2 .* sd - 2 .* b .*
    la .^ 3 + 2 .* b .* la .^ 3 .* sd + 3 .* b .* la .^ 2 .* lp - 3 .*
    b .* la .^ 2 .* lp .* sd));
    Fys=(muy .^ 2 .* tan(alphac) .* Fz .* lp ./ pi ./ abs(lp) .* (muy
    .^ 2 .* tan(alphac) .^ 2 + mux .^ 2 .* sd .^ 2) .^ (-0.1e1 ./
    0.2e1) .* sign(lp) .* pi ./ 0.2e1 - 0.4e1 .* muy .^ 2 .*
    tan(alphac) .* Fz ./ lp ./ pi ./ abs(lp) .* (muy .^ 2 .*
    tan(alphac) .^ 2 + mux .^ 2 .* sd .^ 2) .^ (-0.1e1 ./ 0.2e1) .*
    sqrt((la .* lp - la .^ 2)) .* la + 0.2e1 .* muy .^ 2 .*
    tan(alphac) .* Fz ./ pi ./ abs(lp) .* (muy .^ 2 .* tan(alphac) .^
    2 + mux .^ 2 .* sd .^ 2) .^ (-0.1e1 ./ 0.2e1) .* sqrt((la .* lp -
    la .^ 2)) + muy .^ 2 .* tan(alphac) .* Fz .* lp ./ pi ./ abs(lp)
    .* (muy .^ 2 .* tan(alphac) .^ 2 + mux .^ 2 .* sd .^ 2) .^ (-0.1e1
    ./ 0.2e1) .* asin((-2 ./ abs(lp) .* la + 1 ./ abs(lp) .* lp)) +
    0.8e1 ./ 0.3e1 .* muy .^ 2 .* tan(alphac) .* Fz ./ pi ./ abs(lp)
    .* (muy .^ 2 .* tan(alphac) .^ 2 + mux .^ 2 .* sd .^ 2) .^ (-0.1e1
    ./ 0.2e1) .* A1 .* sd .* la .* sqrt((la .* lp - la .^ 2)) - 0.8e1
    ./ 0.3e1 .* muy .^ 2 .* tan(alphac) .* Fz ./ lp ./ pi ./ abs(lp)
    .* (muy .^ 2 .* tan(alphac) .^ 2 + mux .^ 2 .* sd .^ 2) .^ (-0.1e1
    ./ 0.2e1) .* A1 .* sd .* (la .^ 2) .* sqrt((la .* lp - la .^ 2)));
    Fyp=-(Fya-Fys);
    Fyb=Fyp+Fygamma;

    % Determines the value of the forces at la=lp
    Fxa(Imax)=0;
    Fxs(Imax)=0;
    Fx(Imax)=0;
    Fya(Imax)=0;
    Fys(Imax)=0;
    Fyp(Imax)=0;
```

```
    Fyb(Imax)=0;
end


% Calculates length of adhesion
a1=0.64e2 .* Fz .^ 2 .* A1 .^ 2 .* (abs(sd) .^ 2) ./ pi .^ 2 ./ b .^ 2
./ lp .^ 4 + Fyb .^ 2 ./ muy .^ 2 ./ Kb .^ 2 ./ lp .^ 4;
a2=-(2 .* Fyb .^ 2 ./ muy .^ 2 ./ Kb .^ 2 ./ lp .^ 3) + 0.128e3 .* Fz
.^ 2 .* A1 .* abs(sd) ./ pi .^ 2 ./ b .^ 2 ./ (lp .^ 4) - 0.128e3 .* Fz
.^ 2 .* A1 .^ 2 .* (abs(sd) .^ 2) ./ pi .^ 2 ./ b .^ 2 ./ (lp .^ 3) +
0.2e1 .* ky .* tan(alphac) .* Fyb ./ (muy .^ 2) ./ (1 - abs(sd)) ./ Kb
./ (lp .^ 2);
a3=ky .^ 2 .* tan(alphac) .^ 2 ./ muy .^ 2 ./ ((1 - abs(sd)) .^ 2) +
(kx .^ 2 .* abs(sd) .^ 2 ./ (1 - abs(sd)) .^ 2 ./ mux .^ 2) - 0.192e3
.* Fz .^ 2 .* A1 .* abs(sd) ./ pi .^ 2 ./ b .^ 2 ./ lp .^ 3 + 0.64e2 .*
Fz .^ 2 ./ pi .^ 2 ./ b .^ 2 ./ lp .^ 4 + Fyb .^ 2 ./ muy .^ 2 ./ Kb .^
2 ./ lp .^ 2 + 0.80e2 .* Fz .^ 2 .* A1 .^ 2 .* (abs(sd) .^ 2) ./ pi .^
2 ./ b .^ 2 ./ lp .^ 2 - 0.2e1 .* ky .* tan(alphac) .* Fyb ./ muy .^ 2
./ (1 - abs(sd)) ./ Kb ./ lp;
a4=-0.64e2 .* Fz .^ 2 ./ pi .^ 2 ./ b .^ 2 ./ lp .^ 3 - 0.16e2 .* Fz .^
2 .* A1 .^ 2 .* (abs(sd) .^ 2) ./ pi .^ 2 ./ b .^ 2 ./ lp + 0.64e2 .*
Fz .^ 2 .* A1 .* abs(sd) ./ pi .^ 2 ./ b .^ 2 ./ lp .^ 2;
la=((1 ./ a1) .* ((36 .* a3 .* a2 .* a1) - (108 .* a4 .* a1 .^ 2) - (8
.* a2 .^ 3) + 0.12e2 .* sqrt(0.3e1) .* sqrt((4 .* a3 .^ 3 .* a1 - a3 .^
2 .* a2 .^ 2 - 18 .* a3 .* a2 .* a1 .* a4 + 27 .* a4 .^ 2 .* a1 .^ 2 +
4 .* a4 .* a2 .^ 3)) .* a1) .^ (0.1e1 ./ 0.3e1) ./ 0.6e1 - 0.2e1 ./
0.3e1 .* (3 .* a3 .* a1 - a2 .^ 2) ./ a1 .* ((36 .* a3 .* a2 .* a1) -
(108 .* a4 .* a1 .^ 2) - (8 .* a2 .^ 3) + 0.12e2 .* sqrt(0.3e1) .*
sqrt((4 .* a3 .^ 3 .* a1 - a3 .^ 2 .* a2 .^ 2 - 18 .* a3 .* a2 .* a1 .*
a4 + 27 .* a4 .^ 2 .* a1 .^ 2 + 4 .* a4 .* a2 .^ 3)) .* a1) .^ (-0.1e1
./ 0.3e1) - (a2 ./ a1) ./ 0.3e1);


% Calculate the final lateral forces
if isempty(find(isnan(la)>0.5))> 0,

    % Calculate Longitudinal and lateral forces for la<lp
    % Longitudinal Forces
    Fxa=((b .* kx .* sd ./ (1 - sd) .* la .^ 2) ./ 0.2e1);
     Fxs=(-mux .^ 2 .* sd .* Fz .* (-0.3e1 .* lp .^ 2 .* sign(lp) .* pi
     + 0.24e2 .* sqrt(-la .* (la - lp)) .* la - 0.12e2 .* sqrt(-la .*
     (la - lp)) .* lp + 0.6e1 .* lp .^ 2 .* asin((0.2e1 .* la - lp) ./
     abs(lp)) + 0.16e2 .* A1 .* sd .* la .^ 2 .* sqrt(-la .* (la - lp))
     - 0.16e2 .* A1 .* sd .* la .* sqrt(-la .* (la - lp)) .* lp) ./ lp
     ./ pi ./ abs(lp) .* (muy .^ 2 .* tan(alphac) .^ 2 + mux .^ 2 .* sd
     .^ 2) .^ (-0.1e1 ./ 0.2e1) ./ 0.6e1);
    Fx=(Fxa+Fxs);

    % Lateral Forces
    Fya=(0.3e1 .* b .* (la .^ 2) .* ky .* tan(alphac) .* Kb .* (lp .^
     2) ./ (-6 .* Kb .* lp .^ 2 + 6 .* Kb .* lp .^ 2 .* sd - 2 .* b .*
     la .^ 3 + 2 .* b .* la .^ 3 .* sd + 3 .* b .* la .^ 2 .* lp - 3 .*
     b .* la .^ 2 .* lp .* sd));
    Fys=(muy .^ 2 .* tan(alphac) .* Fz .* lp ./ pi ./ abs(lp) .* (muy
     .^ 2 .* tan(alphac) .^ 2 + mux .^ 2 .* sd .^ 2) .^ (-0.1e1 ./
     0.2e1) .* sign(lp) .* pi ./ 0.2e1 - 0.4e1 .* muy .^ 2 .*
```

```
    tan(alphac) .* Fz ./ lp ./ pi ./ abs(lp) .* (muy .^ 2 .*
    tan(alphac) .^ 2 + mux .^ 2 .* sd .^ 2) .^ (-0.1e1 ./ 0.2e1) .*
    sqrt((la .* lp - la .^ 2)) .* la + 0.2e1 .* muy .^ 2 .*
    tan(alphac) .* Fz ./ pi ./ abs(lp) .* (muy .^ 2 .* tan(alphac) .^
    2 + mux .^ 2 .* sd .^ 2) .^ (-0.1e1 ./ 0.2e1) .* sqrt((la .* lp -
    la .^ 2)) + muy .^ 2 .* tan(alphac) .* Fz .* lp ./ pi ./ abs(lp)
    .* (muy .^ 2 .* tan(alphac) .^ 2 + mux .^ 2 .* sd .^ 2) .^ (-0.1e1
    ./ 0.2e1) .* asin((-2 ./ abs(lp) .* la + 1 ./ abs(lp) .* lp)) +
    0.8e1 ./ 0.3e1 .* muy .^ 2 .* tan(alphac) .* Fz ./ pi ./ abs(lp)
    .* (muy .^ 2 .* tan(alphac) .^ 2 + mux .^ 2 .* sd .^ 2) .^ (-0.1e1
    ./ 0.2e1) .* A1 .* sd .* la .* sqrt((la .* lp - la .^ 2)) - 0.8e1
    ./ 0.3e1 .* muy .^ 2 .* tan(alphac) .* Fz ./ lp ./ pi ./ abs(lp)
    .* (muy .^ 2 .* tan(alphac) .^ 2 + mux .^ 2 .* sd .^ 2) .^ (-0.1e1
    ./ 0.2e1) .* A1 .* sd .* (la .^ 2) .* sqrt((la .* lp - la .^ 2)));
    Fyp=(Fya-Fys);
    Fy=Fyp+Fygamma;
else

    Imax=find(isnan(la)>0.5);
    if length(lp)>1,
        la(Imax)=lp(Imax)-0.0000001;
    else
        la(Imax)=lp-0.0000001;
    end

    % Calculate Longitudinal and lateral forces for la=lp
    % Longitudinal Forces
    Fxa=((b .* kx .* sd ./ (1 - sd) .* la .^ 2) ./ 0.2e1);
    Fxs=(-mux .^ 2 .* sd .* Fz .* (-0.3e1 .* lp .^ 2 .* sign(lp) .* pi
    + 0.24e2 .* sqrt(-la .* (la - lp)) .* la - 0.12e2 .* sqrt(-la .*
    (la - lp)) .* lp + 0.6e1 .* lp .^ 2 .* asin((0.2e1 .* la - lp) ./
    abs(lp)) + 0.16e2 .* A1 .* sd .* la .^ 2 .* sqrt(-la .* (la - lp))
    - 0.16e2 .* A1 .* sd .* la .* sqrt(-la .* (la - lp)) .* lp) ./ lp
    ./ pi ./ abs(lp) .* (muy .^ 2 .* tan(alphac) .^ 2 + mux .^ 2 .* sd
    .^ 2) .^ (-0.1e1 ./ 0.2e1) ./ 0.6e1);
    Fx=(Fxa+Fxs);

    % Lateral Forces
    Fya=(0.3e1 .* b .* (la .^ 2) .* ky .* tan(alphac) .* Kb .* (lp .^
    2) ./ (-6 .* Kb .* lp .^ 2 + 6 .* Kb .* lp .^ 2 .* sd - 2 .* b .*
    la .^ 3 + 2 .* b .* la .^ 3 .* sd + 3 .* b .* la .^ 2 .* lp - 3 .*
    b .* la .^ 2 .* lp .* sd));
    Fys=(muy .^ 2 .* tan(alphac) .* Fz .* lp ./ pi ./ abs(lp) .* (muy
    .^ 2 .* tan(alphac) .^ 2 + mux .^ 2 .* sd .^ 2) .^ (-0.1e1 ./
    0.2e1) .* sign(lp) .* pi ./ 0.2e1 - 0.4e1 .* muy .^ 2 .*
    tan(alphac) .* Fz ./ lp ./ pi ./ abs(lp) .* (muy .^ 2 .*
    tan(alphac) .^ 2 + mux .^ 2 .* sd .^ 2) .^ (-0.1e1 ./ 0.2e1) .*
    sqrt((la .* lp - la .^ 2)) .* la + 0.2e1 .* muy .^ 2 .*
    tan(alphac) .* Fz ./ pi ./ abs(lp) .* (muy .^ 2 .* tan(alphac) .^
    2 + mux .^ 2 .* sd .^ 2) .^ (-0.1e1 ./ 0.2e1) .* sqrt((la .* lp -
    la .^ 2)) + muy .^ 2 .* tan(alphac) .* Fz .* lp ./ pi ./ abs(lp)
    .* (muy .^ 2 .* tan(alphac) .^ 2 + mux .^ 2 .* sd .^ 2) .^ (-0.1e1
    ./ 0.2e1) .* asin((-2 ./ abs(lp) .* la + 1 ./ abs(lp) .* lp)) +
    0.8e1 ./ 0.3e1 .* muy .^ 2 .* tan(alphac) .* Fz ./ pi ./ abs(lp)
    .* (muy .^ 2 .* tan(alphac) .^ 2 + mux .^ 2 .* sd .^ 2) .^ (-0.1e1
    ./ 0.2e1) .* A1 .* sd .* la .* sqrt((la .* lp - la .^ 2)) - 0.8e1
```

```
     ./ 0.3e1 .* muy .^ 2 .* tan(alphac) .* Fz ./ lp ./ pi ./ abs(lp)
     .* (muy .^ 2 .* tan(alphac) .^ 2 + mux .^ 2 .* sd .^ 2) .^ (-0.1e1
     ./ 0.2e1) .* A1 .* sd .* (la .^ 2) .* sqrt((la .* lp - la .^ 2)));
    Fyp=(Fya-Fys);
    Fy=Fyp+Fygamma;

    % Determines the value of the forces at la=lp
    Fxa(Imax)=0;
    Fxs(Imax)=0;
    Fx(Imax)=0;
    Fya(Imax)=0;
    Fys(Imax)=0;
    Fyp(Imax)=0;
    Fy(Imax)=0;
end

% Calculate the moment arms
% Overturning moment
Cmxg=funquad(Cmxgprm,Fz);
Cmxa=funquad(Cmxaprm,Fz);
Mx=-Cmxg.*(Cgamma+Fz).*Rl.*sin(gammat)-Cmxa.*Fyp;

% Aligning moment
Cmz1=funquad(Cmz1prm,Fz);
Cmz2=funquad(Cmz2prm,Fz);
Cmz3=funquad(Cmz3prm,Fz);
Mz=funkz([Cmz1,Cmz2,Cmz3],alphac).*(Fyp.*cos(gammat)+Cgamma.*sin(gammat
));
```

B. Main Subroutine For Off-Road Tire Model

```
function [Fx,Fy,Mx,Mz] = offroadtire(Fz,gammat,sd,alphac,omega)

% Brendan J. Chan 2007
% off-road tire model code
% limits the input to bounded conditions


% ---------------- Parameters ----------------------

% Insert tire/soil parameters here


Tireparam


% ------------------------ Program starts here ----------------------%
inline functions
% N factors
funNq=@(x) (exp(2.*(3.*pi/4-x/2).*tan(x)))/(2.*cos(pi/4+x/2).^2);
funNc=@(x) cot(x).*(((exp(2.*(3.*pi/4-
x/2).*tan(x)))/(2.*cos(pi/4+x/2).^2))-1);
funNg=@(x) 2.*(((exp(2.*(3.*pi/4-
x/2).*tan(x)))/(2.*cos(pi/4+x/2).^2))+1).*tan(x);

% Tire stiffness functions
funcubic =@(coeff,x)
coeff(1).*x.^3+coeff(2).*x.^2+coeff(3).*x+coeff(4);
funquad =@(coeff,x) coeff(1).*x.^2+coeff(2).*x+coeff(3);
funkz=@(coeff,x) coeff(1)+(coeff(2)-
coeff(1)).*(sech(coeff(3).*(abs(tan(x))./(1-abs(tan(x))))));
funsat=@(coeff,x) coeff(1).*(1-exp(-coeff(2).*x));

% Calculate tire curvature as a function of longitudinal coordinate
zcurve=@(arg,coeff) -coeff(2).*(cos(coeff(1))-cos(asin(sin(coeff(1))-
arg./coeff(2))));

% Limits the slip angle and slip ratio
sd=min(abs(sd),0.99).*sign(sd);
alphac=min(abs(alphac),pi/4).*sign(alphac);

% Initial calculation to determine
% Calculate the carcass limit pressure
pc=beta*(alp*p_i+ccons)/(2*Ru^2)*b;
Kz0=pc;

% Calculate initial entry angle
[thetae,costval] = fminsearch(@(x)
thetaefun(x,inc,thetab,Ru,b,kc,kphi,gammas,c,n,Kx,Ky,phi,sd,alphac,Fz),
deg2rad(10),optimset('Display','off'));
theta=thetae:-inc:thetab;

% Calculate initial Radial Stress
```

```
sigmaval=sigman(theta,thetab,thetae,Ru,b,kc,kphi,c,gammas,n,phi,sd);

% Decide whether rigid wheel tire model or flexible ring tire model is
to be used
if pc<max(sigmaval),
    % use flexible tire model
    % Needs the functions
    % thetaefun2.m
    % sigmant.m
    % tauxt.m
    % tauyt.m
    % calculate the entry angle

    % Flexible tire formulation
    % Vertical Stiffness modeling
    initdel=Fz/Kz0;
    Cz1=funcubic(Cz1prm,initdel) ;
    Cz2=funquad(Cz2prm,initdel) ;
    Kz=funkz([Cz1,1,Cz2],alphac).*Kz0;

    % Rolling Radius
    Rl=Ru-Fz./Kz;

    % Calculates thetan
    a=tan(pi./4-phi./2);
     thetaes=abs(atan2(abs(-(-(0.1e1 + sqrt((-2 .* a .^ 2 .* sd + a .^
     2 .* sd .^ 2 - 2 .* a .^ 4 .* sd + a .^ 4 .* sd .^ 2 + a .^ 4)))
     ./ (1 + a .^ 2) + 0.1e1) ./ a ./ (-1 + sd)), abs(-(0.1e1 + sqrt((-
     2 .* a .^ 2 .* sd + a .^ 2 .* sd .^ 2 - 2 .* a .^ 4 .* sd + a .^ 4
     .* sd .^ 2 + a .^ 4))) ./ (1 + a .^ 2) ./ (-1 + sd))));

    % limits thetan to 1/3 of phi, based on the retaining wall problem
    if thetaes>0,
        thetaes=min(abs(thetaes),(1/3).*phi).*sign(thetaes);
    else
        thetaes=min(abs(thetaes),0).*sign(thetaes);
    end

    % Calculate entry angle
    [thetae,costval] = fminsearch(@(x)
     thetaefun2(x,inc,thetab,Ru,b,kc,kphi,gammas,c,n,Kx,Ky,phi,sd,alpha
     c,Fz,beta,Fz/Kz,ccons,alp,p_i,omega,cdamp,pc),thetaes+deg2rad(10),
     optimset('Display','off'));

    % Set up the angle vector
    theta=thetae:-inc:thetab;

    %sweeps the angles to calculate the radial shape
    [Reff] = radialdef(Ru,beta,Fz./Kz,ccons,alp,p_i,omega,cdamp,theta-
     thetaes);

    % Radial Stress Calculations

     sigmaval=sigmant(theta,thetab,thetae,Reff,b,kc,kphi,c,gammas,n,phi
     ,sd,pc);
```

```
% Maximum stress envelope

taum=(c+sigmant(theta,thetab,thetae,Reff,b,kc,kphi,c,gammas,n,phi,
sd,pc).*tan(phi));
taum(1)=0;
taum(end)=0;

% Lateral shear stress

tausy=tauyt(theta,thetab,thetae,Reff,b,kc,kphi,gammas,c,n,Kx,Ky,ph
i,sd,alphac,pc);

% Longitudinal shear stress

tausx=tauxt(theta,thetab,thetae,Reff,b,kc,kphi,gammas,c,n,Kx,Ky,ph
i,sd,alphac,pc);

% Calculate wheel vertical load
if omega==0,
    W = - b.*(trapz(Reff.*sigmaval.*cos(theta)).*inc);
else
    W = - b.*( trapz(Reff.*tausx.*sin(theta)).*inc +
    trapz(Reff.*sigmaval.*cos(theta)).*inc);
end

% Longitudinal Force
if omega==0,
    if sd==0,
        Fx= 0;
    else
        Fx=  b.*( trapz(Reff.*tausx.*cos(theta)).*inc -
        trapz(Reff.*sigmaval.*sin(theta)).*inc);
    end
else
        Fx=  b.*( trapz(Reff.*tausx.*cos(theta)).*inc -
        trapz(Reff.*sigmaval.*sin(theta)).*inc);
End


Cgamma=funsat(Cgammaparam,Fz);
if abs(alphac)<1e-8,
    % Lateral shear stress force
    Fy=0;
    Fycp=0;
    FBD=0;
else
    % Lateral shear stress force
    Fycp= b.*( trapz(Reff.*tausy).*inc );

    % Calculate the bulldozing force
    if abs(thetae)<1e-6,
        % if sinkage is zero, the bulldozing force is zero
        FBD=0;
    else
        xin=inc:inc:2*Ru*sin(thetae);
```

```
            [Ref] =
            radialdef(Ru,beta,Fz./Kz,ccons,alp,p_i,omega,cdamp,asin(sin
            (thetae)-xin./Ru));
            m=tan(pi/4+phi/2);
            qm=(gammas.*Ref.*(2.*thetae-
            sin(2.*thetae)).*xin.*tan(alphac))./(m.*zcurve(xin,[thetae,
            Ref]));

            PBD=(gammas.*(zcurve(xin,[thetae,Ref]).^2).*funNg(phi)+c.*(
            zcurve(xin,[thetae,Ref])).*funNc(phi)+abs(qm).*(zcurve(xin,
            [thetae,Ref])).*funNq(phi)).*cos(atan2(xin.*tan(alphac)./Kb
            ,(Ru-Rw))+gammat).*tan(alphac);
            FBD=trapz(PBD).*inc;

            % calculate the total lateral force
            Fy= -(Fycp+FBD)+Cgamma.*tan(gammat);
        end
    end

    % Overturning moment
    Cmxg=funquad(Cmxgprm,Fz);
    Cmxa=funquad(Cmxaprm,Fz);
    Cgamma=funsat(Cgammaparam,Fz);

     Mx=Cmxg.*(Cgamma+Fz).*Rl.*sin(gammat)+Cmxa.*Fycp+Rl.*cos(gammat).*
     FBD;

    % Aligning moment
    Cmz1=funquad(Cmz1prm,Fz);
    Cmz2=funquad(Cmz2prm,Fz);
    Cmz3=funquad(Cmz3prm,Fz);
    Mz=-
     funkz([Cmz1,Cmz2,Cmz3],alphac).*(Fycp.*cos(gammat)+Cgamma.*sin(gam
     mat))+Ru.*sin(thetae).*FBD;

else
    % use rigid wheel model
    % Needs the functions
    % thetaefun.m
    % sigman.m
    % taux.m
    % tauy.m
    % Rigid wheel formulation

    % Calculates thetan initially
    a=tan(pi./4-phi./2);
    thetaes=abs(atan2(abs(-(-(0.1e1 + sqrt((-2 .* a .^ 2 .* sd + a .^ 2
     .* sd .^ 2 - 2 .* a .^ 4 .* sd + a .^ 4 .* sd .^ 2 + a .^ 4))) ./
     (1 + a .^ 2) + 0.1e1) ./ a ./ (-1 + sd)), abs(-(0.1e1 + sqrt((-2
     .* a .^ 2 .* sd + a .^ 2 .* sd .^ 2 - 2 .* a .^ 4 .* sd + a .^ 4
     .* sd .^ 2 + a .^ 4))) ./ (1 + a .^ 2) ./ (-1 + sd))));

    % limits thetan to 1/3 of phi, based on the retaining wall problem
    if thetaes>0,
        thetaes=min(abs(thetaes),(1/3).*phi).*sign(thetaes);
    else
```

```
    thetaes=min(abs(thetaes),0).*sign(thetaes);
end

% Calculate entry angle
[thetae,costval] = fminsearch(@(x)
 thetaefun(x,inc,thetab,Ru,b,kc,kphi,gammas,c,n,Kx,Ky,phi,sd,alphac
 ,Fz),thetaes+deg2rad(10),optimset('Display','off'));
theta=thetae:-inc:thetab;

% Radial Stress Calculations

 sigmaval=sigman(theta,thetab,thetae,Ru,b,kc,kphi,c,gammas,n,phi,sd
 );

% Maximum stress envelope

 taum=(c+sigman(theta,thetab,thetae,Ru,b,kc,kphi,c,gammas,n,phi,sd)
 .*tan(phi));
taum(1)=0;
taum(end)=0;

% Lateral shear stress
 tausy=tauy(theta,thetab,thetae,Ru,b,kc,kphi,gammas,c,n,Kx,Ky,phi,s
 d,alphac);

% Longitudinal shear stress

 tausx=taux(theta,thetab,thetae,Ru,b,kc,kphi,gammas,c,n,Kx,Ky,phi,s
 d,alphac);

% Calculate wheel vertical load
if omega==0,
    W = - Ru.*b.*(trapz(sigmaval.*cos(theta)).*inc);
else
    W = - Ru.*b.*( trapz(tausx.*sin(theta)).*inc +
    trapz(sigmaval.*cos(theta)).*inc);
end

% Longitudinal Force
if omega==0,
    if sd==0,
        Fx= 0;
    else
        Fx=  Ru.*b.*( trapz(tausx.*cos(theta)).*inc -
        trapz(sigmaval.*sin(theta)).*inc);
    end
else
        Fx=  Ru.*b.*( trapz(tausx.*cos(theta)).*inc -
        trapz(sigmaval.*sin(theta)).*inc);
end

if abs(alphac)<1e-8,
    % Lateral shear stress force at alphac=0
    Fy=0;
    Fycp=0;
```

```
        FBD=0;
    else
        % Lateral shear stress force
        Fycp= Ru.*b.*( trapz(tausy).*inc );

        % Calculate the bulldozing force
        if abs(thetae)<1e-8,
            % if sinkage is zero, the bulldozing force is zero
            FBD=0;
        else
            xin=inc:inc:2*Ru*sin(thetae);
            m=tan(pi/4+phi/2);
            qm=(gammas.*Ru.*(2.*thetae-
            sin(2.*thetae)).*xin.*tan(alphac))./(m.*zcurve(xin,[thetae,
            Ru]));

            PBD=(gammas.*(zcurve(xin,[thetae,Ru]).^2).*funNg(phi)+c.*(z
            curve(xin,[thetae,Ru])).*funNc(phi)+abs(qm).*(zcurve(xin,[t
            hetae,Ru])).*funNq(phi)).*cos(gammat).*tan(alphac);
            FBD=trapz(PBD).*inc;

            % calculate the total lateral force
            Fy= -(Fycp+FBD).*cos(gammat)+Fz.*sin(gammat);
        end
    end

    % Overturning moment
    Mx=-Fz.*Ru.*sin(gammat)-Ru.*cos(gammat).*Fy;

    % Aligning moment
    Mz= Ru.*sin(thetaes).*Fycp+Ru.*sin(thetae).*FBD;

end
```

C. Simulation Parameters for the Model in Chapter 7

Tire Parameters

- Lug height H = 0.03 m
- Lug length from sidewall to sidewall (lateral) L = 0.35 m
- Lug width in the longitudinal direction (b1) = 0.075 m
- Number of lugs = 20
- Tire radius, R=0.65m

Table 10-1. Soil parameters used in generating the results from chapter 7

Soil Parameters	Clay	Sand
Density	1726.22 Kg/m^3	2319.7 Kg/m^3
Poisson's ratio	0.49	0.45
Shear wave velocity	610 m/s	500 m/s
Φ	34 deg	29 deg
Pore pressure parameter	88.3 x 10^3 N/m^2	293N/m^2
γ	15.7 kN/m^3	32 kN/m^3

Vita

Brendan Juin-Yih Chan was born in Kuching, Sarawak, Malaysia. He grew up in the City of Kuching and went to St. Joseph's Secondary School, where he developed a deep interest in understanding how electrical and mechanical systems work. Brendan received his Bachelor of Science degree in Electrical Engineering in 2003 with *Summa Cum Laude* from Michigan Technological University, specializing in electronic applications and control systems, and continued to pursue his graduate degree in Mechanical Engineering at Virginia Tech. His interest in vehicle dynamics started with his involvement with the Automotive Systems Enterprise, where he led a team of mechanical and electrical engineers to develop a semi-active suspension control module for Sport Utility Vehicles. Brendan decided to do his Ph.D at the Advanced Vehicle Dynamics Laboratory (part of the Center for Vehicle Systems and Safety) at Virginia Tech under the supervision of Dr. Corina Sandu to specialize in the field of vehicle dynamics. His dissertation research is on the modeling of off-road capable tire models for vehicle dynamics simulations. His supplementary area of research includes development of control algorithms for vehicle subsystems and multi-body dynamics modeling of mechanical systems. During his time in Virginia Tech, he received the Virginia Tech Graduate School Graduate Research and Development Project Grant in 2006 and the 2007 Virginia Tech Citizen Scholar Award for serving as the Chair of the College of Engineering Graduate Student Committee. Brendan completed the requirements of the quest for his Ph.D. in January 2008 and has accepted a position at Robert Bosch LLC. at Farmington Hills, MI.